



# **Optical Analysis of Impact Features in Aerogel From the Orbital Debris Collection Experiment on the *Mir* Station**

*Friedrich Hörz, Glen Cress, Mike Zolensky*

*NASA Johnson Space Center*

*Houston, Texas*

*Thomas H. See, Ronald P. Bernhard, and Jack L. Warren*

*Lockheed-Martin*

*Houston, Texas*

National Aeronautics and  
Space Administration

Lyndon B. Johnson Space Center  
Houston, Texas 77058

---

August 1999





## EXECUTIVE SUMMARY

The *Mir* Environmental Effects Package (MEEP) was deployed on the *Mir* station by STS-76 and retrieved, following 18 months in space, by STS 86. This payload, managed by Langley Research Center, included the orbital debris collector (ODC) that was designed and built at the Johnson Space Center. The objective of ODC was to capture and return analyzable residues of the man-made and natural particulate environment in low-Earth orbit for a detailed assessment of its compositional makeup and potential origins.

ODC exposed highly porous, low-density ( $0.02 \text{ g/cm}^3$ )  $\text{SiO}_2$  aerogel as the basic collector medium. Based on laboratory impact simulations by a number of groups, this material is ideally suited to gently decelerate and capture hypervelocity particles, as demonstrated by unmolten remnants of silicate and aluminum projectiles fired at velocities as high as 7 km/s. This capability offers a significant improvement over traditional, comparatively dense collector media, including those exposed on the long-duration exposure facility (LDEF). The latter resulted in pervasive melting, if not complete vaporization of many impactors, leaving little or no residue for analysis. The expectation was that ODC would return a larger number and wider diversity of particles than all previous collection efforts in low-Earth orbit.

Even cursory inspection of the returned ODC collectors revealed a surprising variety of impact features. The major class of slender, carrot-shaped penetration *tracks* was as expected from laboratory impacts, including the presence of trapped projectile residue at their termini. The typical length (L) to diameter (D) ratio of these tracks is  $L/D > 20$ , and as high as 40. A second class of features is rather shallow, with  $L/D$  ranging from 0.5 to 5. For the most part, these shallow *pits* did not contain measurable residues, and have no experimental analog at velocities as high as 7 km/s. Impact features exhibiting morphologies intermediate between these two extremes suggest that there is a morphological continuum. We suggest this continuum to be an evolutionary sequence related to impact velocity. The deep tracks reflect modest encounter velocities, consistent with unmolten penetrators at the terminus, while the shallow pits form above some threshold velocity that resulted in pervasive vapor production and thus, shallow penetration, combined with substantial, if not complete, loss of the impactor. Apparently, the utility of aerogel has a velocity dependent limit beyond which complete vaporization of the impactor may not be prevented. This threshold velocity for vaporization is unknown for aerogel but it is undoubtedly higher than for nonporous materials, rendering aerogel the vastly superior collector medium in low-Earth orbit.

A third group of impact features in the ODC aerogel is related to low-velocity impacts of co-orbiting flakes and liquid droplets, all human waste products and the result of wastewater dumps. These features are either very irregular in shape and shallow ( $L/D < 0.5$ ), associated with pervasively crushed aerogel and copious amounts of particulate impactor material, or they are very regular, round depressions of  $L/D = 1$  to 2. The latter possess a thin petri dish-shaped deposit in their bottoms that displays highly concentric qualities (e.g., color shades) suggesting in situ formation by evaporation from a liquid. The encounter with liquid droplets was also reported from other MEEP experiments.

ODC exposed two identical trays, Tray 1 nominally pointing into the ram direction, Tray 2 in the opposite direction. The macroscopic survey of all impact features  $> 3 \text{ mm}$  reveals Tray 1 to be dominated by low-velocity waste impacts,  $\sim 73\%$ , as opposed to 25% on Tray 2. Pits make up  $\sim 16\%$  on Tray 1 and 29% on Tray 2, and tracks compose the remaining 11% and 45% on Tray 1 and 2, respectively. The high-track abundance on Tray 2 is affected by discrete clusters of tracks, all of the same orientation (azimuth and inclination), suggesting that they resulted from a swarm of secondary projectiles from a local, primary impact. Detailed optical analysis of aerogel surfaces is time-consuming and, to date, is limited to features  $> 500 \mu\text{m}$  and to 30% of each tray surface. The distribution of track lengths on both trays is nearly identical. The radiants from which track-forming particles originated are random on both trays, except for the clustered impactors on Tray 2. The ratio of track length to residue size scatters widely, akin to experimental results, and attests to highly idiosyncratic penetration and mass-loss processes for individual aerogel impacts. Therefore, it is not possible to extract meaningful data regarding initial impactor mass from aerogels. As a consequence, particle-flux measurements derived from ODC are rather qualitative, although of the same order of magnitude than those derived from LDEF.

Harvesting and compositional analysis of individual particles is tedious, and significant effort went into the development of suitable techniques, minimizing the inadvertent loss of particles typically 10  $\mu\text{m}$  or smaller. The compositional analyses using scanning electron microscopes/energy dispersive X-ray spectroscopy methods concentrated on a survey-type inventory of diverse particle types and associated impact features. Accordingly, all flake and droplet features typically contain the biogenic elements K, Na, Cl, and P and must be assigned to human-waste products. All highly transparent pit features analyzed to date contain no detectable impactor residue; the latter is presumably vaporized, attesting to the high-velocity origin of these features. The majority of the carrot-shaped tracks contain analyzable residue. Among man-made particles we detected metallic Al, stainless steel, soldering compounds, and paint flakes. The swarm event is apparently due to some natural impactor, containing Fe, Mg, and Ca, that must have fragmented upon impact with a neighboring structure on *Mir*. One cosmic-dust particle was embedded in epoxy, microtomed, and investigated with transmission electron microscope methods, the first unmolten, natural particle ever to be retrieved from low-Earth orbit for such detailed textural and mineralogical studies.

In summary, the optical analysis of the *Mir* collectors is complete, as is the survey type assessment of man-made or natural classes of particles. Although ODC observations suggest that the utility of aerogel for the capture of hypervelocity particles may be velocity limited, its performance is vastly superior to traditional, nonporous media. Hundreds of impactor residues were returned by ODC. Future ODC efforts will concentrate on the compositional analysis of a statistically significant fraction of these particles and an improved assessment of their origins.

## ACKNOWLEDGMENTS

It is a pleasure to recognize the dedication of the STS-76 and STS-86 crews and of the Langley Research Center Mir Environmental Effects Package team under the leadership of G. Stover; without their efforts, skills, and care, the orbital debris collector would not have been successful. We also thank P. Tsou, Jet Propulsion Laboratory, for guidance and advice in handling and mounting the aerogel specimens manufactured in his laboratory. Lastly, substantial discussions with D.E. Brownlee, F. Cardenas, M. Cintala, W. Davidson, G. Haynes, D. Humes, N. Johnson, D. Kessler, W. Kinard, G. Levine, D. Potter, H. Zook and H. Yano improved on detailed instrument design, analytical objectives, instrument analysis, and interpretation of the present data.



# CONTENTS

INTRODUCTION .....	1
INSTRUMENT DESIGN .....	2
EXPOSURE ON <i>MIR</i> .....	4
POSTFLIGHT INSTRUMENT PROCESSING .....	6
MACROSCOPIC INSPECTION .....	10
Tracks .....	13
Pits .....	19
Shallow Depressions .....	27
Flakes .....	27
Liquid Droplets .....	28
Relative Frequencies .....	31
OPTICAL STUDIES .....	33
Procedures .....	33
Track Length .....	35
Residue Size and Flux Considerations .....	35
Track Length versus Projectile Residue .....	38
Particle Trajectories .....	40
DETAILED COMPOSITIONAL ANALYSIS .....	41
Sample Recovery and Preparation .....	42
Representative Results .....	45
Man-Made Particles .....	45
Natural Impactors .....	49
CONCLUSIONS .....	52
REFERENCES .....	53
APPENDIX A .....	57
APPENDIX B .....	133

## Figures

1 (A) 3-D view showing the major components for one of the two ODC trays and (B) Schematic cross-section of ODC showing the relationship of the MEEP container, interface plate, assembly frame, and hold-down grid .....	3
2 Overview of <i>Mir</i> illustrating major subsystems and a docked Shuttle .....	4
3 The orbiting <i>Mir</i> station and detailed view of US DM accommodating the four MEEP containers.....	5
4 On-orbit scenes during retrieval of the ODC experiment with the PPMD experiment in the foreground.....	6
5 Opening of the MEEP container in the FOILS Laboratory at JSC .....	7

6	Close-up photograph of the opened ODC experiment and individual aerogel tiles .....	8
7	Installation of Plexiglas covers that protected the aerogel collectors during most of the disassembly sequence .....	9
8	Removal of the protective Plexiglas cover and hold-down grid in class 1000 flow bench of the FOILS Laboratory .....	9
9	Freestanding assembly frame immediately following the removal of the aerogel tiles using a flexible plunger tool .....	10
10	Complete array of harvested tiles, from ODC tray 1, resting on the interface plate with their original flight orientation preserved .....	11
11	Transfer of the ODC aerogel collectors into individual plastic containers .....	12
12	Detail of the aerogel harvesting and handling procedures illustrating the use of a flexible spatula-like device to pick up the tiles .....	12
13	Representative “mug shot” of an individual aerogel tile showing that optical photography possesses adequate resolution to resolve impact features at scales of <1 mm .....	13
14	ODC collector mug shot showing tile 1F04, which exhibits a more typical track density .....	14
15	Examples of a typical track and pit, illustrating their dramatically different morphologies and the need for detailed morphological classification of all impact features in low-density aerogel .....	14
16	Morphological elements and definition of terms for an ODC track, and comparison with an experimental analog produced by a 50- $\mu$ m-diameter glass sphere at 6 km/s .....	15
17	Typical tracks observed in ODC aerogel .....	16
18	Example of a bifurcated track caused by the fragmentation of the penetrating impactor .....	18
19	Tile 2E01 contained the largest cluster of tracks, all having identical azimuthal orientation, as well as a modest inclination angle from the local horizontal .....	19
20	Detailed views of the swarm event in plan view and cross section .....	20
21	Examples of typical pit features in plan view and cross section .....	21
22	Plan view and cross sections of three pits, including a deep cylindrical cavity, a stubby example, and an essentially hemispherical pit .....	22
23	Largest impact feature observed on ODC, which happens to be a pit whose growth was unfortunately affected/terminated by the ODC assembly frame .....	24
24	Experimental impact features in 0.02 g/cm <sup>3</sup> aerogel .....	25
25	Relatively blunt-nosed, cylindrical cavity associated with a modest-size stylus .....	25
26	Traced outlines of ODC impact features arranged with decreasing L/D ratios illustrating the continuum in L/D ratios and the transitional sequence from tracks to pits .....	26
27	Unusually large flake impact in plan view and cross section .....	28
28	Additional examples of flake impacts, some having rounded and wetted appearances suggesting a mixture of solids and liquids .....	29

29	Typical examples of droplet impacts in plan view and cross section .....	30
30	The distribution of impact features >3 mm classified into three major categories.....	32
31	View of the optical inspection station consisting of scanning platform, binocular microscope, CCD camera, and interactive PC system of the JSC FOILS Laboratory .....	34
32	Location of the 24 tiles that have been scanned to date utilizing the FOILS Laboratory system.....	36
33	Frequency histogram of absolute track lengths > 0.5 mm encountered on ODC.....	37
34	Diameter versus depth relationships of ODC pits, separated into forward- and rearward-facing collector surfaces .....	38
35	The distribution of projectile residue sizes based on in situ measurements in unprocessed aerogel collectors using optical microscopy.....	39
36	Cumulative particle fluxes in the ODC aerogel and comparison with LDEF data .....	40
37	Track length versus diameter of the projectile residues for ODC trays 1 and 2.....	41
38	Azimuthal orientation of 148 tracks on ODC tray 1 and of 435 tracks on tray 2, the latter dominated by swarm particles of uniform direction .....	42
39	Rose diagram of azimuthal track orientations for tray 1 and tray 2; tray 2 is shown with and without the swarm event .....	43
40	Quantitative illustration of track orientations utilizing an equal-area stereo projection .....	44
41	Example of the detailed analysis of an individual droplet feature, including SEM imaging and EDS techniques .....	45
42	Large flake feature previously shown in Figure 29 .....	46
43	Detailed analysis of a man-made particle .....	47
44	Example of a particle, ~10 $\mu\text{m}$ in length, that resided at the terminus of a 1.2-mm-long track.....	48
45	A particle, ~6 mm in size, recovered from the left track in the inserted cross section of what are obviously "swarm" tracks, all of uniform orientation. ....	49
46	Another small particle recovered from the terminus of a typical swarm track ~500 $\mu\text{m}$ in length.....	50
47	Example of a natural particle .....	51

## Tables

1	Absolute and relative frequency of genuine tracks, pit-type features, and flake-depressions.....	31
---	--	----

## ACRONYMS

CCD	charge coupled device
CME	Chemistry of Micrometeoroids Experiment
DM	docking module
EVA	extravehicular activity
FOILS	Facility for the Optical Inspection of Large Surfaces
JPL	Jet Propulsion Laboratory
KSC	Kennedy Space Center
LaRC	Langley Research Center
LDEF	long-duration exposure facility
MEEP	<i>Mir</i> Environmental Effects Package
ODC	orbital debris collector
PPMD	polished plate meteoroid detector
TEM	transmission electron microscope



## INTRODUCTION

Man-made debris in low-Earth orbit (LEO) constitutes a population of hypervelocity projectiles that present a substantial collisional hazard to spacecraft. The damage will range from submicroscopic impact features that can adversely affect critical subsystems to the catastrophic fragmentation of entire spacecraft. Substantial progress has been accomplished during the past decade in characterizing the current debris population and its origins (Johnson and McKnight, 1991; Kessler, 1996). However, substantial uncertainties still exist, including the detailed mass distribution, flux, and origin(s) of debris particles  $< 1$  cm in size. Such small particles are far beyond the spatial resolution of ground-based observations and can only be characterized with in situ observations by flight instruments. The orbital debris collector (ODC) experiment, the subject of this report, is such an instrument. The objectives of ODC were to non-destructively collect debris particles in LEO and to return them to Earth for detailed mineralogical and compositional analyses. This information is indispensable to reconstruct the sources and origins of the debris population, and to develop strategies for their potential mitigation.

The basic instrument concept for ODC was an outgrowth of the successful analysis of hypervelocity impact features on returned materials from the Solar Maximum mission (Warren et al., 1989) or the Long-Duration Exposure Facility mission (LDEF; see Levine, 1991; 1992; 1993). Scanning electron microscope (SEM) methods combined with energy-dispersive X-ray spectroscopy (EDS) revealed the ability to differentiate, on compositional grounds, among man-made and natural impactors (Zolensky et al., 1992). The latter derive from asteroids and cometary sources (Brownlee, 1985) and are an inevitable component of the hypervelocity particle environment in LEO. A variety of compositional subclasses were recognized among the man-made debris particles, including paint flakes, human waste, steel, metallic aluminum, and aluminum oxide. Similarly, various natural particle types exist, including aggregate particles of chondritic bulk composition, and monomineralic silicates or sulfides (e.g., Berthaud et al., 1993; Amari et al., 1992; Hörz et al., 1993).

Of particular interest was the discovery of aluminum-rich particles on surfaces occupying the trailing edge of LDEF (Hörz et al., 1993; Bernhard et al., 1999), where collisions by man-made debris were not expected. These findings suggest particle sources in highly elliptical orbits, generally consistent with transfer vehicles to geosynchronous orbits and associated effluents ( $\text{Al}_2\text{O}_3$ ) from solid-fuel rocket motors (Kessler, 1992). Unfortunately, these detailed observations are confined to a single LDEF tray from the "Chemistry of Micrometeoroids Experiment" (CME) that employed high-purity gold as the cratering substrate. Since most other LDEF surfaces were aluminum, it was not possible to analyze for aluminum in collection media that are themselves composed of aluminum. Using thin Be-foils of low X-ray absorption coefficient that permit for the analysis of oxygen with the above EDS methods, Bernhard et al., (1999) demonstrated the presence of both metallic aluminum (Al) and oxidized aluminum ( $\text{Al}_2\text{O}_3$ ) impactors in the LDEF gold substrates.

The differentiation into metallic or oxidized impactors is significant, since two major source mechanisms are implied. Inadvertent collisional processes most likely produce the metallic particles from structural aluminum, while the oxidized particles are combustion products of solid rocket fuels and the products of deliberate operational design and practice. These Al-rich particles were the most abundant man-made debris type encountered on LDEF's trailing edge and, as a result, are of substantial interest. What is the relative abundance of metallic versus oxidized species? This specific objective requires the exposure of collectors that are made from materials other than aluminum, and as a consequence, the collectors exposed by ODC were made from high-purity  $\text{SiO}_2$ .

The collectors exposed by ODC also took advantage of the substantial progress that had been made during the past decade in the basic technology of hypervelocity particle capture. Specifically, highly porous, foam-like materials have been developed and introduced (Werle et al., 1981; Tsou, 1995). The extremely low density ( $< 0.1$  g/cm<sup>3</sup>) of such materials results in only modest shock stresses being experienced by the impactor, even at high impact velocities. Indeed, the deceleration of hypervelocity particles in such highly porous media seems to be largely governed by classical continuum mechanics (i.e., viscous

drag forces and ablative processes), while shock processes seem to be subordinate, following Anderson and Ahrens (1994). However, this conclusion is valid only if the thickness of the solids, such as membranes or fibers, that compose the collector are small compared to typical impactor dimensions. If the dimensions of the solids are on the order of typical impactor dimensions, the projectile will sense them as relatively massive, if not as infinite half-space targets, and severe shock becomes unavoidable. As SiO<sub>2</sub>-based aerogel is made up of a network of irregular chains and clusters of SiO<sub>4</sub> tetrahedra ~ 40 - 60 Å thick and 200 - 300 Å long, such materials easily meet this thickness criterion and are ideal for the deceleration of micron-sized projectiles. Laboratory impacts at 7 km/s show that the total penetration depth of 50 mm glass projectiles is typically 200 - 300 times the projectile diameter in 0.02 g/cm<sup>3</sup> aerogel, thus necessitating collector thicknesses for flight instruments approaching centimeters (Hörz et al., 1997). The technology to manufacture aerogels of such thicknesses, specifically those based on SiO<sub>2</sub> (Fricke, 1988; Hrubesch and Poco, 1990; Tsou, 1995), is also a relatively recent development, as is the ability to manufacture aerogels of densities as low as 0.02 g/cm<sup>3</sup>.

As summarized by Tsou (1995) and below, SiO<sub>2</sub>-based aerogel was successfully exposed in space and returned to Earth prior to ODC, yet densities were high (0.1 g/cm<sup>3</sup>), collector size was modest, and exposure times were short. The area/time product of the aerogel exposed by ODC is more than an order of magnitude larger than all prior aerogels combined, establishing ODC as the most significant opportunity to evaluate the performance of space-exposed aerogel in capturing analyzable particle residues for return to Earth and analysis. The continued development of optimum capture media for hypervelocity particle must be viewed as an integral part of orbital-debris (and cosmic-dust) studies in Earth orbit, as future experiments will be needed to monitor the short- and long-term evolution of these particle populations to assure safe flight operations in Earth orbit.

Combining these background materials and developments leads to the following justification for the deployment of ODC as part of the *Mir* Environmental Effects Package (MEEP):

- a. Capture and compositional characterization of orbital-debris particles and evaluation of their origins.
- b. Establish the relative frequency of metallic versus aluminum-oxide particles.
- c. Determine the relative roles of man-made debris and natural dust for the collisional hazard in LEO.
- d. Evaluate the performance of SiO<sub>2</sub>-based aerogel for the capture of hypervelocity particles and its utility in the long-term monitoring of the temporal evolution of the hypervelocity particle environment in LEO.

## INSTRUMENT DESIGN

ODC was one of four experiments composing the MEEP, a payload Langley Research Center (LaRC) designed and developed on behalf of the Space Station, and whose objectives were to assess the exterior environment of *Mir* (see <http://setas-www.larc.nasa.gov/setas/meep/meep.html>). This environment may be affected by different operational practices, as well as by different orbital inclination, 51° for *Mir* versus 28° for the Space Shuttle. All MEEP instruments were housed in identical containers that resembled metal suitcases. Each container possessed hinges that permitted the rotation, by 360°, of the top and bottom halves, each half containing an (essentially identical) instrument tray. The inside dimensions of each half container allowed for packages ~ 62 x 62 x 8 cm in dimensions. When closed, the experiment trays were stowed face-to-face; deployment on *Mir* involved rotation of the two halves such that they were back-to-back exposing the two collector surfaces into opposite viewing directions. Nominally, one tray pointed in the general forward (ram) direction, paralleling the orbital motion of *Mir*, with the second tray pointing into the antipodal direction. Deployment and retrieval of the MEEP containers was accomplished via dedicated extravehicular activity (EVA).

ODC employed SiO<sub>2</sub>-based aerogel produced at the Jet Propulsion Laboratory (JPL), Pasadena, California (see <http://eande.lbl.gov/ECS/aerogels/satoc.htm> or <http://stardust.jpl.nasa.gov/index.html>).

Preliminary impact tests with such aerogels and velocities up to 7 km/s revealed that particles residing at the terminus of long, carrot-shaped penetration tracks were essentially unmelted (Tsou et al., 1988; Barrett et al., 1992; Mendez, 1994; Tsou, 1995; Burchell and Thomson, 1996; Hörz et al., 1997). Consistent with JPL's state-of-the-art aerogel manufacture capabilities, we impact-tested a series of aerogels ranging in density from 0.01 to 0.05 g/cm<sup>3</sup>, while most previous tests utilized aerogels of higher densities, typically 0.1 g/cm<sup>3</sup>. As documented in Hörz et al. (1997), track length strongly depends on the aerogel density, yet there is no clear, much less a strong, relationship between track length and mass of the recovered projectile residue. Nevertheless, the particles recovered from aerogels < 0.05 g/cm<sup>3</sup> were generally larger than those recovered from aerogels possessing higher densities. As a consequence, we selected the lowest-density aerogel of 0.02 g/cm<sup>3</sup> that could be reliably manufactured, in late 1995, into monolithic specimens of 10- x 10-cm surface dimension and ~ 11-mm thickness. This thickness was sufficient to terminate a (dense glass) particle of 50 mm diameter (at normal incidence at 7 km/s velocity). Aerogels < 0.02 g/cm<sup>3</sup> were largely experimental products in 1995 and not available in the proper thicknesses to be considered for ODC; they were also excessively cumbersome to handle and process.

Each half of the ODC MEEP package housed an identical instrument tray as illustrated in Figure 1A.

The major component of each tray was the *assembly frame*, fabricated from monolithic aluminum, 0.5" (12.5 mm) thick, containing 36 openings or cells, each 9.60 cm square. Most of the aerogel tiles were modestly over-sized (9.7 - 9.8 mm on a side) relative to the cell dimensions. Indeed, vibration and shock tests performed during flight-acceptance testing revealed that modest compression of aerogel is desirable to firmly secure the tiles within the assembly frame via frictional forces. Aerogel is surprisingly compressible and easily handled at low-strain rates, yet becomes fairly brittle, akin to glass, at high-strain rates. Many tiles were non-planar, on occasion even wavy and upturned at the edges. However, the 12.5-mm-deep assembly frame readily accommodated such deviations from the nominal tile thickness of 11 mm.

The tiles were press-fit into the assembly frame from the rear, with the frame resting face down on a flat surface to ensure a flush fit, and precluding any substantial protrusion(s) of aerogel above the frame surface. Following the installation of

all aerogel collectors, a solid aluminum plate (i.e., *interface plate*; 7 mm thick; see Figure 1) was attached to the back side of the assembly frame, while a red-anodized, 2-mm-thick aluminum *hold-down grid* (see Figure 1b) was attached to the frame's front surface. The openings of this hold-down grid were registered to those of the assembly frame, but possessed only 9.30-cm-square openings. This resulted in a 1.5-mm-wide overlap or

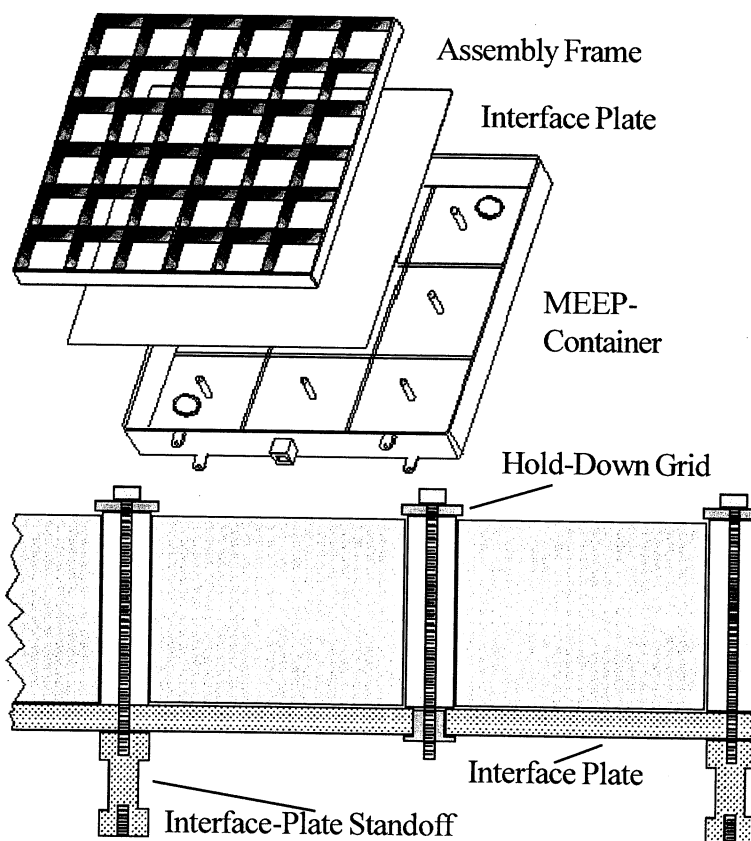


**Figure 1.** (A) 3-D view showing the major components for one of the two ODC trays and (B) Schematic cross-section of ODC showing the relationship of the MEEP container, interface plate, assembly frame, and hold-down grid.



reveal any anomalies with ODC after ~ 18 months of exposure. None of the delicate aerogel tiles seemed damaged, much less missing.

Due to a wide variety of unscheduled and—in part—poorly documented orbital maneuvers precipitated by a number of operational anomalies on *Mir*, the detailed orientation of ODC relative to the station's orbital motion remains poorly understood, as are geometric shielding factors by neighboring structures. Only recently has the detailed attitude data for *Mir* become available, but the time-consuming evaluation and analysis of these data have not been initiated. The neighboring PPMD experiment (see Figure 4) included a pinhole camera, which registered the impingement of atomic oxygen on an Ag-containing sensor surface, and thus, the relative movement of the instrument about *Mir*'s ram direction (Peters and Gregory, 1991). PPMD and ODC pointed into essentially identical directions, which was accomplished by means of registered fiducial marks that had been inscribed on the mounting brackets at Kennedy Space Center (KSC) during fit tests of the flight hardware. The PPMD pinhole camera yielded a substantially diffuse footpad of atomic-oxygen impingement rather than a single, sharp spot. This indicates that the orientation of PPMD (and ODC) relative to *Mir* was highly variable throughout the entire exposure period, and that there was no long-term (or cumulative) exposure in any well-defined pointing direction (Kinard, 1998).

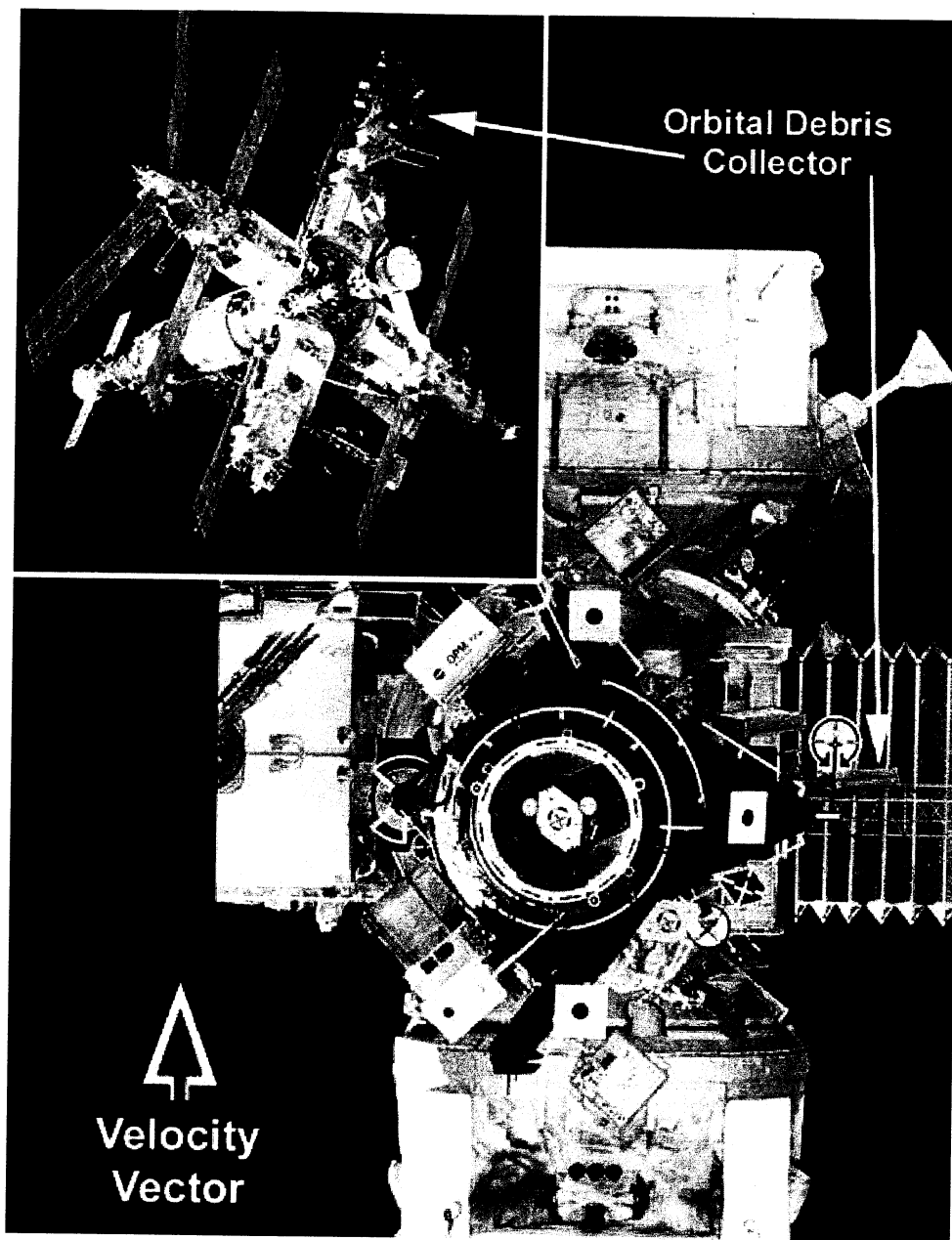


**Figure 3.** The orbiting *Mir* station (insert) and detailed view of US DM accommodating the four MEEP containers (all in the upper, right-hand quadrant relative to the center of the DM). The POSA I (to the right of the 12:00 position) and POSA II (to the right of the 6:00 position) experiments point straight at the viewer, while the two remaining MEEP containers (i.e., ODC and PPMD; between the 2:00 and 3:00 position) are essentially edge on. The PPMD shared a single handrail (white bar above triangular structure) with ODC.

## POSTFLIGHT INSTRUMENT PROCESSING

Following the return of STS 86, the MEEP container housing ODC was removed from the Shuttle's cargo bay at KSC, triple-bagged in a class 10,000 clean room, placed into a dedicated shipping container, and shipped to the Johnson Space Center (JSC), where it was received on October 10, 1997. After uncrating and removal of the outermost bag, the container was transferred to the Facility for the Optical Inspection of Large Surfaces (FOILS) laboratory where it was opened and disassembled. The FOILS laboratory is a class 10,000 clean room that contains two major work areas for the processing, inspection, and documentation of exposed flight

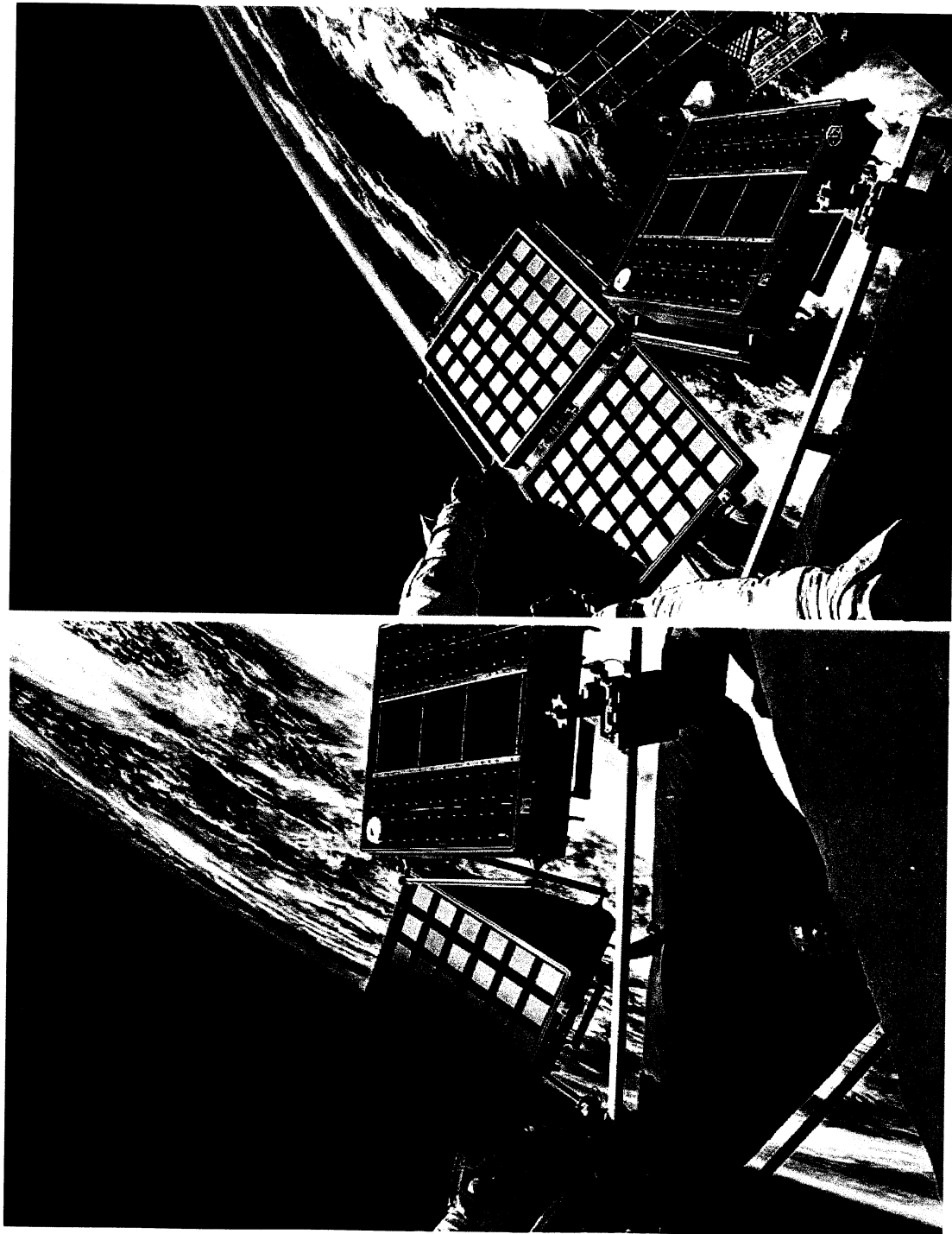


**Figure 4.** On-orbit scenes during retrieval of the ODC experiment with the PPMD experiment in the foreground. Tray 2 has been rotated - 10° (left) and ~ 180° (right) about hinges that permit the collectors to be stowed face-to-face for the return to Earth.

hardware: (a) a class 1,000 flow bench and (b) an automated scanning platform. This platform is equipped with an optical microscope and a high-resolution CCD camera that are controlled by a dedicated PC computer (see below). Note that all aerogel collectors are being processed and stored in the FOILS laboratory for the duration ODC's analysis phase (i.e., ~ 2 - 3 years).

After removing the remaining two protective bags, the exterior of the MEEP container, built from aluminum (6061-T6), was closely inspected for the presence of impact and/or contamination features. In general, the MEEP container's exterior and interior surfaces were relatively clean and pristine, with only modest, honey-colored staining in several exterior areas, akin to some of the LDEF surfaces, although much less pronounced than on LDEF. A total of nine hypervelocity craters, all < 500  $\mu\text{m}$  in diameter, were found

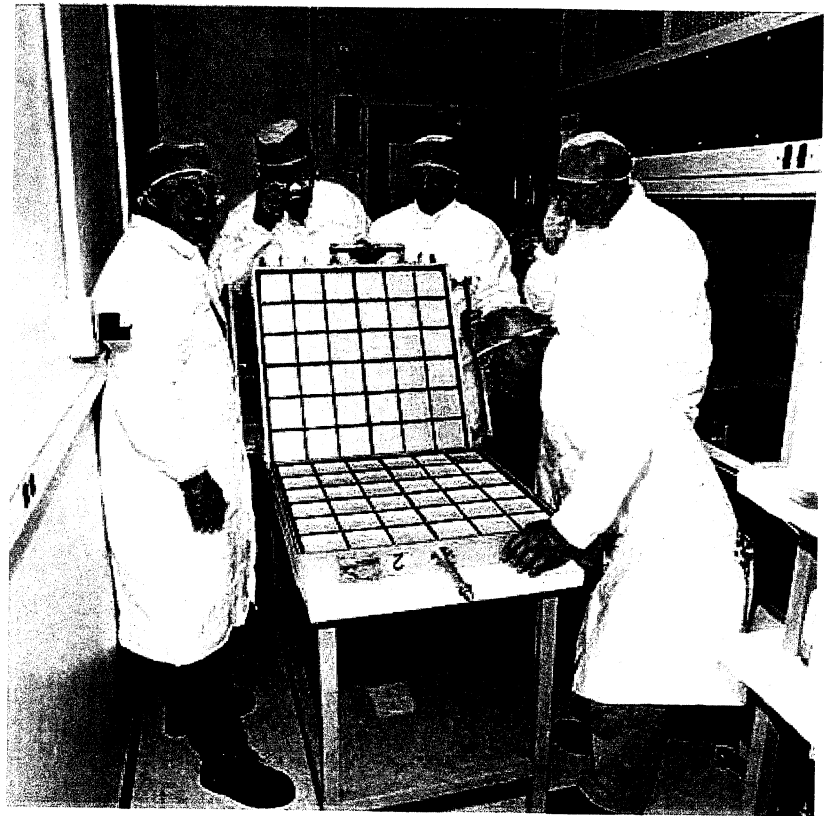


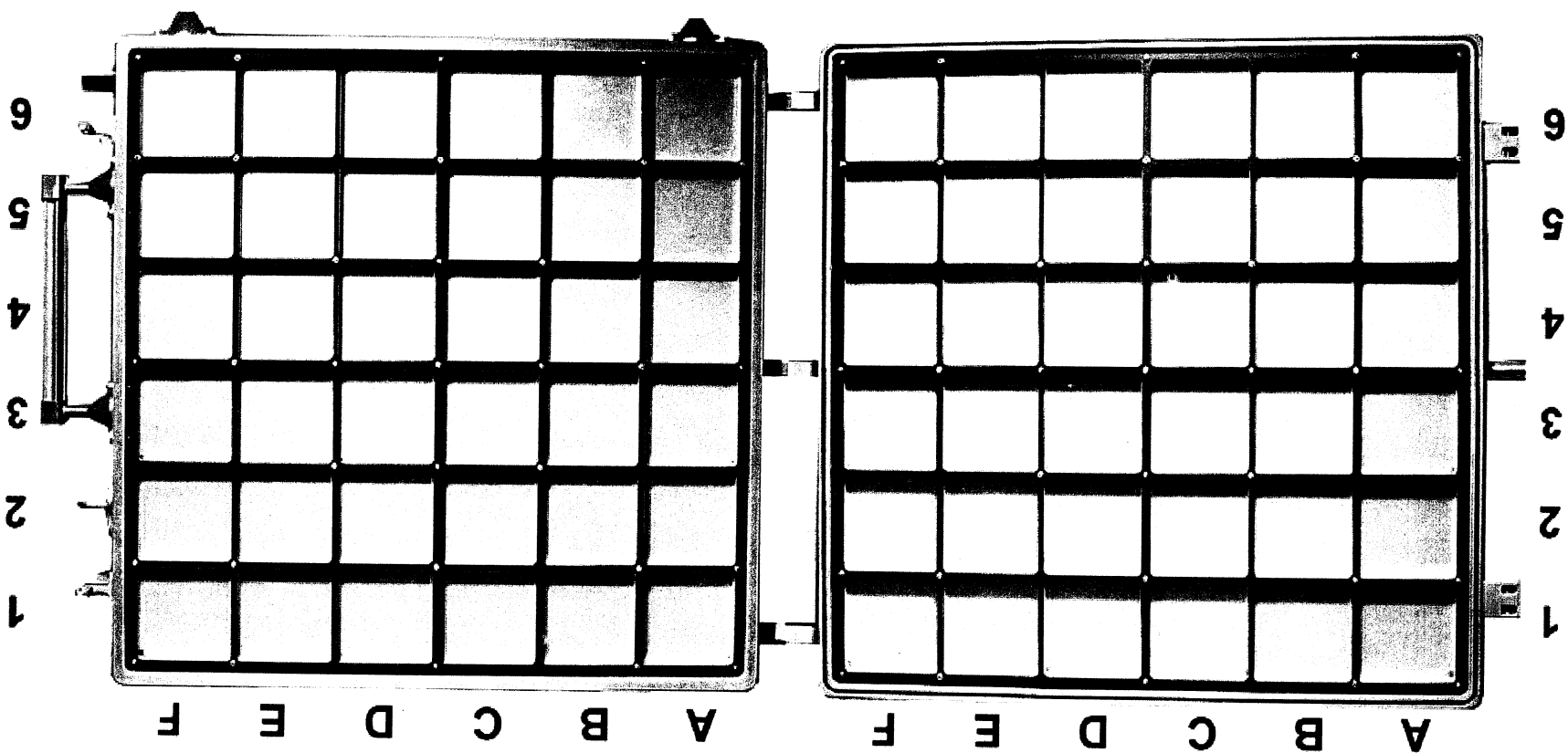
**Figure 5.** Opening of the MEEP container in the FOILS laboratory at JSC. Ram-pointing Tray 1 (foreground) rests on the table, while the wake-point Tray 2 (recognized by the handle bars) is rotated into a nearly vertical position.

on the exposed MEEP container surfaces. Following the inspection of the exterior surfaces, the container was opened as shown in Figures 5 and 6. All aerogel tiles were firmly in place and all but one were exceptionally pristine in appearance, attesting to aerogel's space worthiness and to highly successful EVA operations by the STS 76 and STS 86 crews, respectively. A number of large impact features and penetration tracks were readily apparent upon opening the MEEP container. Figure 6 shows the first images taken of the full trays, in their most pristine state, acquired immediately after opening. Figure 6 also illustrates the identification system we employed for individual tiles via letters (vertical columns) and numbers (horizontal rows). Note that the MEEP half containing the mounting bracket (substantially cropped, middle of left side) is arbitrarily defined as Tray 1, while the Tray 2 half possessed the handle, seen on the right side of Figure 6.

The in-flight orientation of each tile was preserved, with respect to the MEEP container, by placing a small silver dot, from a paint pen, in the lower left-hand corner of each tile. This mark served to orient the individual tiles during the ensuing investigations, with the marked corner representing the (0,0) origin of the X (horizontal) and Y (vertical) axes, permitting each impact feature to be recorded within tray-specific coordinates, which could be transferred to *Mir*, and ultimately to a geocentric frame of reference.

Following the initial photo-documentation of the opened MEEP container, a protective, transparent Plexiglas cover was installed over the exposed surfaces (Figure 7). This cover plate possessed small holes that allowed access to screws that were critical to the continued disassembly of the collectors. By unscrewing the standoff fasteners, each collector could be removed as a unit from the MEEP container to be placed onto a dedicated support structure inside the class 1,000 flow bench for further disassembly. The support structure held the assembly frame from the side for easy removal of the hold-down grid (Figure 8) and interface plate, being held together by bolts that could be unscrewed from the top. No tiles fell out of the assembly frame as the interface plate was removed and lowered ~ 15 mm to the surface of

Figure 6. Close-up photograph of the opened ODC experiment and individual aerogel tiles, each ~ 10 X 10 cm. Horizontal rows were assigned letters A - F (starting on left), while vertical columns were labeled 1 - 6. The two largest impact features on ODC can be seen towards the bottom of tile C04 (Tray 1) and on the extreme right-hand side of the hold-down grid of cell B01 (Tray 2).





the flow bench. At this point, the fully loaded frame was essentially free floating and merely supported at its periphery (Figure 9). Individual tiles could now be pushed downward with a plunger-like tool to land on the interface plate after an  $\sim 3$  cm free fall.

All tiles were dislodged from their respective frames during a single session, initially residing on the interface plate with their relative flight configurations completely preserved as seen in Figure 10. Note that individual tiles varied in color exhibiting shades of tan to brown. This coloration was not present in the tiles before flight and seems to be unrelated to the deposition of surface contaminants, since the color varies abruptly from tile to tile with specific color being relatively uniform for any given tile. The discoloration resulted from exposure to space; specific mechanisms that cause this tanning remain unexplored, yet we suspect that oxidation of organic contaminants was involved that apparently varied in concentration from tile to tile. As shown in Figures 11 and 12, individual tiles were then removed from the interface plate and transferred into clear, pre-labeled storage containers. In general, the aerogel was handled best by placing it carefully onto a stout sheet of paper, preferably black for maximum contrast and ease of seeing and tracking the transparent materials. Tray 1 was completely processed and harvested in this manner before Tray 2 was removed from the MEEP container and processed in an identical manner.

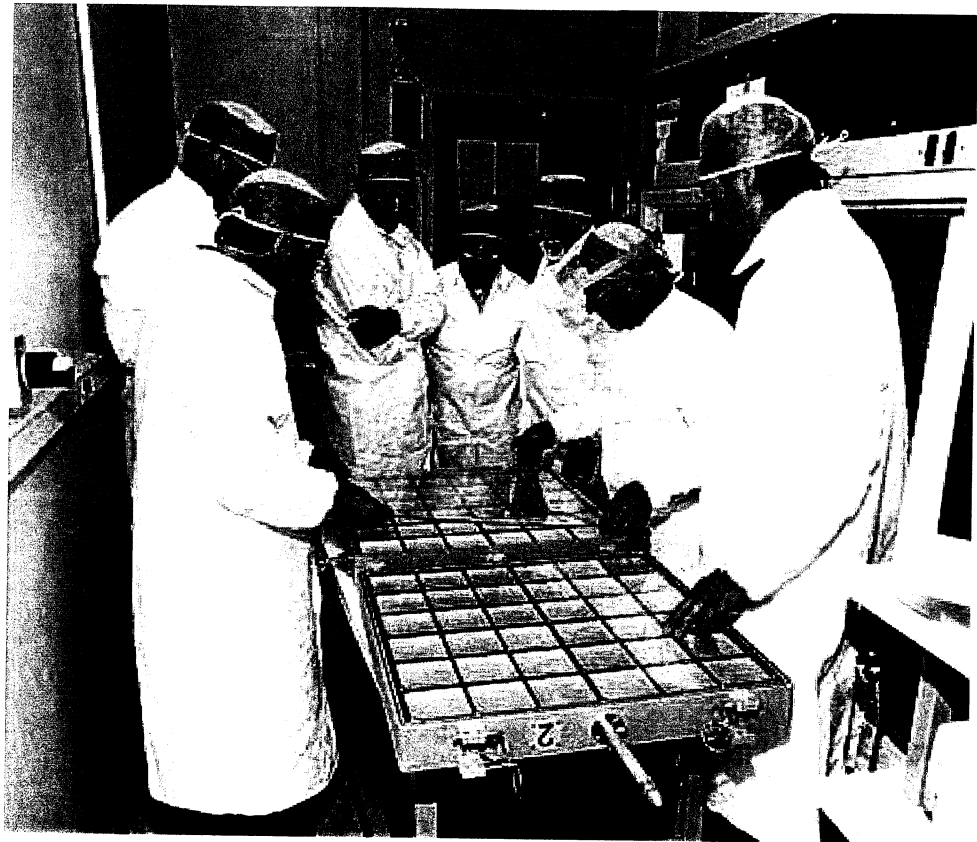


**Figure 7.** Installation of Plexiglas covers that protected the aerogel collectors during most of the disassembly sequence. The covers contained access holes to all critical fasteners below.

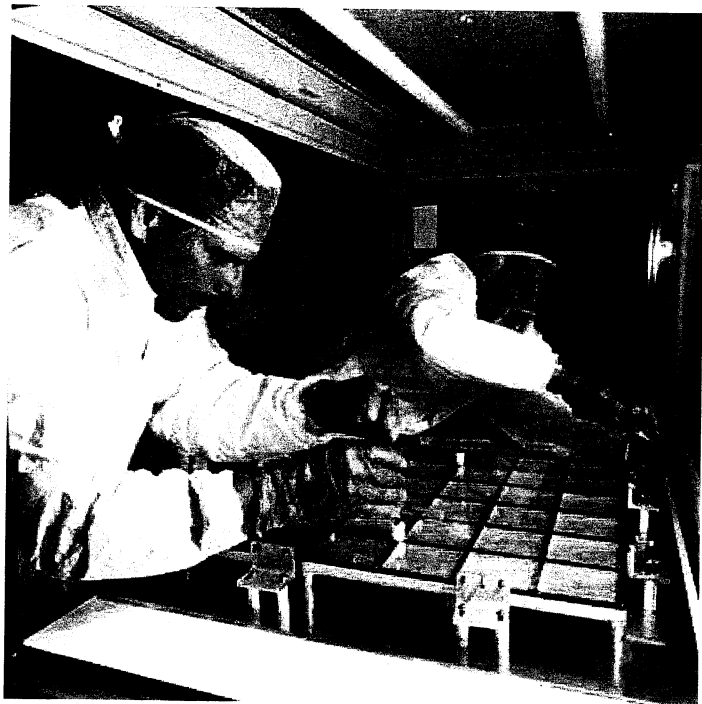


**Figure 8.** Removal of the protective Plexiglas cover and hold-down grid in class 1000 flow bench of the FOILS laboratory.

Following harvesting, each individual tile was photo-documented, presumably in its most pristine state, using high-resolution optical (Hasselblad) photography, referred to as *mug shots*. Examples of this optical photography can be seen in Figures 13 and 14, and a systematic compilation of all mug shots is presented as Appendix A of this report. All mug-shot photographs contain the tile identifier (e.g., 2B01 in the top legend; tray [1 or 2], column [A-F], row [01-06]) and are oriented such that the (0,0) coordinates are in the lower left-hand corner. Although the fairly translucent nature of aerogel makes it a difficult material to photograph, some of the larger impact features ( $> 1$  mm) are readily recognized in

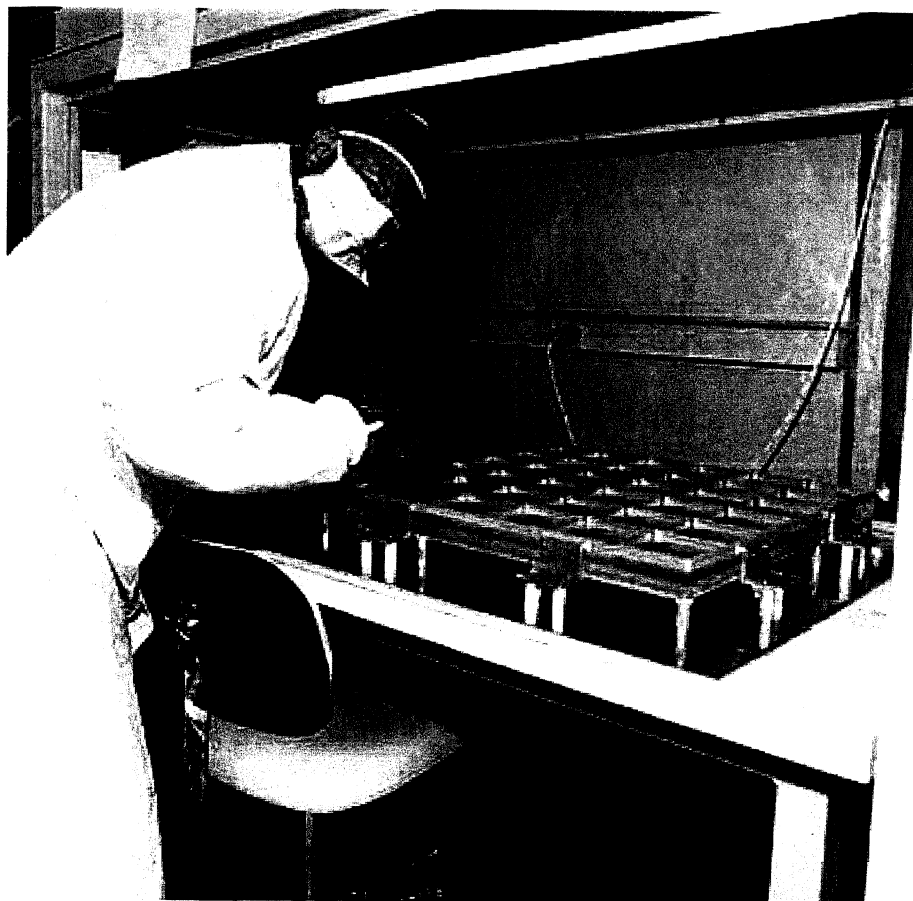


**Figure 9.** Freestanding assembly frame immediately following the removal of the aerogel tiles using a flexible plunger tool. The tiles dropped  $\sim 3$  cm and came to rest on the tray's interface plate.

Figures 13 and 14; many features  $\ll 1$  mm can be seen as well. Tile 2B01 (Figure 13) is unusual in the sense that it suffered not only the largest impact event of ODC (right-hand side), which was affected/terminated by the frame edge, but it also contains many additional features  $> 2 - 3$  mm in size. Figure 14 is more typical of the majority of the ODC tiles, displaying only two large events; a few tiles contain no impact feature  $> 1$  mm in diameter. We used these mug shots extensively during the optical scanning operations and during the preparation of SEM samples, documenting the physical splitting and subdividing of the pristine parent tiles.

## MACROSCOPIC INSPECTION

Following photo-documentation, all tiles were systematically scanned with the naked eye, aided by a hand lens and a flexible, fiber-optic light source to provide variable geometries of illumination. We found that a combination of back and side lighting is best for optimum viewing of impact features of various sizes and geometry in aerogel. This first-order inspection aimed at identifying and cataloging the occurrence of all features  $> 2$  mm in diameter or length, including their relative frequency. Each feature was classified and recorded on a transparent overlay of the individual mug shots. Even the most cursory inspection reveals morphologically distinct classes of impact features, including transitional stages among some. Three basic types of features were distinguished during this macroscopic inspection: (a) *tracks*, (b) *pits* and (c) very *shallow depressions*. Figure 15 contrasts a classical, slender penetration track with a substantially hemispherical pit to simply illuminate the existence of dramatically different features and the

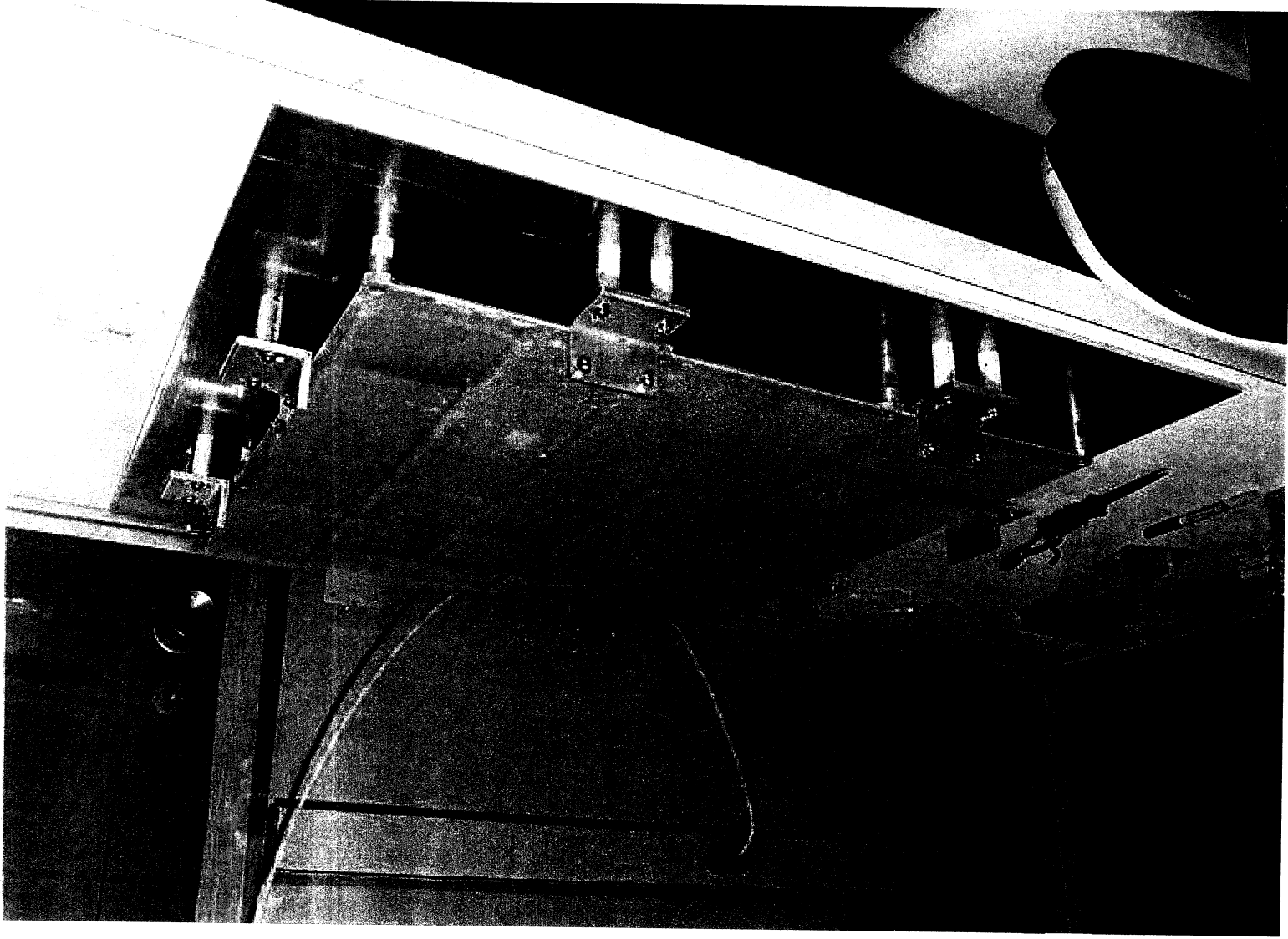
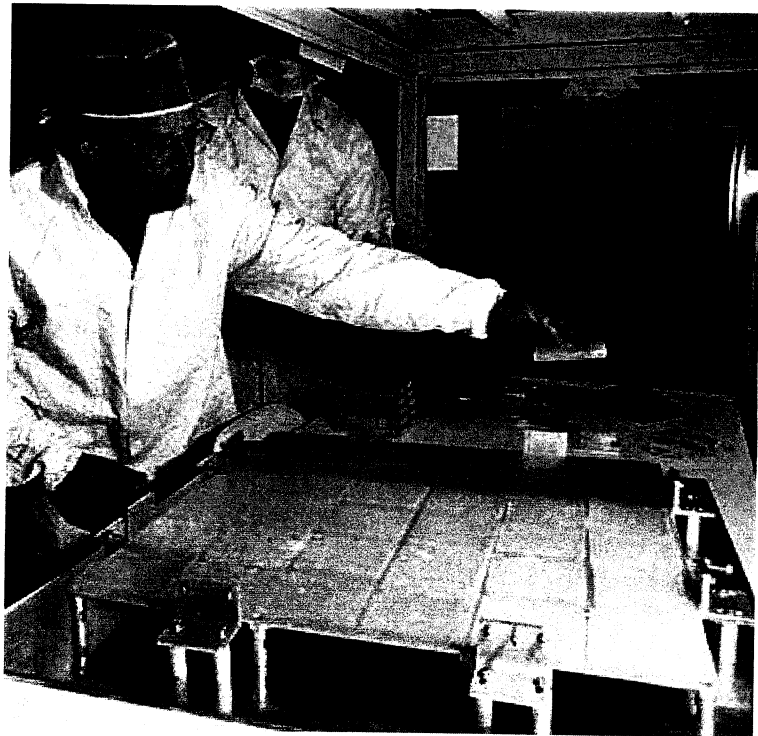


Figure 10. Complete array of harvested tiles, from ODC Tray 1, resting on the interface plate with their original flight orientation preserved. Note the distinct coloration of some tiles and the dramatic color contrasts of neighboring tiles, suggesting that the coloration relates to some intrinsic tile property, and not to some depositional processes of a (gaseous?) contaminant.

need for their classification. We will augment the macroscopic observations of these features with detailed microscopic observations below, to provide a more complete and detailed morphologic description. Such microscopic investigations not only corroborate the macroscopic appearance and classification scheme, but they validated and extended this scheme to very small sizes beyond the resolution of the unaided eye. In addition, the microscopic investigation revealed the existence of specific subclasses of features and the transitional nature of some.

The major criterion employed in classifying the various features was their aspect ratio, defined as the absolute length or depth (L) relative to its diameter (D). The D/L values vary widely from 0.1 to 40. In contrast, most hypervelocity craters in space-exposed metal surfaces have relatively constant diameter/depth relationships, clustering prominently around 0.5 to 0.6 (e.g., Humes, 1991 or Love et al., 1995). The wide range of D/L values in aerogel attests to the superior sensitivity of a very low-density target in recording and preserving highly variable initial impact conditions (e.g., projectile density, shape, and/or impact velocity). It also introduces complexity into the description and interpretation of aerogel features, as total track length is the most significant parameter for very slender tracks. However, we sense that the feature diameter becomes increasingly more important in the understanding of progressively shallower and



**Figure 11.** Transfer of the ODC aerogel collectors into individual plastic containers.

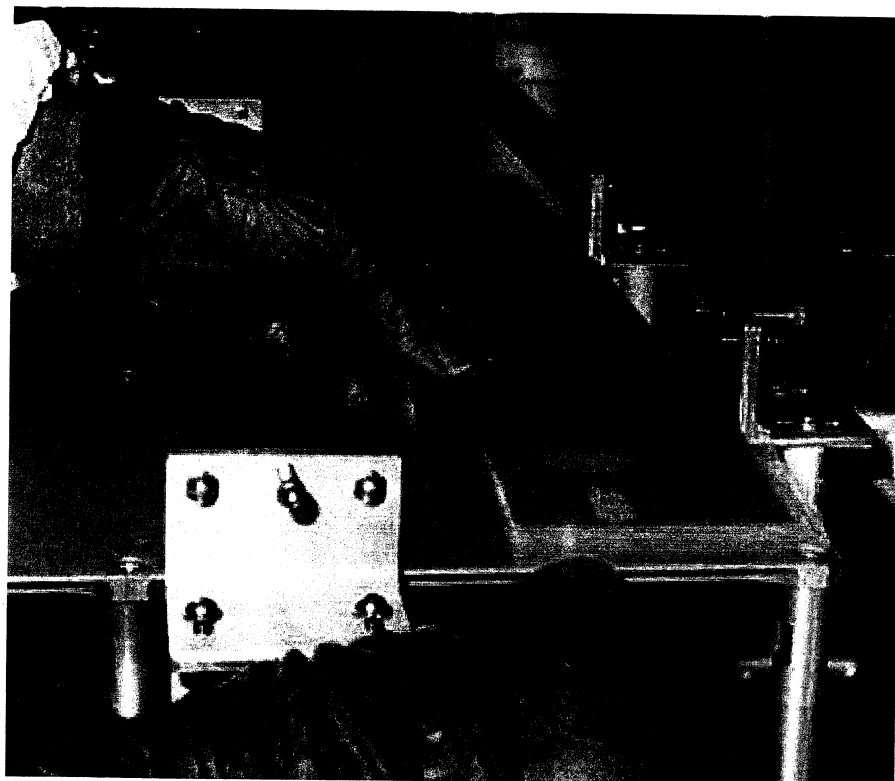


**Figure 12.** Detail of the aerogel harvesting and handling procedures illustrating the use of a flexible spatula-like device to pick up the tiles. Also visible in this image is a detail of the device that supported the ODC assembly frame.

ultimately hemispherical pit structures.

We define  $D$  as the largest diameter of a feature, typically encountered at some depth below the aerogel surface. This maximum diameter is generally larger, commonly by factors of 2 - 4, than the actual projectile entrance hole at the aerogel surface. We classified features as *tracks* if they possessed an  $L/D > 10$ , or as *pits* if  $0.5 > L/D > 10$ , and as *shallow depressions* for  $L/D$  of  $< 0.5$ . However, the  $L/D$  ratio is merely an important guide toward the classification of all impact features and (rare) exceptions to the above rules are permitted;  $L/D$  changes continuously and there are transitional cases. Additional classification criteria may be used, such as the presence or absence of melt-phenomena, pervasively crushed zones of aerogel, or the absence or presence of copious amounts of particulate residue.

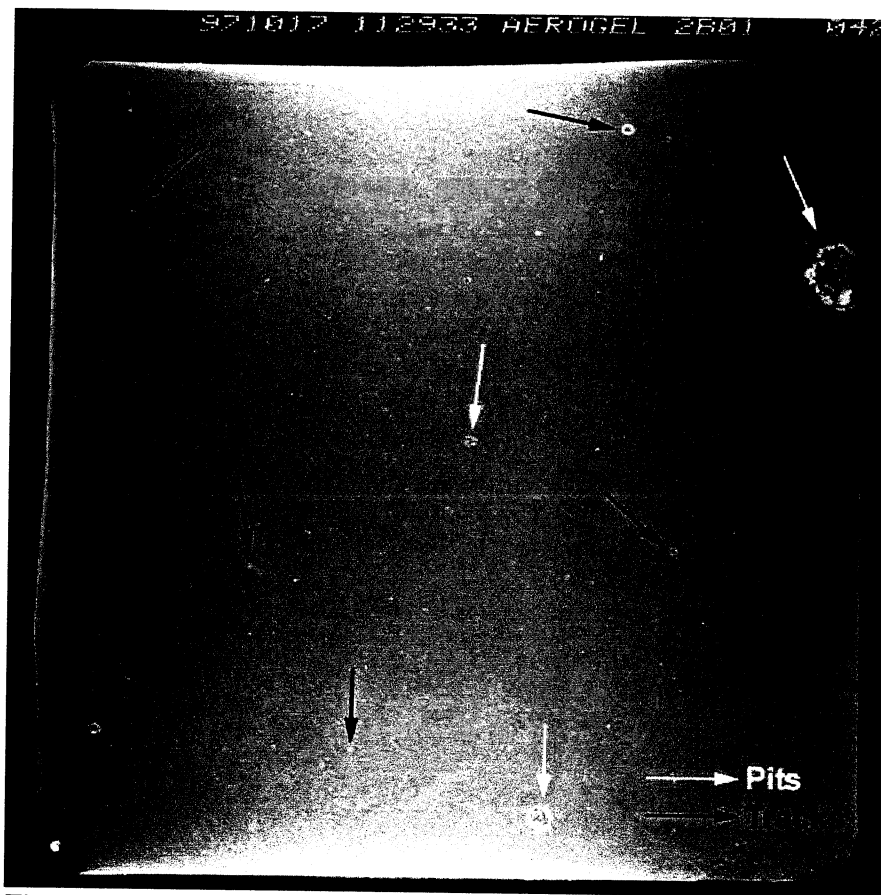


**Figure 13.** Representative “mug shot” of an individual aerogel tile (~10 cm square) showing that optical photography possesses adequate resolution to resolve impact features at scales of  $< 1$  mm. The actual tile (2B01) shown contains an unusually high number of impact features  $> 1$  mm, including circular pits (white arrows) and tracks of various lengths (black arrows). This tile also contains the largest impact feature observed on ODC, an ~9 mm pit that was truncated by the assembly frame (far right).

## Tracks

Tracks are defined as the classic, carrot-shaped, relatively straight and deep penetrations known from any number of experimental impact studies into highly porous and low-density media as summarized by Tsou (1990; 1995), or Hörz et al. (1997). The  $L/D$  values for ODC tracks are by definition  $> 10$ , yet they are commonly on the order of 20 - 30. A typical ODC track and an example of an experimental track are illustrated in Figure 16, including enlargements of the major morphologic components. Most tracks have entrance holes at the surface of the aerogel collector that are smaller than the diameters of subsequent track sections. (Burchell and Thomson, 1996). Such tracks tend to begin to substantially widen immediately after penetration of the aerogel surface, resulting in a relatively large diameter and rather long cavity, which may be as long as some 30% to 50% of the total track length. The wide diameter and length of this cavity account for most of the aerogel mass that was displaced or deformed, and is the reason we refer to this portion of a track as its *main cavity*. For descriptive ease, we refer to the near surface portions of such cavities as the track’s *throat*, which terminates when the maximum diameter ( $D$ ) of the track is reached. By definition, the remainder of the main cavity decreases continuously with depth, yet at highly variable rates. Very long, slender cones may contrast with cavities that are substantially cylindrical in

shape or that are distinctly bulbous, while rare specimens decrease their diameters in a distinctly stepwise fashion. The detailed geometry of the main cavities of such features can vary considerably, yet they all taper into a long and slender, needle-like structure at depth, which we refer to as the track's *stylus*. This stylus can also occupy a substantial fraction of the total penetration path, commonly as much as 50% or more. It is the presence or absence of this slender, needle-like stylus that places such a feature as a genuine track.

In contrast to the main cavity, the stylus continuously tapers to the final tip, which we refer to as the track's *terminus*. Note from the enlarged inserts that these terminal sections are commonly characterized by deformation structures and fractures systems that resemble inverted cones. This cone-in-cone structure is seemingly a characteristic, yet poorly understood mode of failure for aerogel, presumably at high strain rates. The very tip of the terminus is often curved, as the last few cones are misaligned. Projectile residue, if present, typically resides in undeformed host aerogel at a modest distance from the last cone structure.

Figure 17 shows a number of tracks, arranged by decreasing L/D and including select side views to provide a sense for the morphologic diversity (e.g., throats and main cavities) of individual tracks. Note the relatively straight walls and constant tapering of the entire feature for most tracks of  $L/D > 30$  (i.e., for most of the longer tracks). In such continuously tapering cases, it's not possible to differentiate between the main cavity and the stylus. Such tracks are generally characterized by a relatively short throat, reaching maximum feature diameter very close to or at the surface of the aerogel. As throat length gets longer than D, the cavity walls tend to become curved,

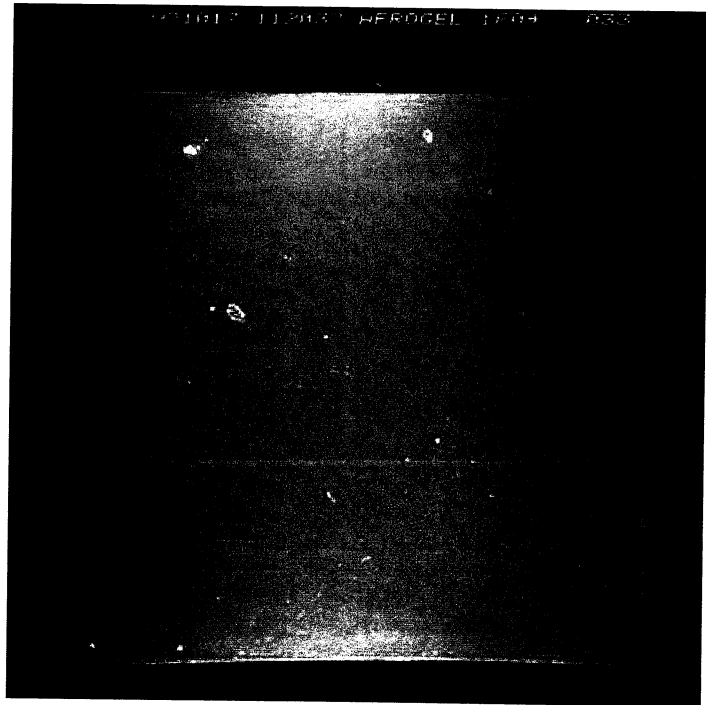


**Figure 14.** ODC collector mug shot showing tile 1F04, which exhibits a more typical track density.

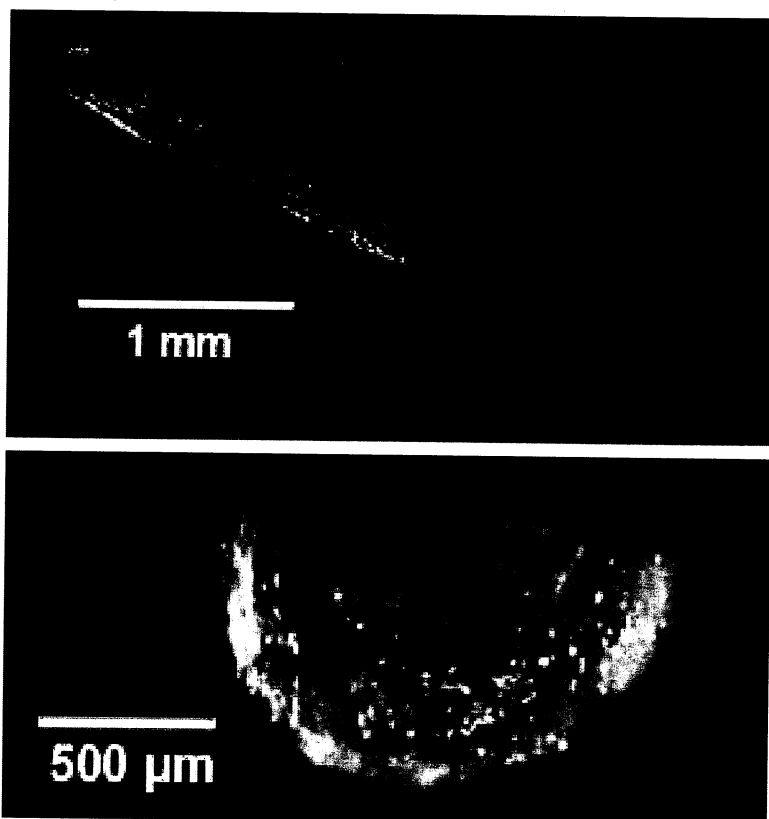


**Figure 15.** Examples of a typical *track* and *pit*, illustrating their dramatically different morphologies and the need for detailed morphological classification of all impact features in low-density aerogel.

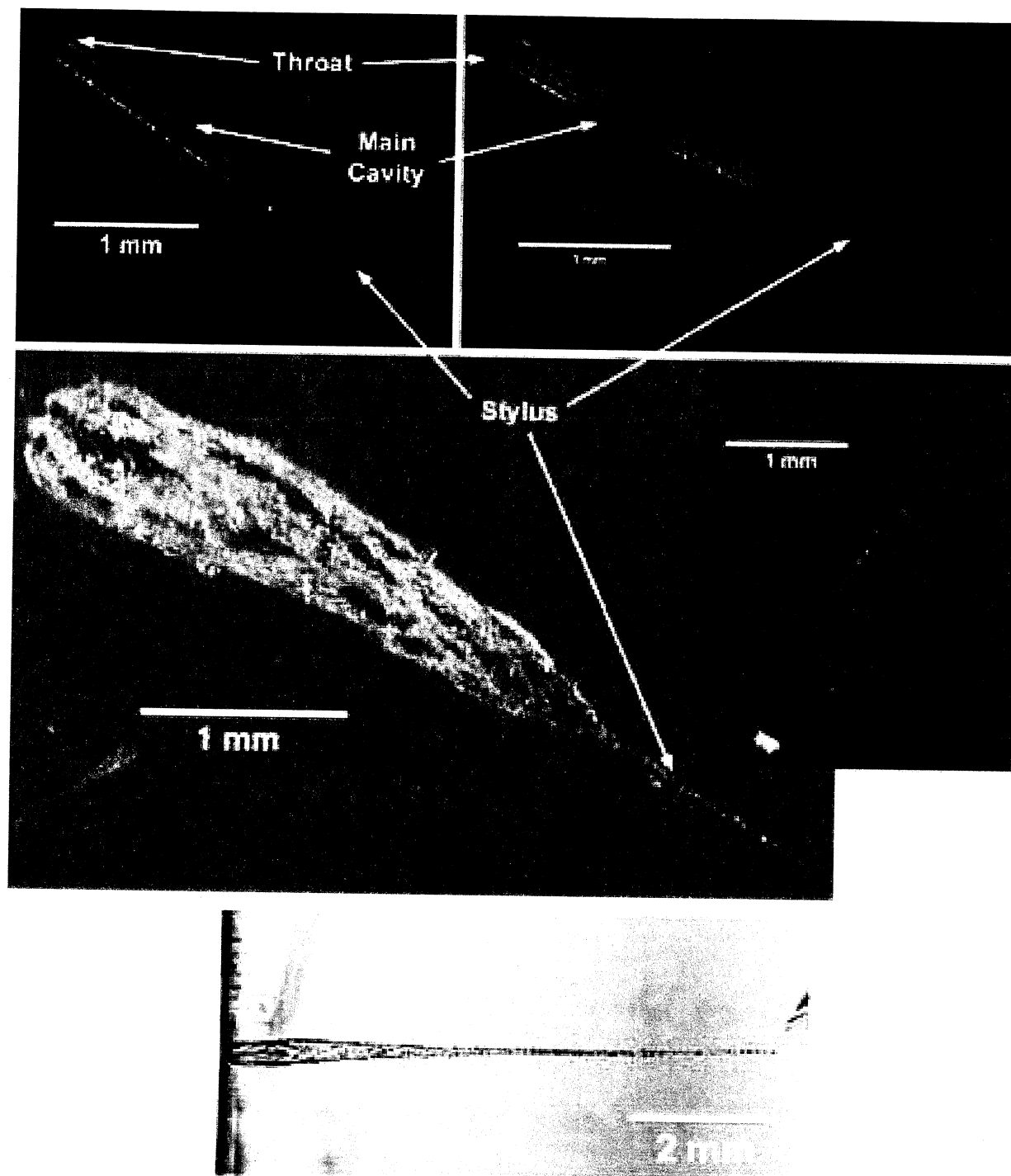


**Figure 16.** Morphological elements and definition of terms for an ODC track, and comparison with an experimental analog produced by a 50- $\mu\text{m}$ -diameter glass sphere at 6 km/s.

forming modestly and distinctly bulged cavities that merge into the stylus in a progressively more abrupt fashion. Ultimately, the main cavity may maintain a constant diameter over a relatively long distance, resulting in distinctly cylindrical geometries that occupy progressively longer portions of the main cavity.

In an idealized sense, cavity shape changes continuously from slender, straight-walled cones, to bulged forms, to cylindrical cavities. In contrast, the stylus remains a relatively invariant, needle-like structure. Distinctly bulbous and cylindrical main cavities display progressively more abrupt diameter changes as the

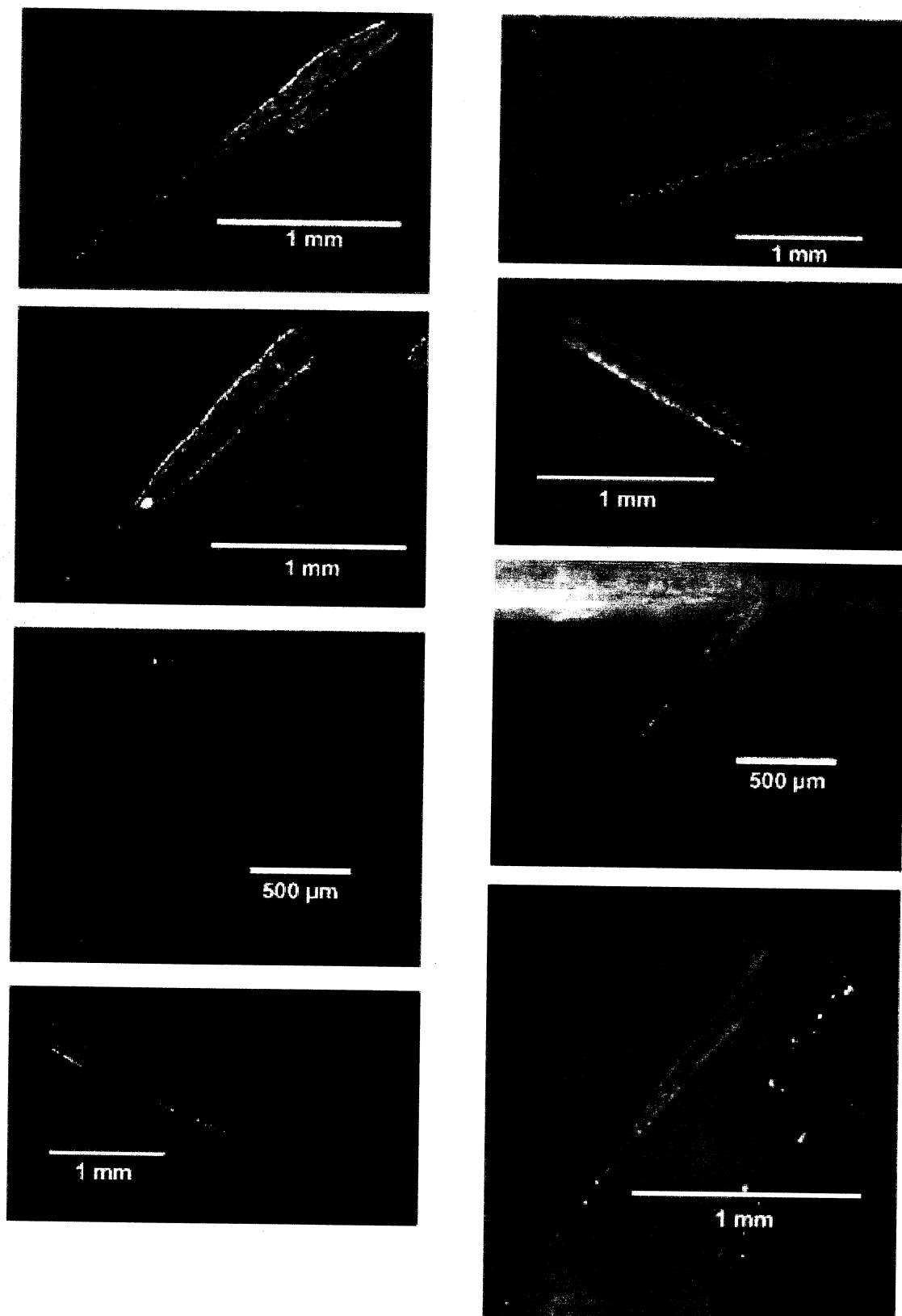


**Figure 17.** Typical tracks observed in ODC aerogel. Note some modest differences in the morphology of the main cavity, ranging from slender cones to slightly bulged.



main cavity transitions into the stylus, with some cylindrical cavities approaching almost discontinuous steps. Clearly, such cylindrical cavities are transitional to deep pits, the latter lacking the needle-like stylus and terminating in blunt-nose fashion (see below).

Note that the concept of an L/D has limited meaning in the case of classical penetration tracks. The diameter D may refer to wedge-shaped, bulbous or cylindrical cavity geometries with the length of the stylus substantially controlling the total track depth (L). The distinction among various subclasses of tracks is based on the detailed shape of the main cavity, rather than on specific L/D measurements. The concept of L/D becomes meaningful only in the context of pits and other, significantly shallower structures present on ODC.

The significance of the subtle morphologic changes described above and illustrated in Figures 16 and 17 is poorly understood at present and attests to a wide range of initial impact conditions. Based on experimental impacts into highly porous media such as sintered alumina (Werle et al., 1981) or styrofoam (Tsou, 1990), total penetration depth systematically increases up to some threshold velocity, beyond which it decreases again. However, the total volume of the track continues to systematically increase with increasing velocity, even beyond the threshold, at least for experiments using styrofoam at impact velocities as high as 7 km/s (Tsou, 1990). This implies that the main cavity diameter must increase at the expense of penetration depth. All of the above experimental series were conducted into porous targets with densities  $> 0.1 \text{ g/cm}^3$ . There is no experimental confirmation for such a velocity-dependent threshold of L/D for the lower density aerogels employed by ODC, at least at velocities as high as 7 km/s (Hörz et al., 1997), yet it may very well exist at  $V > 7 \text{ km/s}$ . We will return to the existence of such a threshold velocity after the description of pit features, which will figure prominently in such considerations.

Classical penetration tracks, as illustrated in Figures 15 - 17, are very common in the ODC aerogel, if not the most common impact feature type. However, they are generally limited to small sizes ( $< 5 \text{ mm}$  in length). The longest track observed on ODC was  $\sim 15 \text{ mm}$  long with an angle of incidence of some  $45^\circ$ , and was terminated by the aluminum interface plate. This was the only track on ODC to completely penetrate the aerogel; the second longest track was  $\sim 7 \text{ mm}$  long. Typically, each aerogel tile contains tracks that are readily seen with the unaided eye. The macroscopic inspection of all tiles yielded a total of 86 tracks  $> 3 \text{ mm}$  in length for the entire ODC, while small numbers of tracks 1 - 3 mm in length, and numerous tracks  $< 1 \text{ mm}$  in length are seen on every tile under the microscope. In addition, microscope inspection reveals that most tracks possess some form of impactor residue at their termini, substantiating that the aerogel on ODC did capture hundreds of impactors large enough ( $> 5 \mu\text{m}$ ) to be analyzed with modern analytical instruments.

As illustrated in Figure 18, it is not unusual to have *bifurcated tracks* or tracks that possess multiple styluses, which attest to the fragmentation of the penetrating impactor. The bifurcation or splitting of the projectile to produce two or more stylus features typically occurs at the end of the main cavity. Furthermore, the longest stylus does not necessarily contain the largest projectile fragment. Small and relatively dense fragments may penetrate more deeply or individual fragments may possess faster velocities than the main mass.

An unusual set of tracks, all confined to the rearward-facing ODC surfaces (i.e., Tray 2), needs mentioning. Some of the tiles in this tray contained distinct *clusters* of tracks as illustrated in Figure 19, which is a mug shot of tile 2E01. In general, the clusters of tracks are of sufficient size and quantity to be seen with the unaided eye. Each cluster may be composed of tens, if not hundreds of (small) tracks, all of grossly similar shapes, and all exhibiting identical azimuthal orientation and identical, relatively shallow angle of incidence,  $\sim 25 - 30^\circ$  relative to the tile surface/local horizontal. The spatial density of tracks  $> 500 \mu\text{m}$  in length occasionally exceeds  $10 \text{ tracks/cm}^2$  in such clusters, with the cluster typically a few cm across, thereby occupying a (small) fraction of the host tile(s). The cluster illustrated in Figure 19 is the largest observed. The density of tracks within a cluster drops off rather sharply, if not abruptly, into the surrounding aerogel. Higher magnification views of some clustered tracks can be seen in Figure 20. Note their limited range of shapes, their constant azimuthal direction in plan view (top panels), and their constant

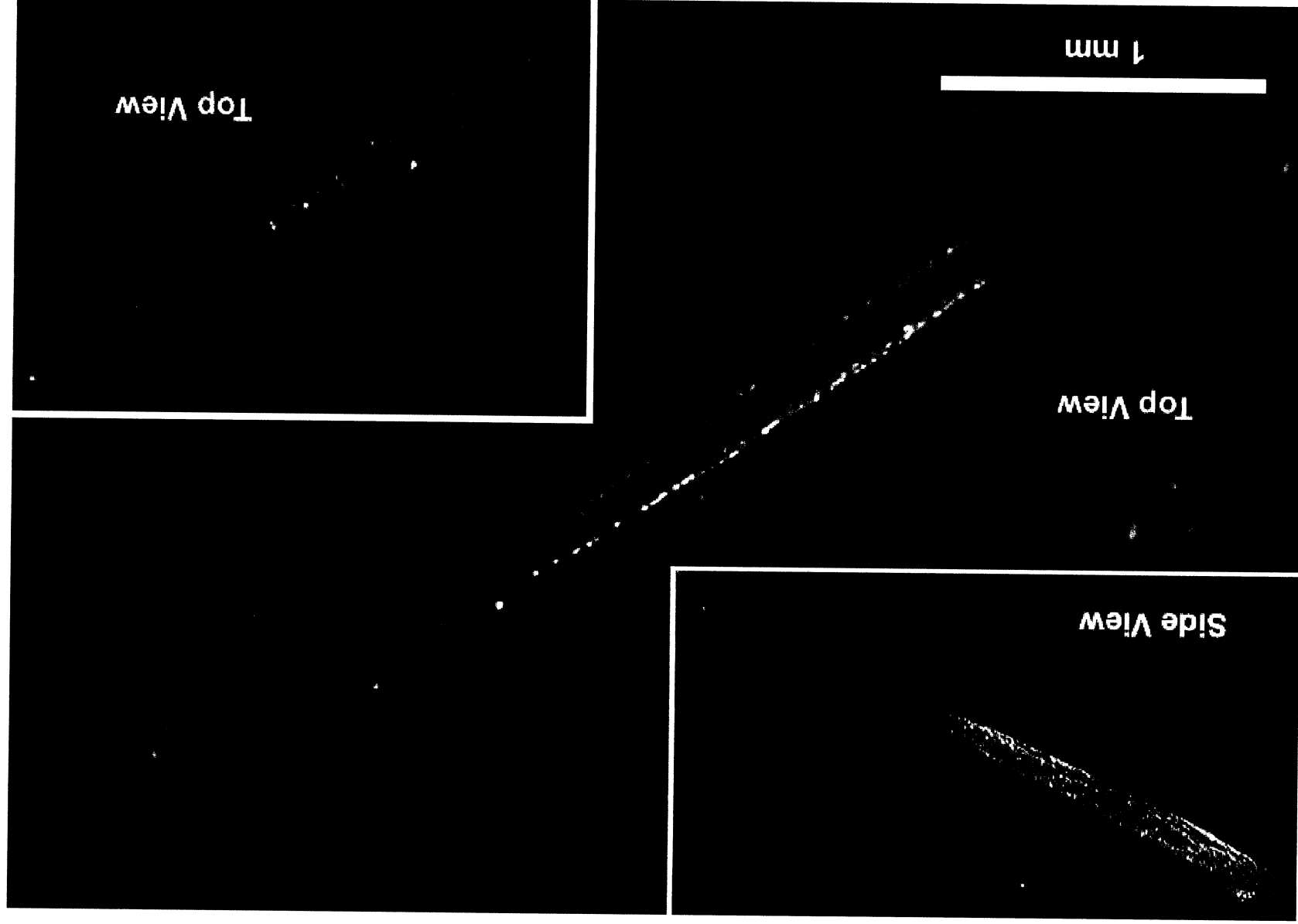


Figure 18. Example of a bifurcated track caused by the fragmentation of the penetrating impactor. Note that the shorter track contains the larger residue.

inclination/trajectories in cross section (bottom panels). These images also illustrate that any cluster may contain tracks of vastly different sizes.

A total of five prominent clusters were observed on Tray 2 of ODC, with the two largest clusters located on neighboring tiles 2D01 and 2E01. However, these two clusters are distinctly separate and do not extend across the tile boundaries; they are two distinct features. The remaining clusters seem randomly distributed. The observed clusters are distributed in an irregular fashion over the entire Tray 2 surface, with individual patches occupying only a small fraction of their respective host tiles.

However, there are numerous individual tracks on most Tray 2 tiles that exhibit features with similar shapes, orientation, and inclination as those associated with these clusters. The sheer frequency of features with identical trajectory elements leaves little doubt that they are associated with the clusters. Evidently, the clusters and the geometrically identical, yet isolated tracks were produced by a distinct cloud of impactors that must have originated locally, most likely as ejecta from an impact on some *Mir* surface. This particle cloud had a distinctly heterogeneous mass distribution, ranging from dense lumps of particles to more dispersed, individual fragments. The distribution of particle size or mass within this cloud was also highly variable, as track lengths vary by more than an order of magnitude. We refer to this particle cloud and its tracks as the “swarm” or “swarm event” throughout the rest of this report.

## Pits

In comparison to tracks, pits seem anomalously shallow for hypervelocity impacts, with typical L/D ratios of 0.5 – 2. The shallowest members are almost hemispherical in shape, yet the deeper features have long, vertical walls, resulting in distinctly cylindrical cavities. All terminate with relatively blunt noses and lack the telltale, slender stylus associated with tracks. Generally, they contain no macroscopic and microscopic evidence of impactor material. Indeed, the lack of any discoloration renders them exceptionally transparent and clear, one of their most outstanding attributes. Such features have no experimental analog to our knowledge, yet we note that they were also found in aerogels that were exposed prior to ODC on the *EURECA* satellite (Brownlee, 1994; personal communications, 1998) or on the Shuttle

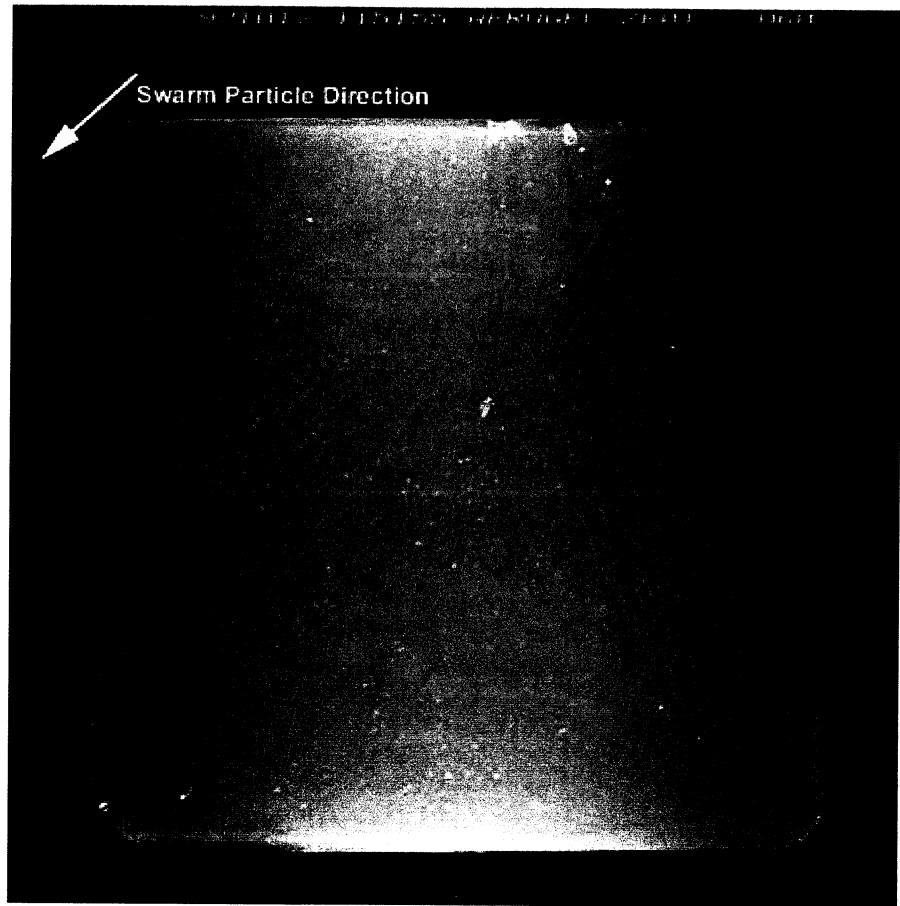


**Figure 19.** Tile 2E01 contained the largest cluster of tracks, all having identical azimuthal orientation, as well as a modest inclination angle ( $\sim 25^\circ$ ) from the local horizontal.

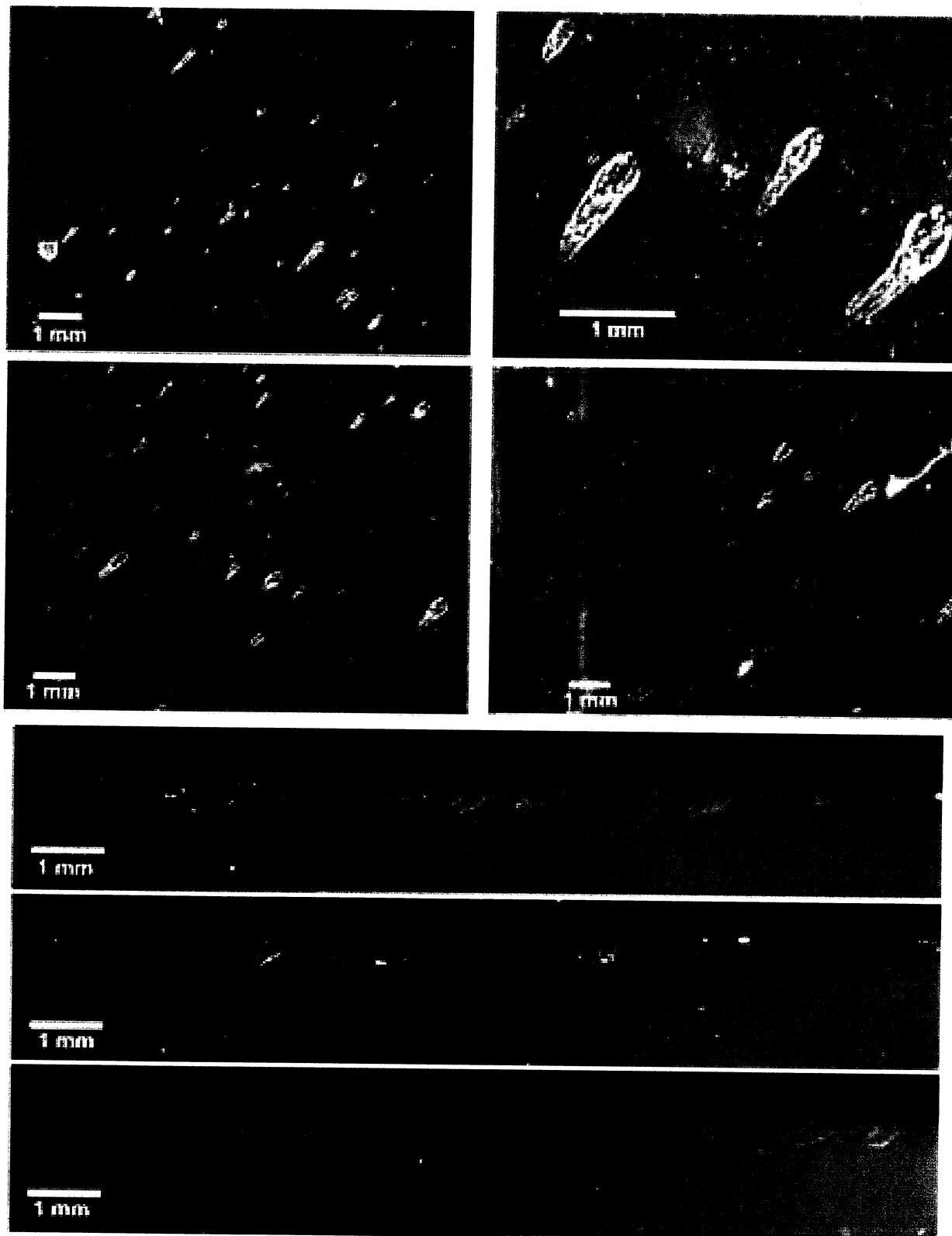


**Figure 20.** Detailed views of the swarm event in plan view and cross section. Note the high spatial density ( $>> 10$  tracks/cm<sup>2</sup>) of tracks and their variable lengths, the latter indicative of widely variable impactor sizes. The main cavities of these tracks are fairly constant, with modestly to distinctly bulbous cavity geometries.

(Westphal, personal communications, 1998). In particular, Brownlee seemed puzzled by such features, as none contained detectable projectile materials, neither under the microscope nor via SEM-EDS. Unfortunately, none of these earlier observations were described in the open literature.

Typical plan views and cross sections of pit structures can be seen in Figure 21, with additional examples, showing their variety, visible in Figure 22. A first-order resemblance with impact craters in dense target media is suggested for some of the shallower features, yet there are also substantial differences, the reason why we refer to these shallow structures as pits and not as craters. For example, even the most crater-like, hemispherical pits lack a raised rim. Furthermore, many of these features exhibit radial fractures (i.e., spike-like features) around their periphery, the reason why Westphal (personal communications, 1998) refers to them as “hedgehogs.” In addition, they lack any concentric spall zones and fractures typical of craters in brittle materials, such as glass (e.g., Schneider et al., 1990). The aspect ratio of pits is typically  $1 > L/D < 5$ . This contrasts with aspect ratios for typical hypervelocity craters in space-exposed aluminum ( $L/D \sim 0.5 - 0.6$ ; Love et al., 1995) and  $L/D \sim 0.2 - 0.3$  in typical silicates and rocks (Gault, 1973). Compared to craters, even the shallow ODC pits are fairly deep. The long cylinders illustrated in Figure 21 are highly unusual for hypervelocity impacts. However, as illustrated in Figure. 22, shallow and deep structures are clearly transitional, thus justifying the term “pit” as a single term for this entire class of features.

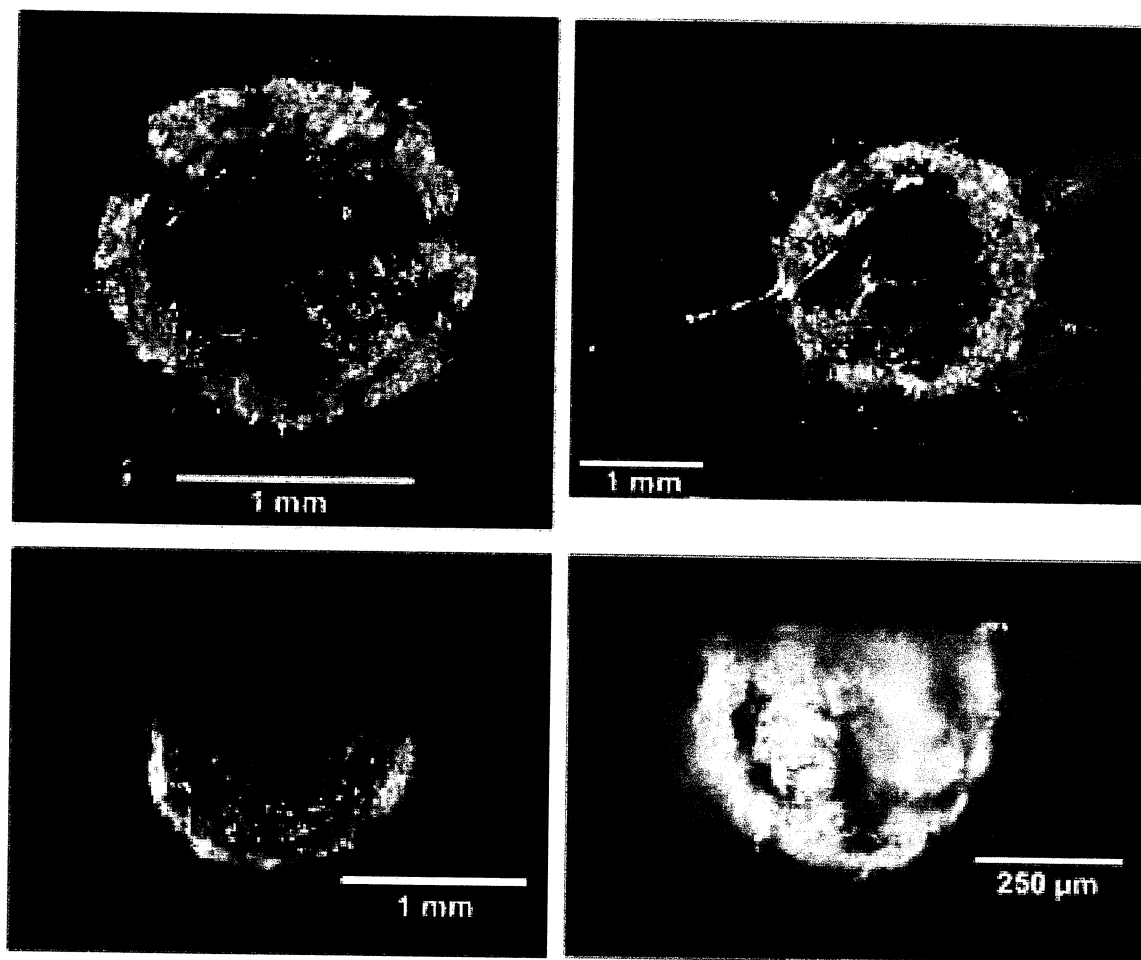


**Figure 21.** Examples of typical pit features in plan view and cross section. Note their relatively shallow nature, the lack of a raised rim, and the lack of concentric fracture systems typical of spall phenomena in glass targets. The structure on the right side has spike-like, radial fractures. Such impact pits in aerogel have no experimental analog.

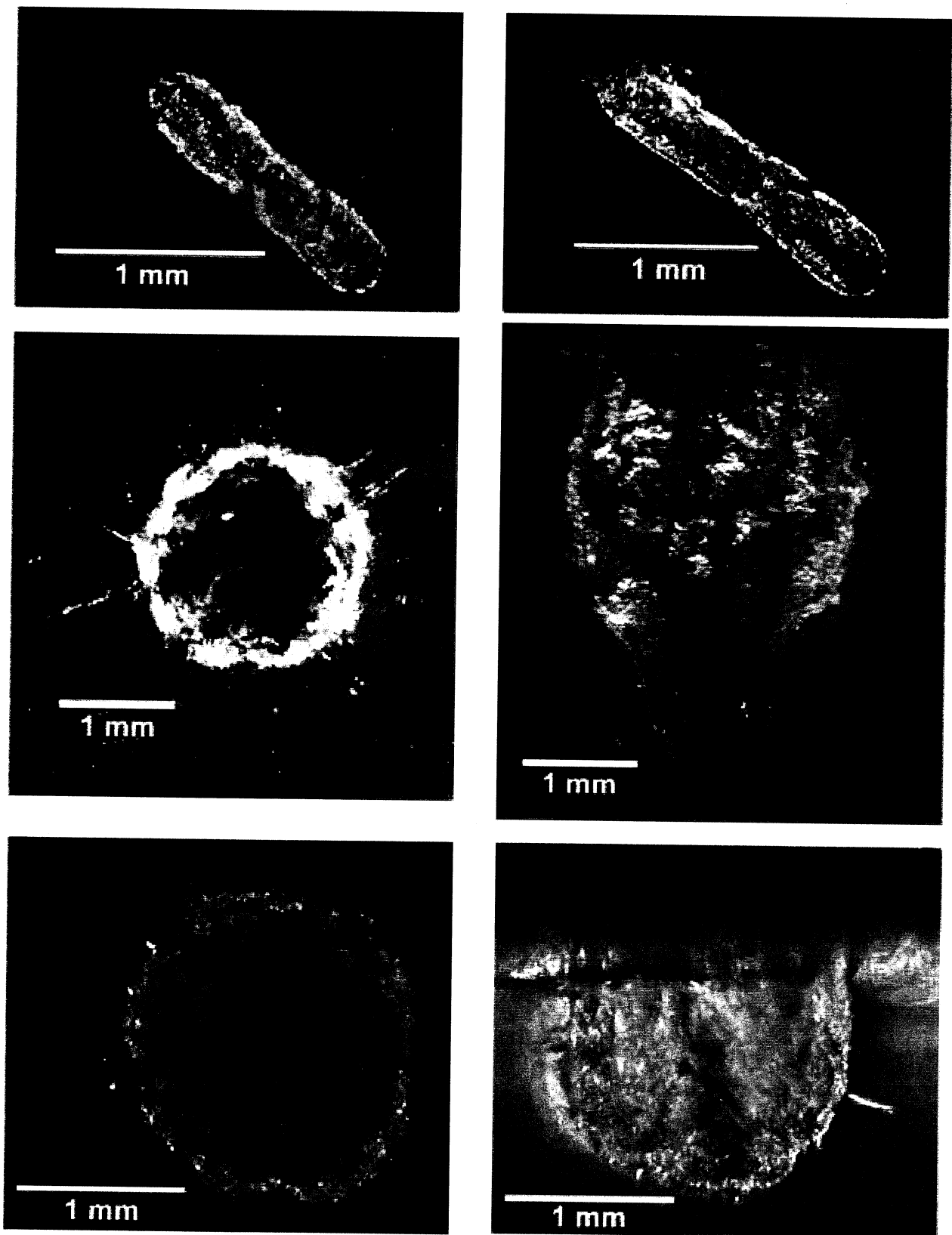


**Figure 22.** Plan view (left) and cross sections (right) of three pits, including a deep cylindrical cavity (top), a stubby example (middle), and an essentially hemispherical pit (bottom).

The interior surfaces of pits (i.e., bottoms and walls) differ from that of tracks in that they tend to be highly transparent. The main cavity walls, especially the deeper portions, of most tracks are modestly opaque and of a mottled appearance, resulting from mechanically deformed, finely crushed aerogel that scatters light. Styluses tend to exhibit similarly opaque walls that commonly grade into the cone-in-cone structure. In fact, it is these observations of the stylus that suggest that this material consists of finely crushed aerogel. In contrast, pit features tend to lack this modestly opaque, mottled zone and, as a result, are highly transparent. Many pit walls are somewhat undulous in appearance, and occasionally contain prominent, bulbous promontories. Similarly transparent walls are observed in the main cavities of some tracks as well, especially those with cylindrical shapes. We interpret these highly transparent, modestly undulous surfaces as evidence of melting, yet we do not imply the presence of a continuous melt liner. The aerogel may merely have shrunk and contracted in response to elevated temperatures. Dedicated SEM studies are needed to characterize the distinctly bimodal appearance of cavity surfaces, and to verify the current interpretations of finely crushed versus molten aerogel.

We note that the entrance hole of many pits is smooth and contains small-scale promontories, sometimes of a beaded appearance, all consistent with if not suggestive of melting.

Significantly, pits generally contain no obvious projectile residues, even when viewed under the microscope. Generally, the feature walls and bottoms do not exhibit the slightest hint of discoloration, a remarkable observation if the above interpretation of molten pit walls is correct. Typically, impact melts found in the interior of experimental craters (e.g., Hörz et al., 1983; Gwynn et al., 1996), on metal substrates flown on LDEF (Bernhard et al., 1992), or on lunar rock and mineral surfaces (e.g., Schaal et al., 1976) are dark-colored, reflecting Fe and other metals present in the impactors. By comparison, the aerogel pits are remarkably colorless and transparent. Brownlee (personal communications, 1998) made identical observations and was somewhat frustrated that none of the pits retrieved from *EURECA* yielded analyzable residue via SEM-EDS methods; we describe similar results below. However, the spike-like cracks surrounding some of these pits do, on occasion, contain dark materials that have not been analyzed to date, and which may be impactor residue.

Another important characteristic of pits is their apparent size dependency. Most of the largest impact features ( $> 5$  mm in L or D) found on the ODC collectors are pits. The largest impact feature to occur on ODC is a pit  $\sim 9$  mm across (Figure 23 and tile 2B01 in Appendix A). Despite its large diameter, this event barely penetrated  $\sim 6$  mm into the aerogel (see cross section in Figure 23) and has an  $L/D < 1$ . Another exceptionally large pit occurs on tile 1C04. Its entrance-hole diameter is modestly smaller than that shown in Figure 23, yet it is  $\sim 8$  mm deep and the associated radial spikes were terminated by the interface plate, producing some discoloration of the plate, yet no physical damage/indentation. It is the only pit feature observed on the entire ODC experiment that (barely) penetrated the entire aerogel layer, despite a fair number of pits that have diameters  $> 5$  mm.

The origin of pits is poorly understood, as they do not have an experimental analog at impact velocities as high as 7 km/s. Superficially, the shallow, hemispherical pits resemble structures produced in aerogel by modestly compressed cocoa-powder at 6 km/s (Hörz et al., 1997). This suggests that shallow pits could be the result of low-density, possibly very fluffy and friable impactors. However, the experimental pits (Figure 24) were loaded with projectile residue, as evidenced by the brown color of their interior surfaces. The absence of impactor residue is the strongest argument against a low-velocity origin of the ODC pits.

Furthermore, impacts of low-density, extended projectiles (i.e., collisionally fragmented glass spheres; Hörz et al., 1997) result in relatively stubby aerogel cavities that are the composite of numerous small impactors. However, many large, individual fragments penetrate beyond the main cavity, producing parasitic tracks (Figure 24). The absence of similar parasitic tracks around the ODC pits is significant and argues against fluffy impactors at modest velocities. Even the shallow, hemispherical ODC pits have no experimental analog, much less the deep cylindrical structures.

We are confident that shallow and deep pits are transitional in nature. More importantly, we suggest that tracks and pits are transitional, as well. A few cylindrical cavities exist that possess a blunt-nosed

terminus, from which a single stylus emerges, as illustrated in Figure 25. Such structures seem crucial to understanding the transitional relationship of tracks and pits. By definition, the stylus requires that the entire feature be classified as a track, yet the properties of the main cavity seem to match all the characteristics of pits. This transitional evolution of track geometries is schematically illustrated in Figure 26.

Slender, gradually tapering cavities merge into bulbous cavity shapes, the latter also developing progressively more distinct stylus features at depth. As the longitudinal extent of the bulbous cavity increases, increasingly larger portions of the cavity become cylindrical in shape. With increasing cylinder length, the transition to the stylus becomes increasingly more abrupt. Ultimately, the long cylinders develop a distinctly blunt-nosed bottom from which a relatively modest-sized stylus emerges. Although we have no quantitative measurements, the relative volume of the main cavity increases throughout this evolutionary sequence relative to that of the stylus, the latter becoming especially small when cylindrical cavities develop the blunt noses. Ultimately, the stylus disappears and a deep, cylindrical pit remains that becomes progressively more shallow, yielding pits of increasingly smaller  $L/D$ , until hemispherical geometries are approached ( $L/D = 0.5$ ).

These highly variable morphologies reflect a wide range of initial impact conditions, foremost impact velocity and/or projectile physical properties, especially density. We favor the view that impact velocity plays the dominant role, rather than the projectile's physical properties. This suggestion rests - in large measure - on experimental evidence, as scant and incomplete as it may be. In analogy to the impact experiments of Werle et al. (1981) and Tsou (1990), there must be a threshold velocity, even for very low-density aerogels, beyond which absolute track depth decreases, producing main cavities of relatively large diameters and volumes, and leading to decreased  $L/D$ . Such systematic, velocity-dependent changes in  $L/D$  are also

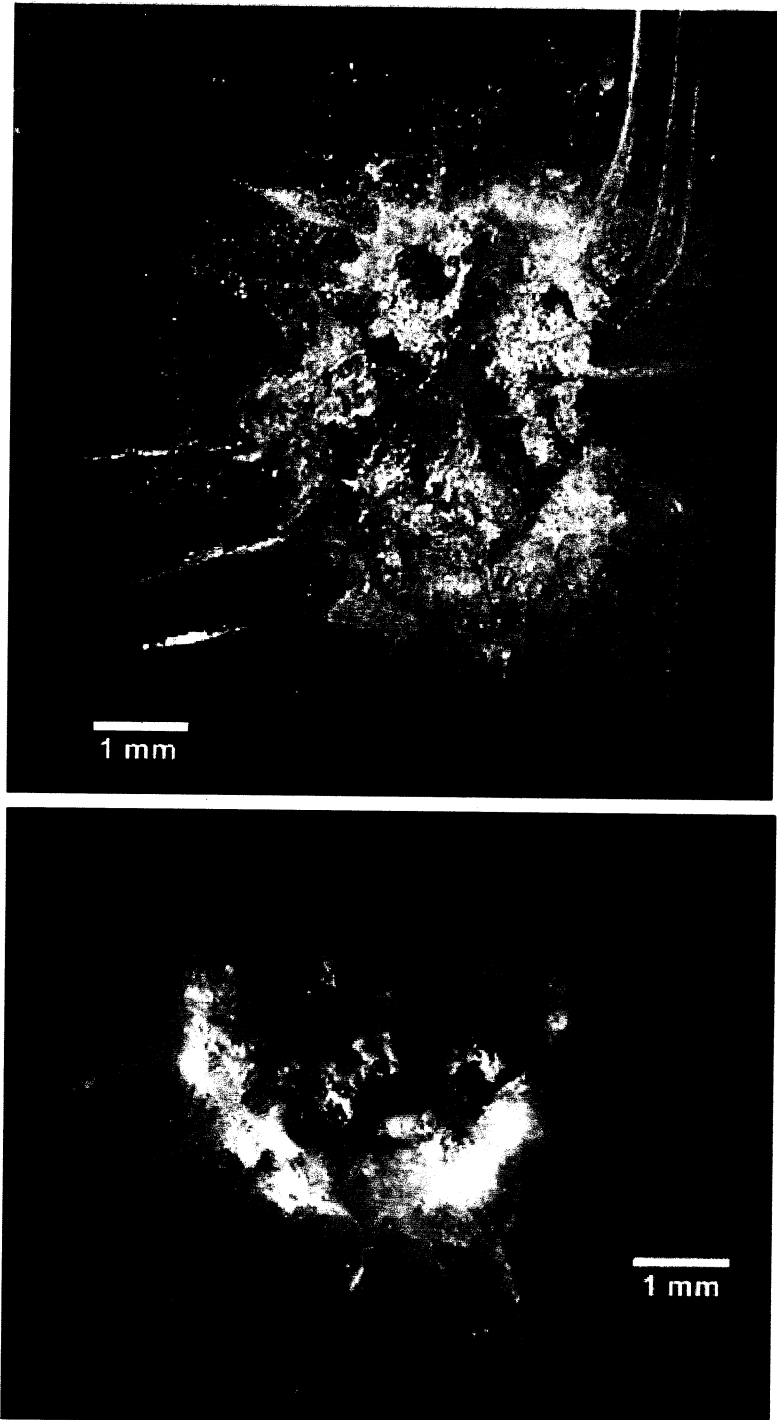


**Figure 23.** Largest impact feature observed on ODC, which happens to be a pit whose growth was unfortunately affected/terminated by the ODC assembly frame (see Figure 13). Top: Plan view. Bottom: Cross section.



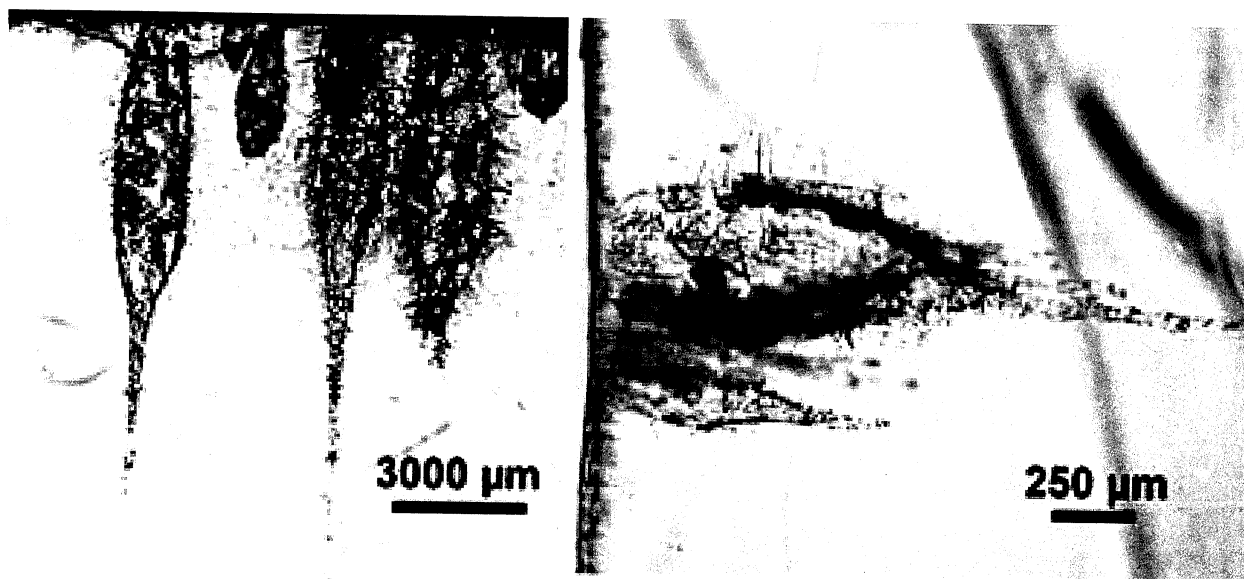


**Figure 24.** Experimental impact features in 0.02 g/cm<sup>3</sup> aerogel. In the left-hand image are impacts at 6 km/s of loosely consolidated clumps of cocoa powder, some composed of pure cocoa (short features) and some containing solid-aluminum spheres of 50 μm diameter that penetrated beyond the main cavity to produce a stylus. On the right are impacts resulting from a collisionally fragmented glass sphere resulting in stubby cavities on many of the parasitic tracks.

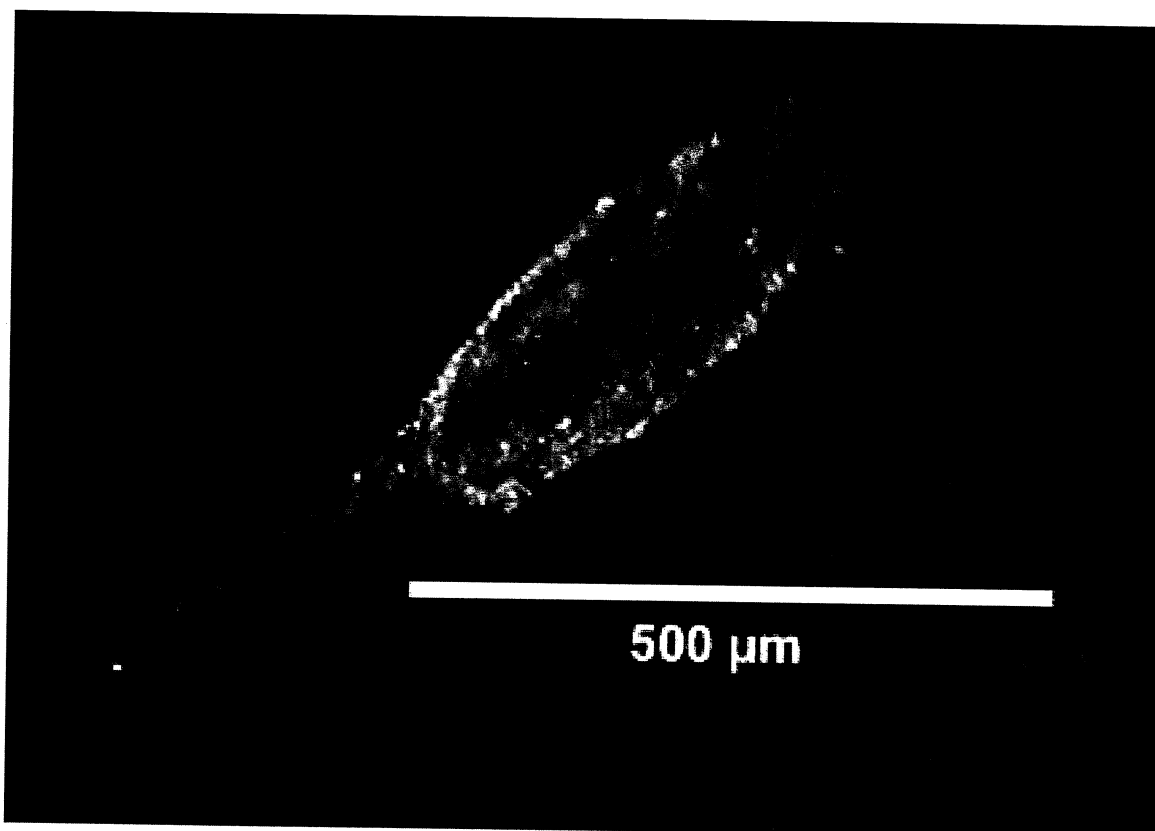


**Figure 25.** Relatively blunt-nosed, cylindrical cavity associated with a modest-size stylus. Such features seem critical for illustrating a morphologic continuum from tracks to pits.

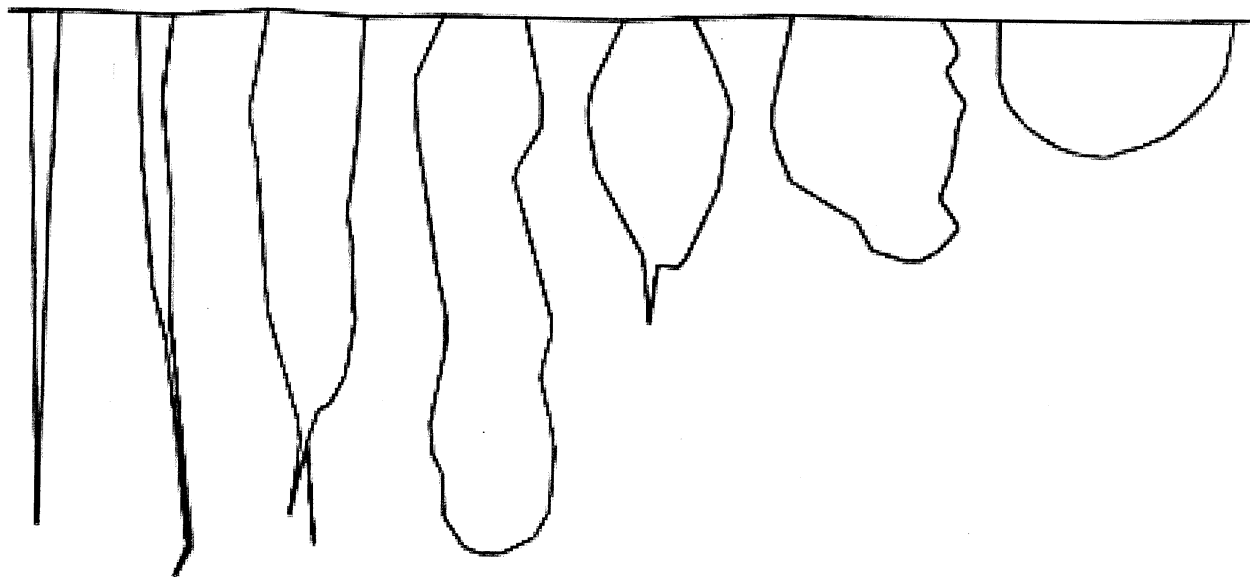


**Figure 26.** Traced outlines of ODC impact features arranged with decreasing L/D ratios illustrating the continuum in L/D ratios and the transitional sequence from tracks to pits.

observed for genuine impact craters. Craters produced by glass projectiles at 1 - 2 km/s in aluminum targets are relatively deep compared to those at 6 - 7 km/s (Murr et al., 1998; Hörz, et al., 1995). Experiments related to the development of orbital-debris shields also reveal that low-velocity impactors penetrate with greater efficiency than those at high velocities (e.g., Christiansen, 1995). The reason for this behavior is that the impactor deforms plastically (or melts and vaporizes at still higher velocities) at some threshold velocity and thus, deforms with ease, leading to decreased penetration efficiency (see also Gault and Wedekind, 1977; Murr et al., 1998).

We invoke an analogous behavior in the case of aerogel targets with the threshold velocity being well beyond light-gas gun capabilities ( $> 7$  km/s) where shock stresses and specific energy will exceed the melt temperature, if not the vaporization threshold. It is our view that the continuously tapering tracks reflect modest-velocity impacts, short of substantial projectile melting, akin to their experimental analogs. Increasingly more bulbous cavities suggest progressively larger degrees of projectile deformation (possibly melting?) and associated increases in the effective cross section of the impactor. The onset of cylindrical cavity sections and their typically highly transparent, glazed walls delineates elevated thermal conditions, which we equate with melting, either by direct shock or assisted by ablative melting, most likely both (Anderson and Ahrens, 1994). However, part of the impactor remains unmolten to form the stylus; the surviving cores or fragments are substantially decelerated, making them into highly efficient penetrators at modest velocities. Projectile residues recovered at the end of some stylus corroborate the unmolten nature of such fragments. We have never encountered a completely molten impactor residue at the terminus of a track, neither in experiments nor on ODC. The morphology of the stylus and the presence of unmolten projectile residues suggest that it is a low-velocity penetration feature, common to all unmolten cores or fragments of particles that were decelerated to below some (unknown) threshold velocity.

By the time the main cavity becomes increasingly cylindrical, the cavity walls assume a highly transparent character, as if molten. This transition is complete for deep, blunt-nosed cavities that are invariably also of cylindrical shape. Some of these cavities may have a modest stylus, depending on whether some small projectile fragment survived or not. Obviously, thermal effects dominate the development of these cylindrical cavities, and cause the cavity walls to melt or shrink. We speculate that these pits have largely formed by an expanding vapor cloud that is sufficiently dense and hot that it displaces and thermally erodes the aerogel, thus forming a relatively cylindrical cavity along the penetration path. The higher the

velocity, the more efficient the production rate of such vapors near the surface, effectively resulting in near surface bursts that produce the very shallow, hemispherical pits. Note that most of the expanding vapor could originate from the aerogel target itself. This vapor may entrain and ultimately eject the molten, if not vaporized, impactor to yield transparent pit interiors that lack even traces of impactor residues.

This velocity-dependent scenario for the morphologic evolution of impact features in the ODC aerogel is largely derived from the two end-members, the continuously tapering track, which contains copious amounts of impactor residue, and the shallow pit that typically contains none. A number of considerations combine to favor velocity as the dominant factor in this evolution, as opposed to the projectile's physical properties. First, none of the cylindrical cavities, much less the shallow pits, can be experimentally reproduced at velocities as high as 7 km/s, and including low-density ( $\ll 1 \text{ g/cm}^3$ ) and low-velocity (3 km/s) projectiles (Hörz et al., 1997). Second, experimental evidence in highly porous targets suggests the existence of a threshold velocity, beyond which the cavity diameter increases at the expense of penetration depth (Werle et al., 1981; Tsou, 1990). Lastly, general shock considerations mandate a systematic progression from melting to vaporization phenomena with increasing velocity. The latter is amply demonstrated by impact craters in space-exposed, nonporous materials, such as aluminum or gold substrates exposed on LDEF; ~50% of these craters did not reveal any impactor residue at the sensitivity level of SEM-EDS methods (Hörz et al., 1993). We consider the pit-structures in aerogel to be equivalent to craters in nonporous targets that contain no projectile residue, both structures primarily the result of impact at very high velocities.

If the projectile's physical properties were largely responsible for the transitional nature of track and pit morphologies, one would assign the very deep, continuously tapered tracks to high-density impactors, and the shallow structures to the low-density extreme. Note that the highest peak stresses and melting or vaporization phenomena in the target would be associated with the tapered tracks, rather than with the shallow pits, in such a scenario. It seems unlikely that all low-density impactors were consistently above the threshold velocity for complete vaporization, as none of them left detectable residues in the pits. We would expect an abundance of parasitic tracks associated with friable, low-density impactors at modest encounter velocities, akin to experimental analogs. As a consequence, the velocity-dependent scenario seems much more consistent with the observational evidence.

Regardless, pit structures contain little or no impactor material(s). This is an important finding as it suggests a practical limit for the utility of aerogels in the capture of hypervelocity particles. While the threshold velocity for successful capture of unmolten particle residues with aerogel is undoubtedly much higher than that for nonporous target media, there will be a velocity-controlled cut-off. Future experiments must address this limit, either by suitable analog experimentation at modest velocities, or by improvement of current launch technologies to achieve much higher projectile velocities, ideally approaching 20 km/s.

## Shallow Depressions

This category of impact feature differs from tracks and pits and can be subdivided into two subclasses, depending on the physical state of the projectiles at the time of impact: (a) solid flakes and (b) liquid droplets. Both impactor types are man-made waste products (as revealed by SEM-EDS analyses; see below) that co-orbit the *Mir* station, resulting in encounter velocities as low as a few meters per second and producing relatively shallow depression upon impact. Typically, these depressions are shallower than pits, possessing  $L/D < 1$ .

*Flakes* - This subclass exhibits  $L/D$  ratios  $< 1$ , commonly  $< 0.2$ . They were termed "flakes" because many such features contain white- to brownish-colored, irregular-shaped, platy materials within the depression. In the extreme case, some flakes have merely stuck to the aerogel, with parts of the flake protruding above the aerogel surface. The damage caused by most flakes is a shallow depression of irregular outline that contains a crushed layer of aerogel at the bottom, as illustrated by an especially large

example in Figure 27; additional examples are illustrated in Figure 28. The copious amounts of impactor material in these shallow depressions, combined with a layer of crushed aerogel, clearly distinguish this class of structures from the transparent hypervelocity pits. Most objects that appear as white dots in the mug-shot photographs (Appendix A) represent such flake impacts, with most tiles containing a number of such features. Their shallow nature, and the fact that some flakes seem to have barely penetrated the aerogel, suggests they result from exceptionally low-encounter velocities, indicative of co-orbiting materials.

*Liquid Droplets* – Akin to flakes, these features are relatively shallow in depth, generally  $L/D < 2$ . Typical examples can be seen in Figure 29. Unlike the flakes, however, this subclass of feature tends to be small in diameter, generally  $< 1$  mm across. Macroscopically they are white specs, akin to flakes, and it takes the microscope to recognize them as a separate class of impact feature. Several characteristics support the conclusion that these depressions were caused by liquid droplets of low-encounter velocity. First, they are highly circular in plan view, totally unlike the irregular flake impacts. Second, there is no fracturing, cracking, crushing, or other disturbed aerogel, unlike all other impact features. The relatively large entrance holes are free of mechanical defects, and thus, hard to spot in plan view. Below the aerogel surface, the feature walls often undercut the entrance hole expanding outward to a bulbous, circular bottom that has the shape of a petri dish (bottom frames of Figure 29). Such depressions differ dramatically from all other impact features, primarily by their regular shapes and lack of aerogel deformation. Third and most importantly, the circular bottoms contain white to tan material that has distinctly concentric color variations and micro-fractures resembling dried mud cracks. There is little doubt that this is a deposit formed in situ by precipitation from some liquid. Preliminary compositional analysis of the precipitate, as detailed below, identifies these deposits as human waste.

It is important to note that the PPMD and POSA experiments also observed round and even elongate, splash-like deposits on a wide variety of surfaces (Kinard, 1998; Pippin, 1998). Thus, there is independent evidence from other MEEP experiments for the existence of liquid droplets. Their detailed spatial distribution pattern on the POSA I instrument and its orthogonal container walls, combined with geometric shielding considerations, suggests the docked Shuttle as the most likely source of this material (Pippin, 1998). The docked Shuttle conducted six wastewater dumps while the MEEP experiments were exposed on *Mir*, each dumping  $\sim 20$  gallons of liquid waste (Visentine, personal communications, 1998).

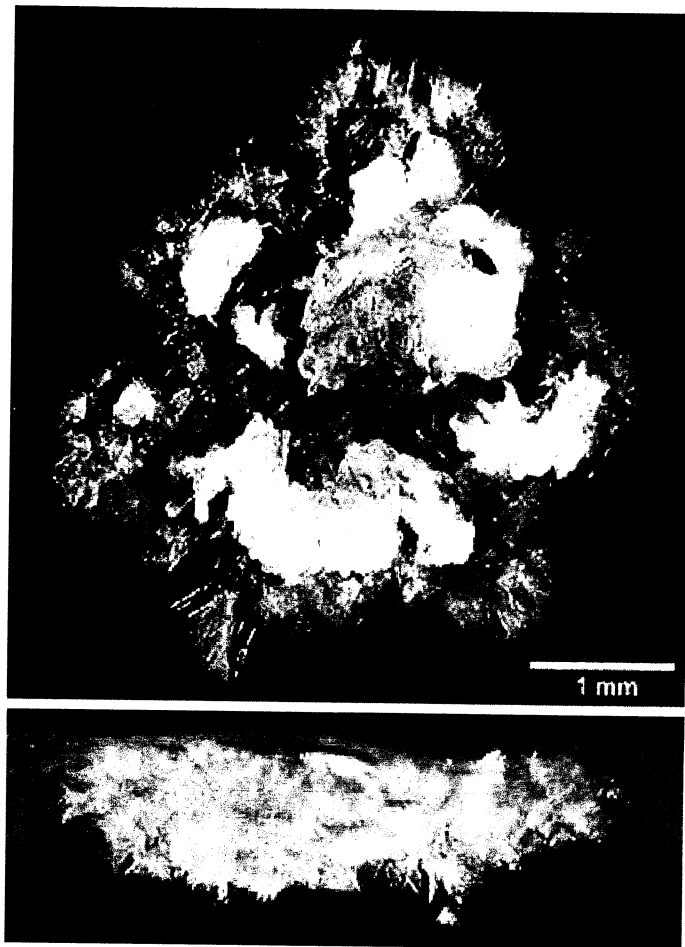


**Figure 27.** Unusually large flake impact in plan view and cross section. Note the highly irregular outline and the shallow depth of penetration. The initial flake actually broke up into a number of pieces, some displaying a distinctly honey-colored hue. The relatively thin layer of highly crushed aerogel suggests a low-encounter velocity.

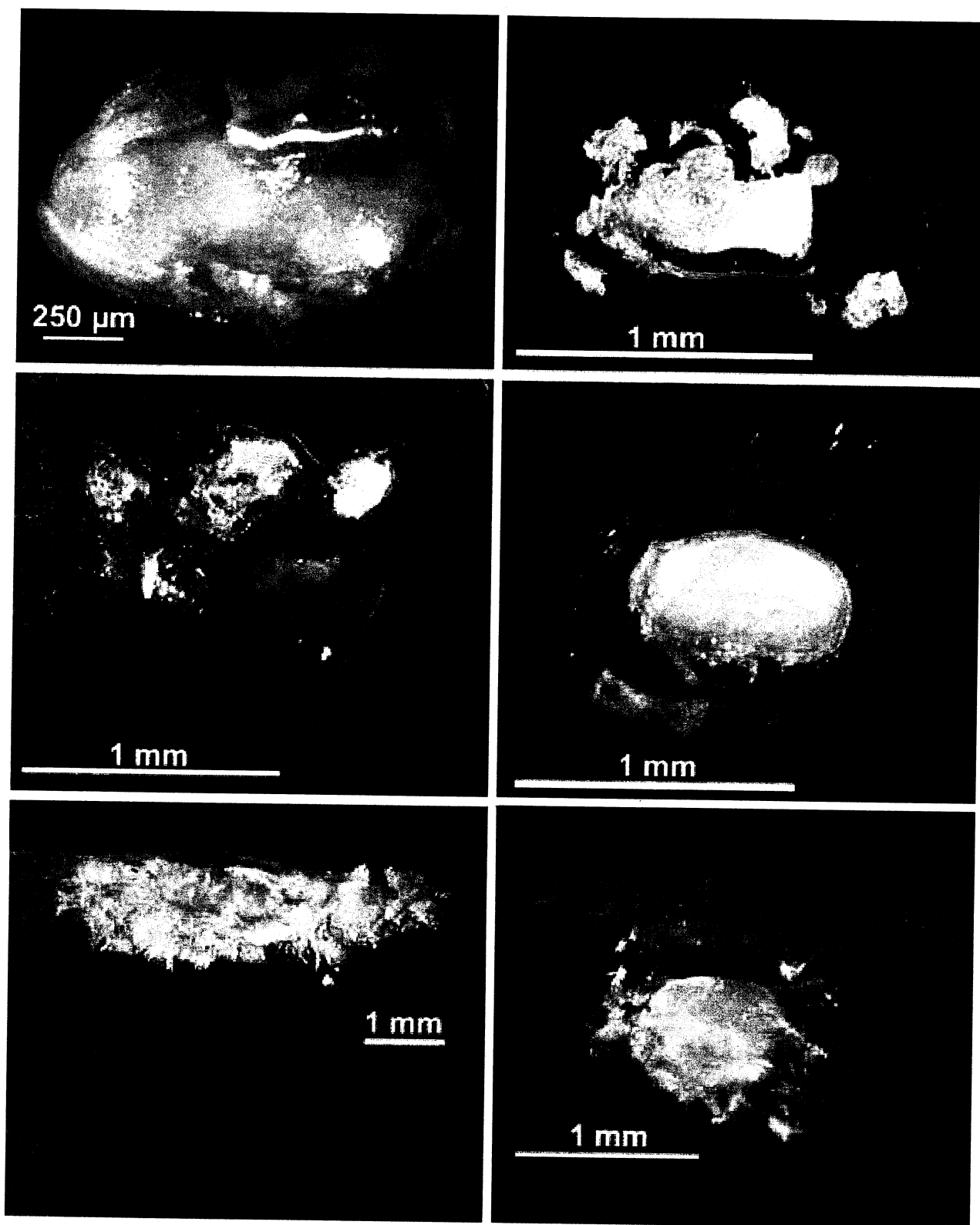


**Figure 28.** Additional examples of flake impacts, some having rounded and wetted appearances suggesting a mixture of solids and liquids (see text).

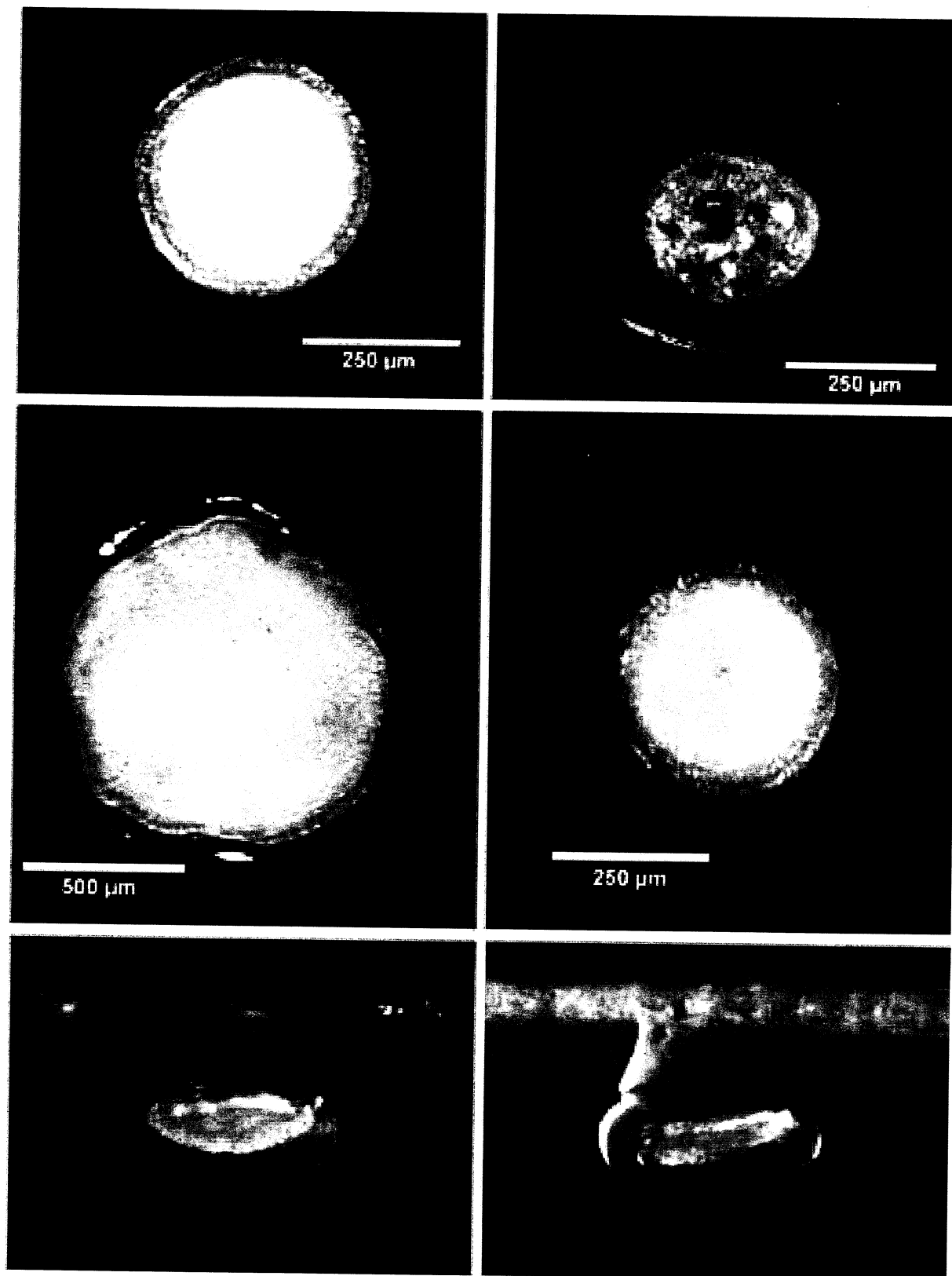


**Figure 29.** Typical examples of droplet impacts in plan view (top four panels) and cross section (lower panels). Note that the petri dish-shaped bottoms contain a distinct deposit that commonly has concentric qualities, especially toward the edges.

Note that some of the flake impacts have substantially rounded portions, either in plan view or cross section (see Figure 28), akin to the much more regular droplet features. This appears consistent with variable mixtures of liquids and solids, all derived from Shuttle's waste management system, and resulting in co-orbiting particles of low-encounter velocities.

## Relative Frequencies

The above descriptions of impact features in space-exposed aerogel included microscopic evidence, if not SEM-EDS analyses, primarily to introduce their morphologic characteristics and to support some of the interpretations. We now return to the first-order, macroscopic survey of all ODC tiles that was to obtain a complete inventory of all features > 3 mm in diameter or depth, which was conducted immediately after harvesting all of the tiles. Although distinct classes of impact features were obvious upon opening the MEEP containers, the detailed interpretations offered above represent our present understanding and were not available and/or appreciated at the time the macroscopic survey was conducted. For this reason, we derived only three types of features during the initial macroscopic survey: (a) tracks, (b) pits, and (c) flakes. Within the current interpretative framework these features now represent (a) low-velocity impacts (b) very high-velocity impacts, and (c) low-velocity encounters with human waste products, both solid and liquid.

The quantitative results of our first-order, macroscopic survey are summarized in Table 1 and illustrated in Figure 30. A first-order observation is that there is a higher frequency of flake and droplet features on Tray 1 compared to Tray 2, corroborating POSA's conclusion (Pippin, 1998) that most of this debris was derived from the direction of the docked Shuttle. The relative frequency of pit features is similar on both surfaces. We realize that this appears inconsistent with a velocity-dependent origin of these structures, because the average encounter velocity of forward- and rearward-facing surfaces should differ dramatically on a non-spinning platform, with much higher velocities prevailing on ram-pointing surfaces (e.g., Zook, 1991). However, the pinhole camera of the co-located PPMD experiment reveals considerable deviation of *Mir* from the ideal of a non-spinning platform. As a consequence, we consider similar pit frequencies on Tray 1 and 2 to be consistent with a velocity-related origin. Genuine, carrot-shaped tracks are about a factor of two higher on Tray 2 than on Tray 1. Although we excluded the obvious clusters of swarm tracks from these frequency data, we had no quantitative means to exclude non-clustered, isolated members of the swarm from the frequency statistics for tracks during the macroscopic survey. Thus, isolated swarm tracks most likely account for the high-track density of Tray 2. In general, it appears as if Tray 1 and Tray 2 intercepted grossly identical populations of particles, except for the human waste-products which dominate Tray 1, consistent with the location of Shuttle and associated practices of waste-dumping.

**Table 1.** Absolute and relative frequency of genuine tracks, pit-type features and flake-depressions > 3 mm that were captured by ODC aerogel of a cumulative surface area of ~0.32 m<sup>2</sup> per tray. The differences between Tray 1 and Tray 2 are given by the 001/002 ratio.

	Tracks	Pits	Flakes	Total
<b>ODC 001</b>	23	33	156	212
<b>Percentage</b>	10.8%	15.6%	73.6%	100.0%
<b>ODC 002</b>	63	41	35	139
<b>Percentage</b>	45.3%	29.5%	25.2%	100.0%
<b>001/002 0.37</b>	<b>0.80</b>	<b>4.46</b>		

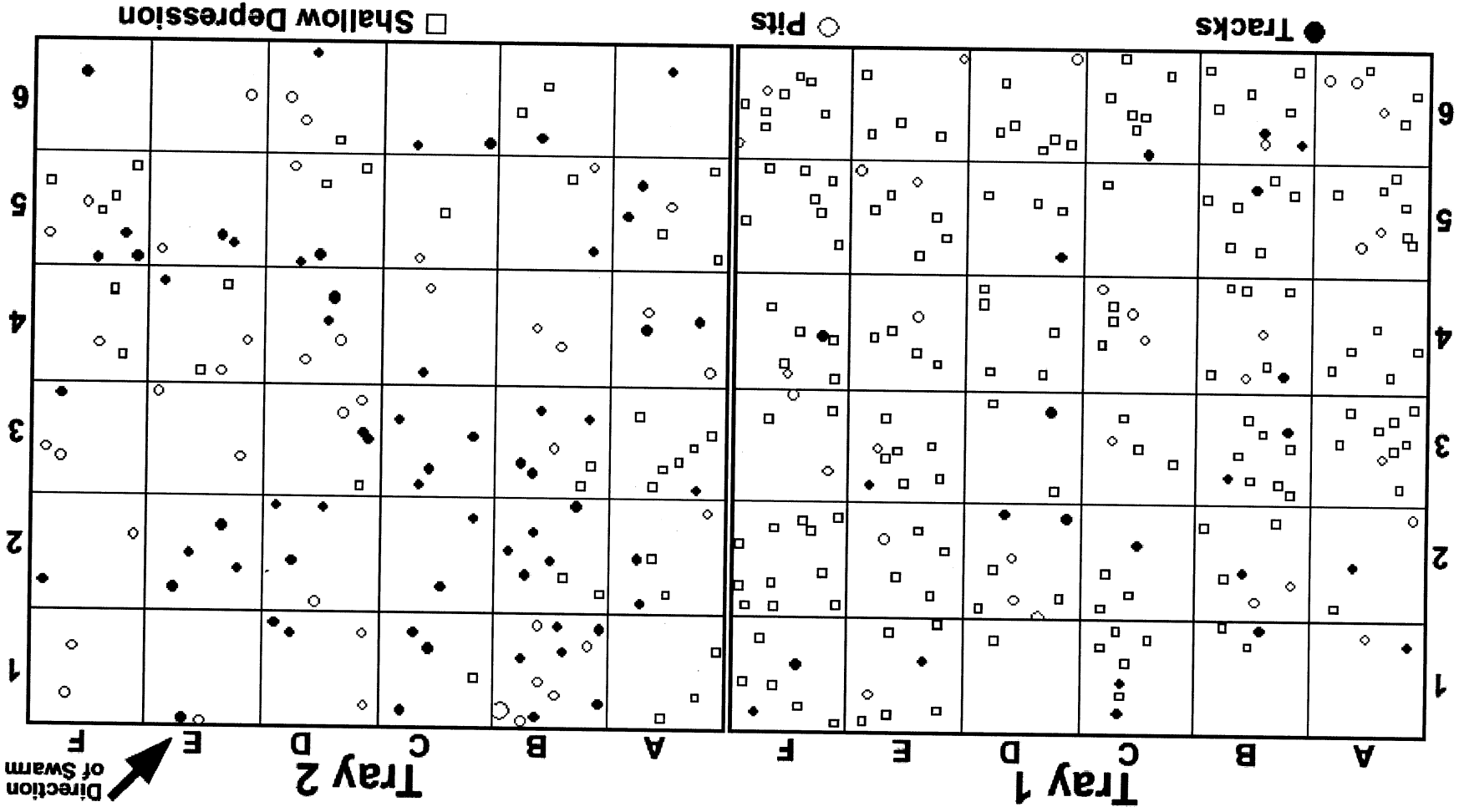


Figure 30. The distribution of impact features > 3 mm classified into three major categories.



## OPTICAL STUDIES

The detailed optical investigations aimed at the identification and dimensional characterization of a statistically significant number of tracks and pits, including structures  $< 3$  mm long. We purposefully excluded the flake and/or droplet impacts from these investigations, because they are of local, somewhat idiosyncratic provenance related to the disposition of waste products, and because they were well characterized by PPMD and POSA. Their inclusion into the time-consuming optical survey would have slowed down operations considerably, thus distracting from the major objective, which was the characterization of high-velocity impactors in LEO. In addition, we did not maintain the distinction between tracks and pits during this portion of our investigation, much less record detailed morphologic subclasses, some of which we only recognized during the course of the microscopic survey and/or SEM investigations. Consequently, we referred to all features as tracks in the microscopic observations and documentation phase.

### Procedures

Detailed optical studies of the ODC tiles were conducted in the FOILS laboratory (see Figure 31), which is equipped with a scanning platform, a binocular microscope, and high-resolution digital-imaging system, all interconnected and controllable by computer. In detail, the FOILS system consists of a large scanning platform (i.e., a modified Mann Comparator) that can be translated horizontally along two directions (X and/or Y axes) by remotely controlled stepping motors with a precision of  $< 2 \mu\text{m}$ . The sample being analyzed (aerogel tile) resides on the scanning platform, which is driven via computer control past a stationary binocular microscope (Wild M8; equipped with diverse lenses, illumination systems, and a beam splitter which accommodates a Sony DKC 5000 CCD camera). A third stepping motor raises and lowers the entire microscope system for purposes of (a) focusing and (b) the measurement of vertical dimensions (Z-axis). The Z-axis is controlled via a rocker switch for focusing the microscope up and down, with individual steps equaling  $4.25 \mu\text{m}$  in distance. The position of all three axes/stepping motors is monitored and continuously displayed on the PC monitor.

Characterization of individual tracks during optical scanning required a minimum of two sets of measurements. The 0,0 corner of each tile is defined as the intersection of the tile edges below and to the left of the silver-paint fiducial mark. Step one involved placing the center of the entrance hole or feature under the crosshair in sharp focus, such that the X/Y coordinates provided for the location in a tile-specific reference frame. The Z-axis readout is then reset to zero (0), as the measurement referred to the local tile surface. The scanning platform is then driven to the terminus of the feature, with the impactor residue—if present—or the deepest point of a pit being brought into sharp focus and centered under the crosshair. A second set of coordinates (i.e., X'/Y'/Z') is recorded. Employing trigonometric relationships, these measurements uniquely define the absolute depth, length, inclination, and azimuthal orientation of each track in a tile-specific reference frame. Additional measurements on select tracks related to residue size or to the diameter of pits were acquired at this time.

The microscope-mounted CCD system also interfaced with the computer and provided for convenient viewing at a wide variety of magnifications, as well as for the capturing of digital images. The majority of images in this report were taken by this system. The bluish background of these images is the result of light scattering by the aerogel during front illumination, the latter provided by either a ring-light for even  $360^\circ$  illumination, or by arbitrarily positioned, flexible fiber optics used to highlight specific details, or both. We also employed traditional, optical (Polaroid) cameras and backlight illumination to highlight specific details of tracks during sample preparation for SEM analyses; this backlit, black and white photography was especially valuable for the documentation of trapped particles.

The rate-controlling factor in the detailed optical analysis of aerogel is undoubtedly the strain on the microscopist's eyes. The intrinsic surface roughness and transparent nature of aerogel is especially taxing, with even the most dedicated individuals not scanning for more than five hours a day, typically split

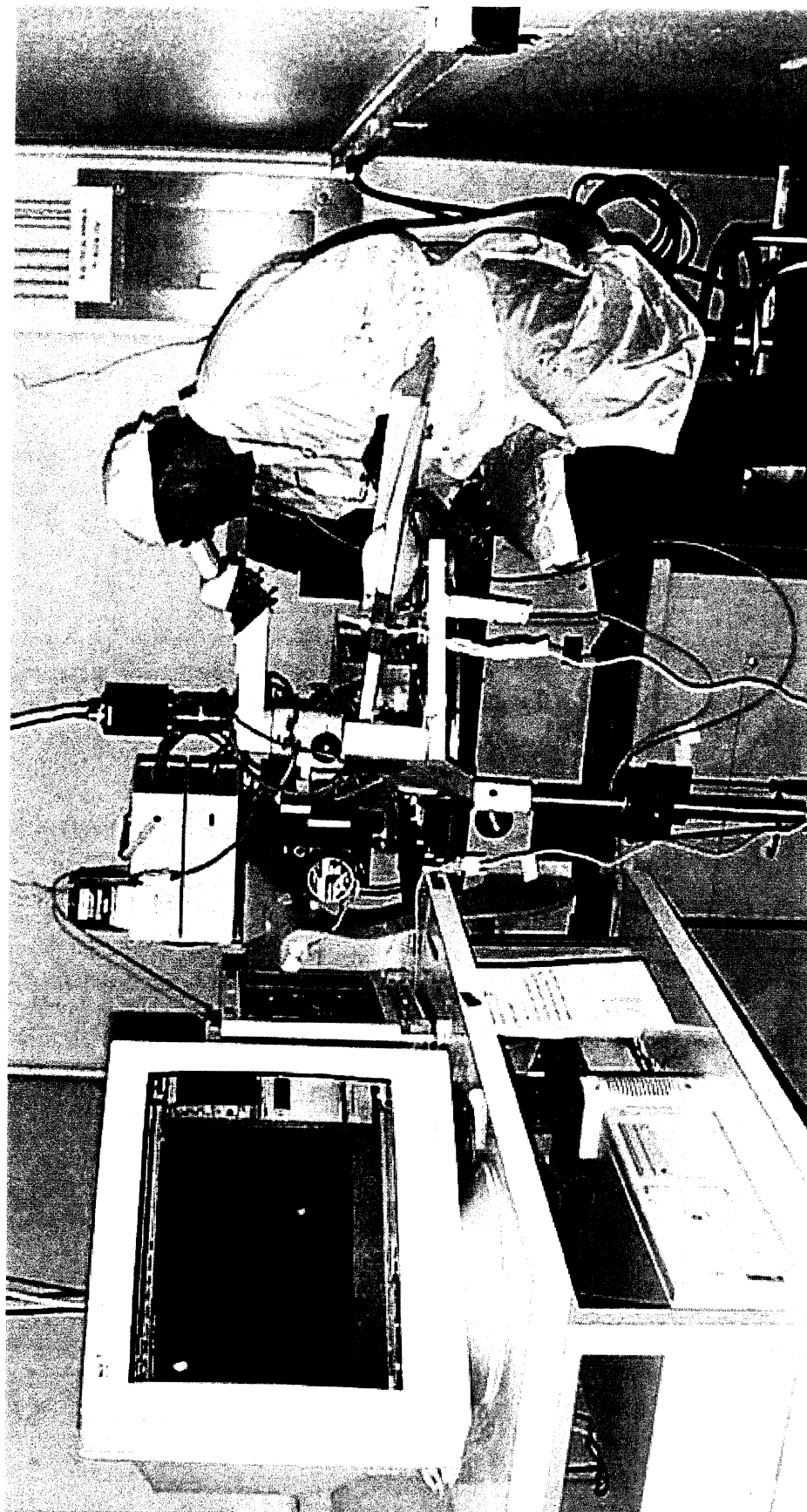


**Figure 31.** View of the optical inspection station consisting of scanning platform, binocular microscope, CCD camera, and interactive PC system of the JSC FOILS laboratory.

between a morning and an afternoon session. Initially, we set out to record all features  $> 50 \mu\text{m}$  in size, mandating an  $\sim 1\text{-mm}$ -wide field of view during scanning operations, and resulting in  $\sim 100$  scan passes to cover an entire  $10\text{-x-}10\text{-cm}$  tile. Each  $1\text{-mm}$ -wide pass took an hour or more to complete, even for the most experienced observer. This resulted in an unacceptably low rate of progress. Therefore, we raised our minimum dimensions to features  $> 100 \mu\text{m}$ . As a result, scan time per tile was reduced to  $\sim 30$  hours, still too slow in view of available resources. Ultimately, we settled for the quantitative recording of impact features  $> 500 \mu\text{m}$  in size, which reduced the scan time to  $\sim 10$  hours per tile, or approximately two working days/tile. To date, we have completely scanned a total of 24 tiles.

As illustrated in Figure 32, the selection of these 24 tiles was by some arbitrary, yet systematic, geometric criterion with the intent of obtaining representative observations for each of the two trays. Our plans are to complete detailed scans of at least half of all tiles (i.e., 18/tray). This plan is substantially motivated by the fact that it is impractical to subject every optically observed track, even on half of the tiles, to compositional analysis via SEM-EDS methods. The large number of impact features recorded by the ODC aerogel was unexpected and is a testimony to its outstanding performance as a particle collector. As a consequence, decisions had to be made that balance the resources available to produce a statistically meaningful data set on the size-frequency distribution of tracks, versus the acquisition of compositional information, the latter being the primary objective of ODC.

## Track Length

The results of our currently completed optical analyses are tabulated in Appendix B. The distribution of track lengths  $> 500 \mu\text{m}$  is summarized in Figure 33. These distributions are remarkably similar for both trays, despite the fact that the Tray 2 data are unquestionably contaminated with swarm tracks. Note that very few features are  $> 5 \text{ mm}$  deep, but the data only refer to 12 tiles per tray, approximately  $1/3$  of the total surface. The grossly similar track populations on both trays imply highly variable *Mir* attitudes, combined with the wide angle viewing geometry ( $\sim 180^\circ$ ) of each tray, such that both trays could sample similar segments of the sky. However, Tray 2 has an approximate factor of 2 more tracks than does Tray 1; this is partly due to contamination with isolated swarm tracks, yet it is possible that Tray 1 was also more shielded than Tray 2.

As previously stated, no distinctions were made between pits and tracks during these optical studies. With increasing appreciation of their significance, we recorded the diameter and depth measurements of pits. These select measurements are summarized in Figure 34. Note that they generally group around  $L/D = 1$ , yet some features are significantly shallower, while others may be much deeper. It appears as if deeper pits occur preferentially on Tray 2 and very shallow structures on Tray 1, yet additional measurements are needed to evaluate whether this is indeed the case.

## Residue Size and Flux Considerations

The size-distribution of projectile residue sizes is plotted in Figure 35. We need to emphasize that these particle-diameter measurements have substantial error, depending on absolute size, possibly as much as 50% for  $< 10 \mu\text{m}$  particles and  $\sim 20\%$  for those  $> 20 \mu\text{m}$ . These uncertainties are related to dimensional measurements at the limit of resolution of the optical system employed, as well as to the difficulty in distinguishing between actual impactor residue and dense, molten aerogel material that envelopes many of these particles (e.g., Barrett et al., 1992). Also note the smaller number of measurements represented in Figure 34 compared to Figure 33, because many tracks did not contain measurable or visible residue at their termini. Nevertheless, note the grossly similar distributions for both trays, separated by  $180^\circ$  in viewing direction.

The particle-diameter measurements from both trays are plotted in cumulative fashion in Figure 36 and versus their cumulative frequency, the latter derived from the total cumulative exposure time (553 days)

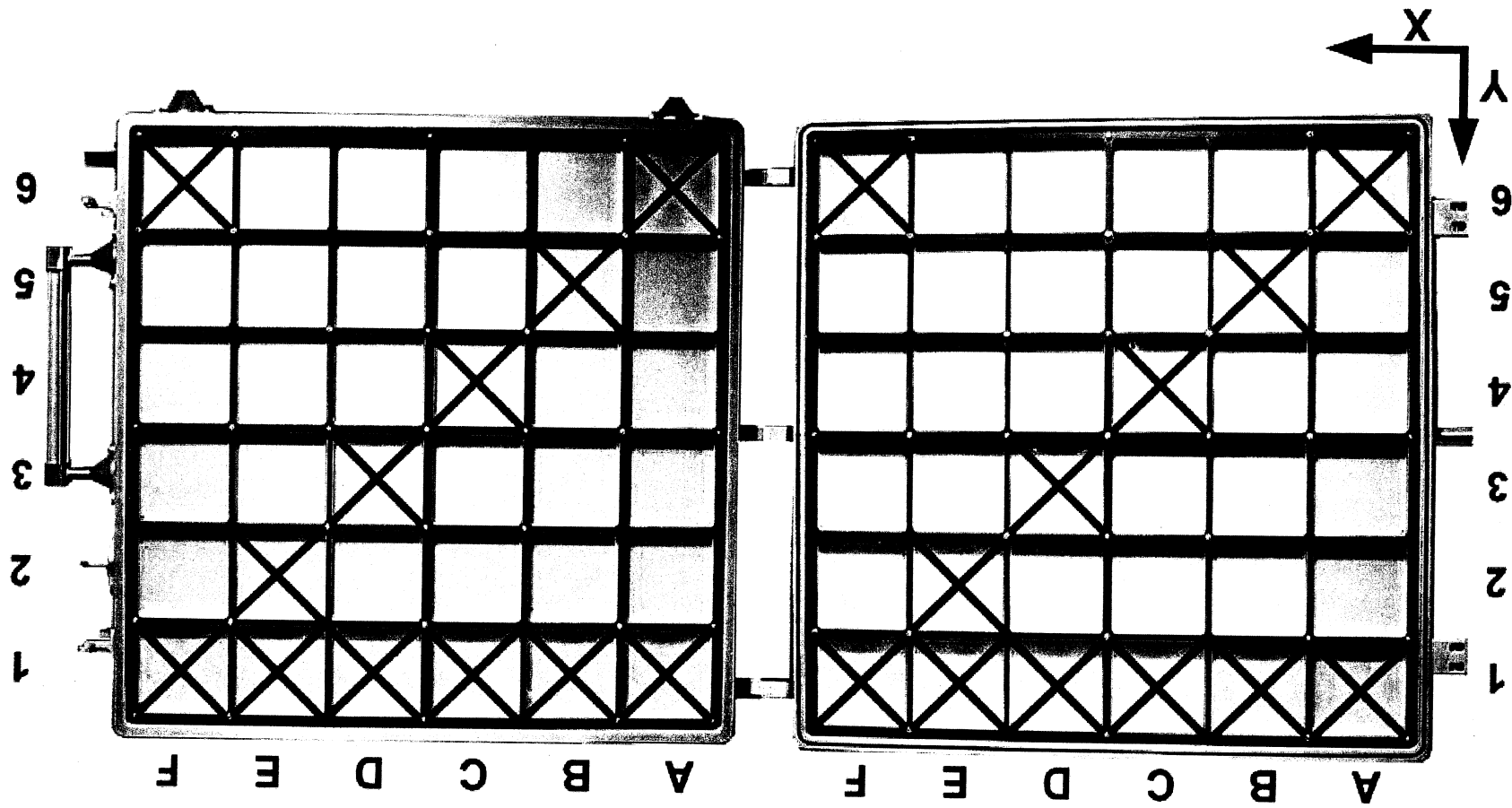
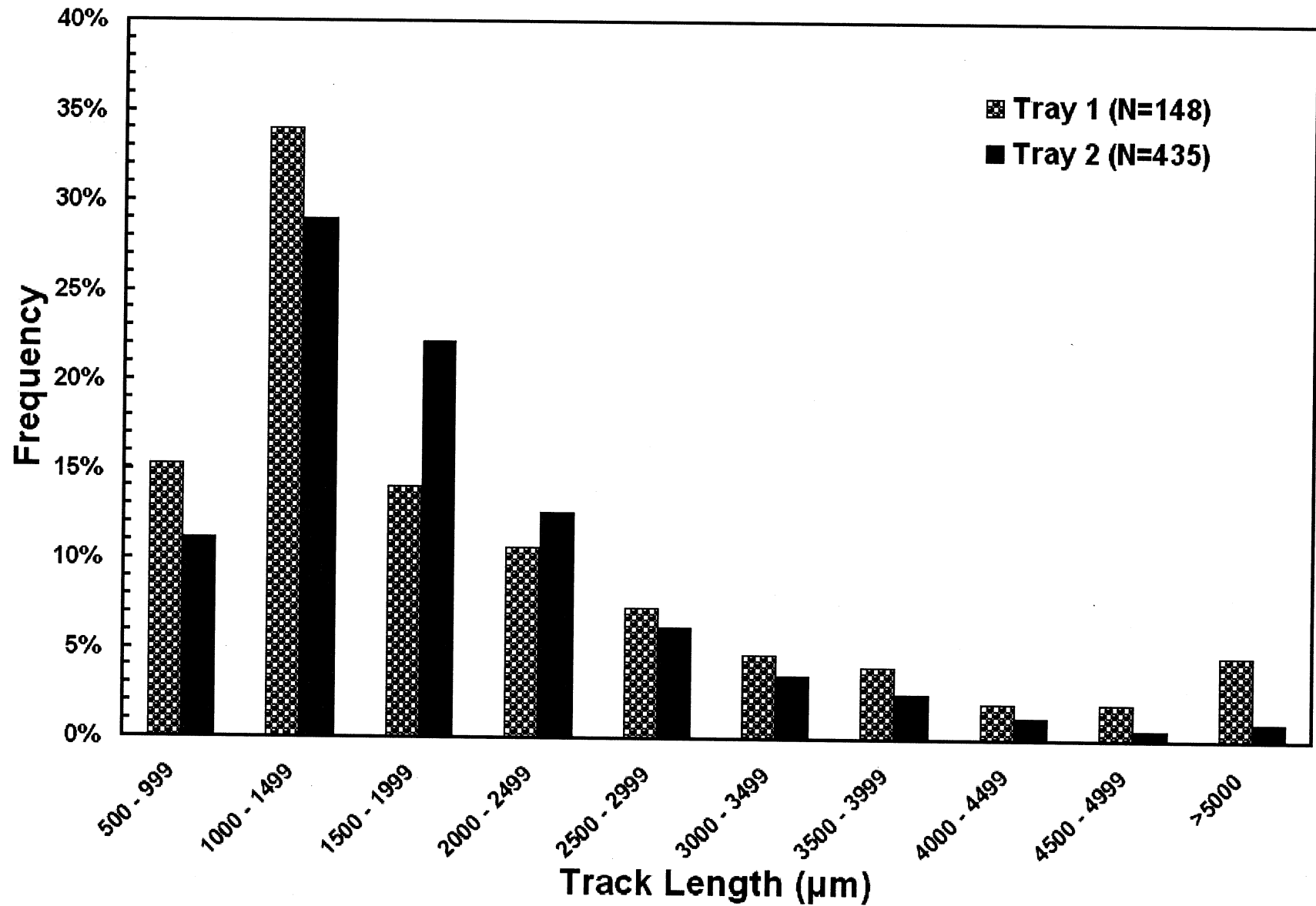


Figure 32. Location of the 24 tiles that have been scanned to date utilizing the FOILS laboratory system.



**Figure 33.** Frequency histogram of absolute track lengths > 0.5 mm encountered on ODC. Note the grossly similar distributions on both trays.

and surface area ( $0.106 \text{ m}^2/\text{tray}$  analyzed optically). For comparison, we plot the LDEF derived mass distributions of small impactors, combining interplanetary dust and man-made debris (e.g., Humes, 1991 and See et al., 1993). Surprisingly, the general shape of these size distributions is fairly similar, and the flux values agree within an order of magnitude. As expected, the ODC particles  $< 10 \text{ }\mu\text{m}$  are much more numerous than those derived from LDEF, due to significant comminution and ablative mass reduction of the ODC residues. In detail,

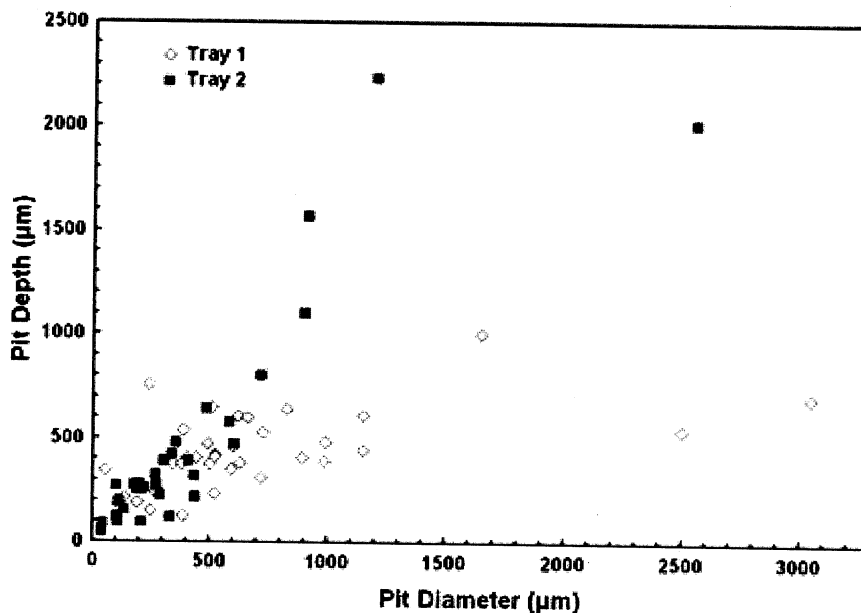
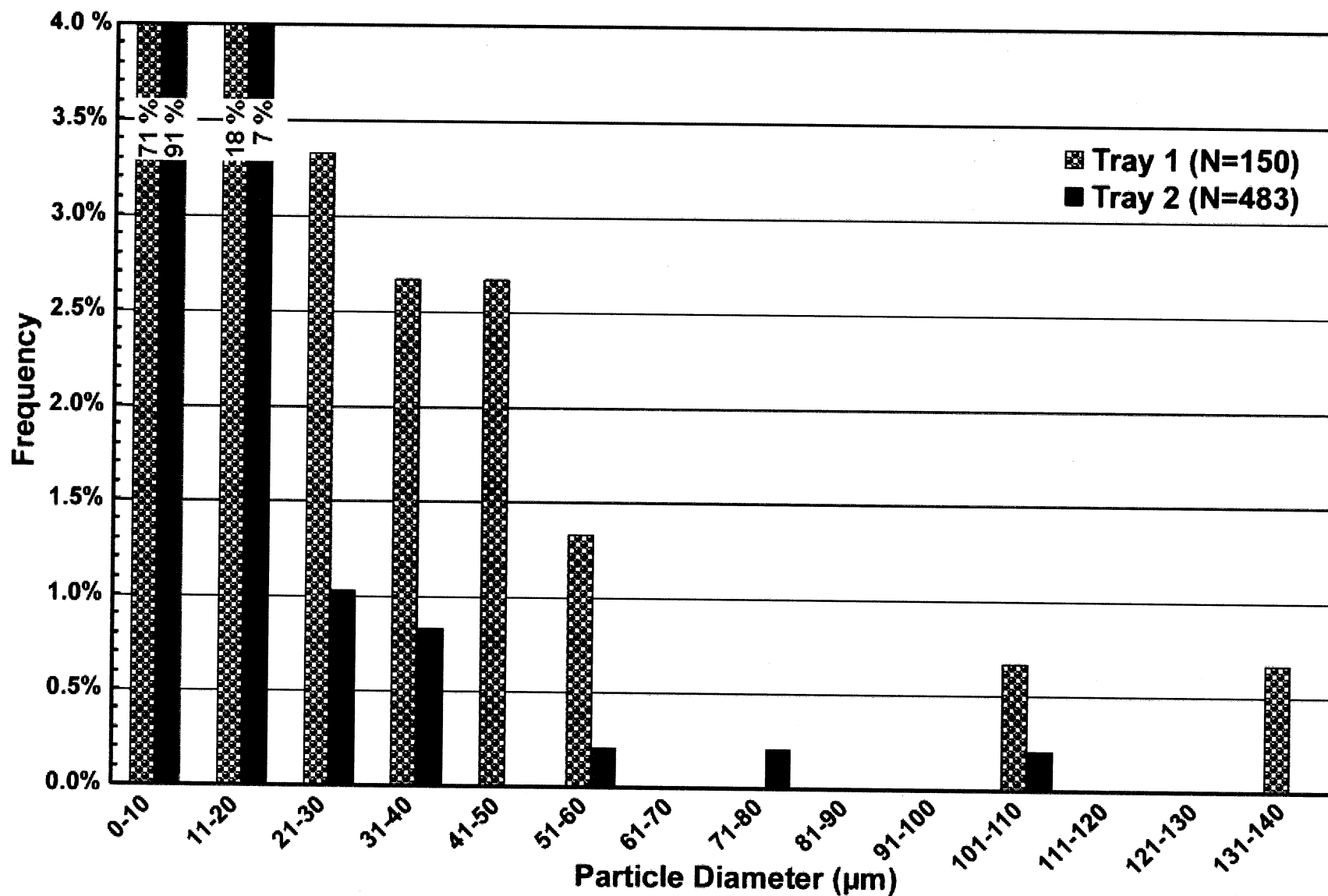


Figure 34. Diameter versus depth relationships of ODC pits, separated into forward- (Tray 1) and rearward (Tray 2)-facing collector surfaces

we do not have a good explanation for the relatively steep curve segments at  $10 - 25 \text{ }\mu\text{m}$  diameter in both ODC distributions, but it is not an effect related to changes in optical resolution, as all scans were conducted at a constant magnification. Within statistical error, the fluxes on Trays 1 and 2 are essentially identical for particles  $> 15 \text{ }\mu\text{m}$ , yet Tray 2 has a much higher flux at  $< 10 \text{ }\mu\text{m}$  sizes, most likely attributable to the large number of small swarm particles.

## Track Length versus Projectile Residue

The interpretation of microcraters in infinite half-space targets, such as on LDEF, is based on laboratory studies that reveal a systematic relationship between crater diameter and the initial impactor size/mass at any given projectile velocity (e.g., Watts and Atkinson, 1992). Typically, any space-produced crater population is converted to a projectile-mass distribution by assuming a constant impactor density, as well as some mean encounter velocity. Unfortunately, the lack of reliable laboratory calibration experiments with aerogel (see Hörz et al., 1997) does not permit such an approach for ODC. However, it may be very instructive to plot the observed residue size versus total track length to empirically explore whether some systematic relationship exists. Figure 37 illustrates the results, characterized by wide scatter. Tracks ranging in length from  $1000 - 3000 \text{ }\mu\text{m}$  are associated with residues that vary by an order of magnitude in size, and by some three orders of magnitude in mass. Conversely, tracks of widely divergent lengths may possess similar-sized, small residues. In particular, most of the longer tracks are associated with relatively small particles, presumably due to ablative or abrasive mass loss of an initially much larger impactor. In addition, note that the largest residues in Figure 37 are associated with tracks that are not unusually long. We conclude that there is no systematic relationship between the size of the particle residue and the length of the associated track for the ODC aerogel. Similar results were reported from laboratory experiments (e.g., Burchell and Thompson, 1996; Hörz et al., 1997), yet Hörz et al. detail that much of the experimental scatter may be due to poorly known impactor mass. The empirical relationships shown in Figure 37 represent a more meaningful test of the desire to extract initial impactor mass (and other dynamic data such as velocity) from space-exposed aerogel. The process(es) of penetration and mass loss in aerogel must be highly idiosyncratic on a particle-by-particle basis and depend on a large number of variables, such as the encounter velocity, physical, and chemical properties of the projectile, and/or preexisting micro-cracks. It does not seem possible to extract major, initial impact conditions and particle properties from



**Figure 35.** The distribution of projectile residue sizes based on in situ measurements in unprocessed aerogel collectors using optical microscopy. These measurements may be afflicted with substantial errors, as it is difficult to optically recognize the extent of molten aerogel adhering to, or invading, the projectile materials. The population is dominated by particles  $< 10 \mu\text{m}$ , close to the limit of the microscope's optical resolution.

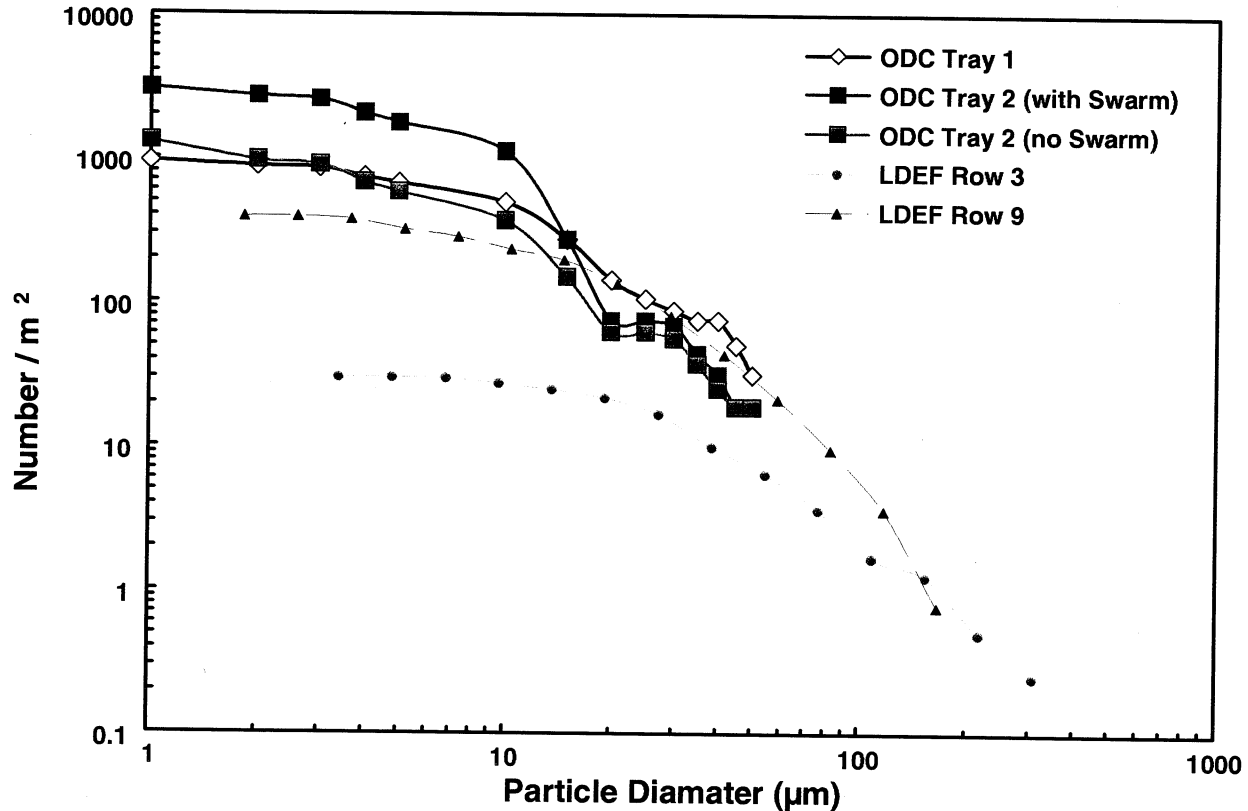


**Figure 36.** Cumulative particle fluxes in the ODC aerogel and comparison with LDEF data. The ODC data refer to direct measurements of (minimum) particle size. In contrast, the LDEF particle sizes are calculated from microcrater diameters in aluminum targets assuming some idealized impact conditions and using the equations of Watts and Atkinson (1993). Note the general agreement between ODC Tray 1 and Tray 2 (after subtraction of the swarm event; see Figures 40b for the quantitative identification of swarm tracks). In addition, note that Row 9 of LDEF occupied the leading edge, thus representing a maximum particle flux, while Row 3 occupied the trailing edge yielding a minimum flux (e.g., Zook, 1991). The ODC data are somewhat deficient at large sizes and overabundant at the small sizes, both phenomena consistent with mass loss during capture.

the dimensional measurements of tracks and associated particle residues. Finally, note that the distributions of track length and residue sizes are similar for both trays, again suggesting that Trays 1 and 2 experienced particle environments consisting of impactors with similar velocity and physical properties.

## Particle Trajectories

The trajectories of track-producing particles can be reconstructed from the measurements of X/Y/Z (entrance hole) and X'/Y'/Z' (end of track); the results of such calculations are illustrated in Figures 38 - 40. For a first-order impression we plotted track orientation from all tiles projected on the area of a single tile in Figure 38. A directional vector of uniform length represents individual tracks, regardless of size, with the arrow pointing toward the terminus. The relatively random distribution on Tray 1 contrasts markedly with the highly lineated distribution of Tray 2, the latter data including tracks associated with the swarm event discussed earlier. The rose diagrams in Figure 39 present a more quantitative perspective. Tray 1 (Figure 39a) includes all tracks as portrayed in Figure 38 and suggests some modest, local maximum. Tray 2 (Figure 39b) is obviously so dominated by the swarm tracks that we subtracted all swarm tracks for a separate portrayal of the remaining population (Figure 39c).



Finally, Figure 40 is a hemispherical (equal area) projection of measured track orientations that not only preserves the azimuth, but also the inclination of individual tracks; this portrayal reflects the true direction/radiant from which a particle approached ODC. A trajectory will enter the reference sphere surface at the plotted location (+), terminating at the center. For those not familiar with such plots, azimuthal relationships are as measured; the center of the plot represents vertical impacts ( $90^\circ$ ), the outer circle horizontal cases ( $0^\circ$ ), with intermediate inclinations linearly related to their radial distance from the center. Again, the trajectories of Tray 1 are generally random, with a modest maximum at approximately the  $45^\circ$  direction and of relatively shallow angles from the local horizontal. In contrast, Tray 2 is characterized by a pronounced maximum that represents the swarm tracks. The remaining tracks on Tray 2 are of fairly random orientations, similar to those of Tray 1. These similarities suggest either that there is no single dominant particle source from a specific radiant (excepting the secondary swarm event on Tray 2), or that the viewing directions of Mir/MEEP/ODC surfaces varied widely throughout the 553-day mission. In addition, one may also conclude that there was no local promontory that shielded large fractions of the field of view of either ODC tray.

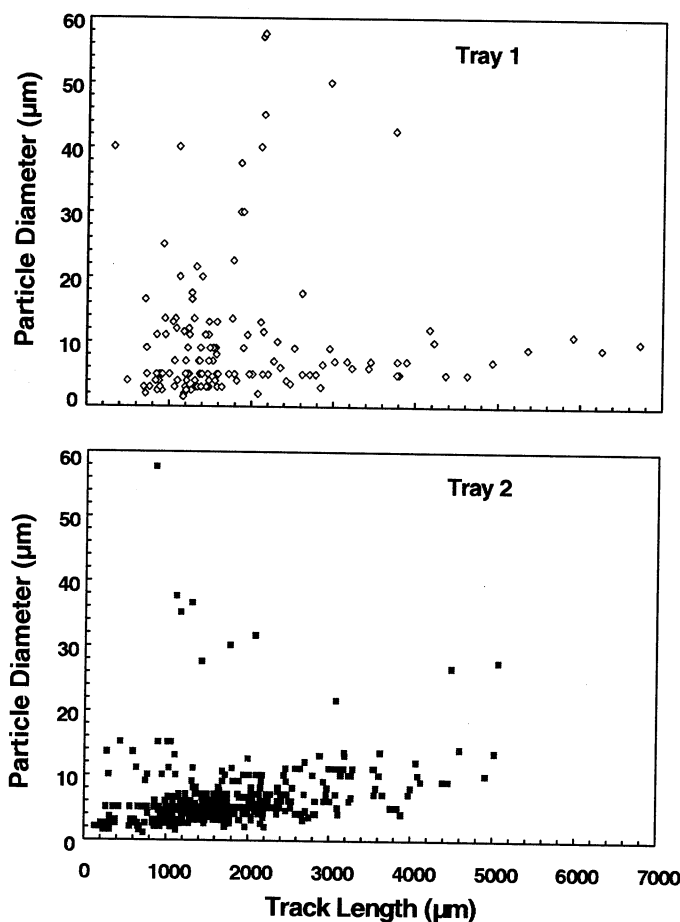


**Figure 37.** Track length versus diameter of the projectile residues for ODC Trays 1 and 2. The non-systematic relationship of residue mass and absolute track depth in aerogel seriously impairs the reconstruction of an initial impactor size and/or of encounter velocity (see text for detailed discussion).

## DETAILED COMPOSITIONAL ANALYSIS

The detailed compositional analysis of ODC particles utilized SEM-EDS methods. These techniques were first applied to space-exposed surfaces of the Solar Maximum satellite (Warren et al., 1989), and became routine in the analyses of LDEF surfaces (Levine, 1991; 1992; 1993). They are also the method of choice for the continued monitoring and evaluation of impact features on Shuttle surfaces (Christiansen et al., 1998). The major difference between these earlier studies and the ongoing ODC work relates to the availability of numerous, essentially unmelted particle fragments, whereas previous studies were largely confined to the analysis of molten impactors. The analyses presented in this section are merely examples of representative particle types to support some of the descriptions and interpretations offered and to illustrate the potential of the SEM-EDS technique(s). In addition, these examples illustrate the significant level of effort needed for any systematic, statistically meaningful assessment of the particle populations captured by ODC.

## Sample Recovery and Preparation

Although the SEM-EDS methods are fairly routine, substantial new efforts went into the development of suitable methods to recover the particle residue from its friable aerogel matrix, and to design suitable sample preparation procedures for the contemplated SEM studies. Major emphasis was placed on minimizing the loss of samples, commonly  $< 10 \mu\text{m}$  in size, as well as on avoiding contamination, both chemical and particulate, during all extraction and sample preparation steps. Most sample extractions are carried out in a class 1000 flow bench, housed inside the FOILS laboratory. Individual aerogel tiles are readily split via a razorblade into subsamples on the order of  $1 \text{ cm}^2$  in surface, with each subsample typically containing a single track. The actual impact feature of interest and its particle is then photographically documented, both in plan and side view with the CCD camera

system or via optical (Polaroid) photography, or both. Following photo-documentation, individual tracks are physically split with a razor blade, generally under a binocular microscope. The track represents a substantial flaw on the scale of the centimeter-sized aerogel samples, the reason why the material fails along the actual track when applying highly localized pressure via the razor blade. Typically, the aerogel is not cut, but cleaves into two halves during such operations. Obviously, this aerogel splitting is not perfect and most of the terminal residue is confined to one half, commonly buried under a thin layer of aerogel. The aerogel-covered residue is then removed from the tile sample with a single-bristle brush. If only small masses of aerogel adhere to the extracted particle, the sample may be transferred directly to a graphite SEM planchette. However, typically the material is transferred to a petri dish for removal of excess aerogel until substantial surface fractions of the residue are exposed for direct electron beam exposure. On rare occasions, particle residue may be exposed immediately after the track-splitting procedure, in which case the entire track and its particle are transferred to a planchette. This procedure works well for tracks as small as  $1 \text{ mm}$ , yet we do not know whether it is suitable for still smaller tracks. The most critical steps are the actual track splitting and the quarrying operations to dislodge materials from the halved terminus. Both result in small samples that tend to charge electrostatically and that are difficult to steady. Electrostatic charging of small, transparent, and difficult to see volumes of aerogel is the major reason for sample loss. Charging, specimen movement, and potential sample loss may even occur during electron-beam radiation inside the SEM's vacuum chamber, because small samples of aerogel are simply difficult to attach and secure to any surface.

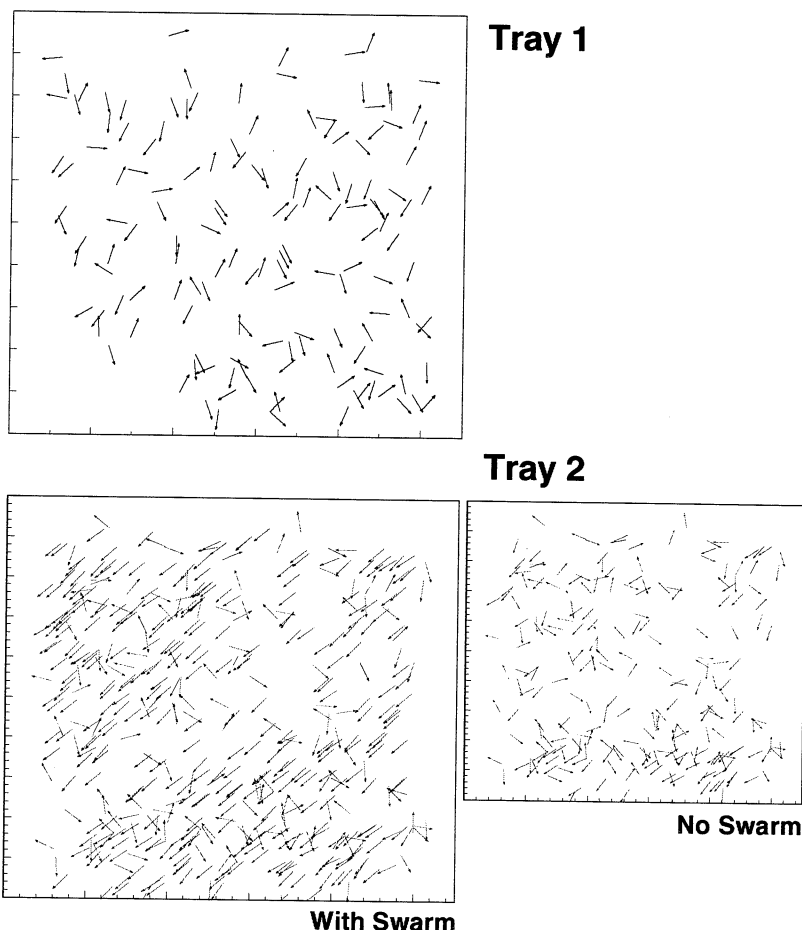


**Figure 38.** Azimuthal orientation of 148 tracks on ODC Tray 1 and of 435 tracks on Tray 2, the latter dominated by swarm particles of uniform direction (see text for details).

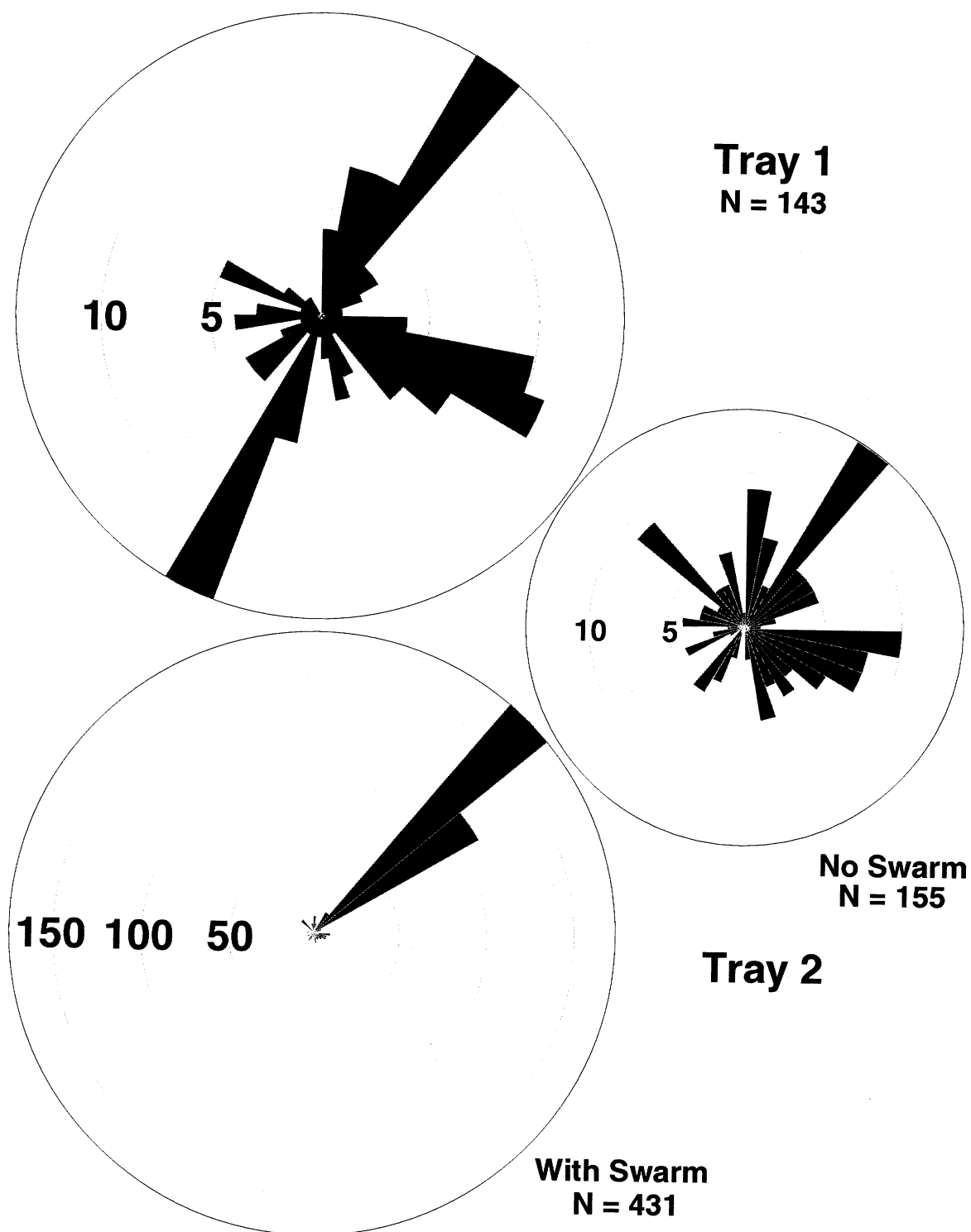


**Figure 39.** Rose diagram of azimuthal track orientations for Tray 1 and Tray 2; Tray 2 is shown with and without (smaller inset) the swarm event. The sporadic populations on both trays display modest, local maxima.

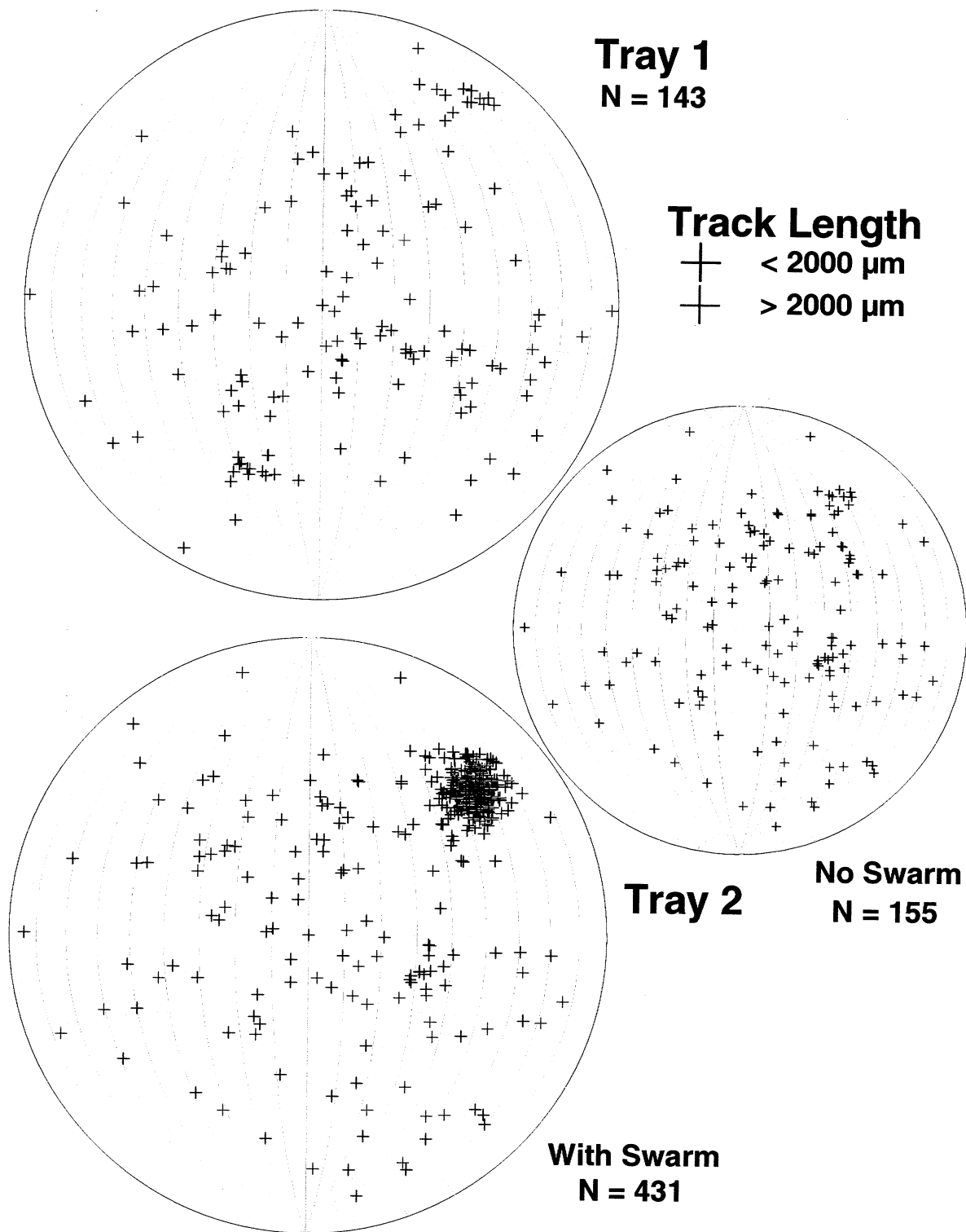


**Figure 40.** Quantitative illustration of track orientations utilizing an equal-area stereo projection. Again, Tray 2 is shown with and without the swarm events included. All tracks within  $15^\circ$  of the center of this cluster were assigned to the swarm event and subtracted from the measured population to yield the sporadic background of Tray 2 for all Figures 39 and 40s.

## Representative Results

Consistent with the above morphologic descriptions of impact features, we offer the following representative examples of shallow depressions, pits, and slender tracks. The detailed documentation for individual particles typically consists of optical images in plan view and cross section, an SEM image, and an EDS spectrum of the recovered residue. In addition, we include transmission electron microscope (TEM) images of an unmelted natural cosmic-dust particle recovered in LEO.

*Man-Made Particles* - The liquid droplet feature introduced in Figure 29 is again seen in Figure 41. With the impactor residue already exposed in the bottom of the feature, little sample processing was required for detailed SEM investigations. The plan view image focuses on the bottom of the feature and the evaporite deposit. Other circular elements, such as the entrance hole, are out of focus and merely hinted at by partial arcs of reflected light. Note the structurally complex, yet highly circular nature of the cavity. An SEM image is presented in the lower left and illustrates the entrance hole and a shoulder

### Human Waste

1C01-8

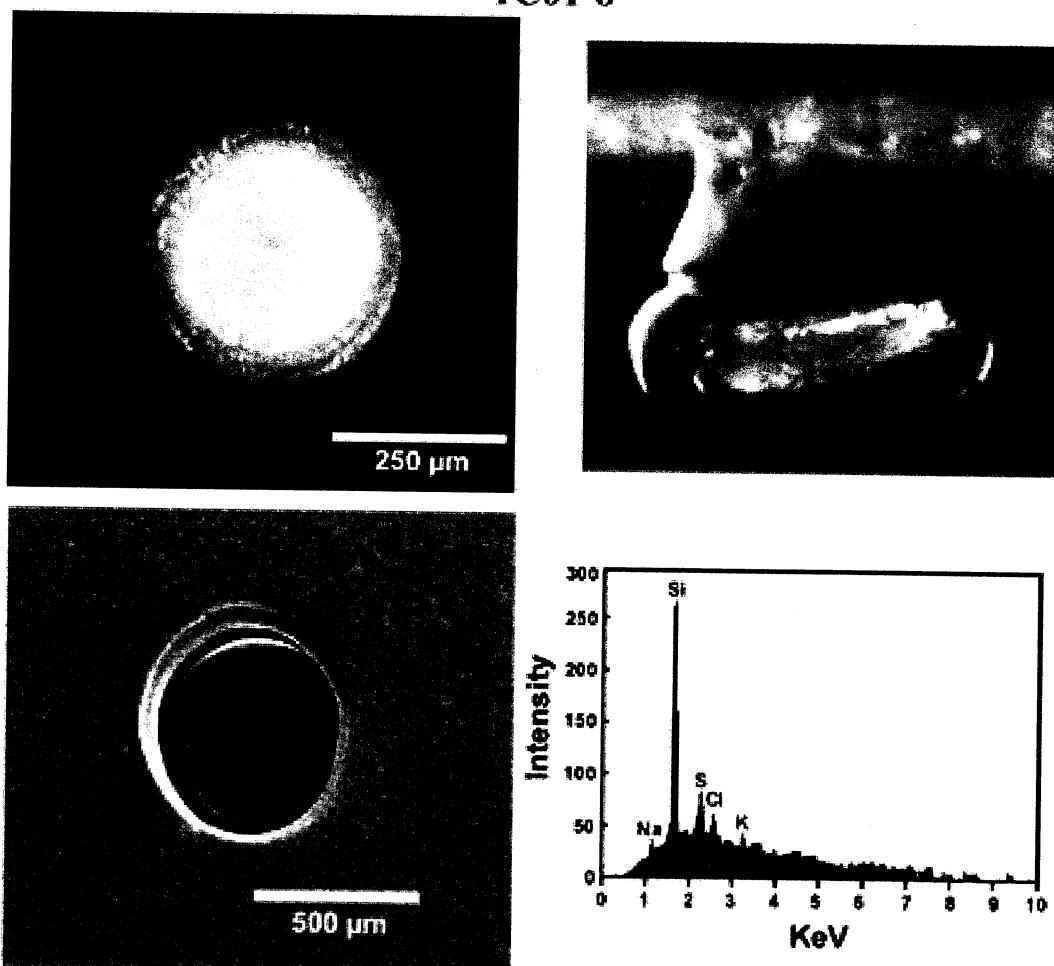


**Figure 41.** Example of the detailed analysis of an individual droplet feature, including SEM imaging and EDS techniques. Note the substantial depth of this feature, its smooth outlines, and the total lack of any mechanically deformed and micro-fractured aerogel. Typically, these structures have an opening at the surface of the aerogel that is narrower than the bottom of the feature. The “projectile” residue is confined to a lens of smaller radius than the bulbous cavity (partial outline visible in top-left plan view). The presence of biogenic elements (i.e., Na, S, Cl, & K) can be seen in the X-ray spectrum; the Si peak is largely caused by the Si-based aerogel substrate.

formed by a peculiar cavity restriction at depth (see cross section). This image also demonstrates the absence of any fracturing and mechanical damage, corroborating our earlier conclusion that such features result from the interaction of aerogel with some liquid, and that they are solution pits and not the products of mechanical displacement. The EDS spectrum of the evaporite deposit reveals the biogenic elements Cl, S, K, and Na; the Si peak is derived from the aerogel substrate. Specifically, the substantial quantities of Cl and S provide the most diagnostic criterion for human waste. Essentially identical spectra were obtained on all ODC droplet-type features analyzed to date, as well as on the evaporite deposits on the companion PPMD and POSA MEEP experiments (Kinard, 1998; Pippin, 1998). There seems little doubt that these features result from Shuttle operations, which currently call for the dumping ~ 20 gallons of wastewater every three days.

Figure 42 shows the large flake impact first illustrated in Figure 27. This particle clearly broke up during impact, and large, irregular, platy fragments adhere to the bottom of a rather shallow depression. The latter mimics the irregular projectile shape in outline. These morphologic characteristics are typical for all flake impacts and they are in stark contrast to the liquid droplet pits shown in Figure 41. Nevertheless, the EDS spectrum of the flake fragments is largely composed of biogenic elements (e.g., Na, P, and S). Unlike the previous example, the sample thickness exceeds the X-ray excitation depth, so that substantial parts, if not all, of the Si peak must be derived from the flake particle itself. The lack of Cl seems highly

## Flake Particle

1C01-07

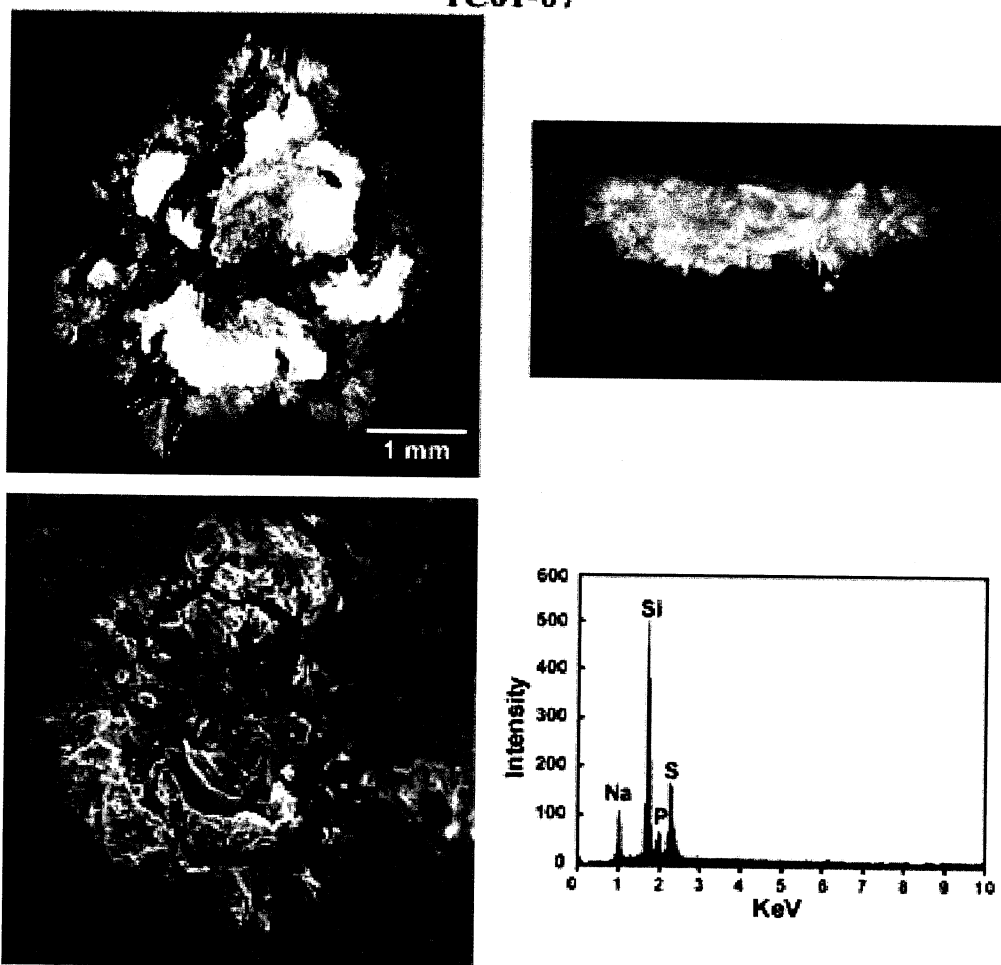


**Figure 42.** Large flake feature previously shown in Figure 29. Note the EDS spectrum contains no Cl, yet it is dominated by the biogenic elements Na, P, and S.

significant for human-waste products; additional ODC examples that contain no Cl could be shown, suggesting a previously unrecognized particle type in the ODC aerogel. However, some flake residues do contain Cl, akin to Figure 41. Cl-bearing materials were frequently observed on LDEF, as well as most other space-exposed surfaces, and are typical for human waste. Such Cl-deficient spectra appear consistent with pure soap, yet we do not know of any specific mechanism that would preserve pure soap particles in Cl-containing wastewater. The source and origin of these Cl-deficient particles is currently unclear.

The terminal sections of a typical, carrot-shaped penetration track and its associated residue are illustrated in plan view and cross section in Figure 43; the aerogel surface illustrated in the cross section is not the original tile surface, but a razorblade-induced fracture. Note the well-developed cone-in-cone structure and the misalignment of the last few cones, causing the track to curve and the particle to reside off the true axis of the track. The residue is the largest particle recovered from ODC to date, ~ 200  $\mu\text{m}$  across. Also note its jagged, sharp corners and what appears to be mechanical striation and abrasion on the particle's surface, both observations arguing against pervasive melting. The EDS spectrum of this particle is dominated by Ti and Zn, which constitute the pigments of many thermal protective paints. Similar particles/spectra are known from most other space-exposed surfaces; thermal protective paints are

## Paint Flake

1A06-17

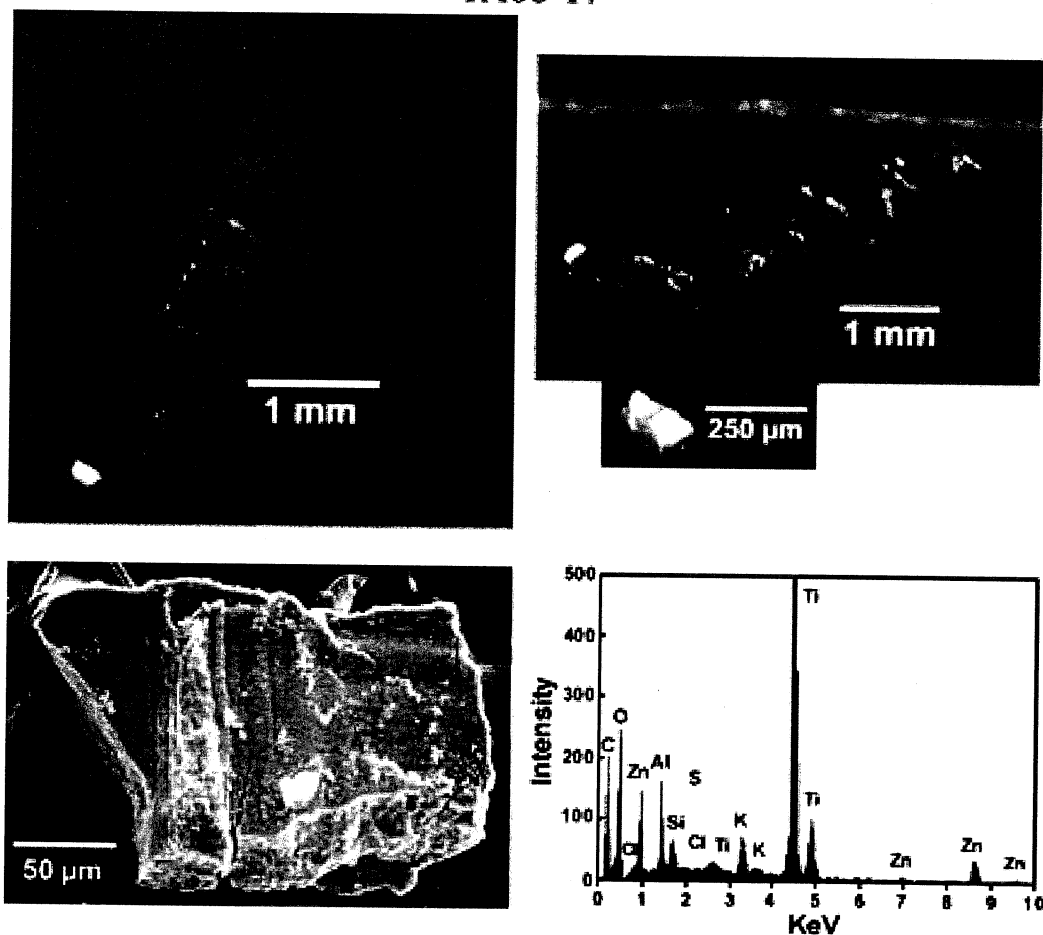


**Figure 43.** Detailed analysis of a man-made particle. Note the cone-in-cone structure and the misalignment of the last few cones with the overall track axis. The recovered particle exhibits a highly irregular, if not jagged and sharp-edged surface, suggesting that very little rounding, much less melting, occurred during the capture process. The dominance of Ti and Zn identifies this particle as paint (pigments), with other elements being part of the organic binder.

prone to substantial abrasion by small-scale impacts, and their largely organic binders degrade when exposed to atomic oxygen and/or UV.

In addition to the two examples shown, we recovered and analyzed ~ 20 residues from ODC that must be classified as man-made debris. These include particles rich in Fe, with subordinate levels of Ni and/or Cr, the latter characteristic of stainless steel. In addition, Cu-rich particles reflect fragments of electronic compounds, some even associated with Ag from silver solders. Unlike LDEF, however, particles dominated by Al seem rare on ODC. Two examples of essentially pure metallic aluminum were found that represent structurally disintegrated components, while only a single  $\text{Al}_2\text{O}_3$  particle was discovered so far. Clearly, more particles need to be analyzed in order to arrive at statistically firm conclusions, or before some significant difference with LDEF can be established.

A relatively large fraction (~ 90%) of all impactors can be classified into man-made or natural-particle categories. Figure 44 represents one of the ambiguous cases. This spectrum was taken with a thin beryllium window that allows analysis of oxygen, thus the significant oxygen signal; the C peak represents carbon-coat to make the particle's surface electrically conductive, while the Si is likely derived from

## Fe Oxide Particle

1C01-13

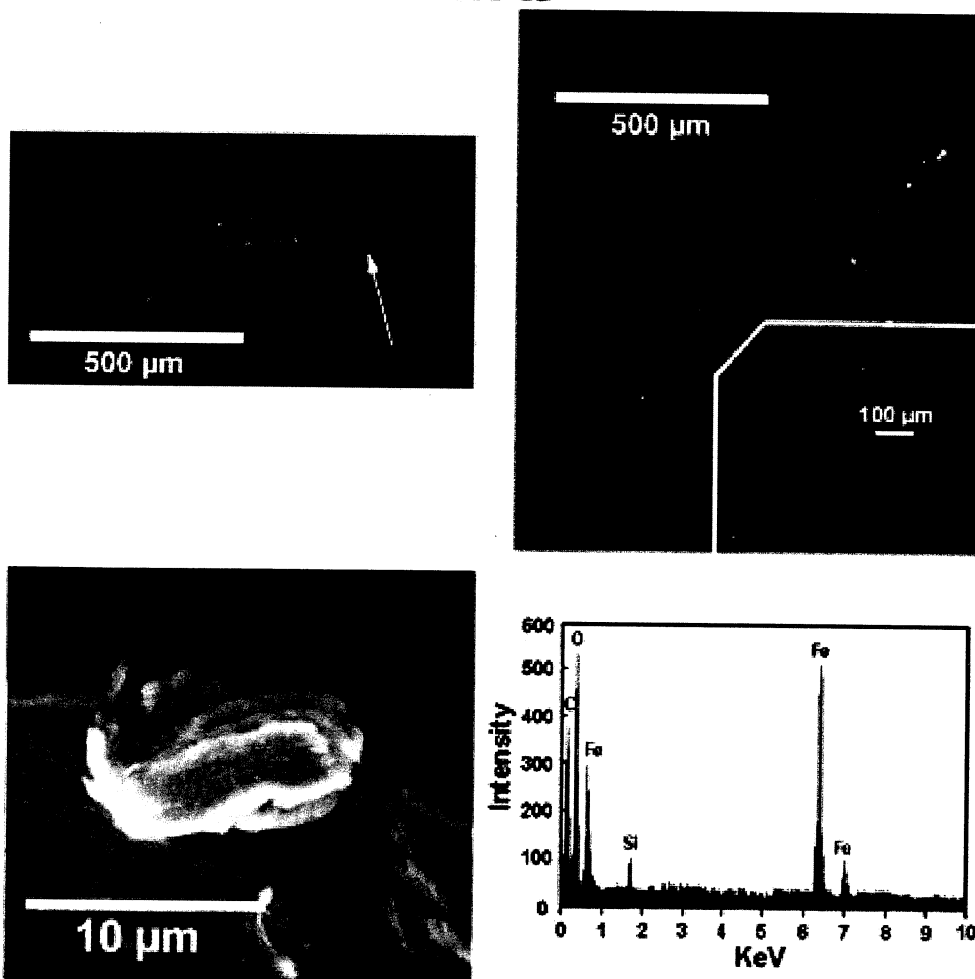


**Figure 44.** Example of a particle, ~ 10 µm in length, that resided at the terminus of a 1.2-mm-long track. Note the shedding of light-colored projectile material along the stylus. This particle appears to have been either plastically deformed or molten during capture process. Compositionally, it is Fe-oxide and could either be man-made or natural in origin.



aerogel adhering to the particle. This identifies this particle as being essentially pure iron oxide, without specifying the exact stoichiometry. It could be natural, such as isolated crystals of hematite ( $\text{Fe}_2\text{O}_3$ ) or magnetite ( $\text{Fe}_3\text{O}_4$ ), known to occur in meteorites, or it could be man-made iron that was oxidized (e.g., during explosive or impact-derived origins). The lack of any alloying component, such as Cr, W, or Ni argues against most popular steels and leads us to prefer a natural source. Nevertheless, the origin of this particle remains ambiguous. In the cross-section image, note that considerable mass was shed from the projectile and deposited along much of the stylus. The recovered residue appears deformed, if not molten. Its maximum diameter ( $D_p$ ) is  $\sim 10 \mu\text{m}$ , which compares to a total track length of  $\sim 1,400 \mu\text{m}$ , resulting in a  $D_p/L = 140$  for this relatively dense impactor. Such  $D_p/L$  values are typical for tracks produced at light-gas gun velocities of 4 to 7 km/s (Hörz et al., 1997) using less-dense glass projectiles.

*Natural Impactors* - The residue,  $\sim 12 \text{ mm}$  in diameter, recovered from an  $\sim 1\text{-mm}$ -long swarm track (left track in optical image) is illustrated in Figure 45. As is common for natural particles, they tend to be composed of very fine-grained aggregates of sub-micron-sized components which in turn leads to modestly variable

## Swarm Particle

2D03-22

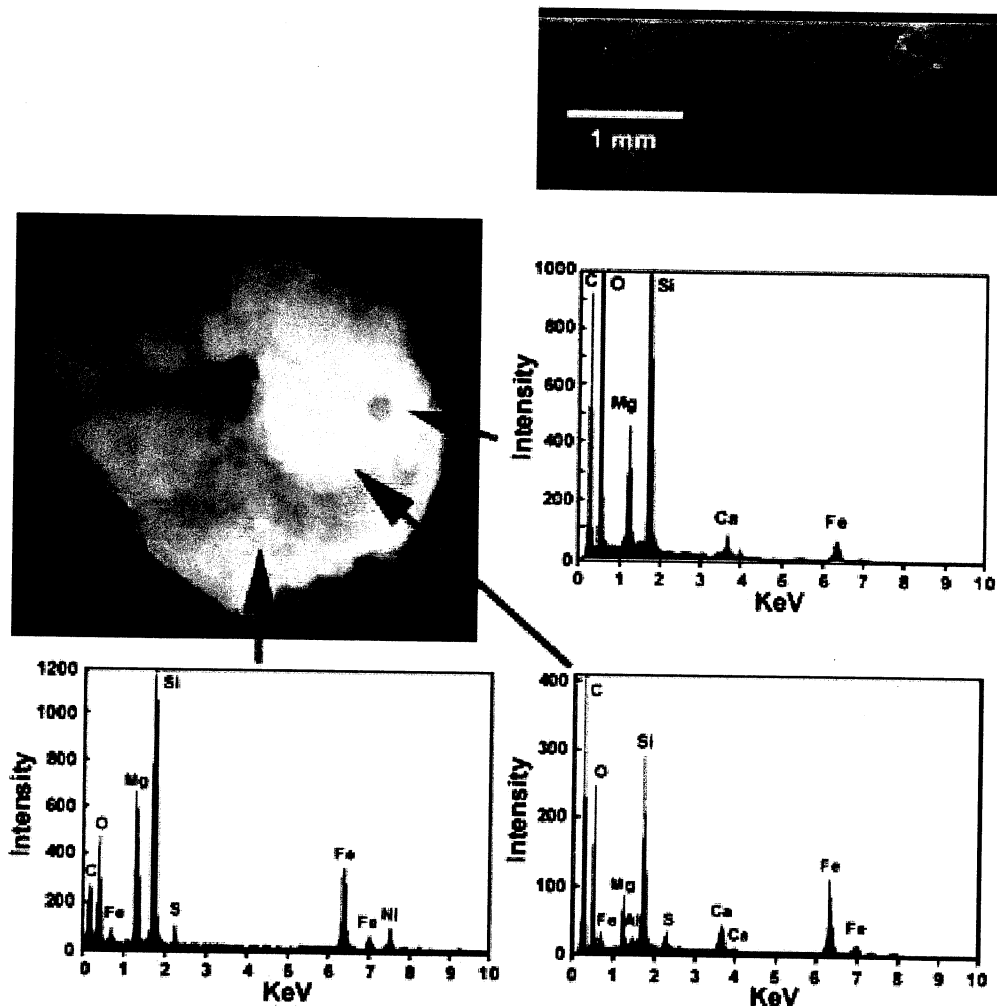


**Figure 45.** A particle,  $\sim 6 \text{ mm}$  in size, recovered from the left track in the inserted cross section of what are obviously “swarm” tracks, all of uniform orientation. Natural particles are commonly aggregates and a number of spectra are presented to show chemical and mineralogical heterogeneity on scales of microns. Note the presence of Mg, Si, and Fe in all spectra, with Ca and S present in two, and Ni detected in only one spectrum.

# Swarm Particle

## 2D03-29

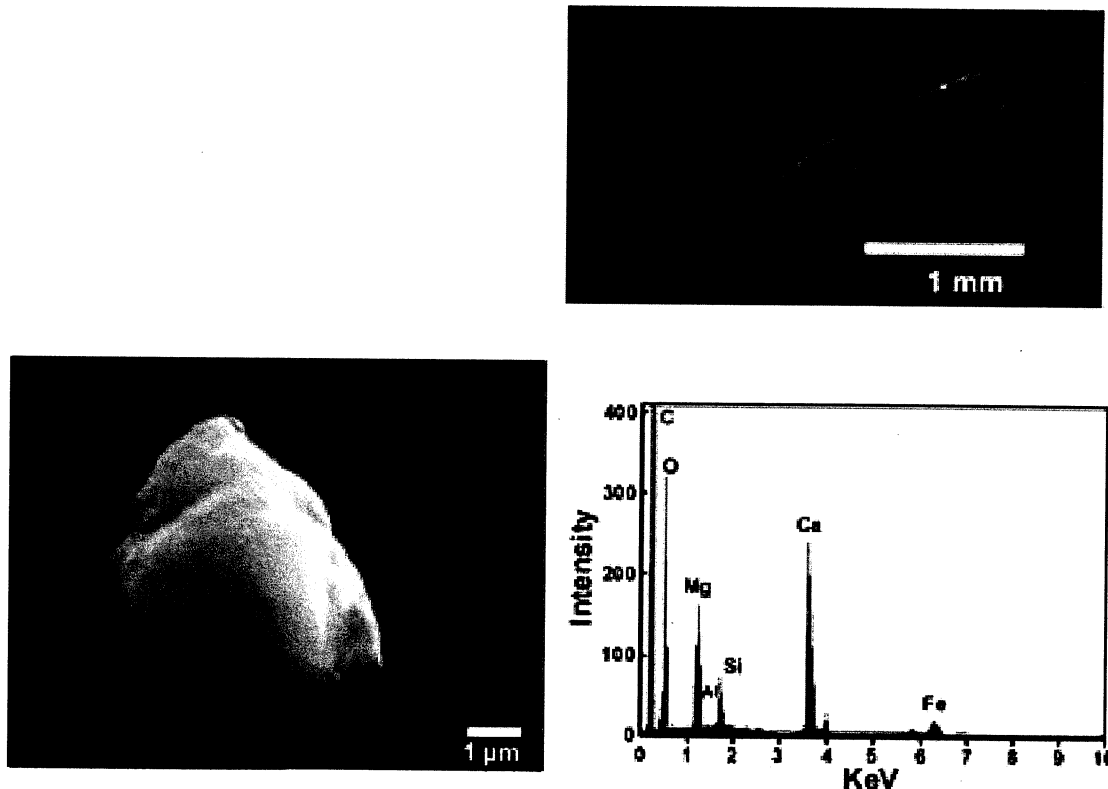


**Figure 46.** Another small particle recovered from the terminus of a typical swarm track ~ 500  $\mu\text{m}$  in length. Note the presence of Fe, Ca, and Mg, along with modest amounts of Al and Si, typical for particles of chondritic composition. Such compositional data identify the swarm event to be caused by a natural impactor.

distributions of the dominant elements, Mg, Ca, and Fe, and substantial variations in minor elements, such as Al, S, or Ni. Nevertheless, most any analysis spot would identify such compositions as *chondritic* in nature and of natural origin (e.g., Brownlee, 1986; Zolensky et al., 1994). Another 1.2-mm-long swarm track that yielded a particle ~ 5 mm across can be seen in Figures 46. Note the similarity of the spectrum to that of Figure 45. An additional 5 residues recovered from swarm tracks are of similar makeup, identifying the swarm to be composed of fragments from a natural impactor. While this is not a surprising result, the preponderance of projectile fragments only composing the debris swarm is somewhat surprising, as one would expect to find fragments of the target as well. In fact, target fragments should dominate, as hypervelocity impactors readily excavate and displace 10 to 100 times their own mass. The current observation that projectile fragments make up the swarm calls for unusual conditions for the primary impact. One scenario is that of a very shallow incidence impact, which led to the decapitation of the impactor and a fragment cloud that is dominated by or exclusively composed of projectile species (e.g., Schultz and Gault, 1990). Alternatively, the impactor may have fragmented upon penetration of a thin film on Mir, such as a thermal insulation blanket, resulting in a debris plume that is utterly dominated by projectile fragments (e.g., Hörz et al., 1995). Additional analyses of swarm tracks are warranted to possibly identify the target material.

Another natural impactor, unrelated to the swarm event, is shown in Figure 47. In this case, the track split fortuitously such that parts of the residue surface were exposed, permitting SEM imaging of the particle in situ. As is commonly observed, a substantial volume of molten aerogel drapes the entire

## Natural Particle 2D03-16

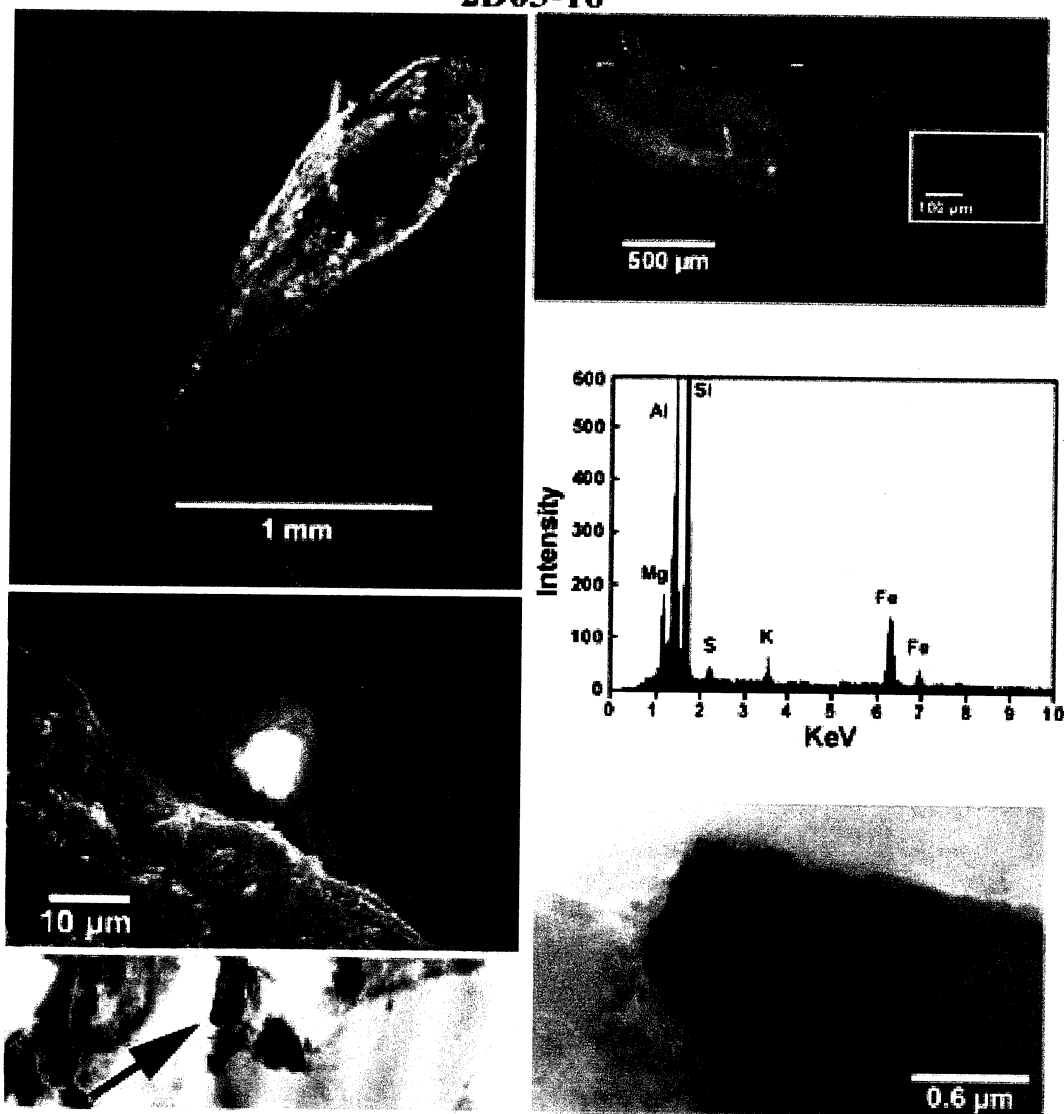


**Figure 47.** Example of a natural particle. The particle was removed from the aerogel host (to avoid the risk of losing a potentially valuable sample). Note that good EDS spectra can be obtained from the exposed surfaces of such samples, although aerogel based Si-contamination is prevalent. The sample was subsequently embedded in epoxy and thin-sectioned via microtome for detailed transmission electron microscope (TEM) analysis. These TEM images (lower panels) show substantial invasion of molten aerogel into the sample (white areas in left-hand figure). A small spinel crystal can be seen in the lower right-hand image.

particle. The EDS spectrum reveals the presence of mafic silicates (Fe, Mg, and Si) and most likely the presence of a K-rich feldspar (Al and K). Following these SEM analyses, the particle was embedded in epoxy and thin-sectioned into 1000-Å-thick slices with a microtome for more detailed mineralogical investigations using TEM as illustrated in the two bottom panels and as described by Hörz et al. (1998). The TEM investigations reveal significant disruption of the parent grain by invading aerogel melt, the presence of hydrated layer-lattice silicates (grey material), and small (sub-micron) oxide grains (dark material); the arrow points to the magnified particle visible in the bottom, right-hand image.

Note that this is the first natural cosmic-dust grain ever to be recovered from space-exposed aerogel collectors and microtomed for detailed TEM analysis. Although a very modest effort in the context of ODC, the successful recovery and subsequent TEM analysis of space-retrieved particles is significant for planetary sciences, and specifically for the in situ characterization of comets and asteroids, the most prominent sources of interplanetary dust. Such dust is generally much more fine-grained and mineralogically diverse than typical man-made materials used in spacecraft, mandating methods more detailed and of higher spatial resolution than SEM-EDS.

## CONCLUSIONS

The Orbital Debris Capture experiment exposed  $\sim 0.6 \text{ m}^2$  of  $\text{SiO}_2$ -based aerogel for  $\sim 18$  months on the *Mir* station, providing a significant opportunity to evaluate the performance of this low-density, highly porous material for the capture of hypervelocity particles. This report summarizes optical studies of the impact features on ODC and provides examples of compositional analyses of individual projectile residues that were extracted from the collectors.

The highly porous, delicate aerogel medium superbly survived the launch and retrieval environment of Shuttle, as well as relatively long-term exposure in LEO. Therefore, it is a suitable material for a variety of missions engaged in the collection of either man-made debris or natural cosmic dust, such as the Stardust mission to comet Wild 2.

Two distinct classes of hypervelocity impact features in aerogel were observed: slender, carrot-shaped tracks and substantially stubby, if not hemispherical, pits. Features of intermediate morphologies between these dominant end-members suggest the presence of a morphologic continuum and of an evolutionary sequence from deep tracks to hemispherical pits. The absence of impactor residue, combined with the presence of distinctly glazed and translucent walls for most pits suggests that they formed—as a group—at higher impact velocities than the slender and very deep tracks, which are characterized by the needle-like stylus, and a largely unmolten projectile remnant. Thus, we propose a velocity dependent continuum between deep tracks and shallow pits.

This interpretation suggests that the soft capture of hypervelocity particles in LEO is velocity-limited. The specific threshold velocity beyond which the soft capture fails is poorly known, yet it is undoubtedly higher for aerogel than it is for all traditional, nonporous collectors. The fact that many superbly preserved and unmolten residues of both man-made and natural dust particles were recovered from aerogel and subjected to SEM and TEM analysis demonstrates that aerogel is a superb capture medium for most particles in LEO. Its dynamic range, although limited at the high-velocity end, is unsurpassed. It is simply unrealistic to expect any single material or capture method to operate successfully over the entire range of initial impact conditions represented by man-made and natural particles in LEO.

A third class of ODC impact features relates to low-velocity encounters with co-orbiting waste materials, either liquid or solid, that result from the periodic venting of the Shuttle's wastewater tank. On a particle frequency basis, such materials dominate those ODC surfaces that nominally pointed in the forward direction of *Mir*'s orbital motion. While the collisional hazard seems minor due to the low-encounter velocities, the high frequency of such events may adversely affect critical components, especially optical quality surfaces.

We measured the relative frequency of track, pits, and shallow depressions for the two collector surfaces of ODC, yet these measurements are difficult to interpret in detail, largely because of poorly known pointing directions of these surfaces relative to *Mir*'s velocity vector. Indeed, some of the observations suggest highly variable exposure geometries to the degree that the substantial differences in mean-encounter velocity and particle flux expected from a non-spinning spacecraft (e.g., Zook, 1991) are simply absent on ODC. This includes the distribution of track lengths (Figure 33) which should be velocity sensitive and, therefore, differ between Tray 1 and Tray 2. Furthermore, the observation of modestly fewer tracks on Tray 1 than on Tray 2 (Table 1 or Figure 36) is inconsistent with prolonged exposures into

forward- and rearward-facing directions on an otherwise stationary platform. *Mir's* attitude must have been highly variable throughout the entire exposure period of ODC, as verified by the pinhole camera of PMPD (Kinard et al., 1998).

Prominently clustered tracks and spatially isolated features of similar size and orientation on Tray 2 demonstrate the presence of debris clouds and the production of sizable populations of impact features caused by secondary impacts on spacecraft. Such clouds may have distinctly heterogeneous mass distribution and contain particles of variable sizes. In this specific case a natural impactor encountered either some *Mir* structure at very shallow incidence, or it penetrated some thin membrane, such that only projectile fragments contributed to the secondary particle swarm.

In conclusion, although the optical analysis and sample preparation for detailed compositional analysis via SEM-EDS or TEM methods are more time-consuming than for nonporous media, this apparent disadvantage is far outweighed by the ability to preserve and trap unmolten residues for most hypervelocity particles in LEO. Aerogel is unquestionably a most superior capture medium and the best that is presently available. Unfortunately, neither conventional, nonporous collectors nor aerogel yield reliable dynamic data for individual particles, including chronological information of collisional events. Such dynamic and chronologic data are ultimately needed to understand the hypervelocity environment in LEO. Active instruments should be developed that measure the mass and trajectories of individual particles that, when combined with aerogel collectors, would provide unambiguous evidence to associate specific particles with either man-made sources and events, or with astrophysical sources, respectively (Zolensky, 1994).

## REFERENCES

- Amari, S., Foote, J., Swan, P., Walker, R.M., Zinner, E., and Lange, G. (1992) SIMS chemical analysis of extended impacts in the leading and trailing edges of the LDEF experiment A0231-2, in *LDEF - 69 Months in Space, Second Post-Retrieval Symposium*, NASA CP 3194, p. 513-528.
- Anderson, W. and Ahrens, T.J. (1994) Physics of interplanetary dust capture via impact into organic foam, *J. Geophys. Res. E*, *V. 99*, p. 2063-2071.
- Barrett, R.A., Zolensky, M.E., Hörz, F., Lindstrom, D., and Gibson, E.K. (1992) Suitability of SiO<sub>2</sub> aerogel as a capture medium for interplanetary dust, *Proc. Lunar Planet. Sci. Conf. 22<sup>nd</sup>*, p. 203-212.
- Bernhard, R. P., See, T.H., and Hörz, F. (1992), Projectile compositions and modal frequencies on the "Chemistry of Micrometeoroid" LDEF Experiment, in *LDEF - 69 Months in Space, Second Post-Retrieval Symposium*, NASA CP 3194, p. 551-574
- Bernhard, R.P., Hörz, F. and Kessler, D.E. (1999) Orbital debris impacts on the trailing edge of the Long-Duration Exposure Facility (LDEF), submitted to *Space Debris*.
- Berthaud, L., Mandeville, J.C., Durin, C., and Borg, J. (1993) Debris and meteoroid proportions deduced from impact crater residue analysis, in *LDEF - 69 Months in Space, Second Post-Retrieval Symposium*, NASA CP 3275, p. 431-444.
- Brownlee, D.E. (1985) Cosmic dust: Collection and research, *Ann. Rev. Earth Planet. Sci.*, *13*, p. 134-150.
- Brownlee, D.E., Hörz, F., Hrubesh, L., McDonnell, J.A.M., Tsou, P., and Williams, J. (1994) Eureka! Aerogel capture of meteoroids in space (abstract), *Lunar Planetary Sci. XXIV*, p. 183-184.
- Burchell, M.J. and Thomson, R. (1996) Intact hypervelocity capture in aerogel in the laboratory, in *Shock Compression of Condensed Matter-1995*, Schmidt, S.C. and Tao, W.C. eds., *AIP Conf. Proc.* *370, Part 2*, p. 1155-1158.
- Christiansen, E.L. (1993) Design and performance equations for advanced meteoroid debris shields, *Inter. J. Impact Engng.*, *14*, p. 145-156.

- Christiansen, E.L. (1998) Orbiter Meteoroid/Orbital Debris Impacts: STS-50 (6/92) - STS-86 (10/97) JSC-28033, 101 p.
- Fricke, L. (1988) Aerogels, *Scientific American*, 258, 5, p. 92-97.
- Gault, D.E. (1973) Displaced mass, depth, diameter and effects of oblique trajectories for impact craters formed in dense, crystalline rocks, *The Moon*, 3, p. 32-44.
- Gault, D.E. and Wedekind, J.A. (1977) Experimental hypervelocity impact into quartz sand II: Effects of gravitational acceleration, in *Impact and Explosion Cratering*, Roddy, D.J., Pepin, R.O. and Merrill, R.B., eds., Pergamon Press, p. 1231-1244.
- Gwynn, D.W., Hörz, F., Bernhard, R.P., and See, T.H. (1996) The dispersion of molten soda-limeglass projectiles following penetration of thin aluminum membranes, *Int. J. Impact Engng.* 20, 1-5, p. 325-336.
- Hörz, F., Fechtig, H. and Janicke, J. (1983) Morphology and chemistry of projectile residues in small experimental impact craters, *Lunar Plant. Sci. Conf. 14<sup>th</sup>, J. Geophys. Res.*, 88, p. B353-B363.
- Hörz, F., Bernhard, R.P., See T.H., and Brownlee, D.E. (1993) Natural and orbital debris particles on LDEF's trailing and forward-facing surfaces, in *LDEF - 69 Months in Space, Third Post-Retrieval Symposium*, NASA CP 3275, p. 415-429.
- Hörz, F., Cintala, M., Bernhard, R.P., Cardenas, F., Davidson, W., Haynes, G., See, T.H., and Winkler, J.L. (1995) Penetration experiments in aluminum 1100 targets using soda-lime glass projectiles, NASA TM 104813, 325 p.
- Hörz, F., Cintala, M., Bernhard, R., Davidson, W. Haynes, G., and See, T.H. (1997) Capture of hypervelocity particles with low-density aerogel: Progress report I (1996), NASA TM 98-201792, 60 p.
- Hörz, F., Zolensky, M., Cress, G., Bernhard R.P., See, T.H., Warren, J.W., Brownlee, D.E., and Tsou, P. (1998) ODC aerogel capture during 18 months exposure on Mir (abstract), *Lunar Planet Sci. XXIX*, Lunar Planetary Institute, Houston, TX, 77058, p. 1773-1774
- Hrubesh, L.W. and Poco, J.F. (1990) Development of low-density silica aerogel as a capture medium for hypervelocity particles, *Lawrence Livermore National Laboratory Report UCLR-CR 105858 SUM*, 12 p.
- Humes, D. (1991) Large craters on the meteoroid and debris experiment impact experiment, *LDEF - 69 Months in Space, First Post-Retrieval Symposium*, NASA CP-3134, p. 399-418.
- Johnson, N.L. and McKnight, D.S. (1991) *Artificial Space Debris*, Krieger Publishing Company, Malabar, FL.
- Kessler, D.J. (1992) Origin of orbital debris impacts on LDEF's trailing surfaces, in *LDEF - 69 Months in Space, Second Post-Retrieval Symposium*, NASA CP 3194, p. 585-594.
- Kessler, D.J. (1996) A Computer based debris environment model for spacecraft design and observations in low-Earth orbit, NASA TM-104825.
- Kinard, W.H. (1998) Oral presentation at space environment effects workshop, June 23-25, MSFC, Huntsville, AL.
- Levine, A.S. (1991) *LDEF - 69 Months in Space, First Post-Retrieval Symposium*, NASA CP 3134.
- Levine, A.S. (1992) *LDEF - 69 Months in Space, Second Post-Retrieval Symposium*, NASA CP 3194.
- Levine, A.S. (1993) *LDEF - 69 Months in Space, Third Post-Retrieval Symposium*, NASA CP 3275.
- Love, S.G., Brownlee, D.E., King, N.L. and Hörz, F. (1995) Morphology of meteoroid and debris impact craters formed in soft metal targets on the LDEF satellite, *Int. J. Impact. Engng.* 16, 3, p. 405-418.
- Mendez, D.J. (1994) "Quicklook," Proprietary contractor report, Lockheed Missiles and Space Co., M. Zolensky, ed., LPI Technical Report 94-05.
- Murr, L.E., Quinones, S.A., Ferreyra, E., Ayala, A., Valerio, O.L., Hörz, F. and Bernhard, R.P. (1998) The low-to-hypervelocity-penetration transition for impact craters in metal targets, *Mat. Sci. Engng.*, A256, p. 166-182.

- Peters, P.N. and Gregory, J.C. (1991) Pinhole cameras as sensors for atomic oxygen in orbit; application to attitude determination of the LDEF, *LDEF - 69 Months in Space, First Post-Retrieval Symposium*, NASA CP 3134, p. 61-68.
- Pippin, H.G. (1998) Oral presentation at space environment effects workshop, June 23-25, MSFC, Huntsville, AL.
- Schaal, R.B. Hörz, F. and Gibbons, R.V. (1976) Shock metamorphic effects in lunar microcraters, *Proc. Lunar Sci. Conf.*, 7<sup>th</sup>, p. 1039-1054.
- Schneider, E., Stilp, A., Bureo, R., and Lambert, M. (1990) Micrometeorite and space debris simulation for Columbus hull components, *Int. J. Impact Engng.* 10, p. 499-508.
- Schultz, P.H. and Gault, D.E. (1990) Prolonged global catastrophes from oblique impacts *Geol. Soc. America Special Paper* 247, p. 239-246.
- See, T.H., Zolensky, M.E., Bernhard, R.P., Warren, J.I., Sapp, C.A., and Dardano, C.B. (1993) LDEF meteoroid and debris special investigation group investigations and activities at the Johnson Space Center, in *LDEF - 69 Months in Space, Third Post-Retrieval Symposium*, NASA CP 3275, Part 1, p. 257-274.
- Tsou, P. (1990) Intact capture of hypervelocity projectile, *Inter. J. Impact Engng.* 10, p. 615-627.
- Tsou, P. (1995) Silica aerogel captures cosmic dust intact, *J. Non-Crystalline Solids*, 186, p. 415-427.
- Tsou, P., Brownlee, D.E., Lawrence, M.R., Hrubesh, L. and Albee, A.L. (1988) Intact capture of hypervelocity meteoroid analogs (abstract), *Lunar Planet. Sci. XIX*, p. 1205-1206.
- Warren, J.L., Zook, H., Allton, J.H., Clanton, U.S., Dardano, C.B., Holder, J.A., Marlow, R.R., Schultz, R.A., Watts, L.A., and Wentworth, S.J. (1989) The detection and observation of meteoroid and space debris impact features on the Solar Max Satellite, *Proc. Lunar Planet. Sci. Conf.* 19<sup>th</sup>, p. 641-657.
- Watts, A.J. and Atkinson, D. (1993) Dimensional scaling for impact cratering and perforation, in *LDEF - 69 Months in Space, Third Post-Retrieval Symposium*, NASA CP 3275, p. 523-535.
- Werle, V., Fechtig, H., and Schneider, E. (1981) Impact accretion experiments, *Proc. Lunar Planet. Sci. Conf.* 12<sup>th</sup>, p. 1641-1647.
- Zolensky, M.E. ed. (1994) *Workshop on particle capture, recovery and velocity/trajectory measurement technologies*, Lunar and Planetary Institute, Houston, TX, LPI Technical Report 94-05, 102 p.
- Zolensky, M.E., Zook, H.A., Hörz, F., Atkinson, D.R., Coombs, C.R., Watts, A.J., Dardano, C.B., See, T.H., Simon, C., and Kinard, W.H. (1992) Interim report of the meteoroid and debris special investigation group, in *LDEF - 69 Months in Space, Second Post-Retrieval Symposium*, NASA CP 3194, p. 277-302.
- Zook, H.A. (1991) Deriving the velocity distribution of meteoroids from the measured meteoroid impact directionality on the various LDEF surfaces, *LDEF - 69 Months in Space, First Post-Retrieval Symposium*, NASA CP 3134, p. 569-581.

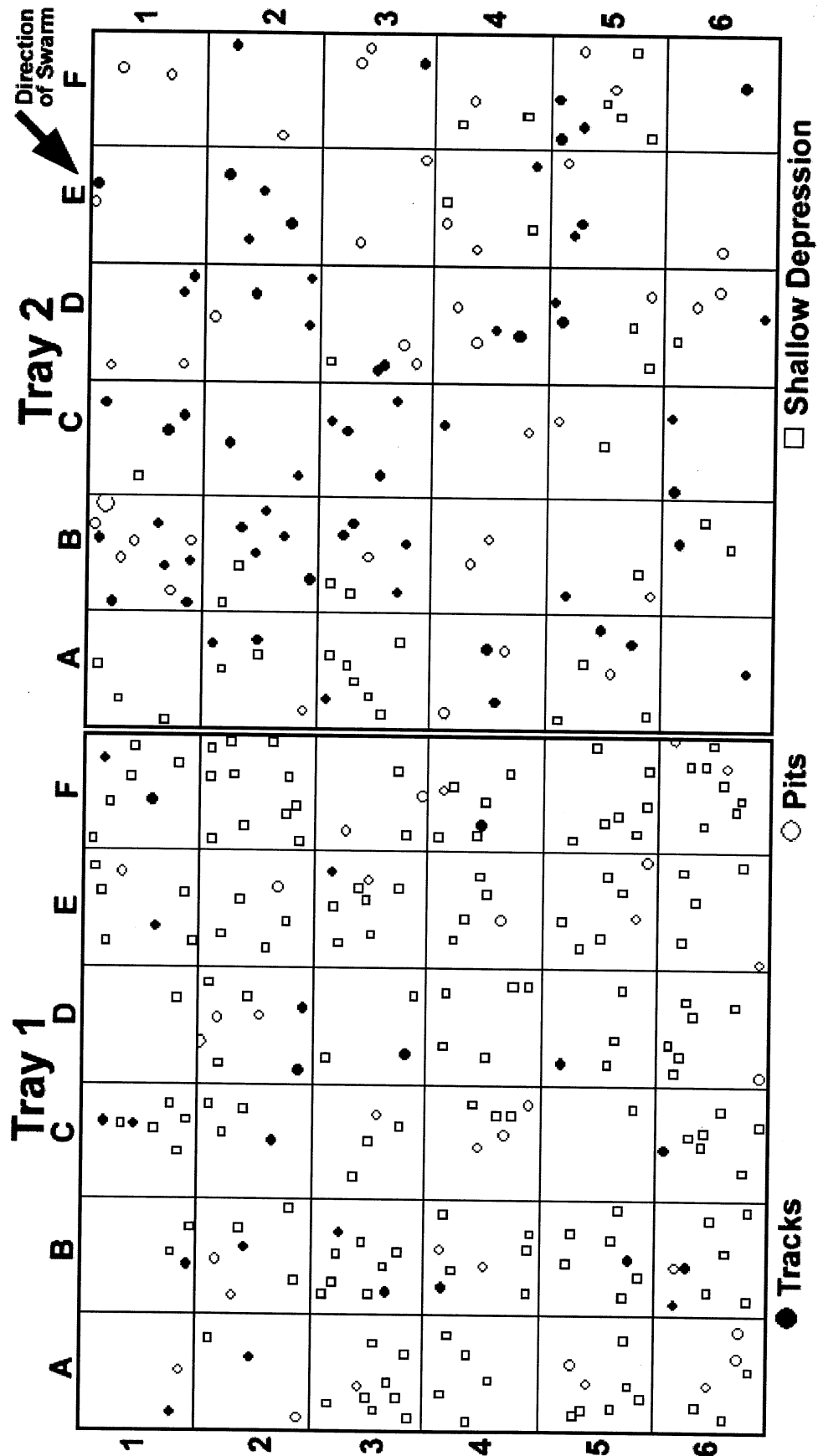


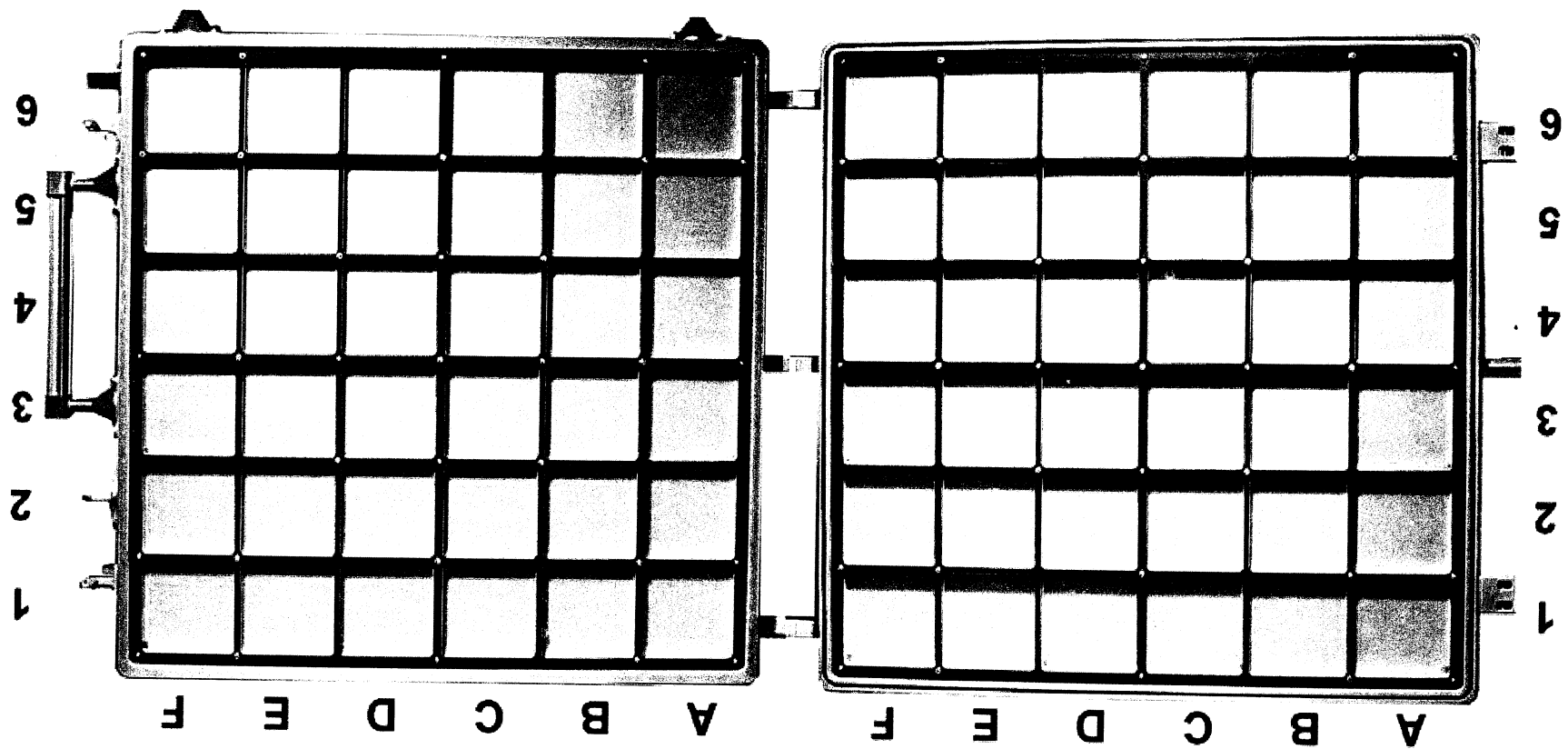


## APPENDIX A

Following the removal of the individual tiles from Trays 1 and 2 of the ODC experiment, each tile was photo-documented, presumably in its most pristine state, using high-resolution optical (Hasselblad) photography, referred to as *mug shots*. All mug-shot photographs contain the tile identifier (e.g., 2B01 in the top legend; tray [1 or 2], column [A-F], row [01-06]) and are oriented such that the (0,0) coordinates are in the lower left-hand corner. Although the fairly translucent nature of aerogel makes it a difficult material to photograph, some of the larger impact features ( $> 1$  mm) are readily recognized; many features  $\ll 1$  mm can be seen. We used these mug shots extensively during the optical scanning operations and during the preparation of SEM samples, documenting the physical splitting and subdividing of the pristine parent tiles.

Before the individual mug shot photographs in Appendix A, we have repeated Figures 30 and 32 from the body of this report. The first figure illustrates the location of the larger track, pit, and shallow-depression type features identified during the initial optical inspection of the samples following their removal from the experiment. The second figure shows the location of the tiles that have undergone the detailed scanning procedures discussed in the body of this report.





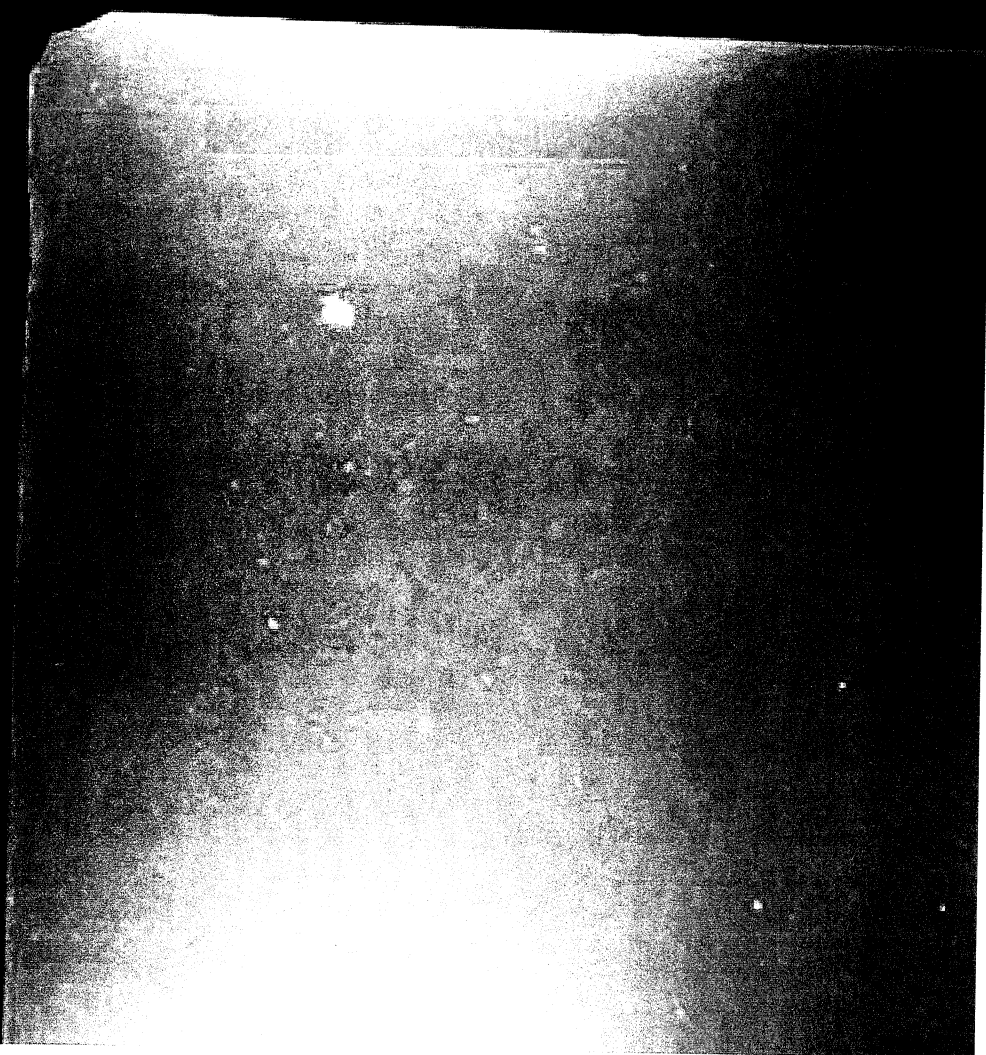
821817 10-4139 DEROGFI 1401 000



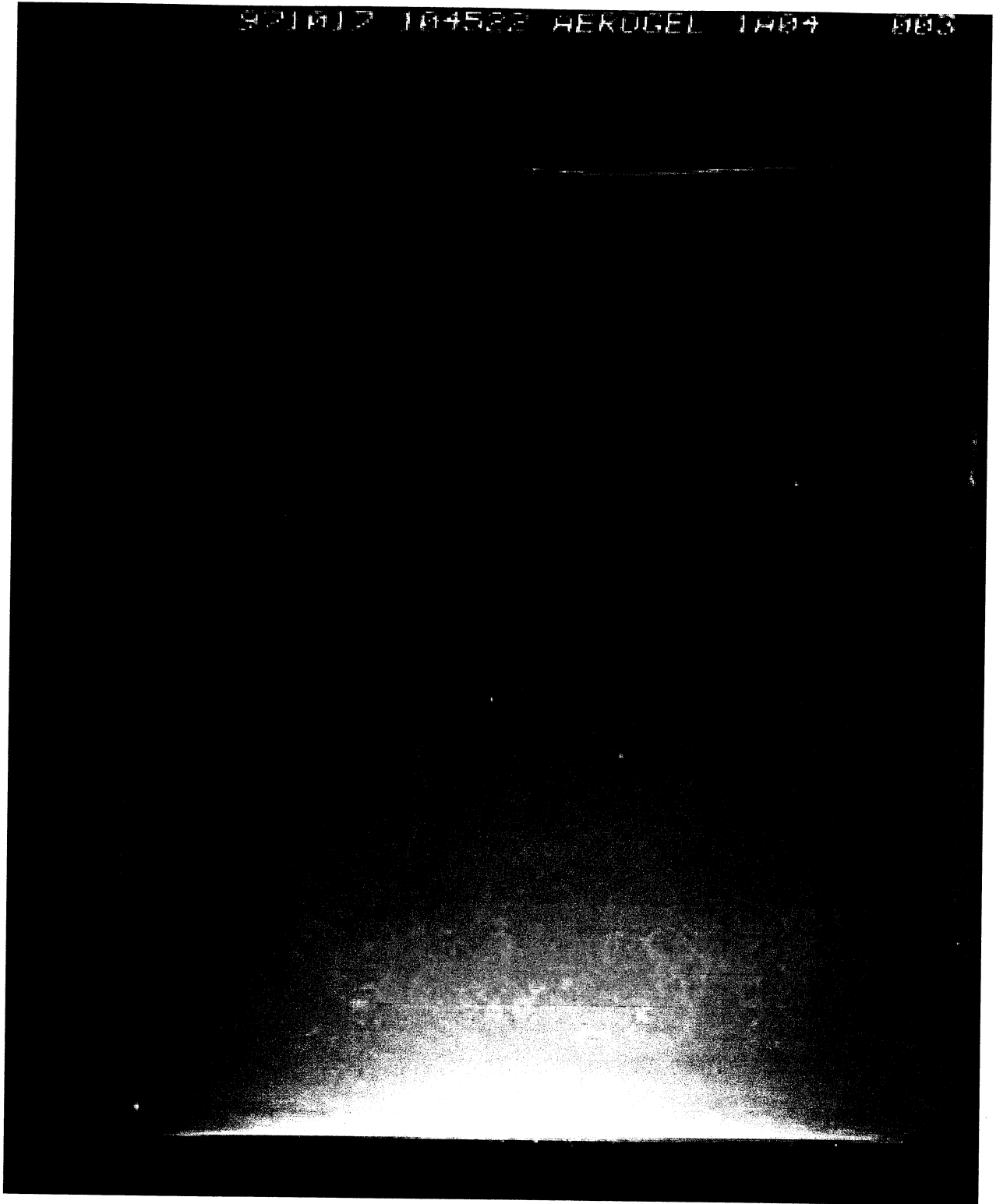
971012 104323 HEROGEL 1402 001

6

921017 104417 AEROGEL 1A03 002



921612 104522 AEROGEL 1404 003



921012 104212 AEROGEL 1004 003



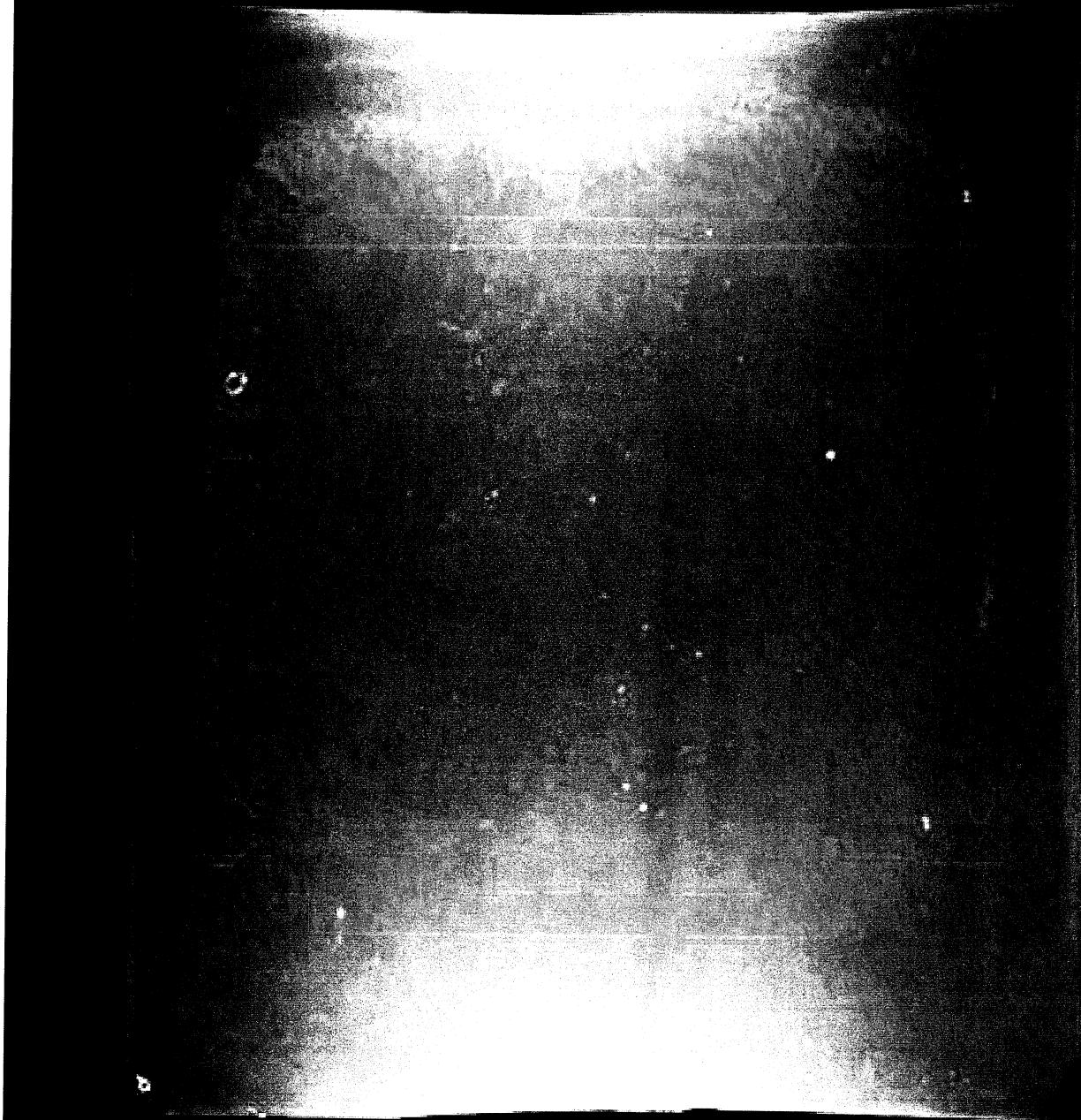
871017 104824 AEROGEL 1405 004

921017 104932 AEROGEL 1A06 005



971017 105040 AEROGEL 1001 005

971017 105127 AERUGEL 1002 000



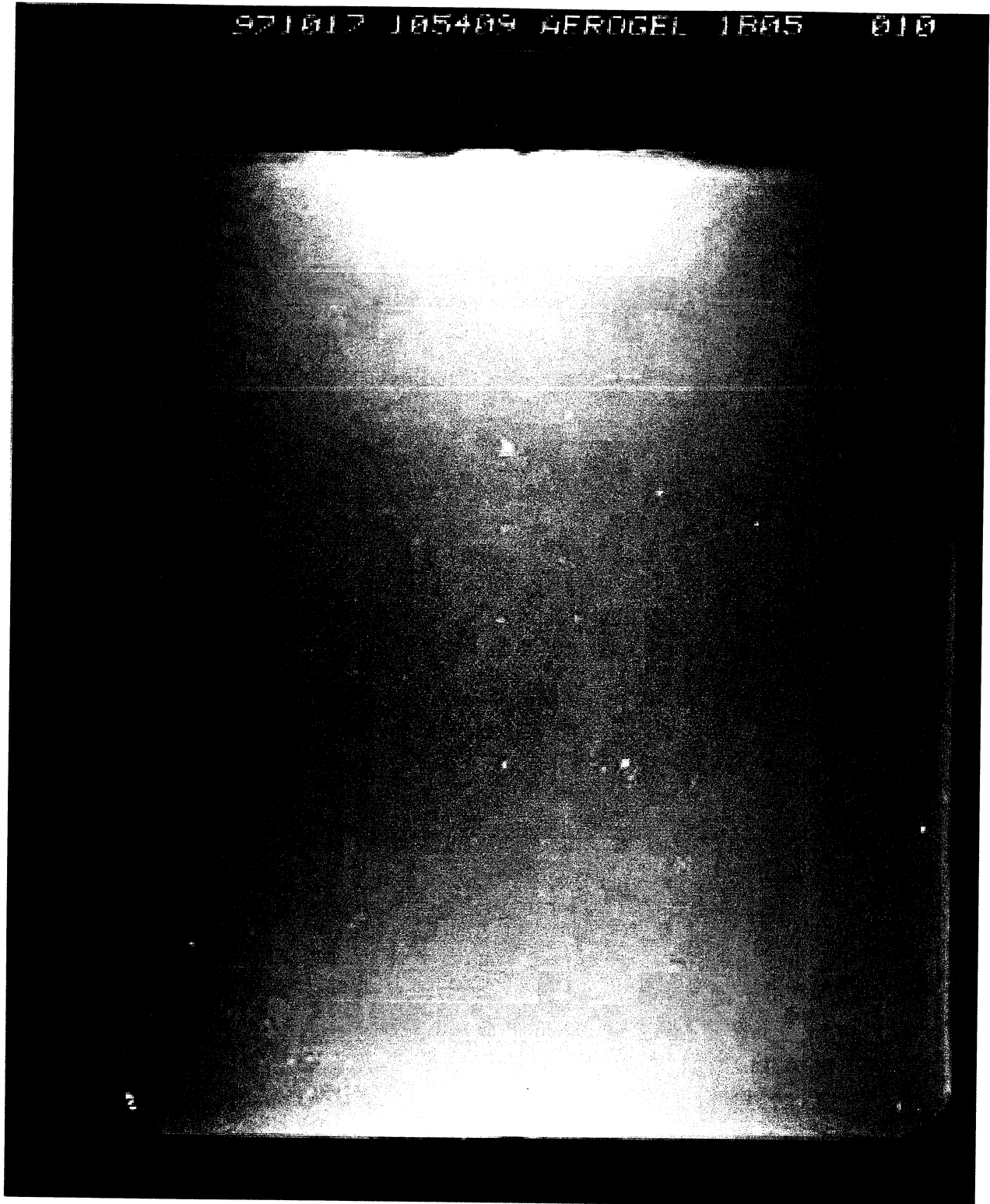
971017 105222 AEROGEL 1803 008



971017 105319 AFRUGEL 1004 005



971017 105409 AEROGEL 1885 010

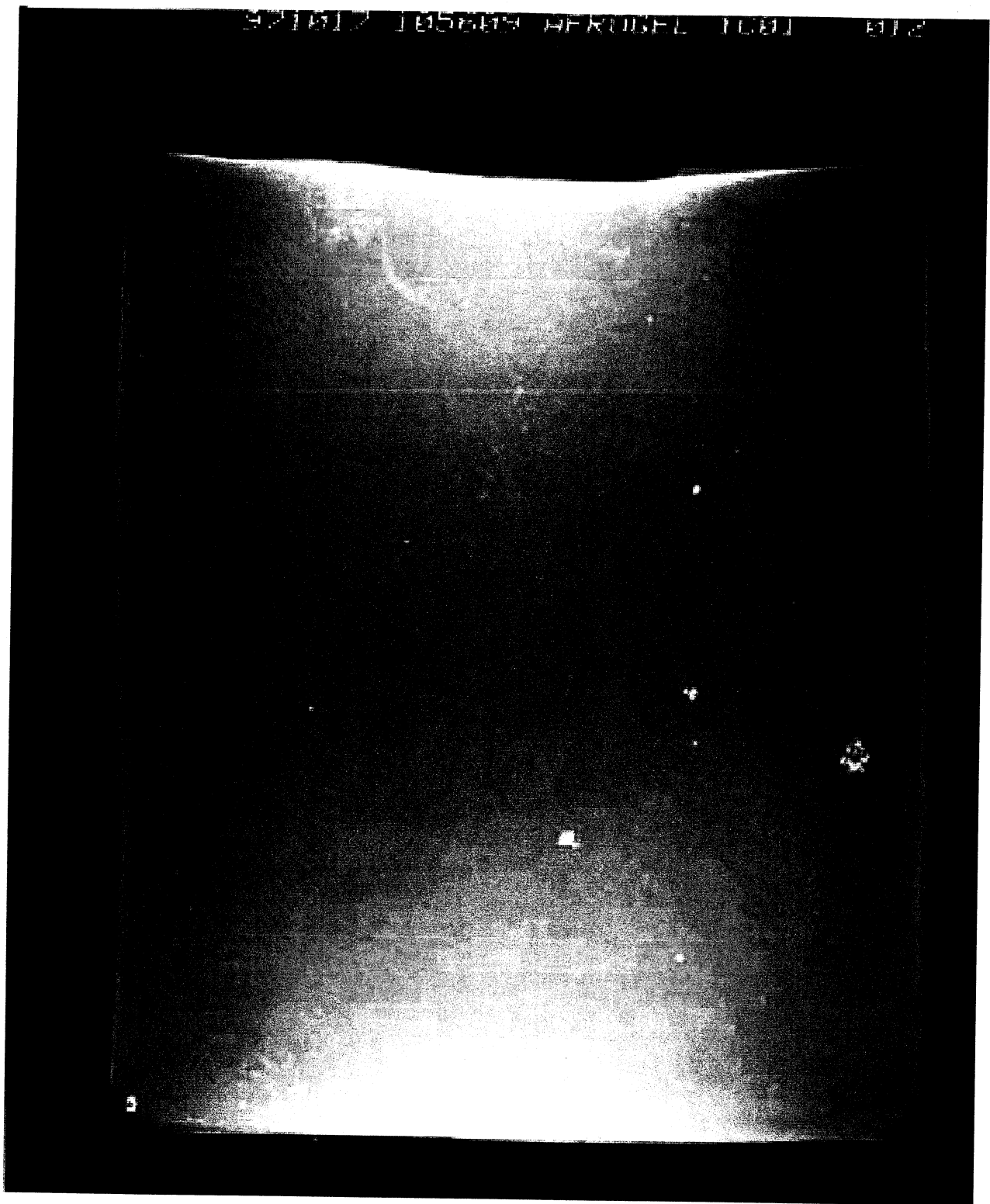


921012 105501 AEROGEL 1006 011





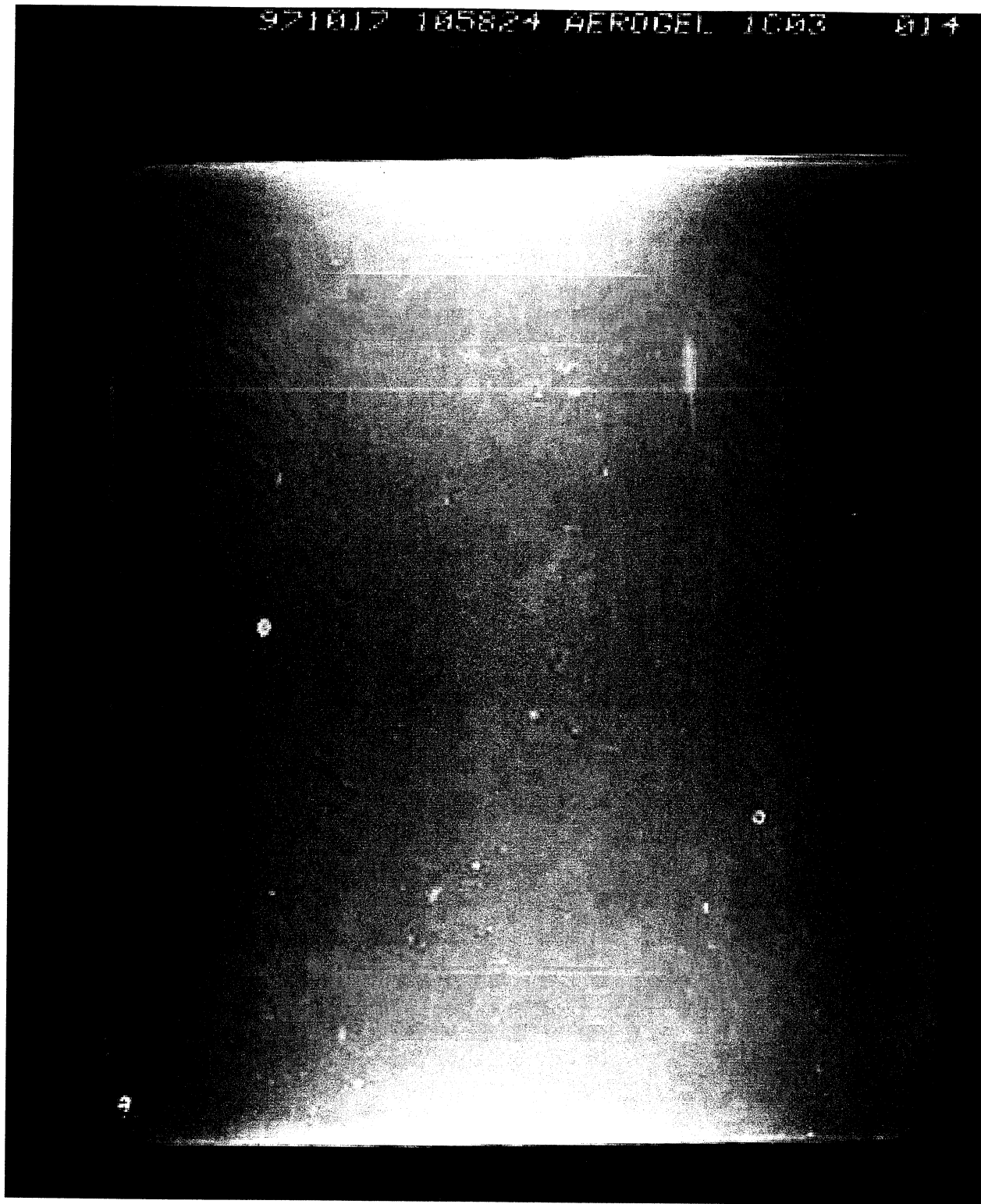
921617 105649 AFKUGEL 1001 012



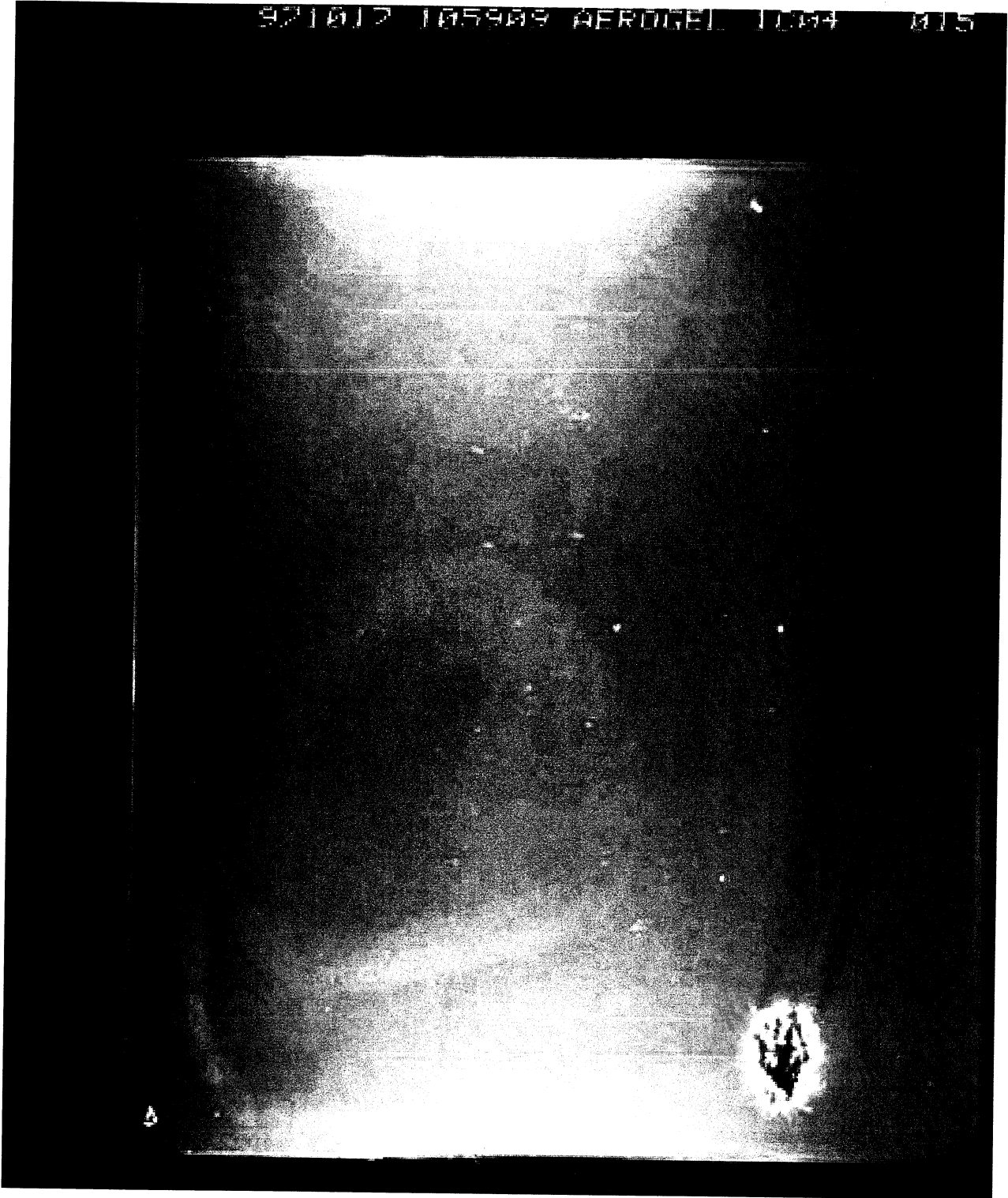
971017 105732 AEROGEL 1002 013



971017 105824 AEROGEL 1003 014



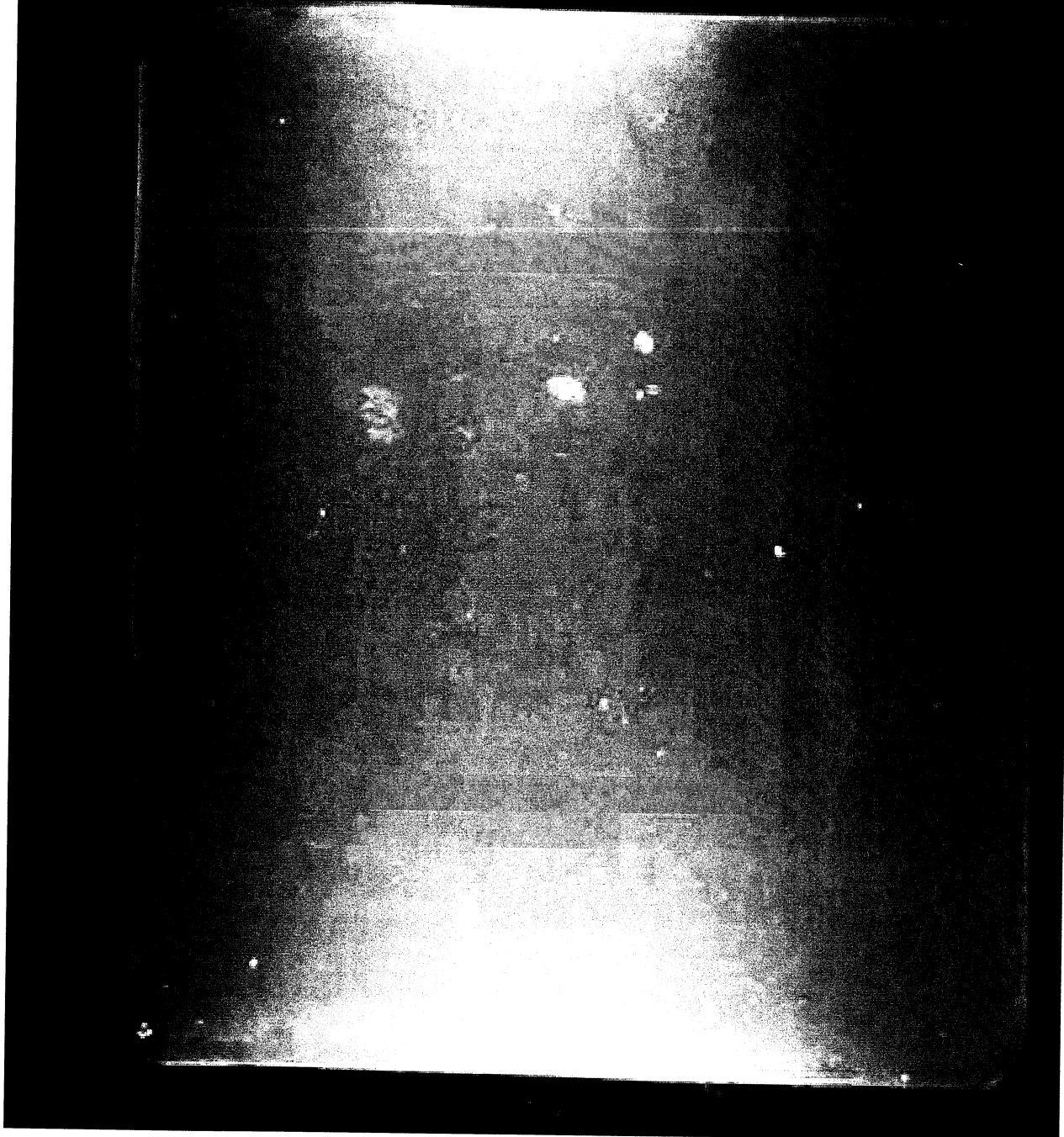
921012 105909 AEROGEL 10M4 M15



971012 110007 HERGEL 1005 016

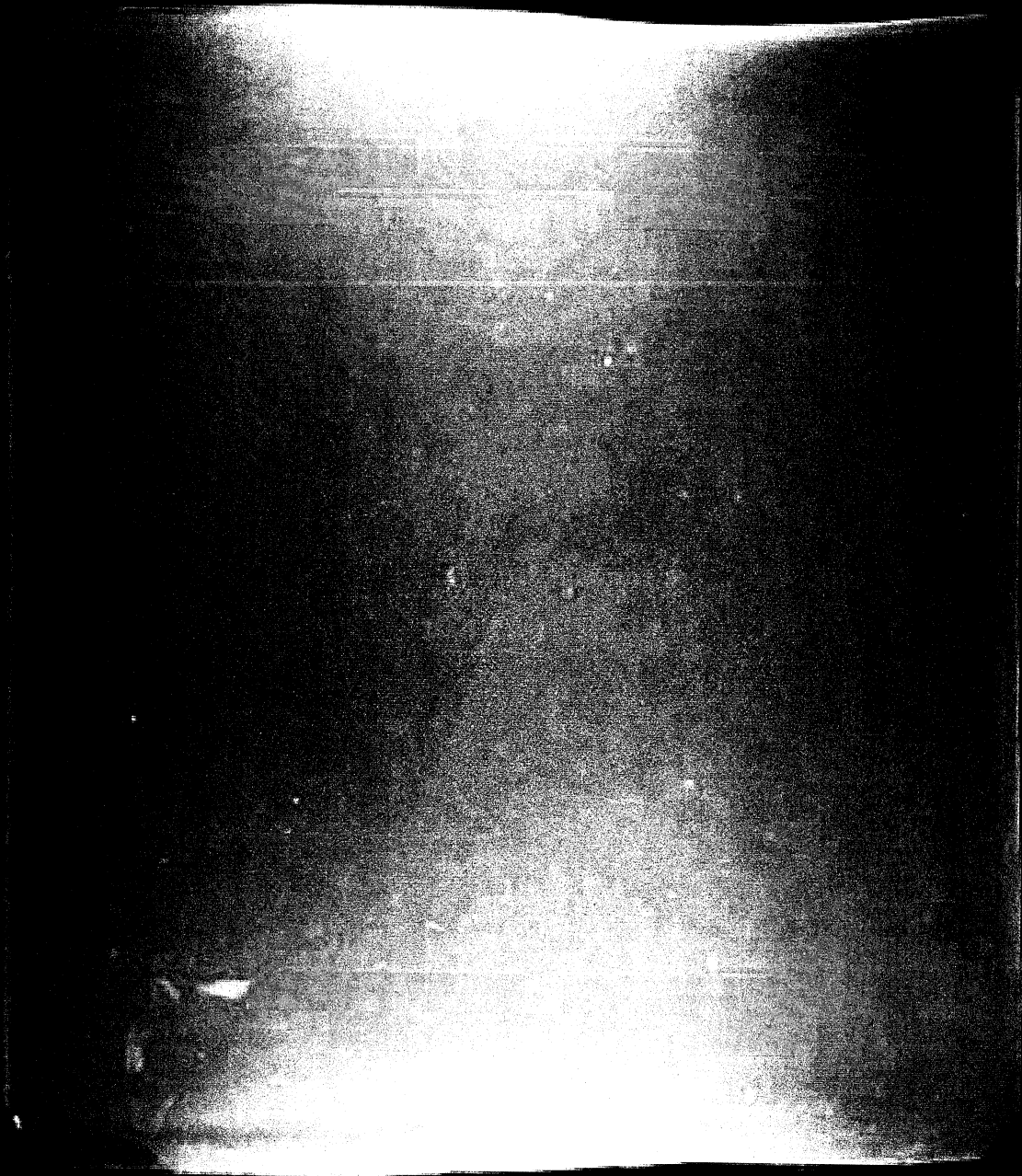


921017 110048 AEROGEL 1000 017

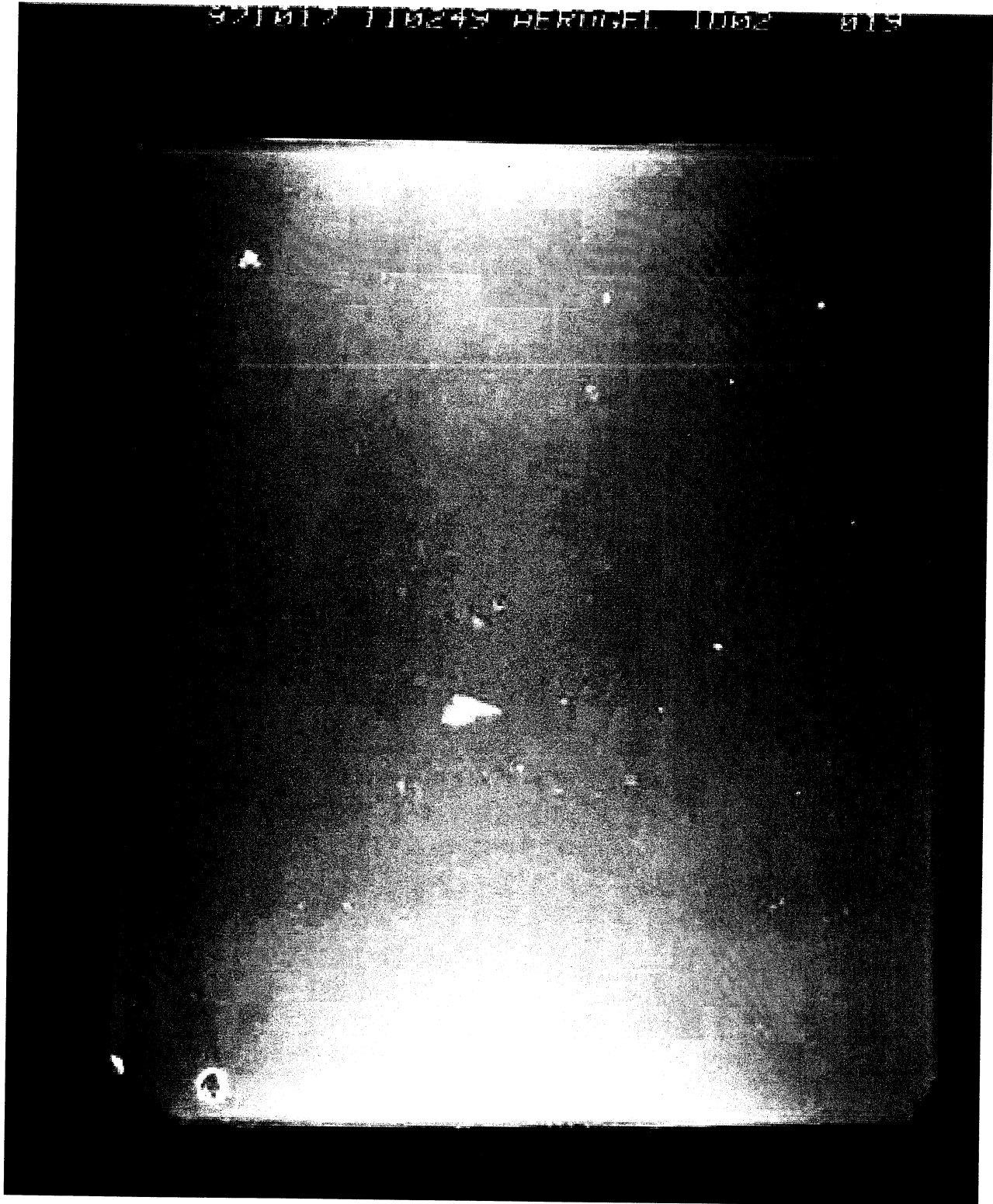




971017 110201 AEROCFI 1001 010

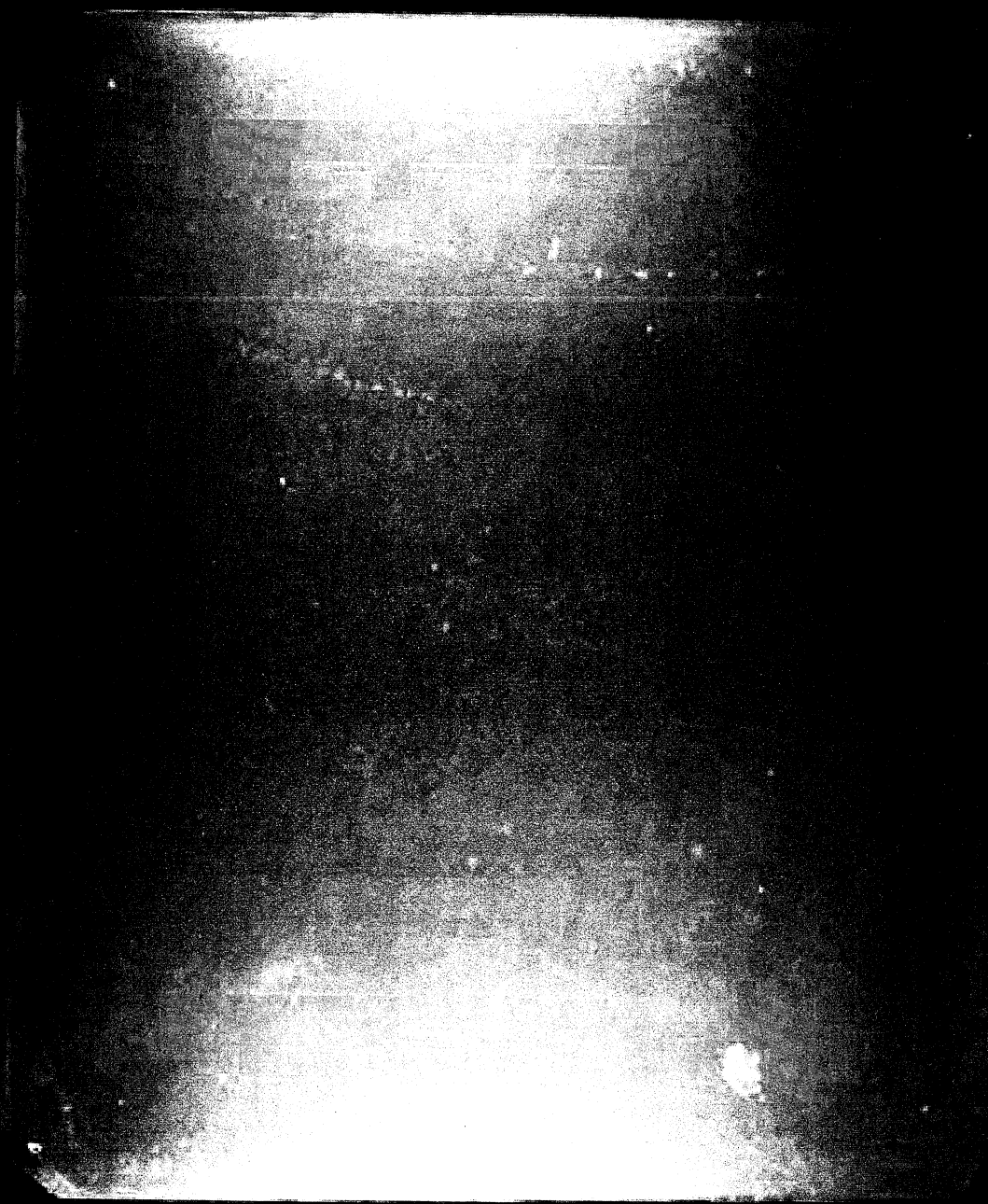


921012 110245 HERINGEL 1002 019

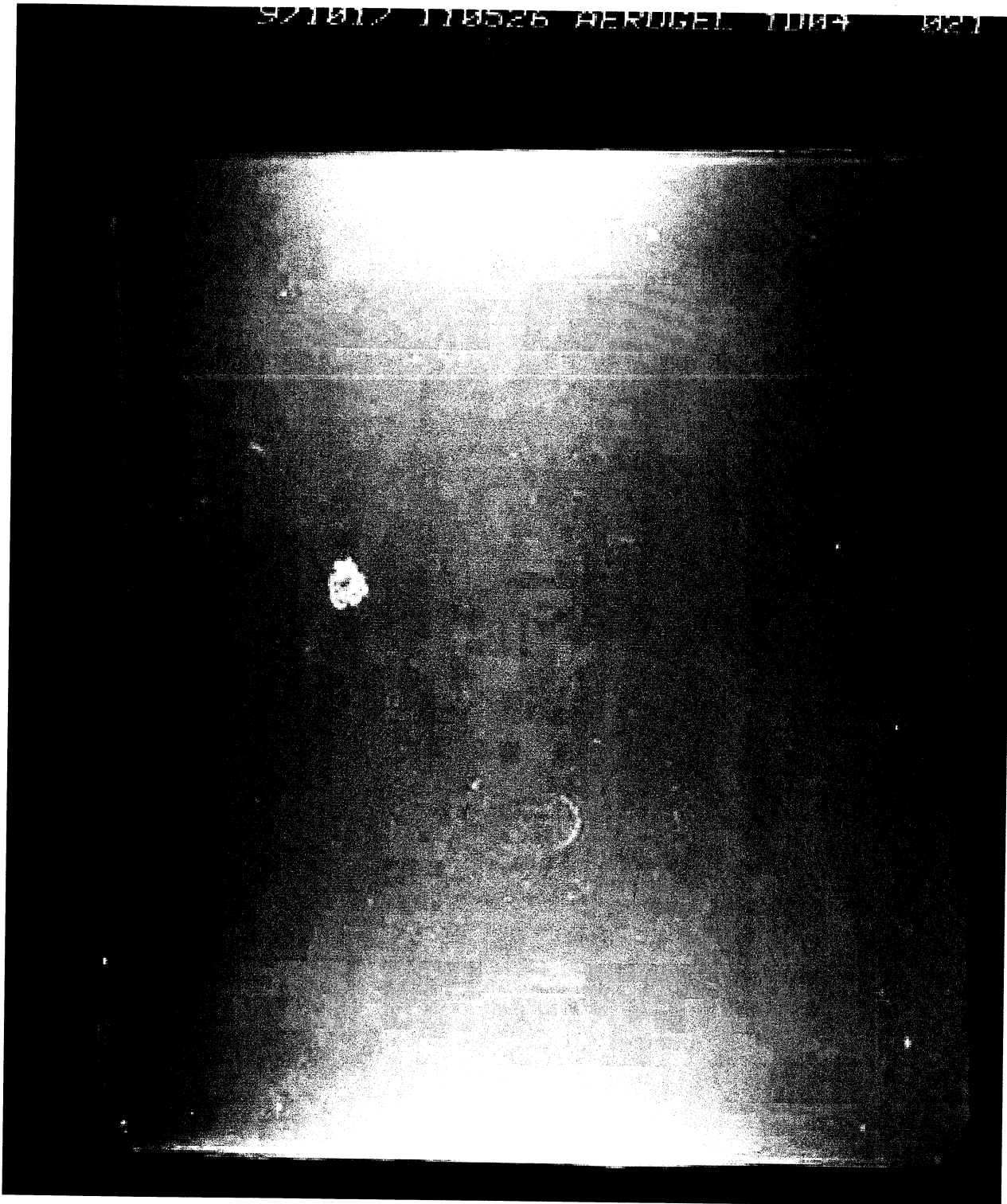




921012 110402 AEROGEL 1003 020



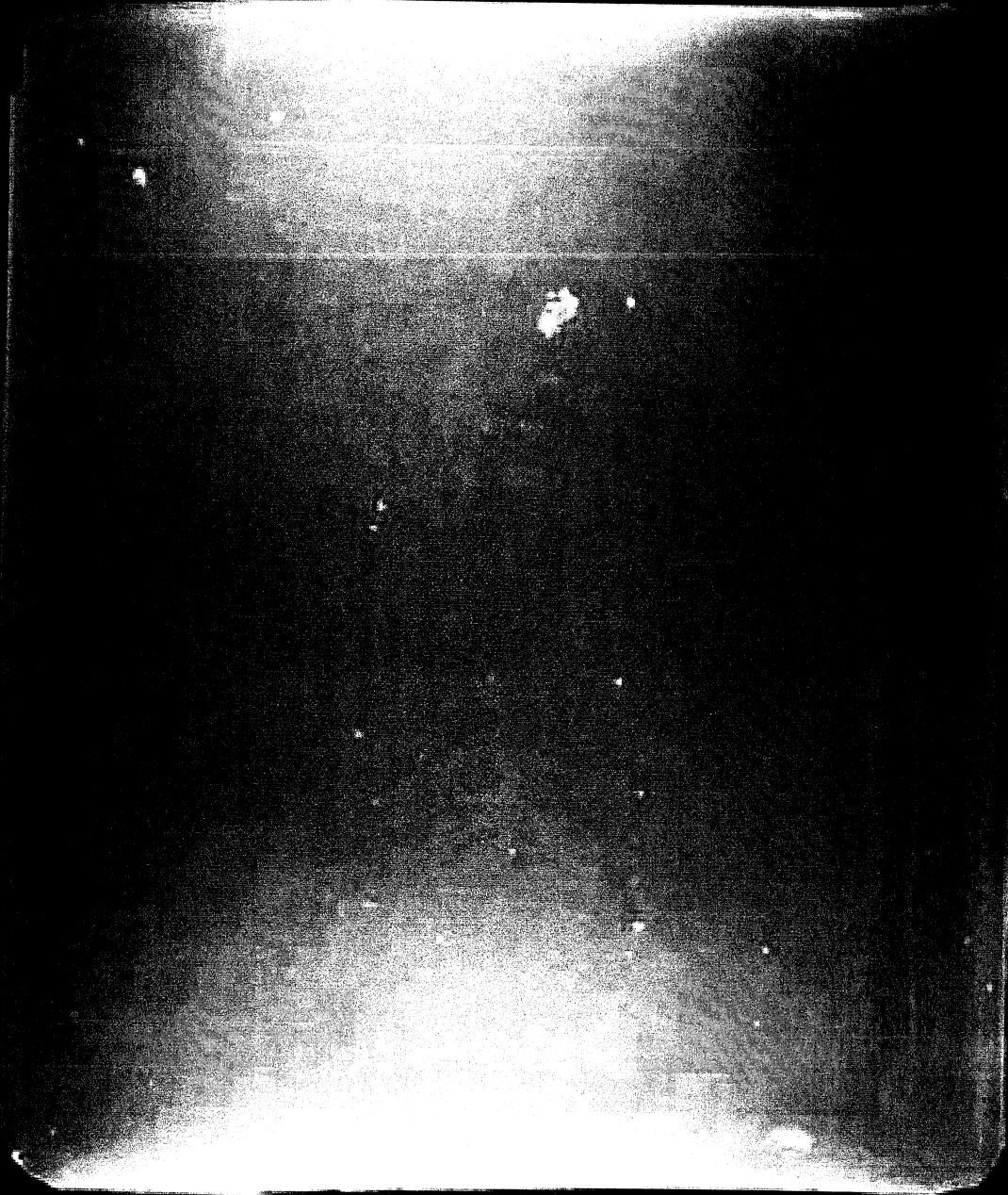
571017 110526 AERUGEL 1004 001



921017 110652 AEROGEL 1005 022



971017 111034 AEROGEL 1005 020



971812 111124 AEROGEL 1E01 027





921017 111241 HERDGEI 1E02 025

871917 111412 AEROGEL 1E03 026



971017 111506 AEROGEL 1E04 027





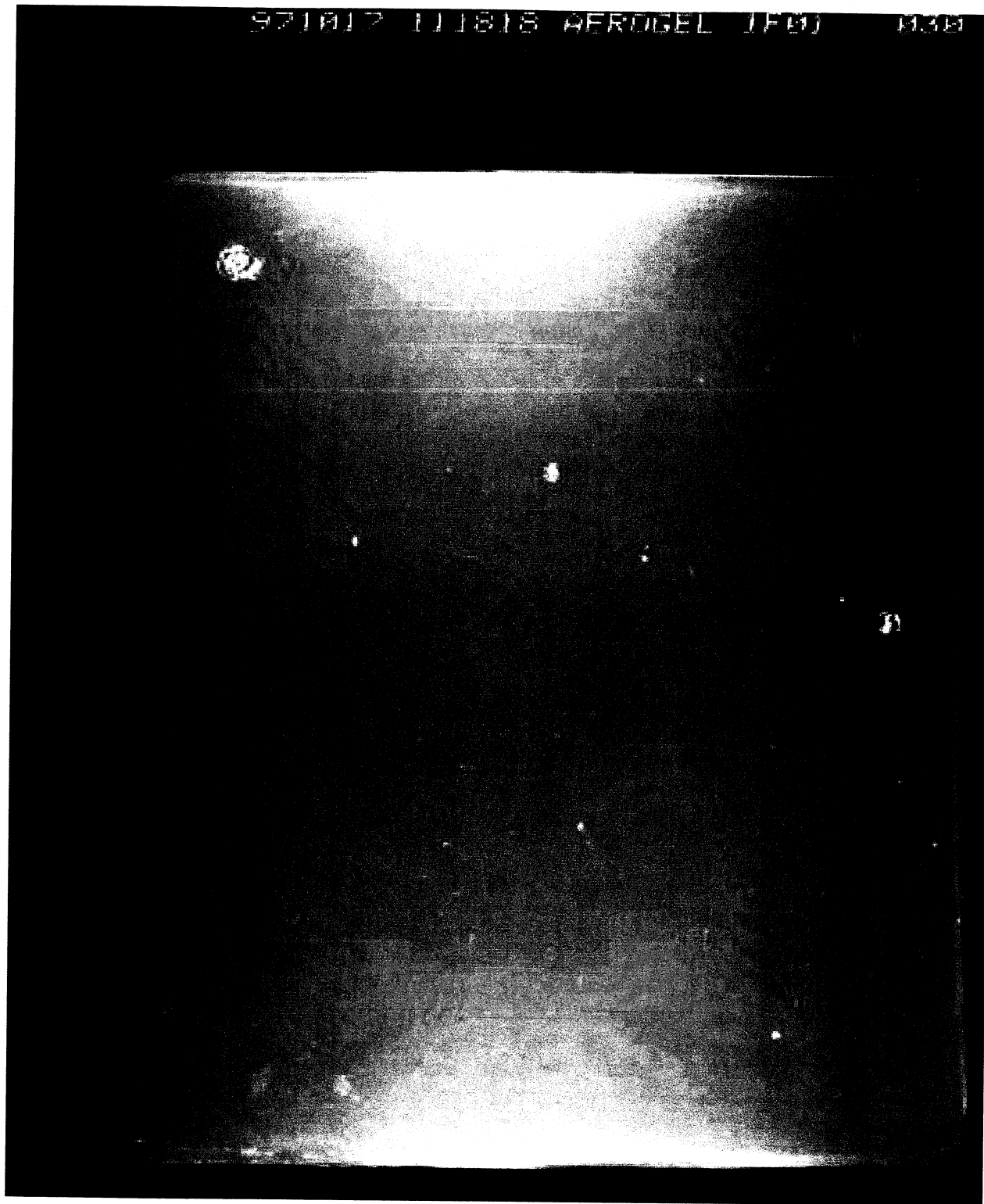
921012 111600 AFRTGFI 1005 028



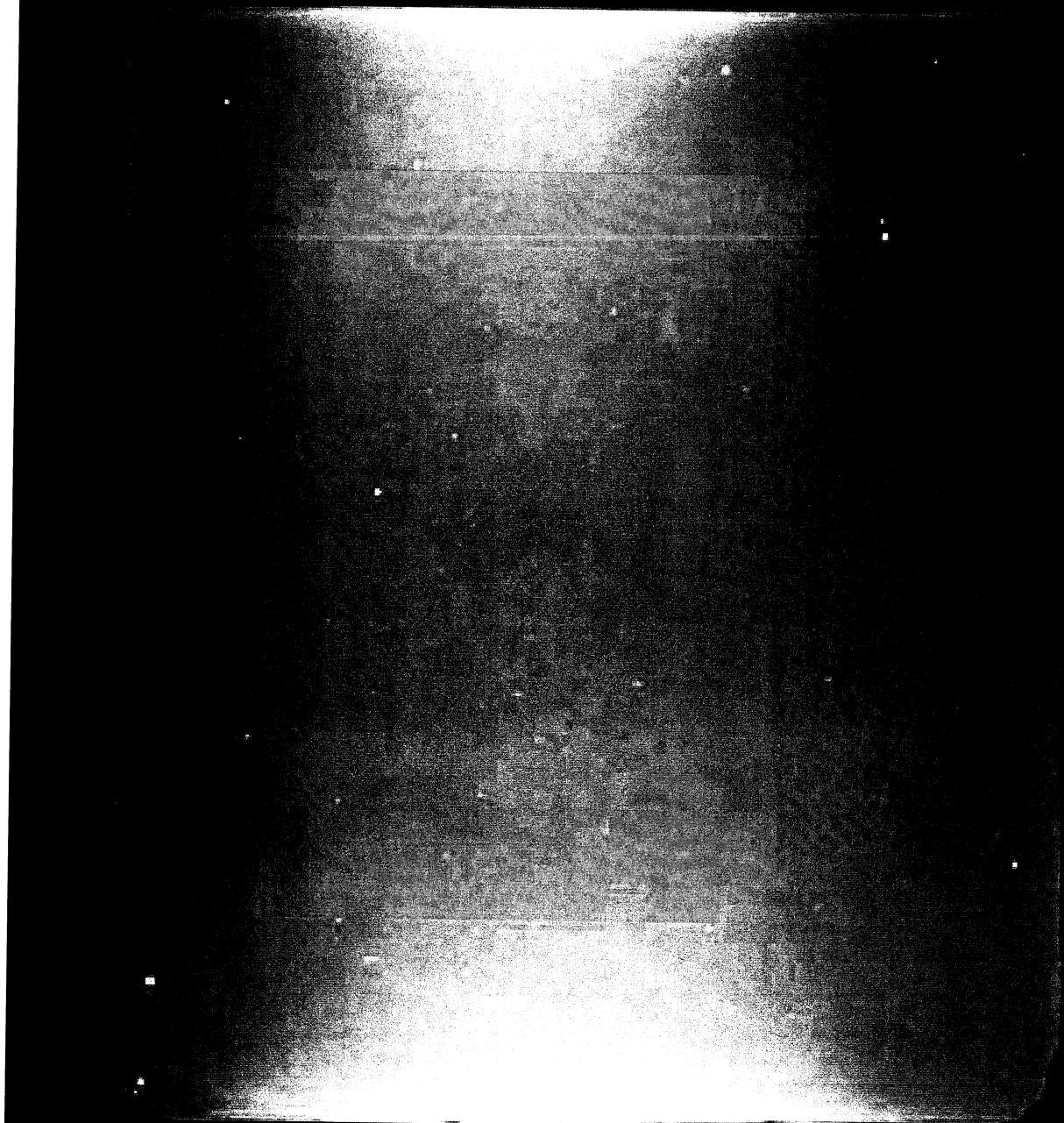
921017 111705 AFROGEL 1E06 029



921017 111818 AEROGEL IFB) 030

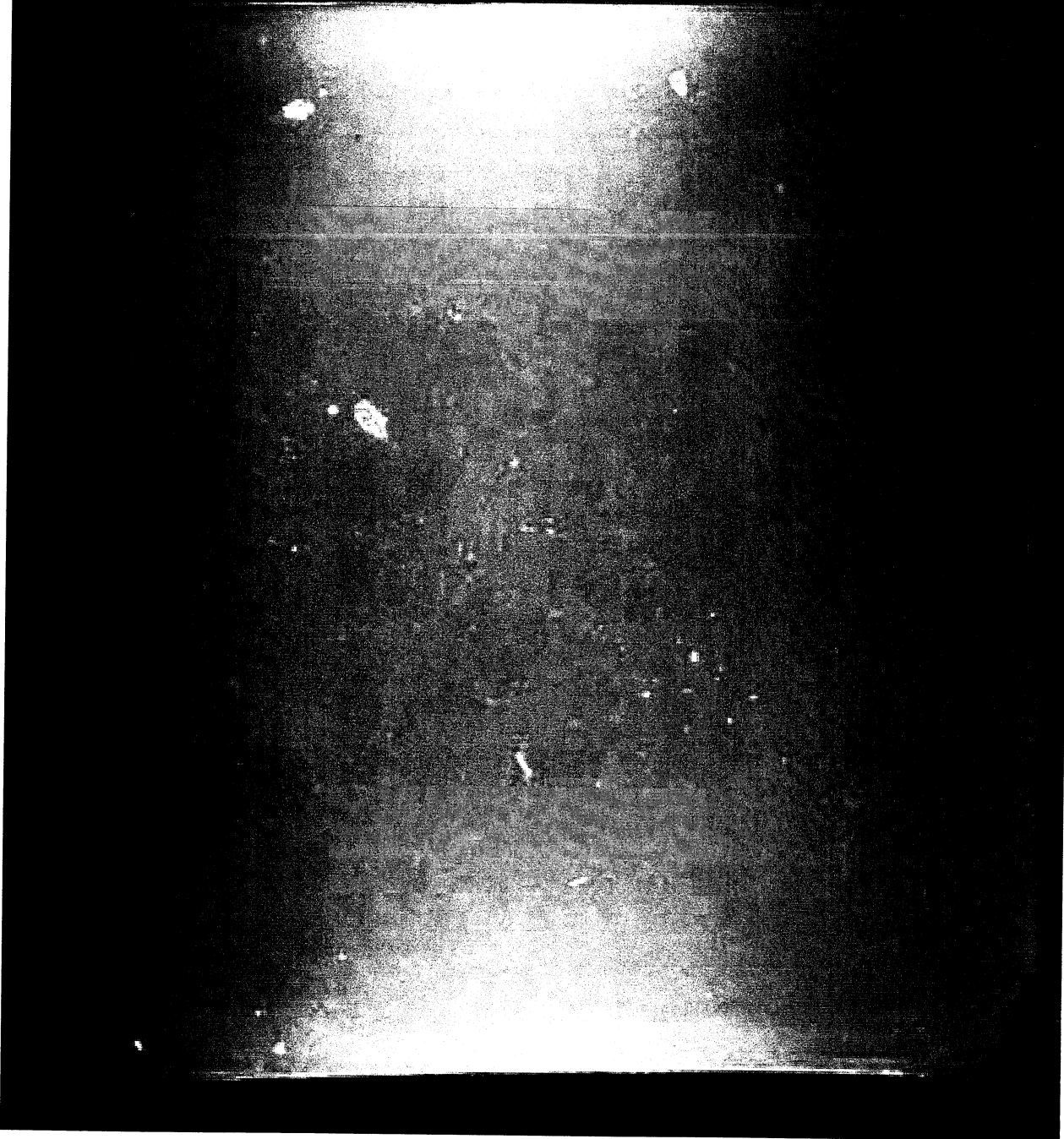


921817 111908 AEROGEL 1F02 R31



971017 111958 AEROGEL 1F03 032

971017 112037 AEROGEL 1F04 033

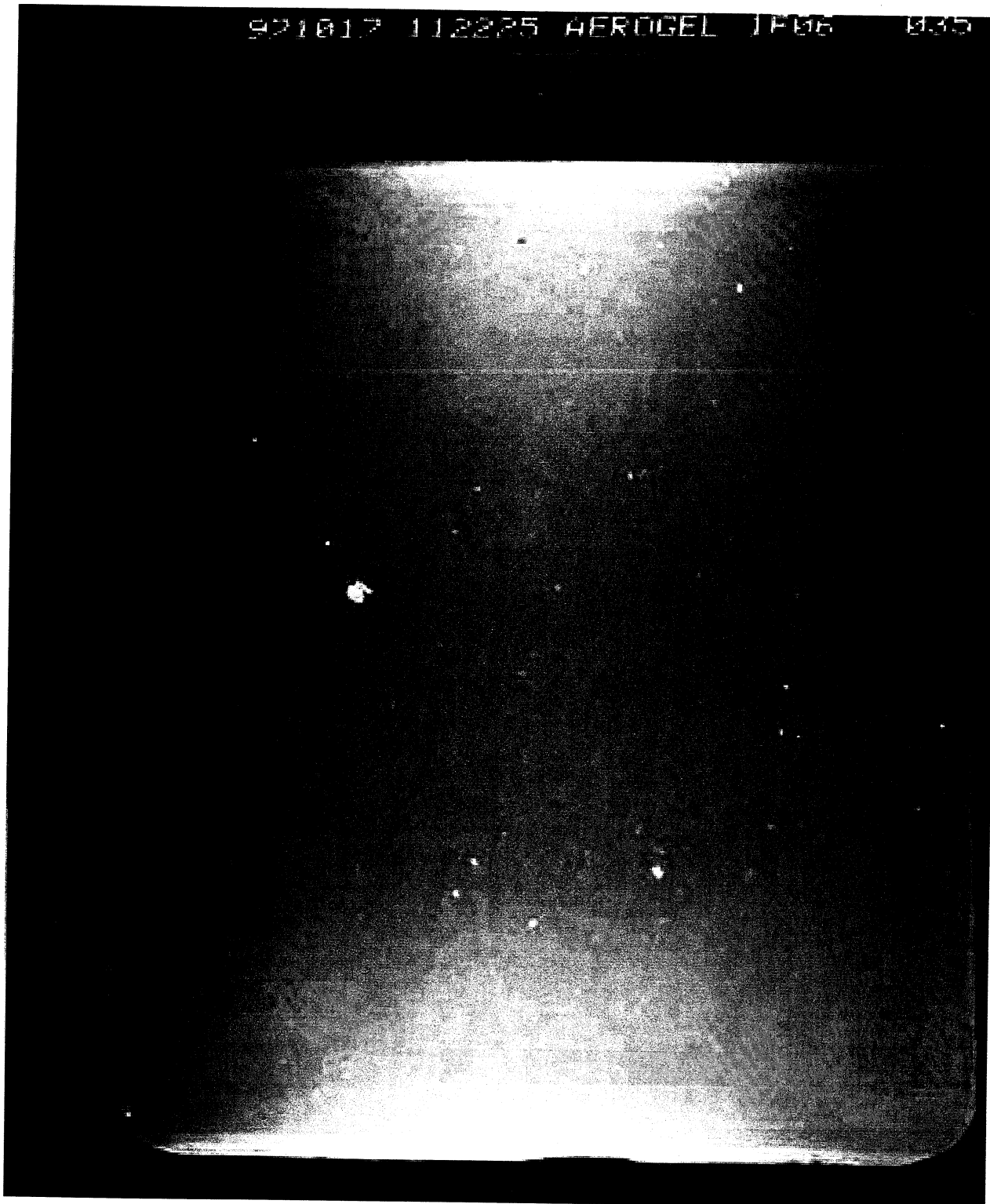




821817 112127 HERUGEL 1F05 034



921017 112225 AEROGEL 1F05 035

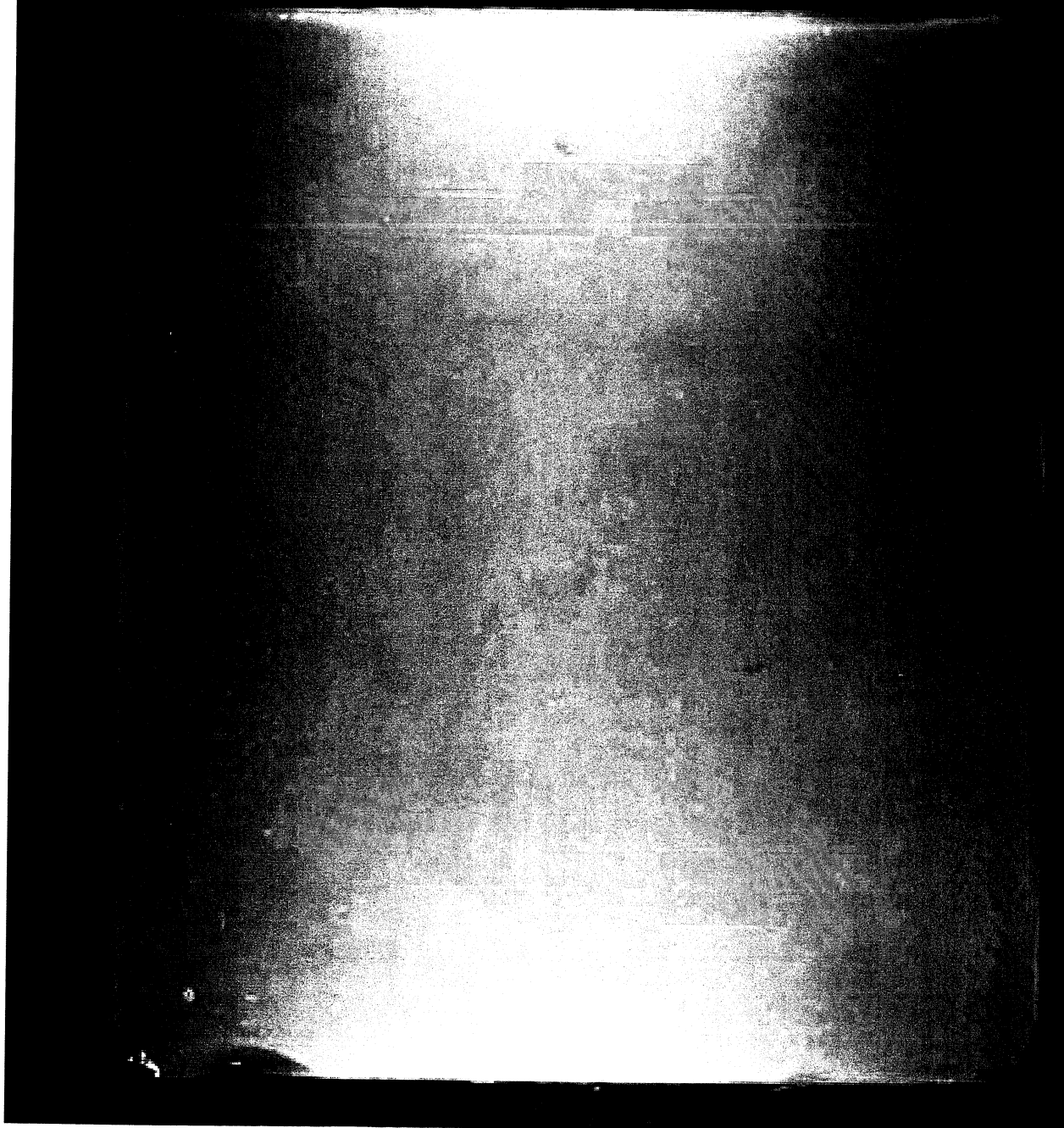




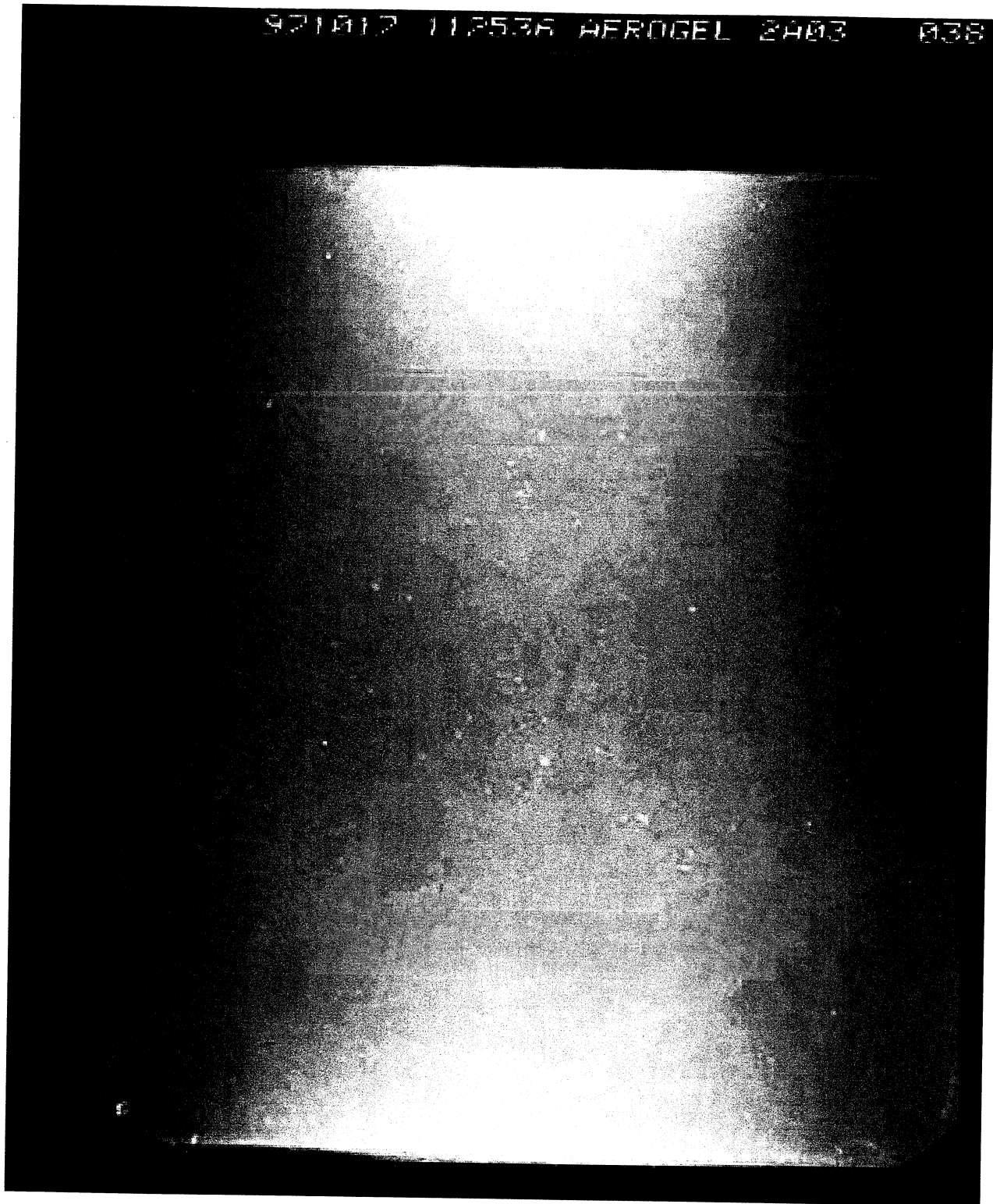
921817 113328 AEROGEL 2401 036



971017 112450 HEROGEL 2402 037



921012 112536 AEROGEL 2403 038



921017 112525 AEROGEL 2404 039

971812 112733 AEROGEL 2405 040





971017 112835 AEROGEL 2406 041



921017 112933 AFRUGEL 2801 042



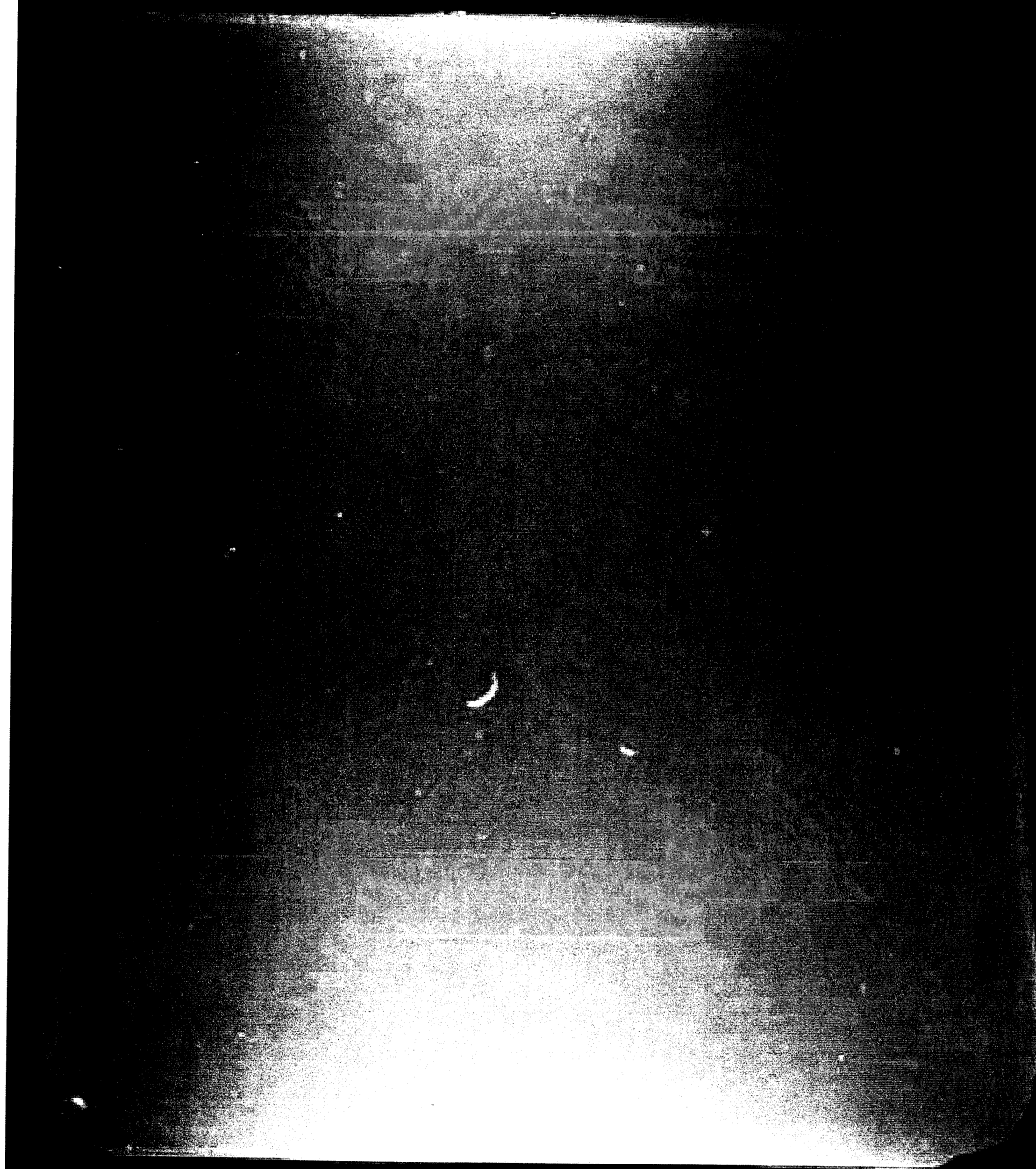
921617 113152 AFRUGEL 2842 M43



521012 113253 HERONEL 2803 044



921012 113355 AEROGEL 3504 045



921012 113811 AFRUGEL 2805 046

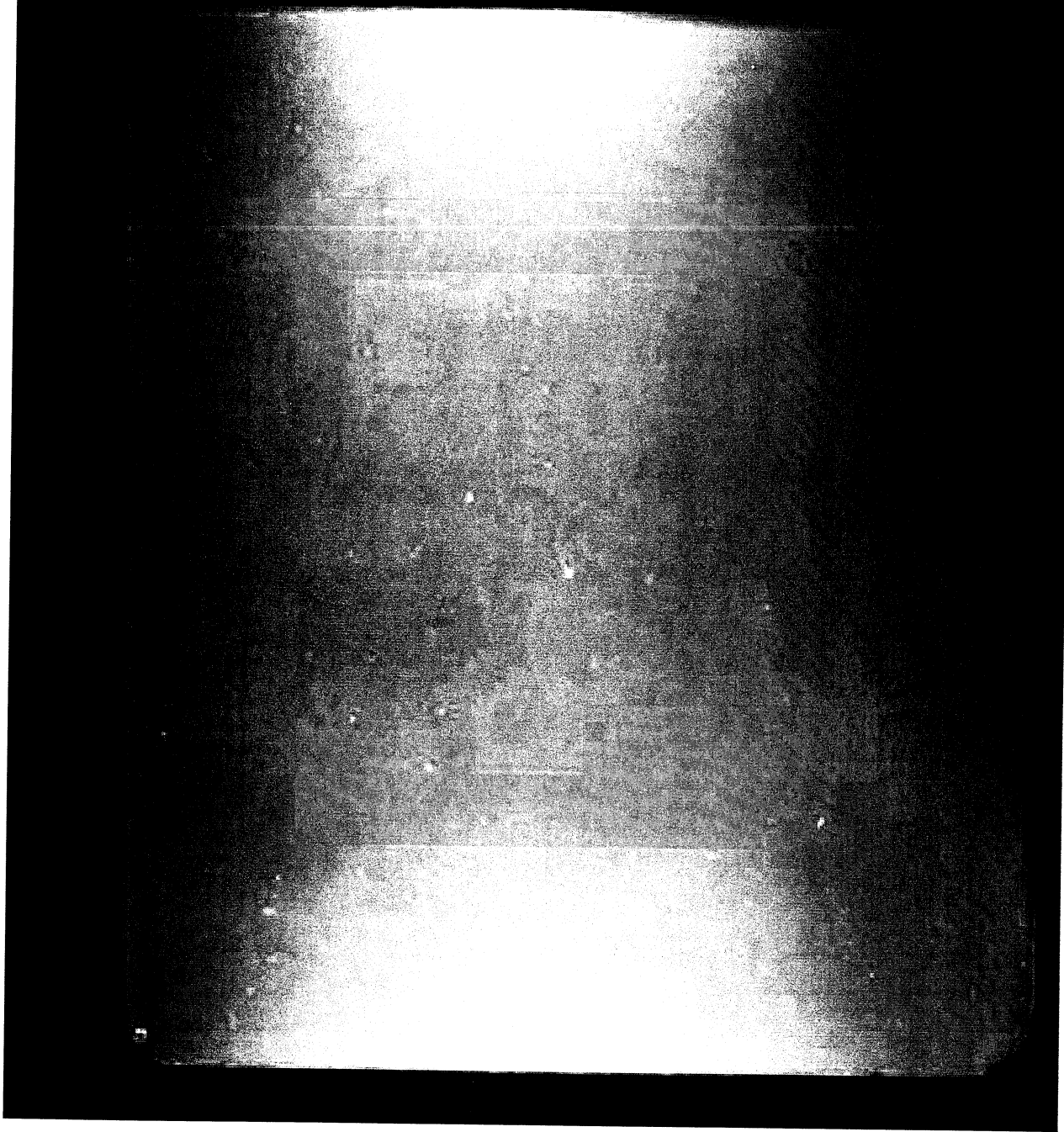


521012 113903 AFRUGEL 2505 047

921012 114038 AEROGEL 2001 0+8

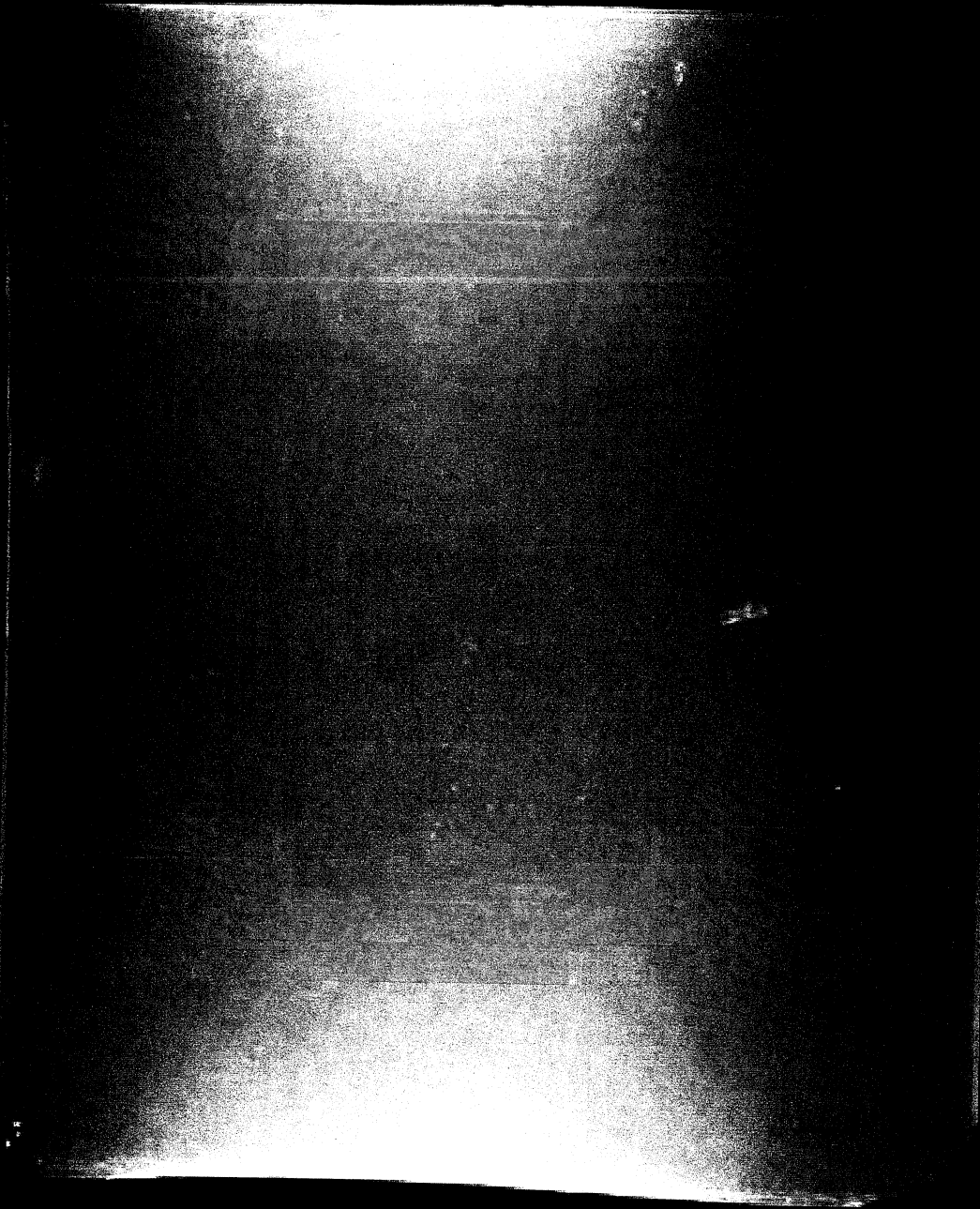


921017 114207 AEROGEL 2002 049





921012 114302 HFDGFL 2003 050

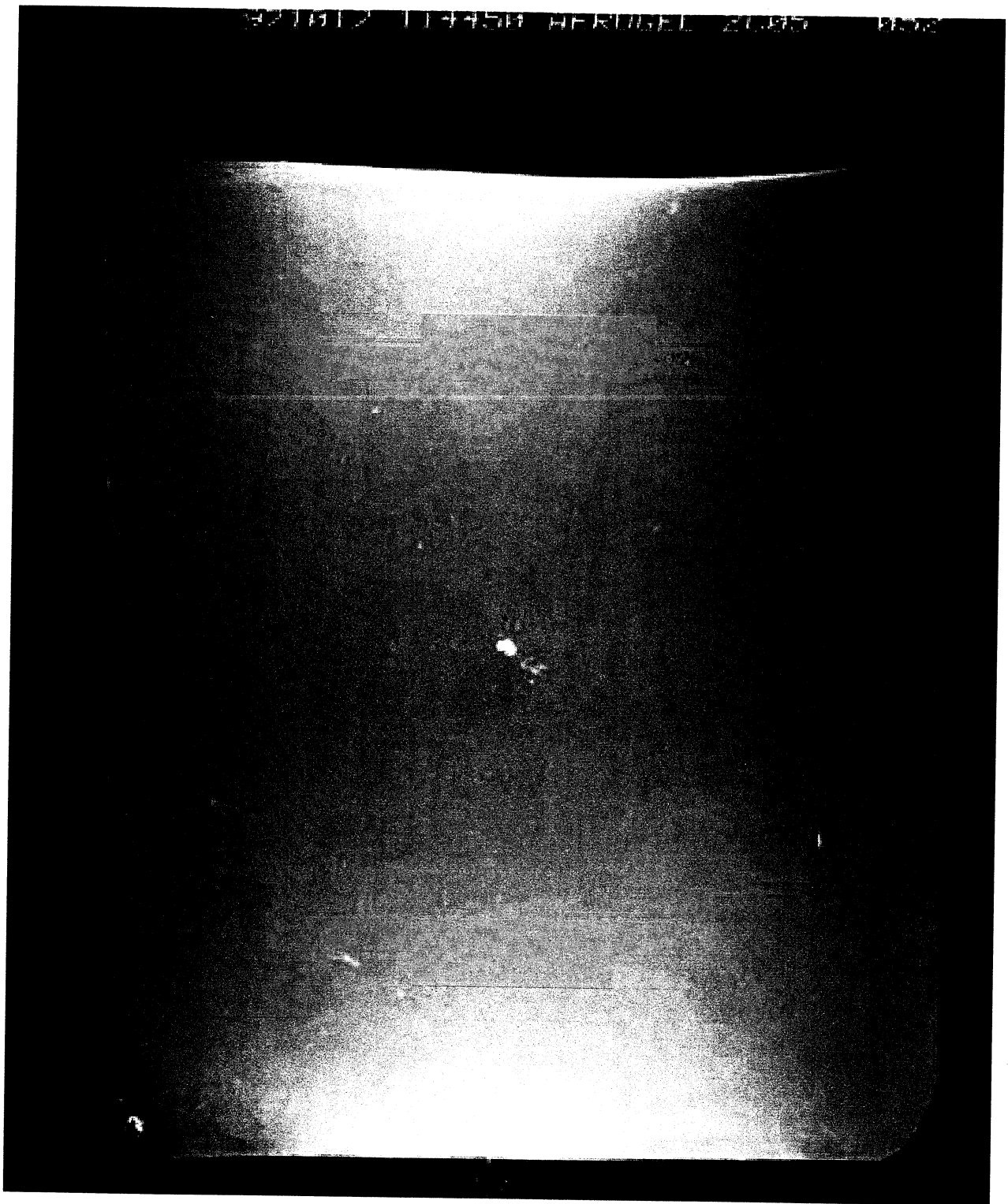


921012 114355 AFMONT 2004 051



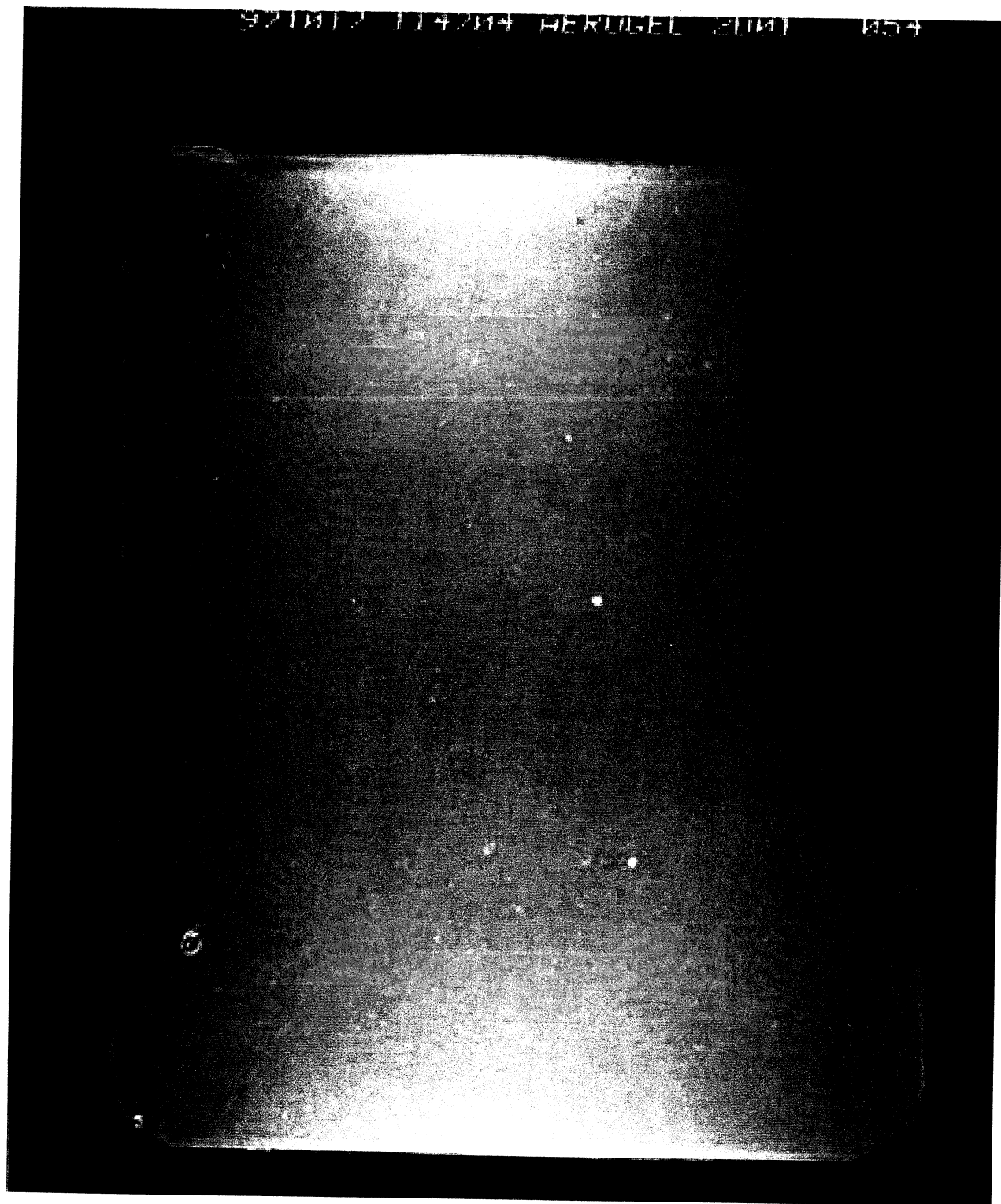


921612 11445H HERMES 2085 PAGE

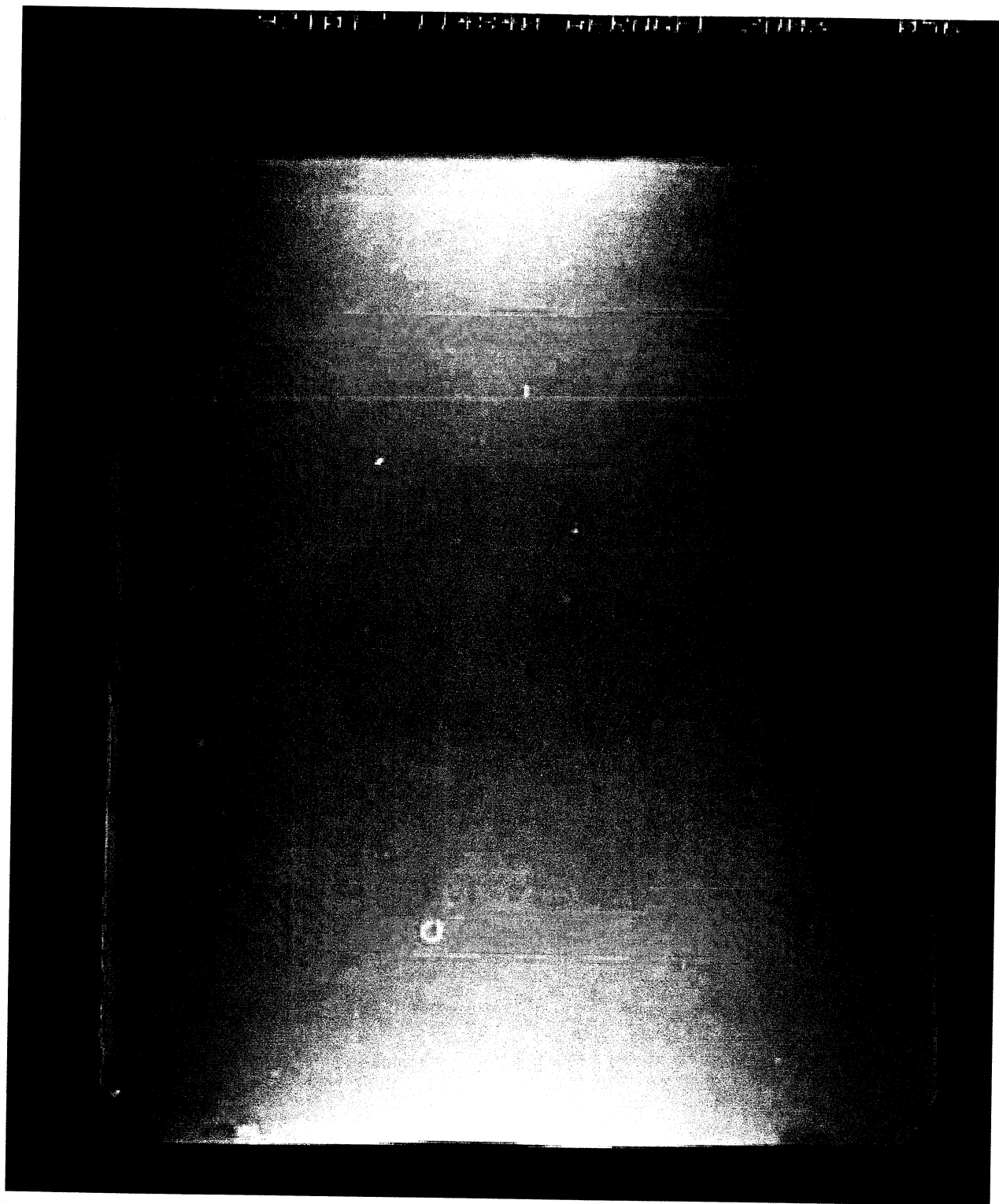


2006

921812 114204 HERUGEL 2101 054

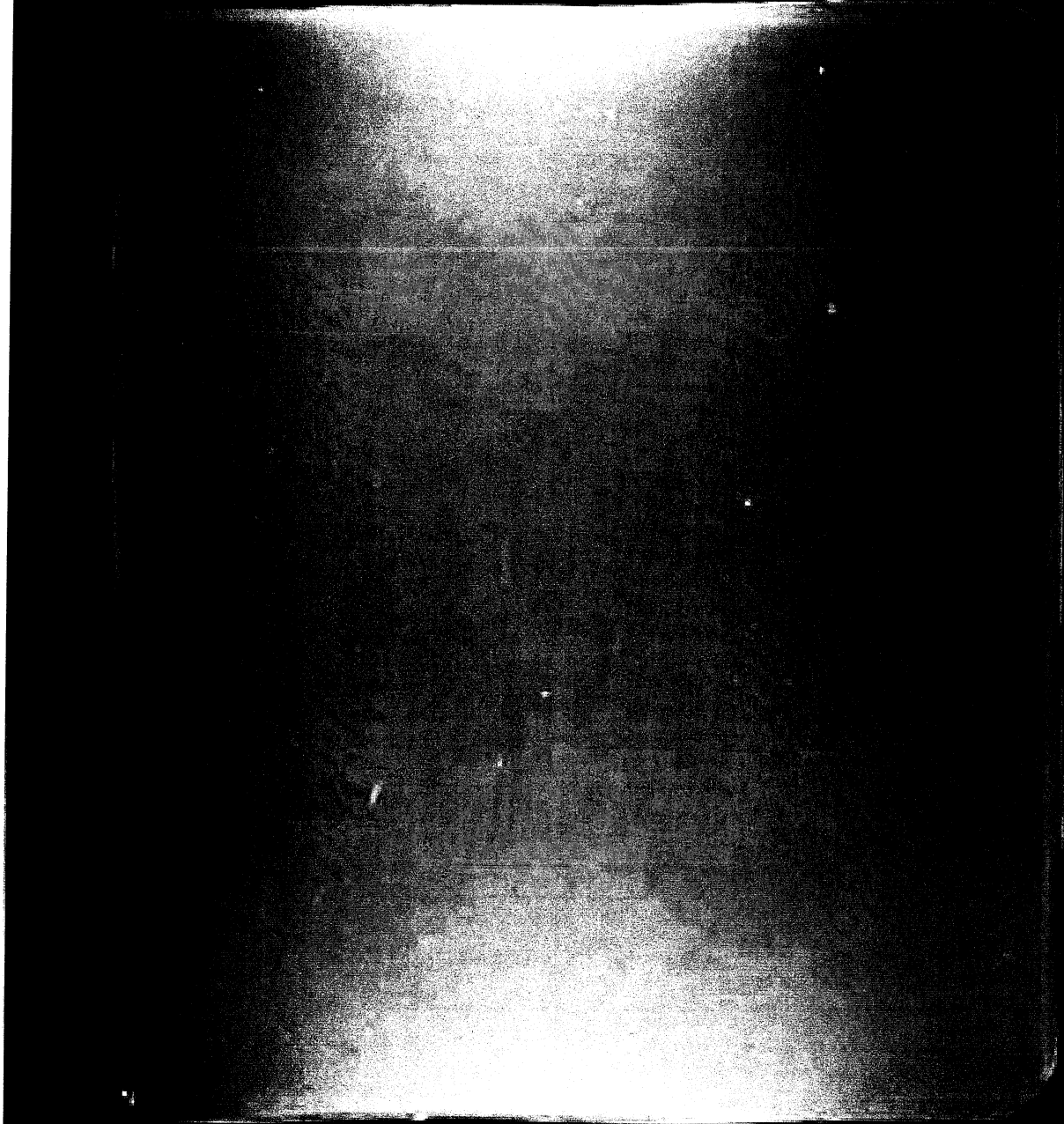


2D02

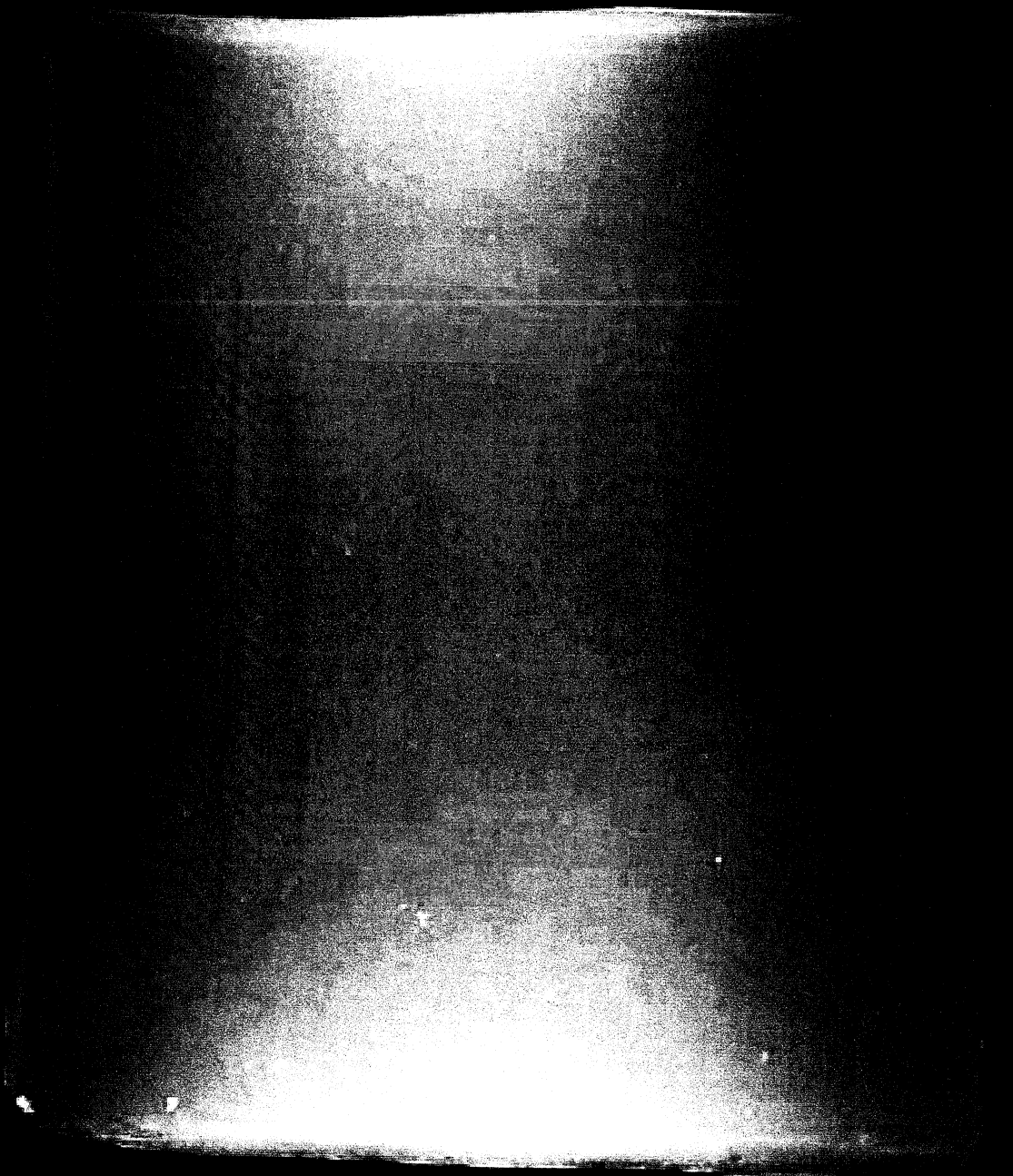




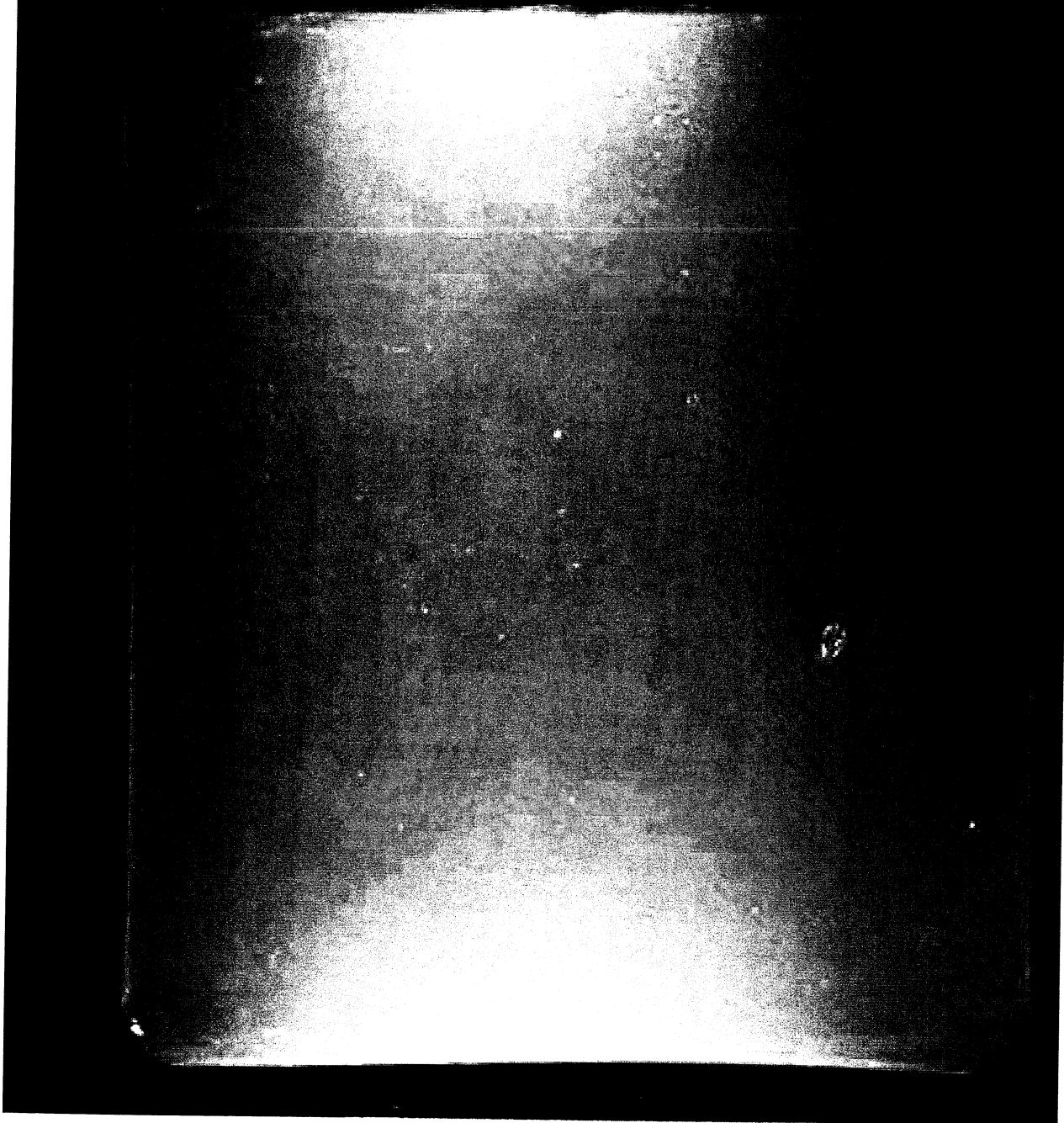
921017 114943 HFRDGE) 2004 057



921012 115024 AFKINGET 2045 053

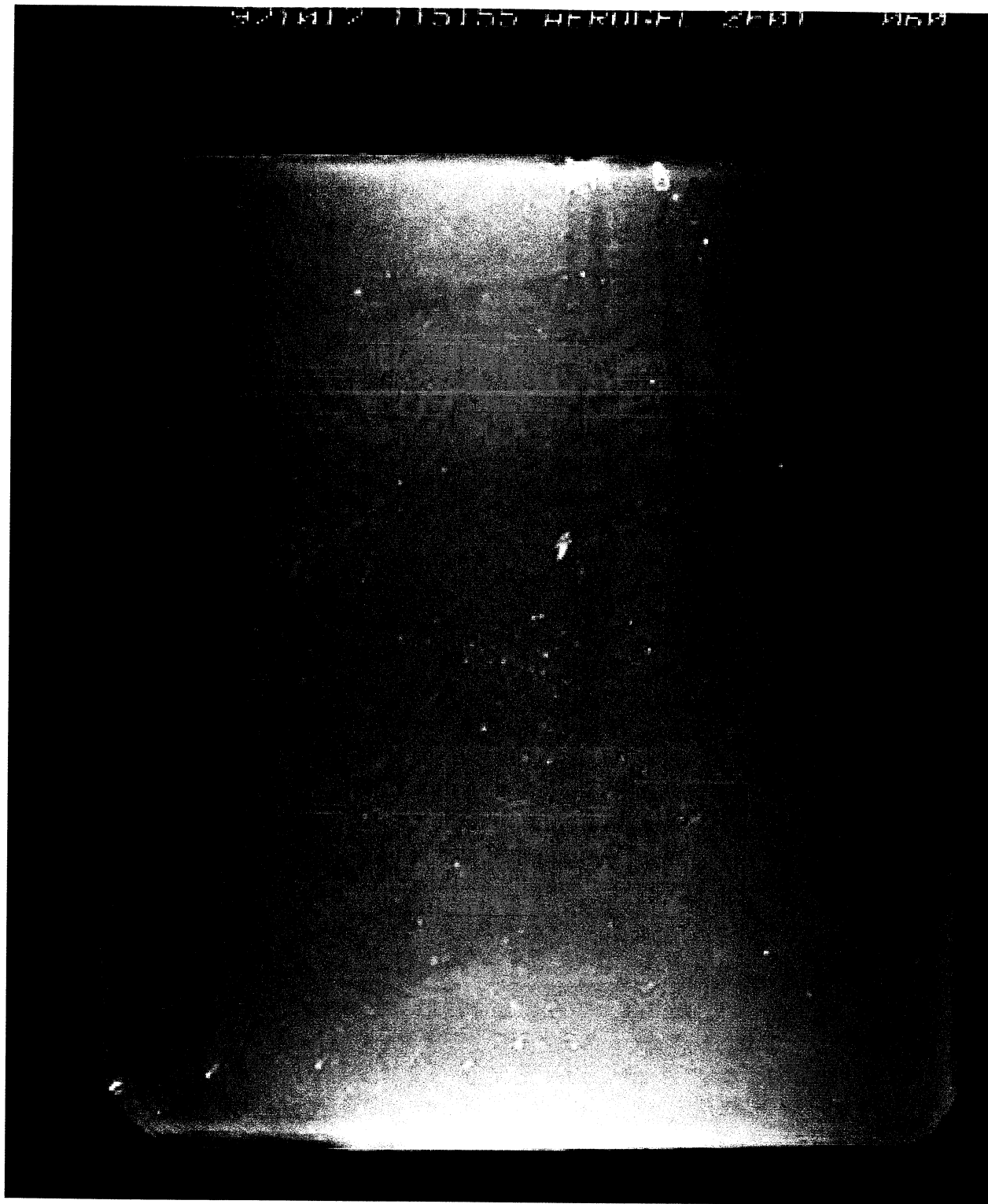


921012 115108 HERCULE 2000 059

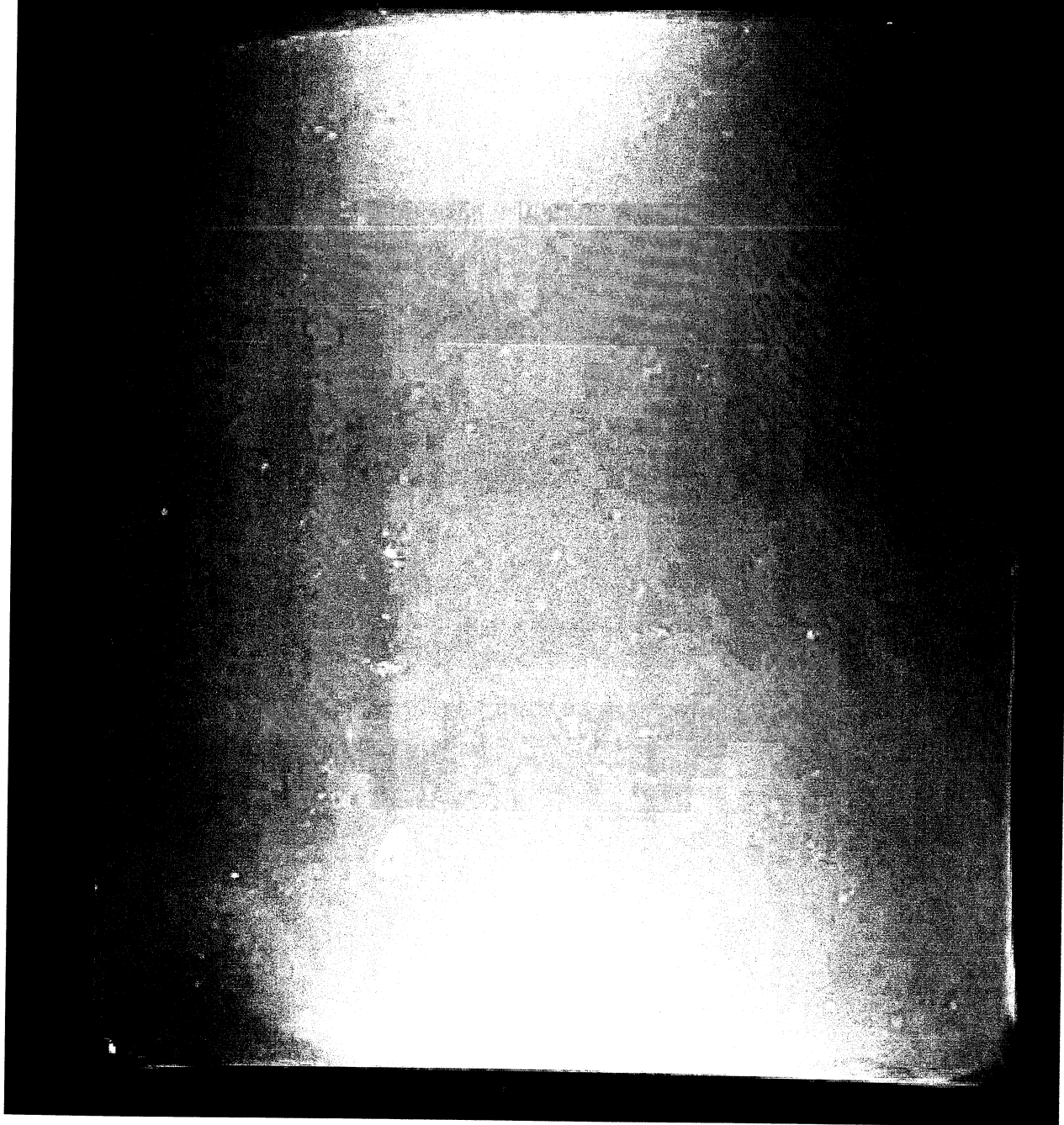




927412 115155 AERONAUT 2501 460



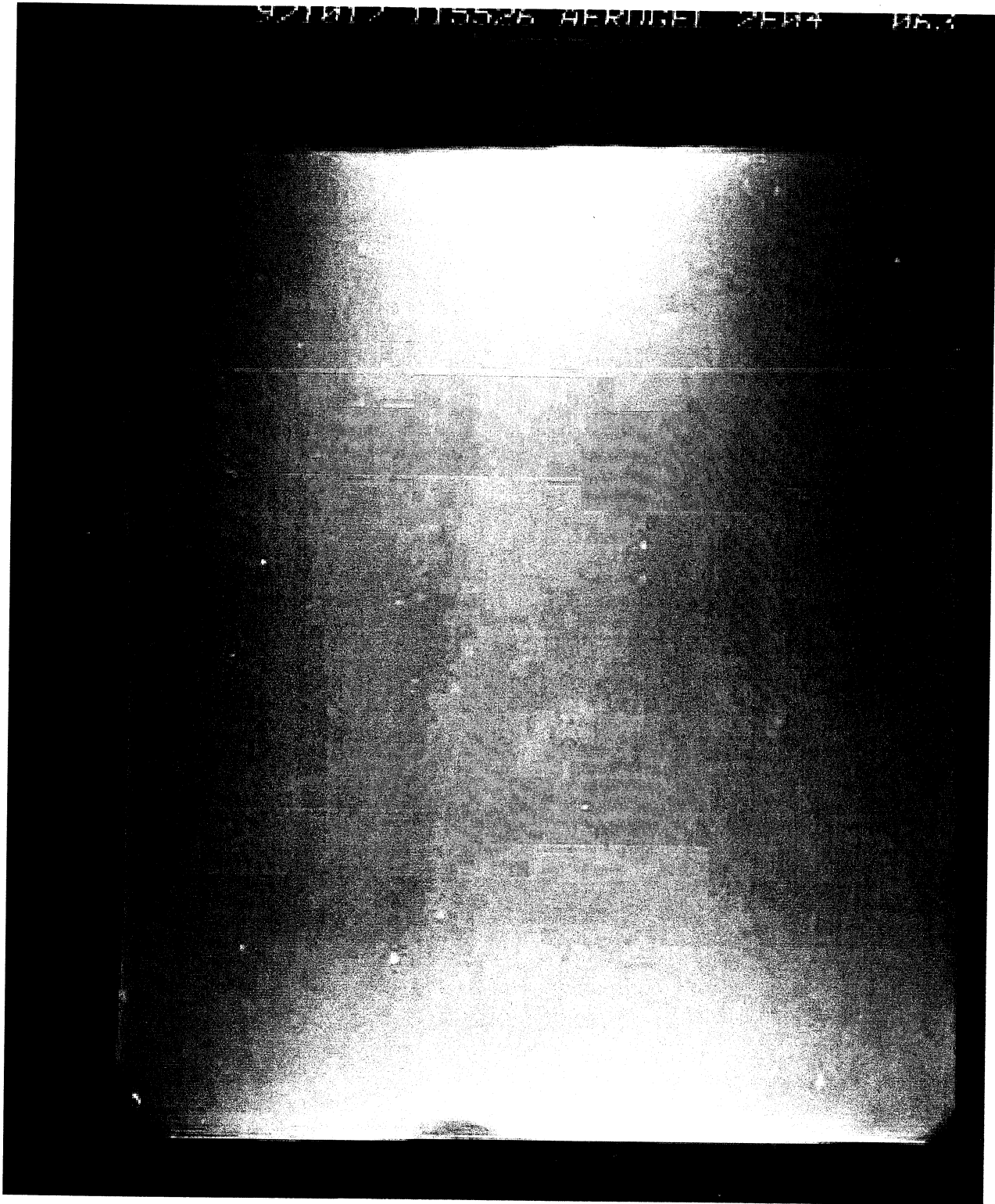
921612 115253 AFR00FI 2F02 061



921017 115411 AEROGEL 2E03 002



921812 115526 AERUGEL 2EN4 06.3



921812 115621 HFRNGE1 2F05 084

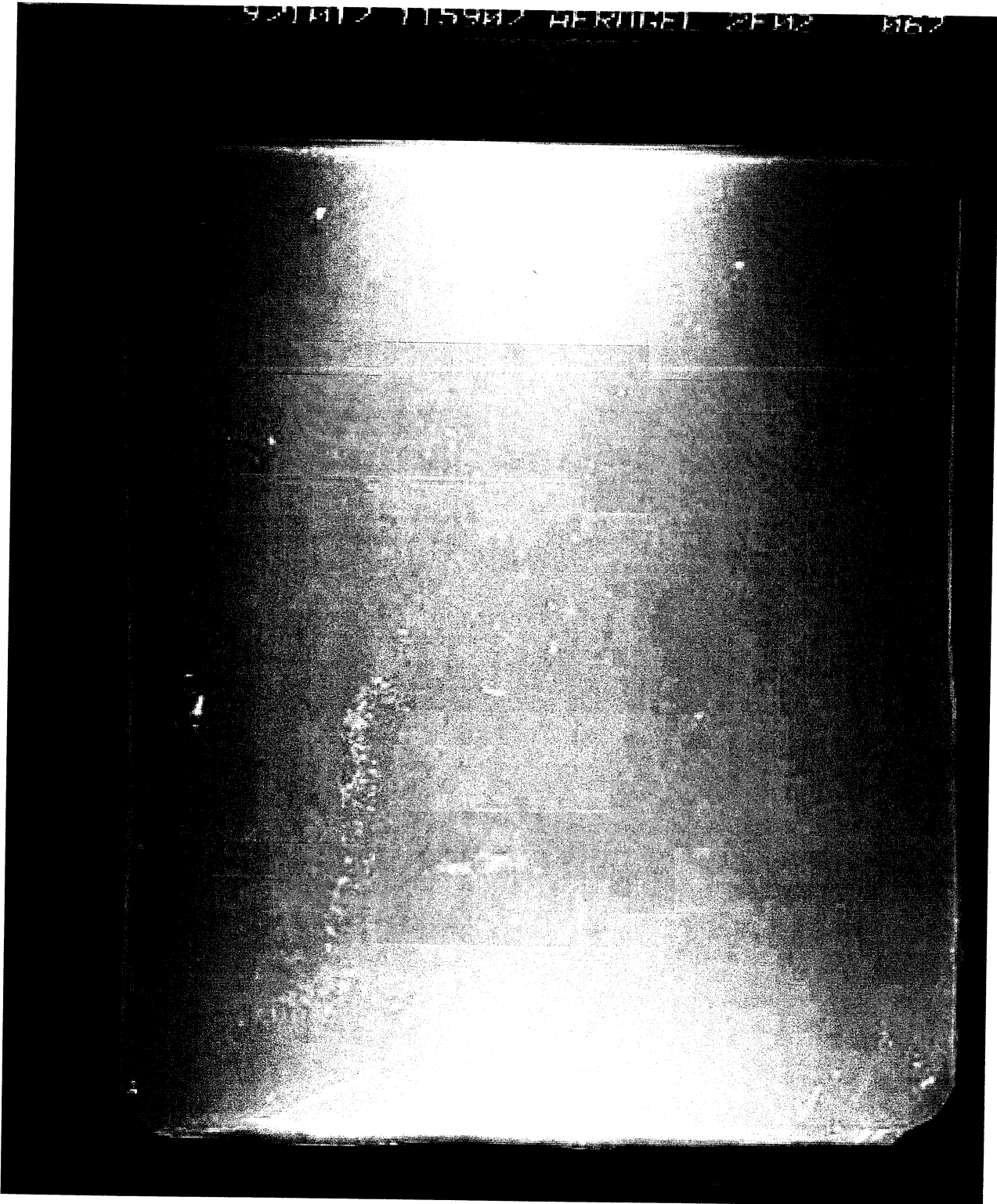


921412 115213 AEROGEL 2F06 065

921017 115815 AFRNGFI 2F01 000

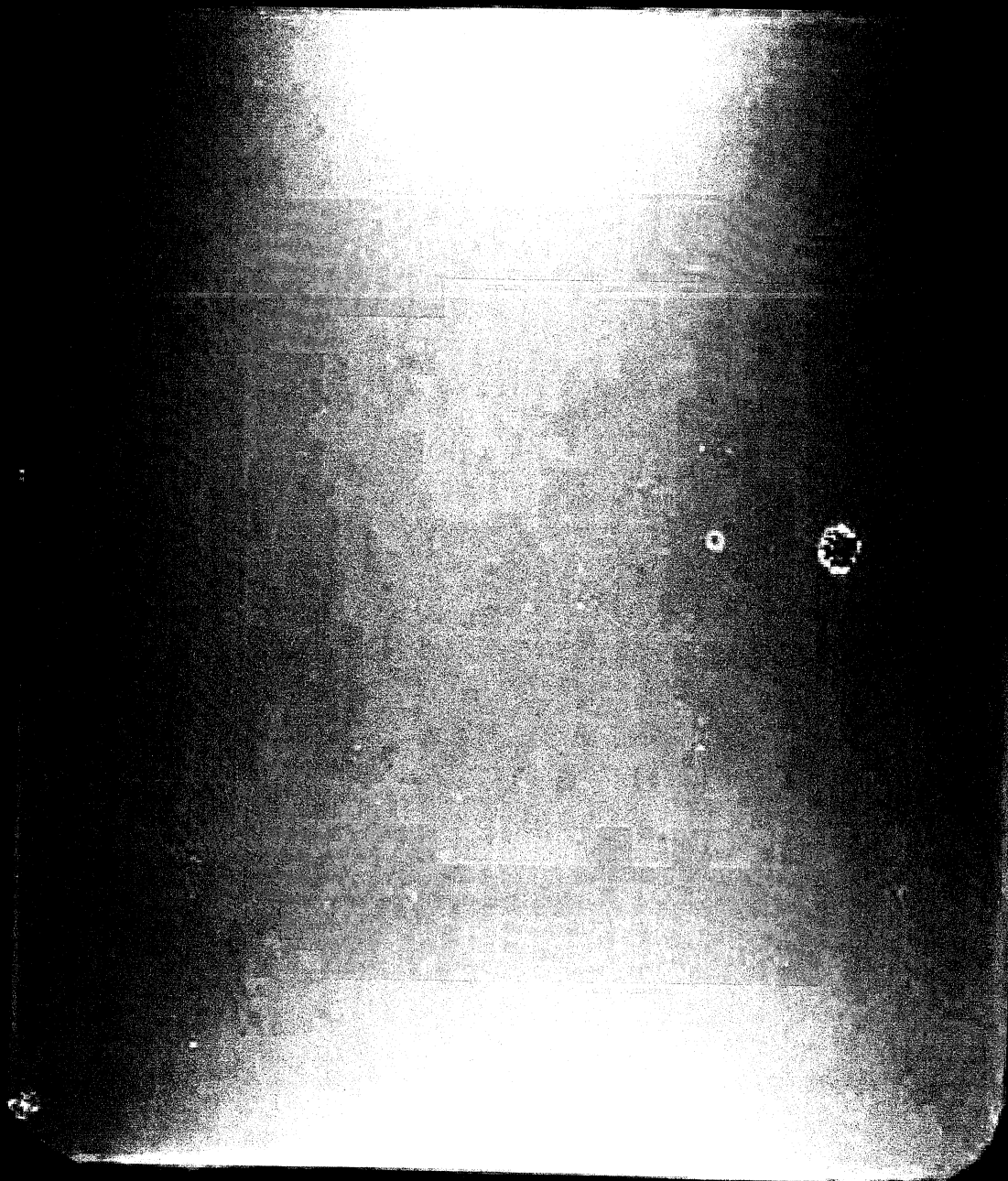


920112 115902 HERINGEL 2F42 062

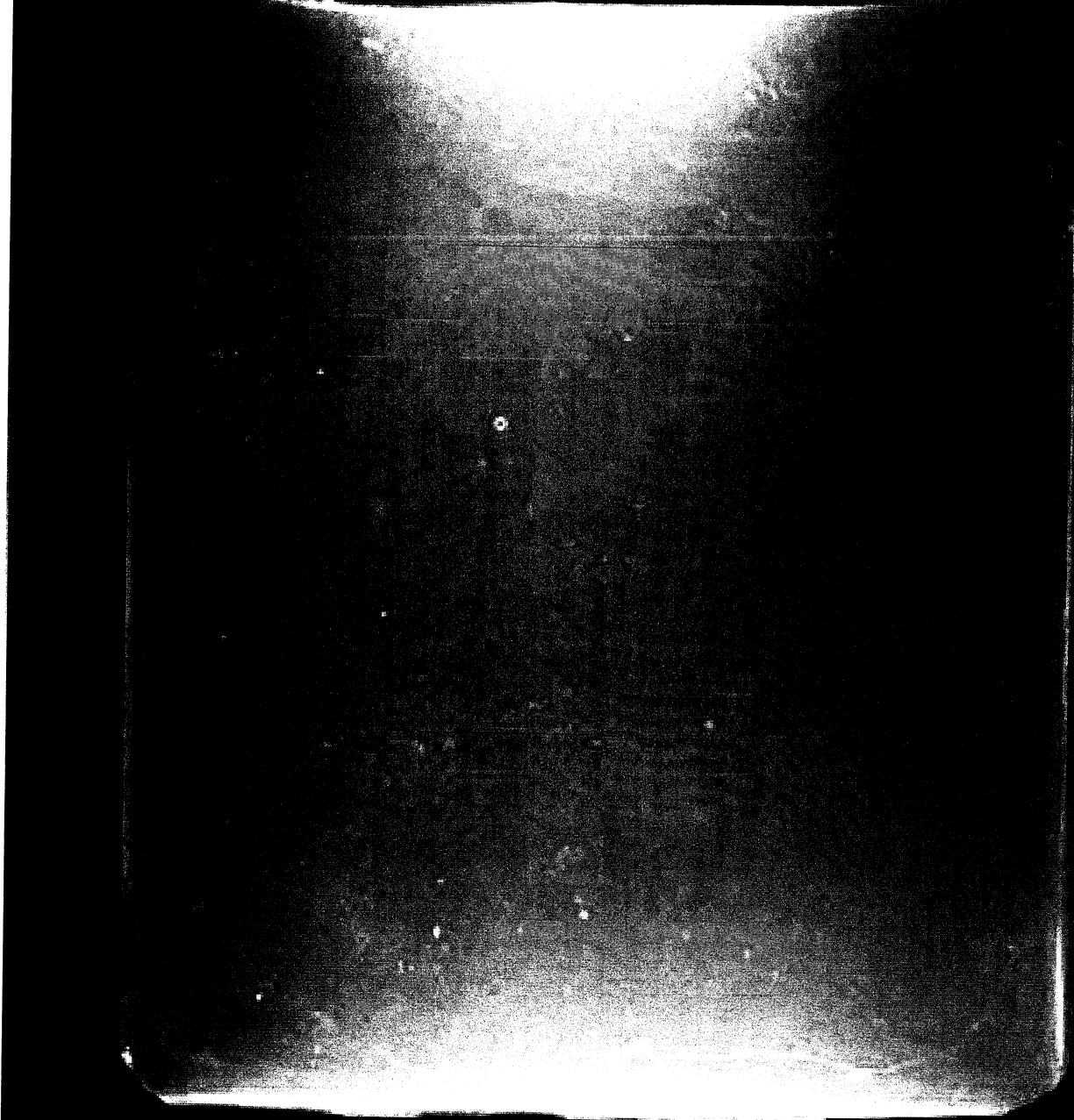




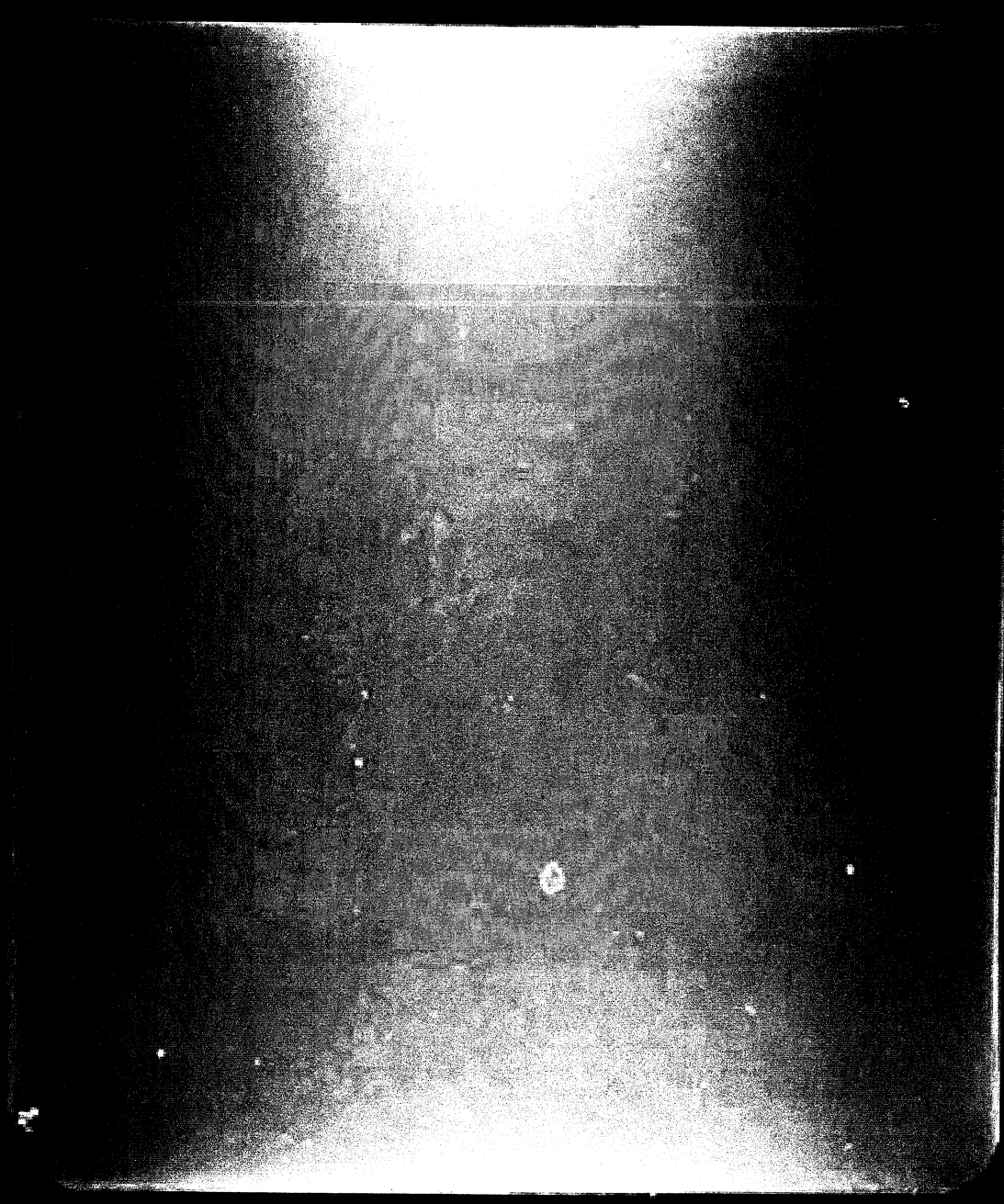
971012 115958 AEROGEL 2F03 068



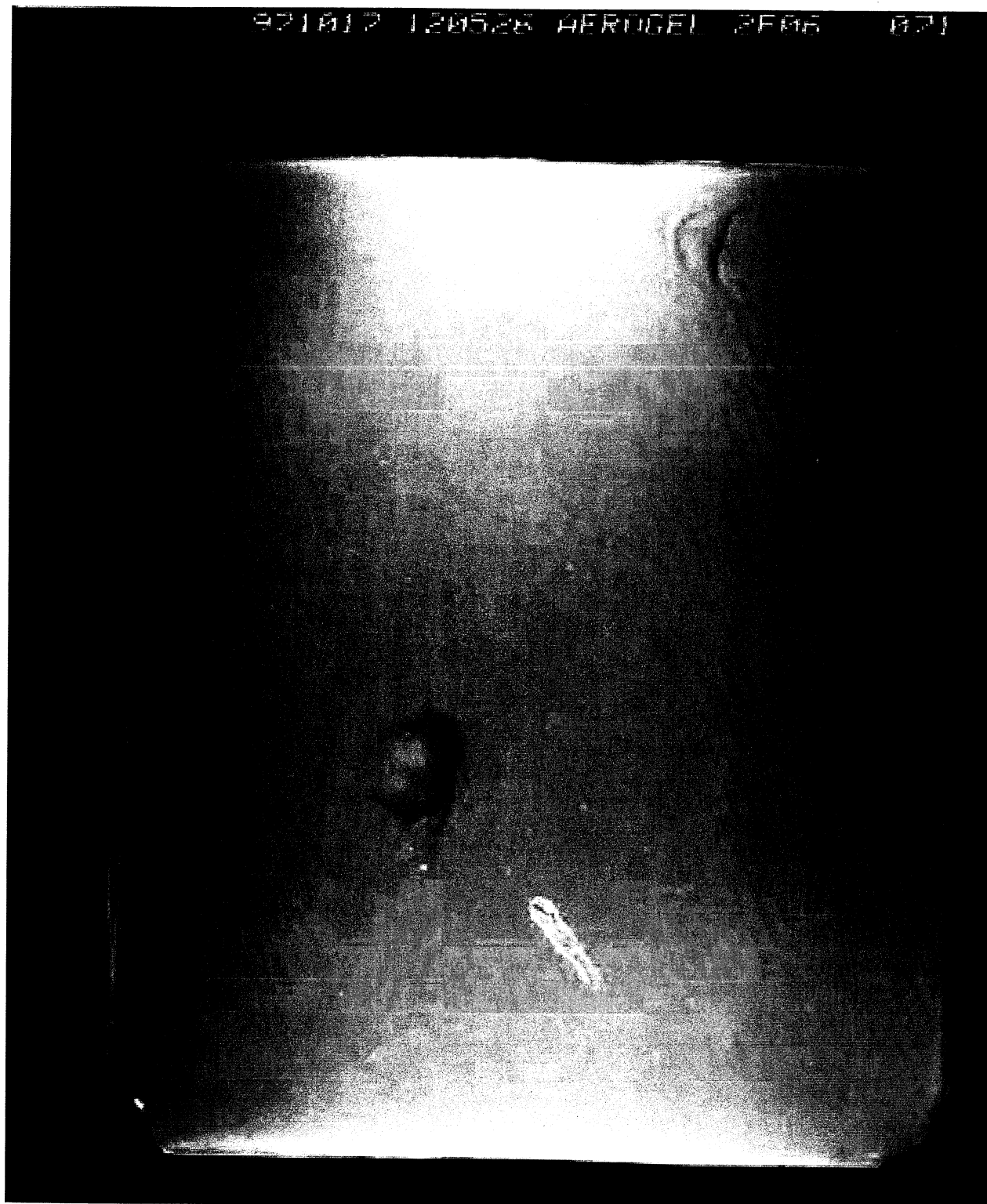
921012 120355 AEROMEL AF04 065



971017 120436 HERUGEL 2F05 020



921812 120528 AEROGEL 2F05 B71



## APPENDIX B

Appendix B contains a data table that provides the major parameters recorded for each impact feature that was documented during the detailed optical scans of the 24 tiles that have undergone the detailed optical inspection.

### Table Definitions:

All dimensions are given in micrometers ( $\mu\text{m}$ ).

**Tile** - provides information related to the tile location within the ODC experiment (e.g., 1A01; tray [1 or 2], column [A-F], row [01-06]).

**Feature #** - individual feature number on a given tile.

**Particle  $D_1$  &  $D_2$**  - if present, provide estimates of the major ( $D_1$ ) and minor ( $D_2$ ) axis particle dimensions determined by microscopist using an eyepiece reticule in the scanning system microscope.

**Entrance Hole  $D_{\text{minor}}$  &  $D_{\text{major}}$**  - if present, provide estimates of the major ( $D_{\text{major}}$ ) and minor ( $D_{\text{minor}}$ ) axis measurements for the entrance hole of the track/pit/shallow-depression determined by microscopist using an eyepiece reticule in the scanning system microscope.

**Track Shape** - Assigned by the microscopist during scanning operations to categorize the feature type being documented. c = carrot, cl = cylinder, p = pit, n = needle, s = split or bifurcated, f = flake. n/s, n/c, cl/c, etc. indicates feature is a combination of two (e.g., n/s = needle type feature that is split or bifurcated).

**Track Length** - Length of track determined by computing the difference in the X/Y/Z coordinates of the entrance hole and the X'/Y'/Z' coordinates of the terminus of the feature.

**Direction** - Indicates the direction, in two dimensions, of the particle or impactor in degrees (plus or minus) from 0 (i.e., 12:00 o'clock position or north).

C = Carrot, Cl = Cylinder, P = Pit, N = Needle, S = Split / Bifurcated, F = Flake

All measurements are in micrometers (µm)

Tile	Feature #	Particle		Entrance Hole		Track Shape	Track Length	Direction
		D <sub>1</sub>	D <sub>2</sub>	D <sub>minor</sub>	D <sub>major</sub>			
1A01	1	6	4	35	35	n/s	1575	34.79
1A01	2			55	55	n		-76.42
1A01	3	10	8	10	10	cl	1898	36.37
1A01	4	12	6	20	20	cl	1563	-71.10
1A01	5			620	680	cl	3855	23.05
1A01	6	6	4	45	45	c	1237	-19.82
1A01	7			330	330	st	2971	29.71
1A01	8	70	44	110	300	cl	2109	50.14
1A01	9	65	35	65	380	cl	2939	53.26
1A01	10	6	4	20	20	c	884	63.02
1A01	11	8	6	20	20	cl/n	1200	-50.63
1A01	12	6	4	35	35	cl/c	1001	9.84
1A01	13	10	8	35	35	cl/n	2521	-86.00
1A01	14	6	4	15	15	n	907	67.36
1A06	1	6	4	20	20	cl/c	732	44.68
1A06	2	6	4	50	50	cl	2011	48.13
1A06	3	8	6	15	20	cl	3165	-68.96
1A06	5	12	12	400	550	c	4165	-59.78
1A06	6	8	6	275	330	c	1356	-73.51
1A06	7	6	4	10	10	cl	848	-56.83
1A06	8	6	2	270	690	c	1309	22.88
1A06	9	70	20	33	33	cl	2129	70.23
1A06	10	6	4	20	20	n	2201	67.04
1A06	11			240	240	st		81.41
1A06	12	8	6	30	30	n	3013	38.11
1A06	13	6	4	25	25	n	1590	42.22
1A06	14	8	6	25	30	cl	1367	-70.95
1A06	15	6	4	10	15	n	1002	72.59
1A06	16	6	4	35	35	n	1971	65.62
1A06	17	135	85	150	150	cl	3408	62.76
1B01	1	15	12	30	30	cl	942	-40.79
1B01	3	3	2	55	55	c	913	34.34
1B01	4	10	10	660	660	cl/s	4217	29.29
1B01	5	15	12	20	20	cl	1070	76.37
1B01	7	4	2	15	15	cl	694	-66.23
1B01	8	8	6	15	15	n	3778	-78.61
1B01	9	6	4	20	20	cl	1369	51.27
1B01	12	13	10	30	30	n/c	1175	-59.96
1B01	13	3	2	30	30	n/c	856	-10.96
1B01	14	8	6	25	25	cl	1528	61.18
1B01	15	30	30	25	25	n	1852	52.15
1B01	16	2	2	20	20	n	1181	63.52
1B01	17	20	15	30	30	n	2610	-68.52
1B01	18	4	2			n	1191	43.38
1B01	19	6	4	30	30	n	3798	-69.43
1B01	20	10	8	15	15	cl	1535	-76.15
1B01	21	4	2	20	20	n	1476	64.02
1B05	2	12	10	25	25	cl	845	72.19
1B05	3	6	4	90	90	c	2135	-63.10
1B05	4	6	4	160	275	c	2617	62.58
1B05	5	15	12	20	20	cl	1761	-87.98
1B05	6	10	8	10	10	cl	1378	66.89
1B05	7	7	5	85	85	c	3430	-67.28
1B05	9	7	5	20	20	n	3225	-30.87
1B05	10	6	4	20	20	n	1396	72.38
1B05	12	150	130	120	120	cl	9686	-70.78
1B05	13	5	3	130	130	c	1481	68.89

C = Carrot, Cl = Clyinder, P = Pit, N = Needle, S = Split / Bifurcated, F = Flake

All measurements are in micrometers (µm)

Tile	Feature #	Particle		Entrance Hole		Track Shape	Track Length	Direction
		D <sub>1</sub>	D <sub>2</sub>	D <sub>minor</sub>	D <sub>major</sub>			
1B05	7	7	5	85	85	c	3430	-67.28
1B05	9	7	5	20	20	n	3225	-30.87
1B05	10	6	4	20	20	n	1396	72.38
1B05	12	150	130	120	120	cl	9686	-70.78
1B05	13	5	3	130	130	c	1481	68.89
1B05	14	65	50	30	30	cl	2129	51.93
1B05	16	14	12	20	20	n	1039	65.33
1B05	17	4	2	35	35	n	1582	9.40
1C01	9			180	220	cl		-40.75
1C01	11	18	15	25	85	cl	704	55.25
1C01	12	8	5	80	110	c/s	2866	36.36
1C01	13	5	3	25	25	c	494	5.87
1C04	2	25	10	40	40	cl	1267	-70.87
1C04	3	6	4	90	90	c	1792	56.64
1C04	4	6	4	440	690	c/s	1723	13.65
1C04	5	6	4	10	15	n	918	71.08
1C04	6	50	35	70	180	cl	3735	-89.40
1C04	7	8	6	45	45	n	3452	66.12
1C04	8			35	35	cl		-70.29
1C04	9	25	18	50	50	cl	1319	69.78
1C04	10	25	25	40	40	cl	920	-33.00
1C04	11	6	4	45	45	c/s	1231	-45.00
1C04	12	4	2	20	20	c/s	887	-73.21
1C04	13	6	2	10	10	c/s	874	-78.67
1C04	14	4	2	50	50	c	2843	16.67
1D01	1	5	3	30	30	n	1817	62.21
1D01	2	45	35	100	100	cl	311	39.08
1D01	4			100	100	st		
1D01	5	4	2	25	25	n	1065	44.33
1D01	6	15	12	20	20	cl	1295	75.98
1D01	7	18	15	25	25	n	1269	57.01
1D01	8	10	8	85	85	n	2951	-64.25
1D01	9	35	25	55	55	cl	1885	55.86
1D01	10	4	2	15	15	n	765	63.55
1D01	12	3	1	130	170	c/s	2077	-10.45
1D01	13	6	4	75	75	c	2783	-84.90
1D03	1	5	3	12	12	cl	835	-57.38
1D03	2	4	2	65	100	c	1456	51.27
1D03	3	12	8	20	20	c	2311	-59.39
1D03	5	12	10	15	15	cl	951	-59.06
1D03	6	12	10	280	360	c	5910	-47.41
1D03	7	14	12	20	20	cl	2105	-62.86
1D03	8	12	10	10	10	n	1244	-28.93
1D03	9	6	4	75	75	c	1469	-44.29
1D03	10	10	8	10	10	cl	1221	-49.05
1D03	11	5	3	15	15	c	1210	62.88
1D03	12	5	3	15	15	n	1556	70.76
1D03	13	4	2	30	30	n	1449	41.50
1D03	14	14	12	20	20	cl	1576	-56.14
1D03	15	14	12	20	20	cl	1478	-52.58
1D03	16	2	1	10	10	n	1170	39.35
1D03	17	8	6	20	20	c	1064	89.91



C = Carrot, Cl = Clyinder, P = Pit, N = Needle, S = Split / Bifurcated, F = Flake

All measurements are in micrometers (µm)

Tile	Feature #	Particle		Entrance Hole		Track Shape	Track Length	Direction
		D <sub>1</sub>	D <sub>2</sub>	D <sub>minor</sub>	D <sub>major</sub>			
1D03	18	10	8	90	90	c	6263	58.14
1D03	19	8	6	120	120	c	3889	-18.71
1D03	20	3	2	20	20	n	1265	66.40
1D03	22	4	3	65	65	c	2472	-5.93
1E01	4	8	6	65	65	cl/n	4930	-48.04
1E01	6	5	3	150	150	c/s	1100	-4.12
1E01	8	10	8	45	45	n	1492	-20.08
1E01	9	12	10	25	25	n/s	1946	26.62
1E01	10	10	8	15	15	cl	725	-70.70
1E01	11	45	35	30	30	cl	1099	-66.48
1E01	12	6	4	175	175	c	4362	-22.72
1E01	13	25	20	70	70	cl	1772	54.36
1E01	14	8	6	20	20	cl/n	2270	51.45
1E01	15	4	2	5	5	n	1311	78.56
1E01	16	45	30	35	35	cl	1852	60.36
1E01	18			1300	1300	c		-0.15
1E01	22	3	1	10	10	n	715	83.99
1E02	2	6	4	30	30	n	3772	49.00
1E02	3	40	40	30	30	cl	2093	-88.41
1E02	5			550	550	st		-9.56
1E02	6	4	2	90	90	c	1341	-10.16
1E02	7	12	10	35	35	c	1475	-60.77
1E02	8	12	10	30	30	c	1435	-62.71
1E02	9	20	20	25	25	cl	1392	57.65
1E02	10	5	3	10	10	n	2422	-64.51
1E02	11	14	10	25	25	n	1235	78.23
1E02	12	3	2	45	45	c	1205	82.88
1E02	13			330	600	st		76.79
1F01	1	25	15	20	20	cl	1120	82.18
1F01	2	7	5	40	40	n	2349	-73.95
1F01	4	15	8	20	50	cl	2140	-83.53
1F01	5	10	8	50	50	n	5357	-66.24
1F01	6	6	4	140	140	c/s	4624	67.63
1F01	8	16	8	20	20	cl	1082	-62.82
1F01	10	4	2	50	50	c	1384	8.54
1F01	11	6	4	20	20	n	1197	75.08
1F01	13	8	6	20	20	cl	1478	72.92
1F01	14	10	6	145	145	c/s	1572	-7.66
1F01	15	12	8	580	580	c/s	6726	-84.20
1F01	16	4	2	40	40	n	1638	-11.27
1F01	18	6	4	30	30	n	2709	4.37
1F06	1	55	28	40	165	cl	2328	66.30
1F06	2	8	6	30	30	n	2865	-17.18
1F06	5	10	8	45	45	n	3462	71.13
1F06	8	10	8	30	30	cl/n	1055	-62.80
1F06	9	12	10	45	45	n	4563	56.54

C = Carrot, Cl = Cylinder, P = Pit, N = Needle, S = Split / Bifurcated, F = Flake

All measurements are in micrometers (μm)

Tile	Feature #	Particle		Entrance Hole		Track	Track Length	Direction
		D <sub>1</sub>	D <sub>2</sub>	D <sub>minor</sub>	D <sub>major</sub>	Shape		
2A01	1	10	10	55	55	c	773	-72.18
2A01	2	2	2	15	15	c	261	30.65
2A01	3	2	2	10	10	c	129	39.26
2A01	4			15	15	c/cl		45.00
2A01	5			20	20	c		29.26
2A01	6	2	2	15	15	c	271	26.57
2A01	7			10	10	c		35.44
2A01	8	2		10	10	c	211	32.04
2A01	9	5		10	10	cl	264	57.55
2A01	10	10		10	10	c	295	51.67
2A01	13			10	12	c		26.81
2A01	15			10	10	c		25.96
2A01	17			55	55	cl		34.33
2A01	18	5	5			cl	354	39.97
2A01	19			15	15	cl		-57.99
2A01	20			10	10	cl/c		26.07
2A01	21	3	3	35	35	c	573	-85.99
2A01	22	2	2	22	22	cl	237	32.77
2A01	23	2	2	12	15	cl	214	34.97
2A01	24	5	5	10	10	cl	422	-66.14
2A01	25			15	20	cl		31.78
2A01	26			10	30	cl		-51.77
2A01	27	3	2	15	20	cl	271	35.24
2A01	28	15	12	55	160	cl	593	-74.22
2A01	29	2	1	15	20	c	231	33.69
2A01	30	3	2	18	18	cl	345	55.65
2A01	31	3	2			cl	742	-39.98
2A01	32	2	1	18	18	cl	252	-57.04
2A01	33	3	2	10	10	cl	592	-44.27
2A01	34	3	2	10	10	cl	206	-72.55
2A01	35	3	2	12	12	cl	254	59.72
2A01	36	3	2	12	12	cl	378	-71.91
2A01	37			16	16	cl		42.03
2A01	38	4	2	10	20	cl	377	-66.12
2A01	39	3	1	8	10	cl	165	33.93
2A01	40	3	2	10	10	cl	247	59.40
2A01	41			20	20	cl		30.05
2A01	42	5	2	8	10	cl	310	-69.02
2A01	43			15	15	cl		41.53
2A01	44			10	10	cl		29.88
2A01	45			10	10	cl		34.99
2A01	46			15	15	cl		-9.99
2A01	47			10	10	cl		49.04
2A01	48			10	10	cl		26.19
2A01	49	5	3	12	12	cl	1583	-43.41
2A01	50	2	1	12	12	cl	264	58.99
2A01	51	60	55	60	65	st	848	
2A01	52			20	20	cl		35.95
2A01	53	3	2	10	10	c	320	33.33
2A01	54	2	1	15	15	c	310	33.28
2A01	55	3	2	20	20	cl	276	-66.75

C = Carrot, Cl = Cylinder, P = Pit, N = Needle, S = Split / Bifurcated, F = Flake

All measurements are in micrometers (µm)

Tile	Feature #	Particle		Entrance Hole		Track Shape	Track Length	Direction
		D <sub>1</sub>	D <sub>2</sub>	D <sub>minor</sub>	D <sub>major</sub>			
2A01	56			30	30	cl		-38.22
2A01	57	5	5	40	60	cl	1147	14.17
2A01	58	5	5	10	10	cl	1612	-44.79
2A01	59	6	6	66	66	c	2978	16.45
2A01	61	5	5	25	25	c	1333	-80.70
2A01	62			25	25	c		25.13
2A01	63			10	10	c		-29.72
2A01	64	5	5	25	25	c	559	-9.72
2A01	65			25	25	cl		72.80
2A01	67			25	25	cl		-64.66
2A01	68	10	10	30	35	cl/c	4083	62.55
2A01	69	5	4			cl	1249	61.81
2A01	70	5	4			c	8189	-14.56
2A06	1			55	55	c		54.03
2A06	2			80	145	cl/p		49.44
2A06	3	12	15	40	45	cl/p	272	46.66
2A06	4	5	1	85	55	cl	993	55.15
2A06	6			440	330	c		-56.39
2A06	9			660	660	cl		-69.76
2A06	10	12	15	20	20	cl	3181	1723
2A06	13	5	5	220	100	c	1017	75.24
2A06	15	15	15	25	25	cl	836	43.11
2A06	16	2	3	75	50	c	663	56.28
2A06	17	2	2	210	85	s	973	48.76
2A06	19	2	3	120	75	c	1049	-68.70
2A06	20	2	3	20	20	cl	725	49.66
2A06	21	0	2	75	50	c	1200	70.94
2A06	22	3	3	20	20	cl	1394	44.61
2A06	23	5	5	65	90	c	927	-67.69
2A06	26	2	2	45	45	cl		84.64
2A06	29			25	25	cl		-45.45
2A06	30			55	90	cl		-49.01
2A06	31	5	5	30	65	cl	1004	85.80
2A06	32	1	2	30	30	cl	674	62.44
2A06	35	3	1	10	10	cl	857	-45.26
2A06	36			20	25	cl		29.04
2A06	37			40	40	c		13.42
2A06	38	5	5	5	15	c	731	-37.57
2A06	39	6	6	90	110	c	2522	-71.08
2A06	41	4	3	55	55	c	2186	45.23
2A06	42	4	3	120	80	c	1481	22.23
2A06	44	4	2	20	20	cl	1179	0.00
2A06	44	22	8	35	35	cl	435	-36.63
2B01	2	3	5	40	40	n	2354	-48.33
2B01	4	6	6	110	110	c	3007	-85.09
2B01	6	25	30	40	40	cl	1422	-33.01
2B01	7	8	10	330	400	c	4453	-56.09
2B01	8	10	10	350	360	c	3271	50.28
2B01	9	3	6	30	30	c	904	32.87
2B01	11	6	8	80	140	c	2140	39.05
2B01	12	6	6	50	60	c	1084	-42.42
2B01	14	3	5	30	30	n	3881	

C = Carrot, Cl = Cylinder, P = Pit, N = Needle, S = Split / Bifurcated, F = Flake

All measurements are in micrometers (µm)

Tile	Feature #	Particle		Entrance Hole		Track Shape	Track Length	Direction
		D <sub>1</sub>	D <sub>2</sub>	D <sub>minor</sub>	D <sub>major</sub>			
2B01	16	2	4	55	55	n	1750	-47.20
2B01	17	5	5	80	80	c	3834	9.06
2B01	18	6	7	10	10	n	1107	76.68
2B05	3	6	4	90	90	c	2357	-51.14
2B05	4	35	18	10	20	n	4486	-86.08
2B05	5	6	4	10	10	n	2245	20.48
2B05	6	3	2	100	100	c	1279	-54.81
2B05	7	6	4	65	90	c	1831	-85.68
2B05	8	4	2	30	30	c	1609	-34.73
2B05	9	6	4	55	100	c	1387	47.24
2B05	10	8	6	90	100	c	1444	47.89
2B05	11	8	6	100	155	c	1648	40.11
2B05	12	3	2	80	110	c	995	47.67
2B05	13	8	6	110	170	c	1234	46.32
2B05	14	4	2	100	165	c	1181	43.99
2B05	15	4	2	265	290	c/s	1904	21.43
2C01	1	6	3	100	220	c	961	61.74
2C01	2	15	10	20	20	cl	1997	85.84
2C01	3	8	8	77	90	c	1640	41.30
2C01	4	6	6	450	550	c/s	2932	49.93
2C01	5	4	2	95	330	c/s	1417	-23.10
2C01	6	25	18	30	30	cl	3072	-86.36
2C01	7	4	4	65	90	c	2588	39.48
2C01	8	5	5	80	90	c	1408	40.12
2C01	9	7	5	60	80	c	1470	39.23
2C01	10	8	6	165	165	c	3077	-48.97
2C01	11	6	3	15	15	n	1030	-79.29
2C01	12	15	15	20	20	cl	1053	-82.80
2C01	13	4	4	55	85	c/s	1068	37.85
2C01	15	5	3	80	160	c	1385	-30.54
2C01	16	8	6	65	85	c	1877	35.75
2C01	17	6	3	45	50	c	1130	35.36
2C01	18	10	10	70	80	c	1720	45.52
2C01	19	8	6	20	20	n	2965	-59.19
2C01	20	6	4	55	70	c	1403	33.63
2C01	21	65	8	70	70	cl	1298	33.06
2C01	22	5	3	65	85	c/s	1463	35.53
2C01	23	35	20	30	30	cl	5056	-86.06
2C04	1	5	3	90	115	c	1382	50.98
2C04	2	8	6	100	170	c	1670	45.05
2C04	3	12	10	20	20	cl	635	84.61
2C04	4	4	2	20	20	n	1431	-44.91
2C04	5	6	4	110	190	c	1776	34.34
2C04	6	4	2	15	15	n	1426	-28.03
2C04	7	5	3	65	110	c	1840	43.90
2C04	8	8	6	80	140	c	1590	49.08
2C04	9	10	8	140	240	c	1688	37.61
2C04	10	3	2	15	15	n	842	51.36
2C04	11	5	3	85	160	c/s	1271	39.91
2C04	12	10	3	15	15	n	1025	
2C04	13	4	2	30	30	n	1387	69.97

C = Carrot, Cl = Cylinder, P = Pit, N = Needle, S = Split / Bifurcated, F = Flake

All measurements are in micrometers (µm)

Tile	Feature #	Particle		Entrance Hole		Track Shape	Track Length	Direction
		D <sub>1</sub>	D <sub>2</sub>	D <sub>minor</sub>	D <sub>major</sub>			
2D01	1	4	2	135	200	c/s	1720	39.24
2D01	2	4	2	85	130	c	1359	41.82
2D01	3	6	6	60	120	c	989	32.56
2D01	4	6	6	110	160	c	1281	39.07
2D01	5	6	6	90	130	c	2243	40.52
2D01	6	10	6	200	300	c/s	3993	43.96
2D01	7	8	8	110	180	c	2044	44.60
2D01	8	5	4	100	130	c	1804	41.17
2D01	9	5	4	80	120	c	1753	40.47
2D01	10	4	3	40	75	c	1193	39.03
2D01	11	6	6	160	220	c	2834	34.33
2D01	12	8	6	110	165	c	1750	43.74
2D01	14	4	4	55	85	c	1704	37.01
2D01	15	4	4	100	150	c	1602	35.41
2D01	16	6	6	100	150	c	2247	38.50
2D01	17	8	8	140	230	c	2365	35.82
2D01	18	8	10	30	30	cl	4384	22.31
2D01	19	10	10	140	280	c	3609	43.40
2D01	20	10	2	130	175	c	1607	41.56
2D01	22	3	3	40	40	c	2679	39.53
2D01	23	6	3	100	120	c	1704	40.61
2D01	24	4	2	65	90	c	1399	41.02
2D01	25	8	6	90	120	c	1684	40.61
2D01	26	8	6	120	150	c	2478	41.67
2D01	27	4	4	55	55	n	2811	-60.05
2D01	28	5	4	100	130	c	1417	39.36
2D01	29	5	4	55	75	c	1506	36.70
2D01	30	8	6	100	145	c	1734	46.83
2D01	31	8	6	55	75	c	1638	41.25
2D01	32	5	4	55	60	c	2708	40.10
2D01	33	5	4	65	145	c	1971	38.34
2D01	34	5	3	75	110	c/sc	1420	36.42
2D01	35	6	5	110	155	c	2178	42.65
2D01	36	5	4	50	60	c	1058	40.78
2D01	37	6	4	75	115	c	1866	43.55
2D01	38	5	4	100	135	c	1790	34.73
2D01	39	6	3	110	155	c	1941	41.91
2D01	40	10	10	120	175	c	3236	38.98
2D01	41	6	4	60	65	c	1467	45.96
2D01	42	7	5	60	110	c	2233	44.00
2D01	43	6	5	75	120	c	2155	42.50
2D01	44	12	12	130	220	c	4060	45.77
2D01	45	8	6	75	110	c	1727	41.65
2D01	46	8	6	120	170	c	2111	40.32
2D01	47	6	4	75	95	c	1700	43.39
2D01	48	6	4	70	110	c	1955	38.81
2D01	49	4	2	30	30	n	1149	36.05
2D01	50	11	9	20	20	cl	2441	-75.86
2D01	51	6	4	150	150	c	1350	43.51
2D01	52	8	6	95	160	c	1412	41.02
2D01	53	8	6	90	110	c	1357	25.88

C = Carrot, Cl = Clyinder, P = Pit, N = Needle, S = Split / Bifurcated, F = Flake

All measurements are in micrometers (µm)

Tile	Feature #	Particle		Entrance Hole		Track Shape	Track Length	Direction
		D <sub>1</sub>	D <sub>2</sub>	D <sub>minor</sub>	D <sub>major</sub>			
2D01	54	8	6	90	160	c	2061	42.78
2D01	55	8	6	50	50	c	1444	42.00
2D01	56	6	4	110	165	c	1963	45.16
2D01	57	4	3	25	25	cl	987	37.45
2D01	58	5	3	40	40	n	1359	-66.29
2D01	59	5	3	75	120	c	1081	36.44
2D01	60			30	30	cl		-74.51
2D01	61	4	2	55	85	c	1585	37.81
2D01	62	4	2	80	80	c/s	1776	45.39
2D01	63	12	10	15	15	cl	1325	-31.41
2D01	64	4	3	60	60	n	2752	42.09
2D01	65	8	6	120	190	c	2406	43.54
2D01	66	9	7	85	140	c/s	2973	39.95
2D01	67	6	4	65	120	c	1282	43.58
2D01	68	7	5	100	150	c	1675	40.97
2D01	69	2	1	60	80	c	1118	44.69
2D01	70	10	10	100	120	c	2097	39.27
2D01	71	7	5	90	130	c	2415	37.22
2D01	72	6	4	130	200	c	2010	44.05
2D01	73	11	9	55	55	n	3135	-33.62
2D01	74	2	2	30	30	n	882	-13.77
2D01	75			50	50	n		-13.45
2D01	76			70	70	c		35.53
2D01	77	6	4	65	65	c/s	1151	41.20
2D01	78	2	2	90	155	c	1968	36.27
2D01	79	8	4	80	120	c	1560	38.17
2D01	80	8	6	50	50	c	1586	39.89
2D01	81	8	6	45	45	n	1683	42.03
2D01	82	10	8	15	15	cl	748	-23.22
2D01	83			100	140	c		30.34
2D01	84			230	230	st		0.00
2D01	85	35	25	30	30	cl	1768	37.65
2D01	86	10	10	60	95	d/s	2015	32.87
2D01	87	6	4	110	140	c	1311	36.62
2D01	88	6	4	120	200	c/s	1312	40.44
2D01	89	6	5	50	75	c	1359	40.02
2D01	90	12	8	20	20	cl	1112	82.30
2D01	91	10	8	110	170	c	2471	34.29
2D01	92	10	8	110	70	c	1828	48.27
2D01	93	6	4	70	70	c	2043	32.94
2D01	94	5	3	90	160	c	1219	40.34
2D01	95	6	4	120	160	c	1663	41.37
2D01	96	7	5	85	110	c	2821	39.15
2D01	97	3	2	50	50	n	2157	-23.07
2D01	98	10	8	65	120	c	1312	39.44
2D01	99	6	4	40	40	c	1312	40.26
2D01	100	100	60	45	45	cl	1158	-40.07
2D03	1	6	4	55	55	c	1110	44.46
2D03	2	6	4	65	70	cl/c	2391	-18.97
2D03	3	4	2	110	165	c	1449	42.10
2D03	4	6	4	110	115	cl/n	1628	-81.12

C = Carrot, Cl = Clyinder, P = Pit, N = Needle, S = Split / Bifurcated, F = Flake

All measurements are in micrometers (µm)

Tile	Feature #	Particle		Entrance Hole		Track Shape	Track Length	Direction
		D <sub>1</sub>	D <sub>2</sub>	D <sub>minor</sub>	D <sub>major</sub>			
2D03	6	5	3	30	30	n	1663	44.59
2D03	7	7	5	165	220	c	1492	46.97
2D03	8	6	4	110	165	c	1218	52.22
2D03	9	6	4	120	165	c/s	1415	46.73
2D03	10			80	275	n		-10.79
2D03	11	11	9	85	170	n	2015	40.00
2D03	12	4	2	85	130	c	1303	38.76
2D03	13	8	6	30	30	n	2119	38.94
2D03	14	8	6	45	45	n/s	3656	27.98
2D03	15	9	7	50	50	n/s	2547	-27.44
2D03	16	14	12	300	570	c	2876	47.47
2D03	17	6	4	50	75	c	1603	44.78
2D03	18	8	6	75	100	c	1497	42.51
2D03	19	7	5	75	100	c	1177	48.86
2D03	20	6	4	55	80	n	1770	-15.67
2D03	21	14	8	120	210	c	3286	47.80
2D03	22	7	5	150	240	c/s	1588	46.37
2D03	23	45	30	45	45	cl	1105	72.63
2D03	24	35	28	30	30	cl	2078	-80.85
2D03	25	10	10	75	155	c	2170	38.08
2D03	26	12	9	120	275	c	1683	45.35
2D03	27	12	8	60	60	n/s	3146	-74.00
2D03	28	6	4	110	165	c	1416	43.07
2D03	29	12	10	130	220	c	3034	44.32
2D03	30	12	8	120	270	c	2095	37.37
2D03	31	12	8	120	220	c	2796	47.00
2D03	32	12	8	110	110	c	1333	44.77
2E01	1	8	8	80	80	c	1813	36.19
2E01	2	6	4	80	80	c	3178	55.44
2E01	3	12	10	130	130	c	2699	41.74
2E01	4	13	11	110	220	c	1711	43.58
2E01	5	6	4	85	85	c	1711	41.51
2E01	6	6	4	90	185	c	1866	44.77
2E01	7	5	3	80	80	n	1946	37.32
2E01	8	5	3	120	165	c	1997	40.76
2E01	9	15	12	120	180	c	3621	53.15
2E01	10	6	4	60	60	c	1703	41.29
2E01	11	12	10	110	150	c	3535	45.39
2E01	12	6	4	65	130	c	1584	42.46
2E01	13	6	4	160	330	c/s	1813	49.25
2E01	14	4	2	50	50	c/s	961	26.49
2E01	15	5	3	80	80	c	928	37.37
2E01	16	4	2	30	30	n	1027	44.50
2E01	17	4	2	70	70	c	863	43.43
2E01	18	4	2	110	150	c	1344	42.41
2E01	19	6	4	90	150	c	1786	-11.12
2E01	20	5	3	20	20	n	1337	-8.68
2E01	21	4	2	40	40	n	1310	39.38
2E01	22	7	4	140	230	c/s	2114	-10.25
2E01	23	4	2	30	30	n	945	44.02
2E01	24	12	10	110	195	c	1803	
2E01	25	12	10	110	150	c	2992	39.31



C = Carrot, Cl = Clyinder, P = Pit, N = Needle, S = Split / Bifurcated, F = Flake

All measurements are in micrometers (µm)

Tile	Feature #	Particle		Entrance Hole		Track Shape	Length	Direction
		D <sub>1</sub>	D <sub>2</sub>	D <sub>minor</sub>	D <sub>major</sub>			
2E01	26	8	6	160	200	c/s	2278	38.52
2E01	27	6	4	80	80	c/s	3103	43.08
2E01	28	6	4	60	60	c	1331	37.52
2E01	29	20	10	20	20	cl	897	80.54
2E01	30	15	13	160	190	c	4592	40.94
2E01	31	6	4	110	110	c	1806	39.12
2E01	32	9	7	95	95	c	3569	42.20
2E01	33	6	4	50	50	c	1906	38.34
2E01	34	6	4	100	160	c/s	2044	38.96
2E01	35	5	3	130	130	c/s	1761	43.86
2E01	36	10	3	60	110	c	1978	34.93
2E01	37			30	40	c/p		-74.27
2E01	38	6	4	55	110	c	1510	38.22
2E01	39	5	3	75	110	c	1965	35.94
2E01	40	6	4	30	30	c	1562	39.38
2E01	41	5	2	70	70	c	1499	38.13
2E01	43	5	2	110	180	c	2045	43.84
2E01	44	7	5	70	70	c	2540	35.70
2E01	45	6	3	130	230	c	1715	39.62
2E01	46	7	5	90	150	c	2364	36.04
2E01	47	15	12	120	170	c	5016	46.81
2E01	48	14	12	110	160	c	3188	42.57
2E01	49	7	5	150	230	c/s	2506	36.94
2E01	50	6	4	130	230	c	2226	46.89
2E01	51	5	3	120	140	c	1493	43.14
2E01	52	3	1	40	40	n	2204	-40.86
2E01	53	8	6	110	110	c	2692	40.10
2E01	54	10	12	150	220	c	2461	38.15
2E01	55	5	3	130	190	c	2622	47.05
2E01	56	8	5	110	170	c/s	1900	37.07
2E01	57	7	5	220	220	c/s	2057	45.02
2E01	58	10	8	165	240	c	4119	41.88
2E01	59	12	10	160	250	c	3554	40.72
2E01	60	5	3	150	150	c/s	2667	43.07
2E01	61	5	3	100	100	c	2834	38.55
2E01	62	4	2	110	110	c/s	1653	35.92
2E01	63	8	6	60	60	c	2039	41.46
2E01	64	6	4	160	160	c	1711	37.12
2E01	65	5	3	110	160	c	2189	39.29
2E01	66	8	8	120	230	c	2153	46.35
2E01	67	8	7	160	160	c	2362	36.64
2E01	69	6	4	75	140	c	2137	38.55
2E01	70	6	4	50	50	n	2528	-14.76
2E01	71	5	3	130	130	c	2127	42.07
2E01	72	5	3	35	35	c	1703	-72.46
2E01	73	8	6	90	130	c	1742	37.70
2E01	74	6	2	115	170	c	1205	35.23
2E01	75	4	2	90	165	c	1475	42.02
2E01	76	8	4	100	200	c	1452	39.49
2E01	77	5	3	85	85	c	1555	39.88
2E01	78	6	4	130	190	c	1844	42.89

C = Carrot, CI = Clyinder, P = Pit, N = Needle, S = Split / Bifurcated, F = Flake

All measurements are in micrometers (µm)

Tile	Feature #	Particle		Entrance Hole		Track	Track	Direction
		D <sub>1</sub>	D <sub>2</sub>	D <sub>minor</sub>	D <sub>major</sub>	Shape	Length	
2E01	79	6	4	100	130	c	1834	39.92
2E01	80	5	3	60	60	c	1518	44.33
2E01	81	8	6	80	100	c	1680	43.62
2E01	82			200	200	st		-25.62
2E01	83	10	10	115	170	c	1962	39.71
2E01	84	6	4	120	200	c	2104	38.67
2E01	85	4	2	90	150	c	1582	41.89
2E01	86	7	5	100	125	c	2154	38.51
2E01	87	6	4	55	80	c	1307	39.91
2E01	89			700	700	c		-79.97
2E02	1	4	2	30	30	n	1028	46.55
2E02	2	4	2	12	12	n	614	54.85
2E02	3	11	5	130	260	c/s	2372	49.89
2E02	4	6	4	60	60	n	3757	-25.36
2E02	5	4	2	30	30	n/c	1122	-44.00
2E02	6	3	1	55	75	c/s	1050	49.32
2E02	7	6	5	75	130	c	1220	41.80
2E02	8			1100	1100	st		72.78
2E02	9	10	10	10	10	n	950	-77.59
2E02	10	3	2	200	410	c/s	1468	37.87
2E02	11	3	2	15	15	n	655	79.20
2E02	12	8	4	65	110	c	2018	47.84
2E02	13	3	2	75	130	c	1219	44.89
2E02	14	10	10	75	120	c	2159	47.23
2E02	15	6	4	140	230	c	1803	41.90
2E02	16	3	1	65	110	c/s	1101	43.86
2E02	17	5	3	65	75	c	1430	48.55
2E02	19	10	10	100	100	n	4906	-11.72
2E02	20	3	1	140	250	c	1716	43.41
2E02	21	5	3	75	150	c/s	1692	42.94
2E02	22	12	10	110	190	c	2641	39.08
2E02	23	12	10	100	165	c	3096	50.09
2E02	24	10	8	50	50	c	1817	39.34
2E02	25	3	2	200	370	c	1779	46.30
2E02	26	10	8	55	55	n/s	2930	-1.59
2E02	27	4	2	50	50	n	1293	9.81
2E02	28	7	2	120	220	c/s	2082	42.63
2E02	29	14	12	165	330	c	2886	46.30
2E02	30	14	12	20	20	cl	1104	-80.98
2E02	31	4	2	55	100	c	2044	43.15
2E02	32	4	2	25	25	n	840	46.80
2E02	33	6	4	75	140	c	1361	44.50
2E02	34	8	6	120	120	c	3971	-55.20
2E02	35	8	6	85	165	c	1610	43.03
2E02	36	5	3	20	20	n	3108	-63.57
2E02	37			55	55	st		45.04
2E02	38	160	55	110	110	cl	2507	53.94
2E02	39	4	2	40	40	c	1456	-10.88
2E02	40	4	2	20	20	n	1458	78.71
2E02	41	4	2	40	40	n	1346	-24.09
2E02	42	4	2	10	10	n	1443	-70.50

C = Carrot, Cl = Cylinder, P = Pit, N = Needle, S = Split / Bifurcated, F = Flake

All measurements are in micrometers (µm)

Tile	Feature #	Particle		Entrance Hole		Track	Track	Direction
		D <sub>1</sub>	D <sub>2</sub>	D <sub>minor</sub>	D <sub>major</sub>	Shape	Length	
2E02	43	3	2	40	40	n	995	23.64
2E02	44	6	5	75	115	c	1566	40.35
2E02	45	6	5	20	20	n	1734	72.25
2F01	1	5	5	70	70	n	766	-86.04
2F01	2	2	2	20	20	c	555	85.80
2F01	3			15	15	n		78.43
2F01	4			290	290	bell/st		-80.00
2F01	5	8	6	55	55	cl/s	3553	-50.38
2F01	6	9	6	50	50	cl	1653	-17.18
2F01	9	5	5	75	75	c	1079	45.18
2F01	10			40	40	cl		-85.81
2F01	11	4	2	100	100	c	1380	42.55
2F01	12	40	30	40	40	cl	1161	73.25
2F01	13	10	8	170	500	c	1887	37.50
2F01	14	8	6	160	220	c	2225	34.98
2F01	15	4	2	110	130	c	1171	46.13
2F01	16	4	2	140	195	c	1122	47.55
2F01	17	4	2	165	300	c	1169	40.68
2F01	18	4	2	80	120	c	1289	43.19
2F01	19	5	5	270	400	c/s	1980	44.85
2F01	21	10	10	110	185	s/c	1946	45.16
2F01	22	4	2	130	265	c	1042	39.44
2F01	23	6	4	155	295	c	916	43.95
2F01	24	3	2	55	65	c	1142	40.80
2F01	25	8	6	165	300	c	1496	43.59
2F01	26	8	6	120	180	c	1418	43.34
2F01	27	6	4	80	120	c	1143	43.53
2F01	28	8	6	100	165	c	1154	45.17
2F01	29	7	5	70	100	c	1298	40.80
2F01	30	7	5	110	140	c	1705	43.84
2F01	31	8	4	145	220	c/s	3245	48.02
2F01	32	6	4	50	55	n	913	42.74
2F01	33	4	2	110	145	c	1893	42.29
2F01	34	4	2	110	125	c	1659	42.20
2F01	35	4	2	40	45	c	1079	44.53
2F01	36	4	2	110	190	c	1087	51.49
2F01	37	4	2	220	310	c	1363	40.40
2F01	38	4	2	60	70	c	1078	44.53
2F01	39	4	2	80	110	c/s	1051	36.93
2F01	40			55	55	c		41.85
2F01	41	10	6	45	45	c	1364	44.69
2F01	42	6	4	110	160	c/s	855	47.25
2F01	43	6	4	110	200	c	2113	43.31
2F01	44	6	3	220	380	c	2471	40.52
2F01	45	6	4	135	190	c	1525	36.70
2F01	46			95	100	c		76.86
2F01	47	4	2	130	220	c/s	1903	47.15
2F01	48	4	2	110	190	c	1196	44.14
2F01	49	8	5	170	285	c	1438	38.41
2F01	51			85	130	c	1258	41.03
2F01	52	3	2	95	115	c	1015	37.69

C = Carrot, CI = Clyinder, P = Pit, N = Needle, S = Split / Bifurcated, F = Flake

All measurements are in micrometers (µm)

Tile	Feature #	Particle		Entrance Hole		Track	Track	Direction
		D <sub>1</sub>	D <sub>2</sub>	D <sub>minor</sub>	D <sub>major</sub>	Shape	Length	
2F01	53			130	185	c		26.06
2F01	54	6	4	20	20	cl	657	12.01
2F01	55	7	5	110	165	c	1747	49.13
2F01	56	6	4	75	110	c	1152	41.37
2F01	57	7	5	85	110	c	1273	41.66
2F01	58	12	10	120	220	c	2578	40.79
2F01	59	6	4	75	110	c	2308	47.00
2F01	60	6	4	95	125	c	2198	45.95
2F01	61			120	130	c		39.65
2F01	62	6	4	90	175	c	1335	37.06
2F01	63	10	8	120	330	c	2164	46.59
2F01	64			95	130	c		42.82
2F06	1	5	5	12	15	cl	1610	-59.78
2F06	2	5	5	55	55	cl/c	1394	-89.07
2F06	3	5	5	30	30	c	1210	-45.14
2F06	4			1110	1110	cl		-48.16
2F06	6	7	5	30	40	c	2179	64.80
2F06	7	7	5	20	25	c/s	862	56.76
2F06	8			40	50	c		-19.03
2F06	9	7	5	35	35	cl	1228	62.86
2F06	10	8	5	55	55	cl/c	3270	-62.98
2F06	11	5	3	25	30	c	776	-18.54
2F06	13	12	10	10	15	cl	1029	81.44
2F06	14			45	50	cl		-20.14



REPORT DOCUMENTATION PAGE			Form Approved OMB No. 0704-0188	
Public reporting burden for this collection of information is estimated to average 1 hour per response, including the time for reviewing instructions, searching existing data sources, gathering and maintaining the data needed, and completing and reviewing the collection of information. Send comments regarding this burden estimate or any other aspect of this collection of information, including suggestions for reducing this burden, to Washington Headquarters Services, Directorate for Information Operations and Reports, 1215 Jefferson Davis Highway, Suite 1204, Arlington, VA 22202-4302, and to the Office of Management and Budget, Paperwork Reduction Project (0704-0188), Washington, DC 20503.				
1. AGENCY USE ONLY (Leave Blank)	2. REPORT DATE August 1999	3. REPORT TYPE AND DATES COVERED Technical Memorandum		
4. TITLE AND SUBTITLE Optical Analysis of Impact Features in Aerogel From the Orbital Debris Collection Experiment on the Mir Station		5. FUNDING NUMBERS		
6. AUTHOR(S) Friedrich Hörz, Glen Cress, Mike Zolensky, Thomas H. See*, Ronald P. Bernhard*, Jack L. Warren*				
7. PERFORMING ORGANIZATION NAME(S) AND ADDRESS(ES) Lyndon B. Johnson Space Center Houston, Texas 77058		8. PERFORMING ORGANIZATION REPORT NUMBERS S-849		
9. SPONSORING/MONITORING AGENCY NAME(S) AND ADDRESS(ES) National Aeronautics and Space Administration Washington, DC 20546-0001		10. SPONSORING/MONITORING AGENCY REPORT NUMBER TM-1999-209372		
11. SUPPLEMENTARY NOTES * Lockheed-Martin				
12a. DISTRIBUTION/AVAILABILITY STATEMENT Available from the NASA Center for AeroSpace Information (CASI) 7121 Standard Hanover, MD 21076-1320 Subject category: 88		12b. DISTRIBUTION CODE		
13. ABSTRACT (Maximum 200 words) The Mir Environmental Effects Package (MEEP) was deployed on the Mir station and retrieved after 18 months in space. The payload included the orbital debris collector (ODC), designed and built at the Johnson Space Center to capture and return analyzable residues of the man-made and natural particulate environment in low-Earth orbit for a detailed assessment of its compositional makeup and potential origins. The ODC exposed 2 identical trays, with highly porous, low-density SiO <sub>2</sub> aerogel as the basic collector medium, pointed in opposite directions. The aerogel was expected to gently decelerate and capture hypervelocity particles, as opposed to other media that resulted in melting or vaporization of many impactors. Even cursory examination of the returned ODC collectors revealed a surprising variety of impact features. The compositional analyses using scanning electron microscope-energy-dispersive X-ray spectroscopy concentrated on a survey-type inventory of diverse particle types and associated impact features. Detections, in the form of carrot-shaped tracks and shallow pits, included metallic Al, stainless steel, soldering compounds, human waste, and paint flakes. Many pits contained no detectable impactor residue (it was assumed to have vaporized), but most of the tracks contained analyzable residue. The study showed that aerogel would be useful for future low-velocity impact analysis.				
14. SUBJECT TERMS orbital debris; space debris; debris; aerogel; orbital debris collector; microscopes; spectroscopy;		15. NUMBER OF PAGES 158	16. PRICE CODE	
17. SECURITY CLASSIFICATION OF REPORT Unclassified	18. SECURITY CLASSIFICATION OF THIS PAGE Unclassified	19. SECURITY CLASSIFICATION OF ABSTRACT Unclassified	20. LIMITATION OF ABSTRACT Unlimited	